Developing and Modelling 3D-printed Soft Active Elastocaloric Regenerators

An exploration for green cooling

Wang, Kun

Publication date:
2023

Document Version
Publisher's PDF, also known as Version of record

Doctor of Philosophy
Doctoral thesis in Energy conversion and storage

DTU Energy
Department of Energy Conversion and Storage

Developing and Modelling 3D-printed Soft Active Elastocaloric Regenerators

An exploration for green cooling

Kun Wang

Kgs. Lyngby 2023

DTU

Principal supervisors:
Prof. Dr. Rasmus Bjørk,
Department of energy conversion and storage, DTU, Denmark
Dr. Christian R.H. Bahl
SUBRA A/S, Denmark
Co-supervisors:
Dr. Kurt Engelbrecht
Viegand Maagøe, Denmark

Assessment committee:
Prof. Dr. Stefan Seelecke,
Department of Systems Engineering, Saarland University, Germany
Ass. Prof. Dr. Jaka Tušek
Faculty of Mechanical Engineering, University of Ljubljana, Slovenia
Prof. Dr. Ming Chen,
Department of energy conversion and storage, DTU, Denmark

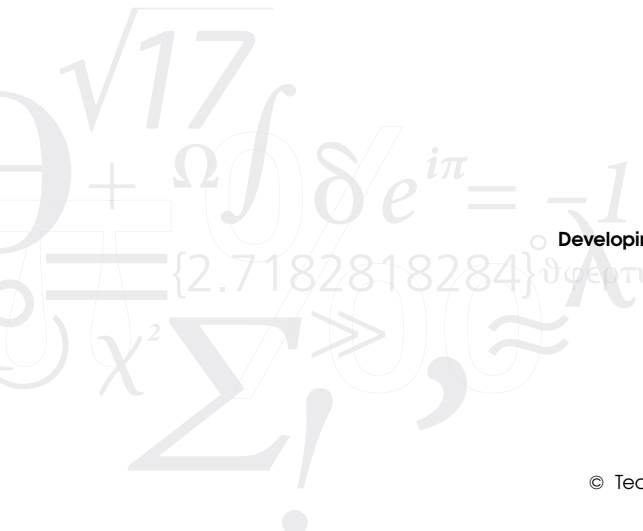

DTU Energi
Department of Energy Conversion and Storage
Technical University of Denmark
Anker Engelunds Vej
Building 301
2800 Kongens Lyngby, Denmark

Developing and Modelling 3D-printed Soft Active Elastocaloric Regenerators

Kun Wang
PhD thesis
November 2023

Preface

This PhD dissertation is submitted to the Department of Energy Conversion and Storage, in the partial fulfillment of the requirements for acquiring the PhD degree, at the Technical University of Denmark (DTU). The work has been performed over a period of three years, from 1 December 2020 to 30 November 2023, at the two Sections for Continuum Modelling and Testing (CMT) and for Structural Analysis and Modelling (SAM), Department of Energy Conversion and Storage, Technical University of Denmark.

This PhD project was conducted under the supervision of Dr. Christian R. H. Bahl, Dr. Kurt Engelbrecht, and Professor Dr. Rasmus Bjørk. Valuable knowledge and inspiration has been gained during a four-month external research stay in the Soft Robotic Matter group at the AMOLF institute in Netherlands, under the supervision of Ass. Prof. Dr. Bas Overvelde. The majority of this work was carried out at DTU energy, with a partial work conducted at the AMOLF institute.

The outcome of this research is reflected in four scientific articles provided in Appendix A. The Chapter 3 and 4 of the thesis are a compilation of two publications, highlighted at the beginning of each chapter. The remaining two chapters of the investigation part are based on the two articles in preparation. The supervisor team and department section changed during the last six months of the PhD project, but this project has been accomplished seamlessly with the guidance of my present supervisor Rasmus Bjørk.

Copenhagen, 29th November 2023

Kun Wang

Abstract (English)

Worldwide, heating and cooling account for the largest contribution to energy consumption and greenhouse gas emissions [1]. Decarbonizing heating and cooling is crucial for achieving net-zero carbon dioxide emissions. However, existing technologies continue to heavily rely on the combustion of natural gas for heating and the compression of volatile greenhouse gases for cooling. It is thus crucially important to explore the next generation of green cooling and heating to replace vapour compression.

Elastocaloric cooling has been recommended as the most promising non-vapor compression technology by the US Department of Energy and EU Commission, utilizing the temperature change of materials in response to uniaxial strain. In this PhD thesis, low-stress regenerative elastocaloric cooling employing printable soft elastomers is explored. Soft elastocaloric elastomers exhibit a much lower applied stress requirement to induce the elastocaloric effect (eCE) compared to alloys. Implementing additive manufacturing (AM) facilitates the fabrication of fully-printed elastocaloric regenerators with customized heat-transfer microchannels. Moreover, AM allows the design of 3D-printed regenerators in a compact configuration. Prior to regenerator printing, five commercial thermoplastic filaments were screened as potential elastocaloric elastomers, suggesting thermoplastic polyurethane (TPU). NinjaFlex TPU demonstrates a notable material coefficient of performance (COP_{mat}) of 3.2 and a maximum adiabatic temperature change (ΔT_{ad}) of 12 K at 5.7 MPa.

Importantly, operating in an active elastocaloric cooling cycle, these regenerators display an asymmetric fluid exchange, due to the large required strains and associated volume change. A finite-element (FE) model is developed to qualitatively predict regenerator volume changes, and is shown to demonstrate a good agreement with experimental measurements. Furthermore, the regenerator volume changes and geometrical information obtained from FE simulations can be supplied to an improved 1D numerical model for modeling large-deformation elastocaloric regenerators. This combination facilitates numerical investigations for the active regenerator performance and parametric optimization. A theoretical maximum temperature span of 11.9 K is achieved at a Utilization of 0.7 in square-channel regenerators based on NinjaFlex TPU.

The experimental proof-of-concept was performed on a volume compensation flow system using three 3D printed regenerators with different microchannels. Due to the need for watertight regenerators, the regenerator fabrication is compromised

to employing the FilaFlex TPU with a lower ΔT_{ad} of 2.5 K. The results show a REG3 regenerator with a low porosity ϵ of 19.4%, achieving a maximum temperature span of 4.7 K and a cooling power of 2.5 W, while a REG2 regenerator (ϵ = 27.2%) attains a maximum COP of 1.7. The 3D printed regenerator achieves remarkable regeneration ratio of 1.84 and specific cooling power of 1850 W/kg, comparable to some polymer-based and NiTi-based prototypes. Overall, such 3D-printed eCE regenerators could inspire research in low-stress regenerative elastocaloric cooling using cost-efficient elastomers, paving the way for wide-ranging applications in cooling and heating systems.

Abstract (Danish)

Globalt udgør opvarmning og køling den største del af energiforbruget og udledningen af drivhusgasser [1]. Dekarbonisering af opvarmning og køling er afgørende for at opnå netto-nul udledning af kuldioxid. Eksisterende teknologier er dog stadig baseret på forbrænding af naturgas til opvarmning og komprimering af flygtige drivhusgasser til køling. Dette understreger vigtigheden af at udforske næste generation af grøn køling og opvarmning for at erstatte kompressionsteknologien.

Elastokalorisk køling er blevet anbefalet som den mest lovende køleteknologi uden kompression af det amerikanske energiministerium og EU-kommissionen. Den udnytter temperaturændringen af materialer som respons på ensrettet belastning. I denne PhD-afhandling udforskes lavspændings regenerativ elastokalorisk køling ved hjælp af printbare bløde elastomerer. Bløde elastokaloriske elastomerer kræver betydeligt mindre påført mekanisk spænding for at inducere den elastokaloriske effekt (eCE) sammenlignet med legeringer. Anvendelse af additiv fremstilling (AM) muliggør fremstilling af fuldt printede elastokaloriske regeneratorer med tilpassede varmeoverføringsmikrokanaler. Desuden tillader AM design af 3D-printede regeneratorer i en kompakt konfiguration. Før regeneratorprintning screenes potentielle elastokaloriske elastomerer i fem kommercielle termoplastiske filamenter, hvilket antyder termoplastisk polyurethan (TPU). NinjaFlex TPU viser en bemærkelsesværdig materialeydelseskoefficient (COP_{mat}) på 3,2 og en maksimal adiabatisk temperaturændring (ΔT_{ad}) på 12 K ved 5,7 MPa.

Vigtigst af alt viser regeneratorerne, når de opererer i en aktiv elastokalorisk kølecyklus, en asymmetrisk fluidudveksling på grund af de store påkrævede tøjninger og den tilknyttede volumenændring. En finite element (FE) model er udviklet til at forudsige regeneratorvolumenændringer kvalitativt og viser god overensstemmelse med eksperimentelle målinger. Desuden kan regeneratorvolumenændringer og geometrisk information fra FE-simulationer integreres i en forbedret 1D-numerisk model til at simulere elastokaloriske regeneratorer under store tøjninger. Denne kombination muliggør numeriske undersøgelser af den aktive regeneratorpræstation og parametrisk optimering. En teoretisk maksimal temperaturspænding på 11,9 K opnås ved en udnyttelse på 0,7 i regeneratorer med firkantede kanaler baseret på NinjaFlex TPU.

De eksperimentelle proof-of-concepts udføres på et volumenkompensationsflowsystem ved hjælp af tre 3D-printede regeneratorer med forskellige mikrokanaler. På grund af behovet for vandtætte regeneratorer anvendes FilaFlex TPU med en lavere

ΔT_{ad} på 2,5 K. Resultaterne viser, at en REG3-regenerator med en lav porøsitet ϵ på 19,4%, opnår en maksimal temperaturspænding på 4,7 K og en kølingseffekt på 2,5 W, mens en REG2-regenerator (ϵ = 27,2%) opnår en maksimal COP på 1,7. Den 3D-printede regenerator opnår en bemærkelsesværdig regenerationsforhold på 1,84 og specifik kølingseffekt på 1850 W/kg, sammenlignelig med polymerbaserede og NiTi-baserede prototyper. Overordnet set kunne sådanne 3D-printede eCE-regeneratorer inspirere forskning inden for lavspændingsregenerativ elastocaloric køling ved hjælp af omkostningseffektive elastomerer og åbne muligheder for omfattende anvendelser inden for køle- og varmesystemer.

Acknowledgements

In sharing this thesis, I do so with deep gratitude for this doctoral journey that has unfolded over the past three years, marked not only by academic growth but also by the invaluable support and encouragement of those around me. This period has been filled with scientific exploration, self-discovery, and exceeding happiness: there was the joy of finding new things, the joy of getting experiments working out, the joy of solving a long-standing confusion, the joy of sharing little achievements with friends. There are also countless moments of frustration, exhaustion, sleepless nights struggled with hardships, and self-doubt, while it made the journey more profound and worthwhile. Each facet of this journey has been a teacher, shaping my path to here and encouraging me to be fearless. Hereby, I want to extend my heartfelt thanks to every moment, the guidance of mentors, and the unwavering support of family and friends who are always there with me throughout this doctoral voyage. Without you all, it is impossible for the fulfillment of this thesis.

First and foremost, I would like to express my heartfelt gratitude to my previously principle supervisor, **Dr. Christian R. H. Bahl**, and co-supervisor, **Dr. Kurt Engelbrecht**. **Christian**, I am deeply thankful for the opportunity that you gave me to study at DTU and for the plenty time and effort that you invested in me and in my research. I really enjoyed to work with you as your PhD student and admirable to your profound theoretical knowledge. You are patiently instructing me when I was confused with some basic concepts and guiding me to find out the reason step by step on a white board, always being clear finally. You never impose your view or opinions; instead, you always entrust and encourage me, allowing the freedom to explore my own ideas. It has had a significant impact on developing my research independence. **Kurt**, for me your are a phenomenal supervisor and an incredible fountain of inspiration. Your profound expertise ranging from practical setups to numerical simulations consistently yields fruitful ideas and distinctive insights, which are always inspiring. You generously devoted your time in aiding me, whether in building my experimental setup or advancing my simulation work. I have been very fortunate to have you as my supervisor. Next, I want to convey my sincerest thanks for my principle supervisor, **Prof. Rasmus Bjørk**. You ensured a smooth handover of my project when it was placed under your supervision. Previously you provided an excellent working experience as my section head in CMT section. As a supervisor, you are responsible and are willing to spend a lot of time to make sure that my project can be accomplished smoothly, guiding my experiments and revising ar-

ticles. It has been an extraordinary experience to be working with you. Looking forward to continued collaboration with you in the future. I also want to express my sincere appreciation to our SAM section head **Prof. Luise Theil Kuhn**, for your assistance in extending the duration after my thesis hand-in, which is really helpful for me to finish the rest of works.

I have been very fortunate to have the opportunity to external study in the Soft Robotic Matter group at AMOLF institute in Netherlands. My sincere thanks to **Assoc. Prof. Bas Overvelde** for your supervision and supportive guidance for my FE simulation and experiments, and many insightful suggestions, helping me dive deeper into my research results. You have versatile knowledge in soft robotics, soft matter, 3D printing, and mechanics, which is infectious to me. I will never forget our research discussions in group meetings and many daily coffee breaks with interesting group members, and also marvelous soft robotics, and charming metamaterials. Additionally, I am grateful to wonderful group members: **Niels Commandeur, Dr. Shibo Zou, Dr. Sumit Mohanty, Paul Ducarme, Sergio Picella, Katrien Van Riet, Charlotte Bording, Alberto Comoretto, Mannus Schomaker, Luca Zanetti, Arthur Walker** – for the countless help to me and the frequent meetups where unfiltered discussions on wide-ranging topics were always with beers. Thanks to **Niels** for your numerous help in my 3D printing and experiments, and you add the 3D printer with "magic wings". Also thanks to you and **Charlotte** for introducing me to the joy of bouldering. Thanks to **Paul** and **Alberto** for your assistance in learning and using APDL scripts, as well as for **Paul** introducing me to the football team. I want to express my appreciation to **Shibo** for valuable discussions of my experiment design and a special farewell gift. **Sergio**, I want to thank you for bringing me to the first glimpse of the lab and group and helping me to use the fluidic setup. **Katrien**, thanks for sharing office with you and **Sergio**, and introducing your fantastic toolkit and interesting Dutch things.

Life in Denmark would not have been the same without the companionship and support of all the amazing colleagues and friends I met here. I would like to thank to my office mates in our 143 office at DTU energy – **Dr. Stefan Pollok, Dr. Kai Knobloch, Dr. Sina Jafarzadeh, Dr. Jierong Liang, Dr. Emil Poulsen, Sreejith Sasi Kumar, Christina Basse Riel, Nikka Mosleh, Dr. Berian James, Dr. Theodoros Diamantopoulos**. **Stefan**, you are a gregarious captain in our office and passionate to various sports and board games. Thanks to you and **Emil** for our previous badminton matchups, also for a heart ginger biscuit from Munich. **Kai**, for me, you are high-energy, infectious, and helpful. Thank you so much for your encouragement in my first try of a half marathon and learning Danish, also for the honey from your hometown with a funny picture, I cannot forget your Danish classes in the office. **Sina**, I want to thank you for working on 3D printing together and your helping in my experiments. **Jierong**, I am grateful for your advice and countless conversations in my simulation and experiments. I admire your responsibility and hard work both in work and life. **Kumar**, it has been a nice experience to work and to be friend with you, thankful for inviting me to experience interesting Indian cultures and foods. **Christina**, thanks to you for bringing the office alive with your nice plants

and sharing the Danish cultures. **Theodoros**, thanks to you for attending academic conference together and discussing in wide-ranging interesting topics.

I am thankful for the friendship of the residents when I am first coming to Copenhagen in sharing an apartment with: **Kai Zheng**, **Hua Liu**, and **Yang Du**. Interestingly, we are also in a same department at DTU. We cooked together and celebrated the new year during the pandemic, which brought a lot of pleasure, and we turned to be good friend. I want to express my appreciation to my friends and colleagues at DTU: **Shu Wang, Baichen Liu, Zhipeng Zhou, Dr. Zhongtao Ma, Yifan Xia, Xiaosheng Zheng, Lujing Lin, Bo Wan, Yichen Wu, Yijing Shang, Dr. Andrea Roberto Insinga, Dr. Lucia Ianniciello, Dr. Carlos Imbaquingo, Dr. Peyman Khajavi, Pooria Dabbaghi, Mahmoud Mobin, Ashwin Nambi**, and many more friends, for many valuable discussions and help. Special thanks to my friends **Shu, Kai, Hua, Baichen**, for always helping me out whenever there are hardships, and for frequent chef shows yielding amazing dishes. I cherish the many football matchups with "wind-chasing" boys, **Zhipeng**, **Yifan**, **Kai**, **Zhongtao**, **Hua**, etc, which brought a lot of pleasure to life at DTU. I also want to extent my thanks to **Lucia** for guiding me in operating the active flow system and suggesting me in the flow system improvements. Meanwhile, thanks to **Carlos** for the valuable suggestions in my LabView programming. I also would like to acknowledge **Dr. Bruno G. F. Eggert**, for a nice collaboration in the in-field DSC measurements for magnetocaloric materials.

Ultimately, I want to express my gratitude to the members of the assessment committee – **Prof. Stefan Seelecke, Ass. Prof. Jaka Tušek, Prof. Ming Chen**, for your valuable suggestions in advancing the fulfillment of this PhD thesis. I would like to thank the secretaries of DTU energy, particularly **Signe Dan Jensen**, **Tina Høiberg Jensen**, and **Connie Munch Westergaard**, for friendly assistance in the administrative tasks. I also want to convey my appreciation to the technician team at DTU energy, particularly **Mike Wichmann** for the help in 3D printing, **Larisa Seerup** for helping in use of the SEM, **Matthew Thomas Bishop** for the helpful instruction for the TMA device.

Finally, I want to express my thanks to my parents, my sister, and other family members, for their unconditional and unwavering support throughout my experience at DTU! They supported me during tough times and were always ready to provide valuable advice beyond distance.

Nomenclature

Abbreviations

Abbreviations	Description
1D	One dimensional
3D	Three dimensional
AER	Active elastocaloric regenerator
AM	Additive manufacturing
AMR	Active magnetocaloric regenerator
APDL	ANSYS Parametric Design Language
AT	Air tank
BCE	Barocaloric effect
CD	Center differential
CHEX	Cot heat exchanger
CR	Cold reservoir
CV	Check valve
DSC	Differential scanning calorimetry
eCE	Elastocaloric effect
ECM	Elastocaloric material
FE	Finite-element
FEA	Finite element analysis
FFF	Fused filament fabrication
GWP	Global warming potential
HEX	Heat exchanger
HFC	Hydrofluorocarbon
HHEX	Hot heat exchanger
HR	Hot reservoir
IR	Infrared radiation
NR	Natural rubber
MCE	Magnetocaloric effect
MCM	Magnetocaloric material
PDE	Partial differential equation
PP	Parallel plate
PR	Poisson's ratio/Pressure regulator

Abbreviations	Description
REG	Regenerator
RMSD	Root-mean-square deviation
SEM	Scanning electron microscope
SIC	Strain-induced crystallization
SMAs	Shape memory alloys
SCP	Specific cooling power
SV	Solenoid valve
TPU	Thermoplastic polyurethane
TPPE	Thermoplastic polyester
TPEs	Thermoplastic elastomers

Variables

Variables	Description	Unit
A	Area	[m^2]
A_c	Cross-section area	[m^2]
$\boldsymbol{B}$	Left Cauchy-Green deformation tensor	[-]
$\boldsymbol{C}$	Right Cauchy-Green deformation tensor	[-]
COP	Coefficient of performance	[-]
c_p	Specific heat capacity	[$Jkg^{-1}K^{-1}$]
D_h	Hydraulic diameter	[m]
$\boldsymbol{e}$	Strain tensors	[-]
f	Frequency	[Hz]
f_F	Friction factor	[-]
F	Helmholtz free energy	[J]
$\boldsymbol{F}$	Deformation gradient	[-]
h	Convection heat transfer coefficient	[$Wm^{-2}K^{-1}$]
H	Crystallization enthalpy	[J/g]
i	Spatial node number	[-]
J	Jacobian	[-]
i	Temporal node number	[-]
k	Thermal conductivity	[$Wm^{-1}K^{-1}$]
L	Length	[m]
m	Mass	[kg]
$\dot{m}$	Mass flow rate	[kgs^{-1}]
Nt	The number of time nodes	[-]
Nu	Nusselt number	[-]
Nx	The number of spatial nodes	[-]
P	Pressure	[MPa]
Q	Cooling/heating work	[J]
$\dot{Q}$	Cooling/heating power	[W]

Variables	Description	Unit
r	Radius	[m]
Re	Reynolds number	[-]
s	Specific entropy	[$Jkg^{-1}K^{-1}$]
S	Entropy	[JK^{-1}]
$\boldsymbol{S}$	Second-order tensor	[-]
SR	Solidity ratio	[-]
S_P	Piston stroke	[mm]
t	Time	[s]
T	Temperature	[K]
ΔT	Temperature change	[K]
U	Utilization	[-]
V	Volume	[m^3]
v_p	Piston velocity	[m/s]
v_s	Superficial velocity (open velocity)	[m/s]
W	Work	[J]
$\mathcal{W}$	Strain energy function	[J]
x	Axial position/uniaxial tensile coordinate	[m]
X	x coordinate after stretching	[m]

Greek symbols

Greek	Description	Unit
ε	Strain	[-]
ε_{ijk}	Levi-Civita symbol	[-]
σ	Stress	[MPa]
ρ	Density	[kgm^{-3}]
λ	Elongation/stretches	[-]
Δ	Difference	
τ	Period time	[s]
ϕ	Porosity	[-]
ν	Possion's ratio	[-]
φ	Deformation factor	[-]
μ	Dynamic viscosity	[sPa]
δ	Thickness	[mm]
δ_{ij}	Kronecker's delta	[-]
χ	Crystalline fraction	[-]
ζ	Regeneration ratio	[-]

Sub-/Super- scripts

Sub-/superscripts	Definition
ad	Adiabatic
amb	Ambient
c	Cooling/Cold-to-hot blow
cyc	Cyclic
disp	Dispersion
eff	Effective
f	Fluid
h	Heating/Hold-to-cold blow
in	Inlet/Inflow
iso	Isothermal
loa	Loading
m	Mass
mat	Material
max	Maximum
min	Minimum
r	Regenerator
s	Solid/Sample
stat	Static
out	Outlet/Outflow
unl	Unloading
*	Undergoing deformation

Contents

List of Figures

List of Tables

Part I

Introduction, Theory and Methods

CHAPTER 1

Introduction

"道虽迩，不行不至；事虽小，不为不成。"
("Even the shortest journey can't be finished without taking the first step; Even the most trivial task can't be completed without taking actions.")

— Xunzi (荀子) (Chinese philosopher, 310−238 BCE)

"Human meditation has no limits. At his own risk and peril, it analyzes and digs deep into its own bedazzlement."

— Victor Hugo (French novelist, 1802−1885)

Current cooling and heating in homes and businesses account for 30% of global final energy consumption and CO_2 emissions, and among them heating is responsible for around half [1, 2]. Due to the warming climate, population growth, and increasing urbanization trends, the global demand for cooling is growing rapidly and could more than triple by 2050 [3–5]. At present, vapour compression-based systems are largely dominant in heating and cooling markets. These are based on a cycle employing gaseous refrigerants alternately compressed and expanded to achieve cooling or heating. Vapor compression systems have significant environmental impact associated with leakage of their working refrigerant, such as typical hydro-chloro-fluoro-carbons (HCFCs) and hydrofluorocarbons (HFCs), as well as system losses that reduce efficiency [6]. These emission gases contribute to thousands times higher global-warming potential (GWP) than that of CO_2, and must be phased out by the year 2047 under carbon-neutrality and environmental concerns [7, 8]. To achieve deep decarbonization and mitigate climate change, calls are to the next-generation technologies for green cooling and heating to replace vapour compression. It is expected to employ non-toxic, non-flammable, greenhouse-gas-free, lower-carbon refrigerants. In addition, it is also essential to develop affordable, scalable and higher energy efficiency refrigeration systems for widespread commercialization. Prominent alternative cooling technologies based on a variety of caloric materials, i.e., solid-state caloric cooling technologies, which exploit the field-induced temperature changes of solids, are attractive to provide an eco-friendly and efficient cooling solution. Over the past decades, substantial efforts have been devoted to the development of various caloric materials and prototype devices, shaping the pathway towards upcoming commercializing caloric cooling. In this chapter, we provide

an overview for state-of-the-art caloric materials and caloric cooling technologies, meanwhile introducing the motivations and significance of this work on developing 3D-printed elastocaloric regenerators.

1.1 Solid-sate caloric cooling

Solid-state cooling (and heating) technologies are based on caloric materials, which employ so-called caloric effects (magnetocaloric [9–13], electrocaloric [14–16], elastocaloric [17–22], barocaloric [23–26]). It has been emerging as an exciting front-runner with the potential as environmentally-friendly, sustainable, and high-efficient alternatives to vapor compression refrigeration. This technology essentially employs solid materials to achieve heating or refrigeration without the need of harmful refrigerants and mechanical components (like compressor, condenser, evaporator, etc.). Hence, it doesn't involve the circulation of refrigerants and friction losses associated with the above-mentioned mechanical components, resulting in reduced energy consumption. Moreover, it also has intrinsically high energy conversion efficiency. Although solid-state cooling technology possesses many advantages, it still confronts challenges on the way to widespread commercialization, such as high costs, limited cooling capacity, insufficient material stability and compact system construction. It is crucial for ongoing research to develop excellent and cost-efficient caloric materials and high-performance cooling systems to overcome these issues for future commercial applications.

Basically, the research and development of excellent caloric materials are fundamental and crucial to the breakthrough of solid-state cooling technologies. The caloric materials are operated alternately with the application and removal of different external fields. In general, the caloric effects of materials are typically categorized into distinct types based on the applied fields, such as a magnetic field for the magnetocaloric effect (MCE), electric field for the electrocaloric (ECE), uniaxial strain for the elastocaloric effect (eCE), and hydrostatic pressure for the barocaloric effect (BCE). Following is a brief overview of a variety of typical caloric materials and the origin of their caloric effects.

1.1.1 Mechanisms of caloric materials

Herein, some typical caloric materials are introduced and summarized in Figure 1.1, which is reproduced from [27]. For all of them, the caloric effect is manifested by a temperature change in materials due to the entropy change from field-induced phase transitions. Figure 1.1 **a** and **b** show the phase-transition process from paramagnetic to ferromagnetic state for $Gd_5Ge_2Si_2$ when a magnetic field is applied. During this process, the magnetic moment of atoms evolves from magnetic disorder to magnetic order accompanying with the magnetic entropy decrease and the lattice entropy increase [9]. In the case of electrocaloric materials, the ECE originates from the align-

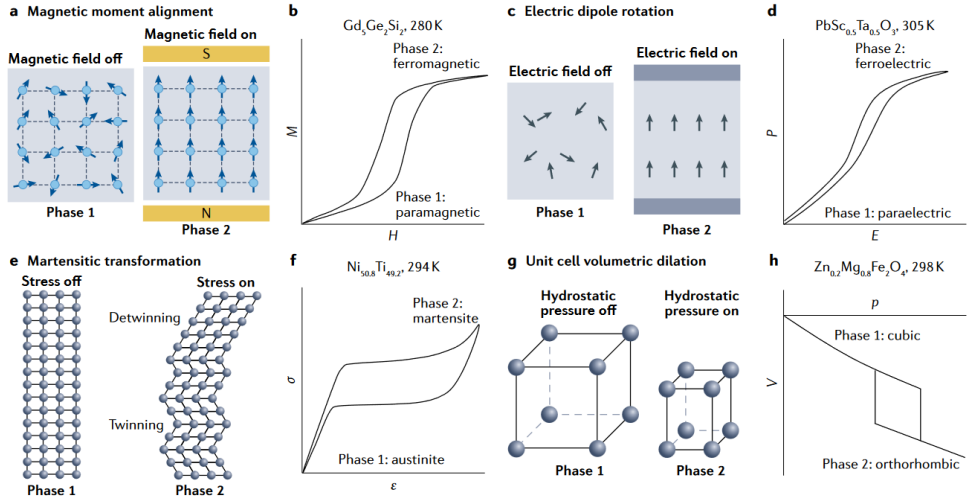

Figure 1.1. Mechanisms of typical caloric materials for solid-state caloric cooling. Reproduced from [27].

ment of electric dipoles induced by the application of electric fields, as observed in a typical electrocaloric material $PbSc_{0.5}Ta_{0.5}O_3$ in Figure 1.1 **c**, **d** [28]. In the case of elastocaloric materials, the application of uniform stress compression/tension to a typical Ni-Ti alloy leads to the austenite-martensite transformation, as visually represented in Figure 1.1 **e**, **f** [29]. Regarding barocaloric materials, as shown in Figure 1.1 **g**, **h**, the hydrostatic pressure can lead to the crystal lattice distortion from cubic to orthorhomebic structure for the BCE material [30, 31]. Interestingly, the phase transition temperatures are varied with the composition of materials, and some materials are capable of tunable transition temperatures by elemental doping or composition [32–35]. In accordance with their transition temperatures, caloric materials can be implemented in wide-ranging cooling fields, including room temperature for household refrigeration, and low temperature for cryogenics like liquefaction of natural gas and hydrogen [36–39].

Among the implementations for these caloric materials, magnetocaloric cooling has been most explored both in material and device aspects, and a kilowatt-level prototype has been demonstrated with a temperature span about 11 K and a system COP of 6.7 [40, 41]. However, the MC demonstrators are easily subjected to geopolitical risks, due to highly relying on permanent magnets (offering magnetic fields, > 1 T) and magnetic materials, which require the rare earth metals as raw materials [42, 43]. It remains less competitive for commercialization by multi-considerations in expenditure and supply security. The research on the electrocaloric effect and ECE prototypes has been rapidly increasing during the past years, and several ECE demonstrators have been recently constructed based on regeneration and solid-state

cascades [44, 45], which shows enhanced temperature spans as high as 10 K. It manifests great potential for small-scale applications[46], such as the electronics cooling with requirements of localized temperature control.

1.1.2 Typical mechanocaloric effects

The mechanocaloric effect is characterized by the significant intrinsic temperature changes compared to the MCE and ECE (commonly attaining a few Kelvin temperature change), which is primarily operated in two mechanical-force configurations, i.e., elastocaloric and barocaloric. For instance, the barocaloric effect triggered by hydrostatic pressure has been observed with a giant entropy change and adiabatic temperature change as high as 389 J/kgK and 50 K, respectively, in some superionic conductors[47], plastic crystals[24] and spin-crossover compounds[25, 48]. Yet, the barocaloric prototypes are at a nascent stage of development, with less verified results of experimental proof-of-concepts but some ideas of design [49, 50]. The application is probably limited by the challenges such as performing under low applied pressures as well as designing efficient heat-transfer configurations.

In addition to the barocaloric effect, there is also an existing family of 'deviatocaloric' effects proposed in the literature [27] for the taxonomy of mechanocaloric effects, as shown in Figure 1.2. Typically, it was categorized by the stress state of a

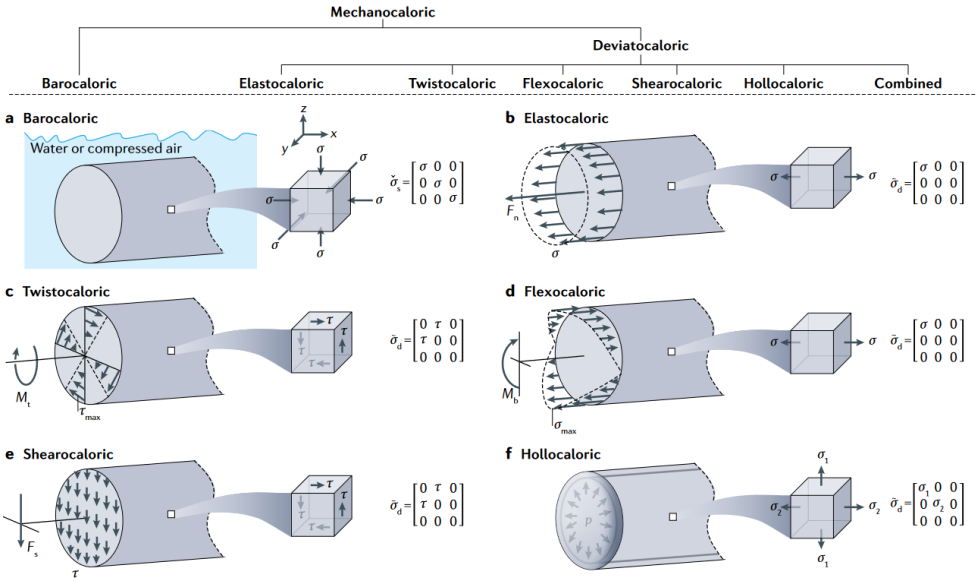

Figure 1.2. Categorization of state-of-the-art mechanocaloric effects based on various applied stress. Reproduced from [27].

point in the solid body: uniaxial stress tensor for elastocaloric; torsional stress tensor for twistocaloric; bending stress tensor for flexocaloric; shear stress tensor for shearocaloric; plane stress tensor for hollocaloric. Some of them have been demonstrated with the experimental proof-of-concepts, such as elastocaloric, twistocaloric, flexocaloric, but the rest remains in concepts. Recently, the twistocaloric has been systematically studied in the materials ranging from natural rubber fibers to NiTi shape memory wires, showing the potential for solid-state cooling [51]. The demonstrator based on thin strips of NiTi in operation with the concept of flexocaloric has been designed using reciprocating bending, capable of low force and compact refrigeration [52, 53]. Among them, the elastocaloric is the most common mechanocaloric cooling mode, which was first observed in elastic rubbers and was related to the elastocaloric effect by Joule in 1859 [54, 55]. To date, it has been intensively investigated in a variety of elastocaloric materials, such as superelastic shape-memory alloys (SMAs) [17, 20] and rubber-like elastomers [56, 57]. The adiabatic temperature changes in some elastocaloric alloys, such as Ni–Mn–Ti–B and TiNi, are measured to be 31.5 K at 900 MPa, and 38.5 K at 900 MPa [20, 58], respectively, by some direct methods including thermography and thermocouples. Elastocaloric cooling specifically was selected as the most promising non-vapor compression refrigeration technology by the US Department of Energy in 2014 [59] as well as by the EU Commission [60]. The investigation of high-performance elastocaloric materials and regenerators is crucial to the progress and widespread adoption of elastocaloric cooling technologies.

1.1.3 Elastocaloric materials and low-stress eCE cooling

Elastocaloric materials are attracting increasing attention and have been recommended as the most promising alternative to non-vapor compression technology. These materials exhibit an increase in temperature when a uniaxial strain is applied and a decrease in temperature when the strain is released adiabatically. Devices based on these materials are usually operated by applying a linear strain either in tension or compression to the material, and also some other novel driving methods such as bending and torsion as above-mentioned. In recent years, shape memory alloys with a austenitic–martensitic phase transformation at room temperature have been intensively explored, among these NiTi-based SMAs [61–63], Cu-based SMAs [64, 65], and NiMn-based Heusler-type magnetic SMAs [13, 20, 66]. Particularly, the NiTi-based SMAs are most commonly employed for solid-state cooling/heat-pumping system demonstration both in numerical simulation and experimental aspects [67–69]. However, driving the eCE of SMAs requires large tensile stresses as high as several hundreds of MPa to thousand. The applied stress to trigger eCE of up-to-date typical SMAs in different shapes, such as films, microwires, ribbons, bulks and foams, is plotted in Figure 1.3 to provide an overview to understand the magnitude of required stresses. It is found that the commonly used Ni-Ti alloys when developed as a cooling device require large stresses as high as 1000 MPa under compression [70]. Nonetheless, the foam SMAs seemingly achieves a quite lower applied

stress around 60 MPa, but the high manufacturing cost and limited fatigue life impedes their applications. Overcoming the challenge of high applied stress remains an ongoing engineering endeavor in elastocaloric refrigeration, hindering the miniaturization of cooling systems and their potential applications.

Polymer elastomers such as natural rubber (NR) were initially reported to have elastocaloric properties by Joule in 1859, namely the Gough-Joule effect [55]. In comparison to most SMAs, the stress to trigger the eCE in the elastomers is one or two orders of magnitude less than that of SMAs. Additionally, the advantages of elastomer materials include their softness, low cost, sustainability, and lack of toxic materials. This has driven increasing research into exploiting various elastomers in recent years, which opens new avenues for eCE refrigeration [87–90]. The eCE in rubbers and thermoplastic polyurethane (TPU) elastomers has been increasingly studied and the softening effect (namely, the Mullins effect) on its caloric cooling application was elucidated as well [88, 91–94]. TPU elastomers have been observed with considerable eCE with a 8 K temperature change at 400% at room temperature, due to strain-induced crystallization (SIC) associated with a partial crystallization of the elastomer caused by deformation [95, 96]. The inherent SIC in elastomers enhances their mechanical functionality and improves the eCE cooling performance [91, 92, 97]. More recently, a novel elastocaloric cooler based on SIC using an inflating-deflating rubber membrane was developed with an attractive specific cooling power of 20.9 W/g, showing that elastomers can absorb a high cooling load per mass [91]. High cooling power has been demonstrated in vulcanized NR fibers and polyethylene wires by means of twisting, untwisting, and stretching simultaneously [51]. Thermoplastic

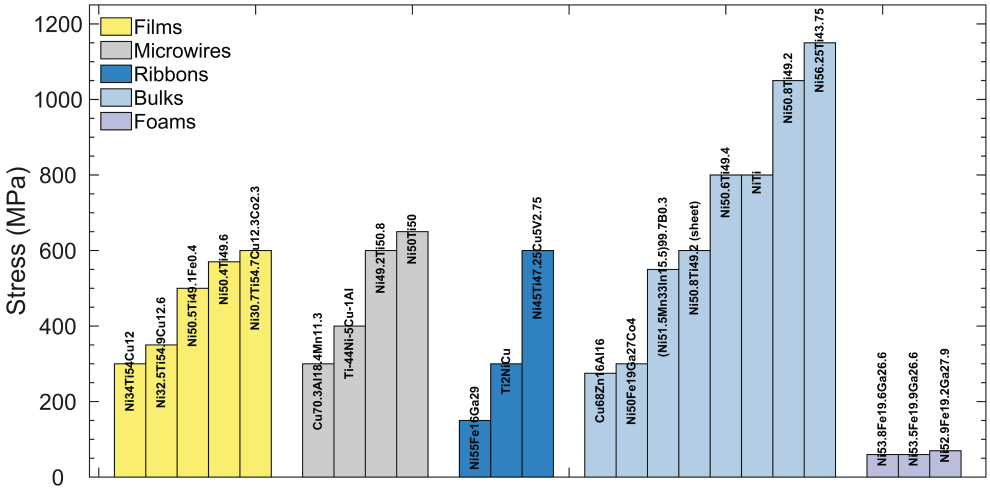

Figure 1.3. The applied stress for some typical SMA-based elastocaloric materials in dimensions of films [61, 71–74], microwires[29, 65, 75, 76], ribbons[77–79], bulks[62–64, 70, 80–83], and foams[84–86].

elastomers with uniform molecular chain lengths were synthesized, and the elastocaloric effect was shown to be improved [57]. These achievements in the search for eCE elastomers and in developing practical cooling prototypes based on them demonstrate the promise of regenerative elastocaloric cooling/heat-pumping systems based on elastomers.

1.2 Elastocaloric cooling prototypes

In analogy to the typical cycles utilized in the magnetocaloric cooling, such as Brayton cycle, Ericsson cycle, Carnot cycle, and the cycle based on cascaded configuration[98], the elastocaloric cooling can usually be simplified to a Brayton-based cycle, as described in the Figure 1.4a for active regeneration with oscillated heat-transfer fluids. The Figure 1.4b is related to the elastocaloric SMAs in which the temperature variation in the thermodynamic cycle is resulting from the reversible austenite-martensite transformation when the stress was applied and removed. The temperature changes in eCE polymers are associated with the SIC and entropic elasticity in the molecular chain, indicating by the variation in the molecular chain state between disordering and SIC in Figure 1.4c. In state-of-the-art constructions for elastocaloric prototypes, exploiting this thermodynamic cycle, they are classified primarily into two types by heat exchange modes: direct mechanical contact with heat sink/source (Figure 1.5a); active regeneration with the heat transfer medium (Figure 1.5b). When using SMAs in Figure 1.5a, upon stress loading, the temperature increases, with the warmed material directly touching the heat sink; upon unloading, the temperature decreases, switching the connection to the heat source. In this scheme, heat transfer happens mainly on either the front or back sides, which requires a large heat transfer area and a smaller thickness of the material. Therefore, the state-of-the-art prototypes are implementing the SMAs films with a thickness around 20 μm [99]. In fact, the heat contact scheme is not common in the other caloric cooling demonstrators because of their comparably low adiabatic temperature changes for the MCE and ECE. As the aforementioned reviewing for mechanocaloric effect, which has a large temperature change for the BCE and eCE materials, capable of exceeding 20 K in some SMAs, plentiful demonstrators based on the mechanical heat contact scheme have come into being over past years beneficial from their higher temperature changes.

1.2.1 Heat transfer based on mechanical contact

Some SMAs-based typical demonstrators are listed in the Table 1.1, which transfer their heat implementing mechanical contact. Their performance parameters are also summarized in the table for comparison.

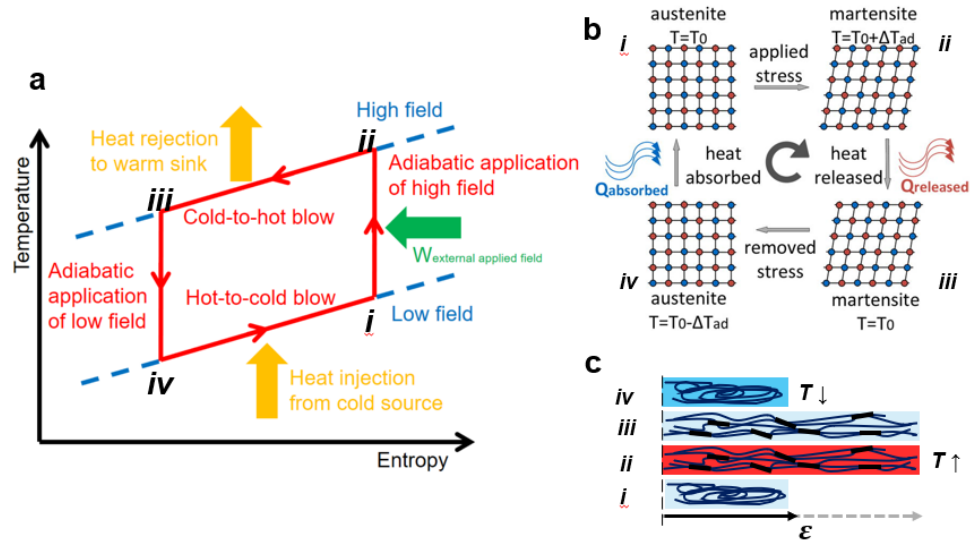

Figure 1.4. The caloric Brayton cycle for a common active caloric regenerative cycle in a, associated with typical eCE SMAs b and polymers c. Images were reproduced from [18, 100, 101].

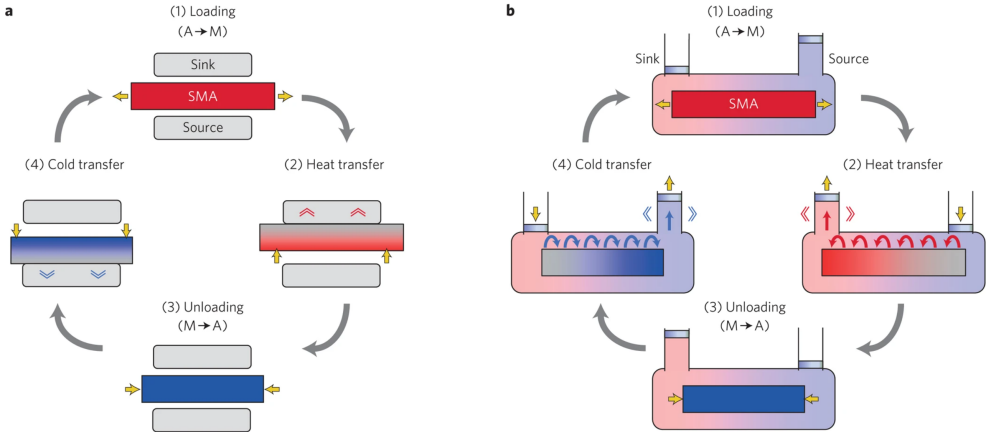

Figure 1.5. Two typical heat-transfer methods for elastocaloric cooling: a. mechanical contact; b. active regeneration employing heat-transfer fluid periods. The image was reproduced from [102].

Table 1.1. Several typical elastocaloric coolers based on mechanical contact for heat-transfer. The applied stress (σ), temperature span, COP, cooling power ($\dot{Q}$), and specific cooling power (SCP) of the system are given, in which NA means not observed in the literature.

Heat-contact prototypes	Performance	Description
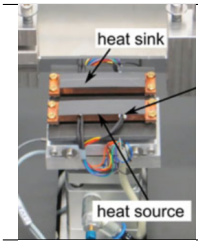	• σ = 750 MPa • Tspan = 5.1 K • COP = 2.1 • $\dot{Q}$ = NA • SCP = 0.23 W/g	• Material: Ni-Ti-Cu-V alloy • Single-stage prototype • Reported from Saarland 2016 [77]
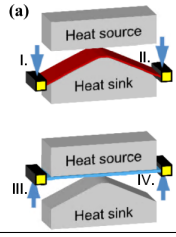	• σ = ∼410 MPa • Tspan = 2 K • COP = 3.1 • $\dot{Q}$ = 23.1 mW • SCP = NA	• Material: TiNi and TiNiCuCo films • Bridge-based eCE cooler (single-stage) • Reported from KIT 2016 [99]
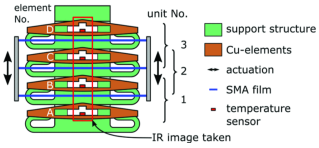	• σ = ∼390 MPa • Tspan = 7.6–15 K • COP = 1.9–5.7 • $\dot{Q}$ = 0.025–0.14 W • SCP = 17 W/g	• Material: Ti-Ni-Cu-Co films • Cascaded SMA-film cooler (multi-stage) • Reported from KIT 2019 [103]
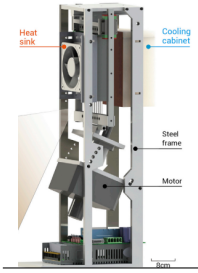	• σ = 980 MPa • Tspan = 9.2 K • COP = 1.38 • $\dot{Q}$ = 3.1 W • SCP = 0.34 W/g	• Material: NiTi wires • A compact elastocaloric refrigerator (paralleled) • Reported from XJTU, NIMTE 2022 [104]

Table 1.2. Several typical elastocaloric demonstrators based on active regeneration. The applied stress (σ), temperature span, COP, cooling/heating power ($\dot{Q}$), and specific cooling power (SCP) of the system are given, in which the NA means not observed in the literature.

Regenerative prototypes	Performance	Description
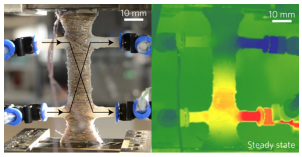	• σ = ∼400 MPa • Tspan = 15.3 K • COP = 3.5–7.0 • $\dot{Q}$ = 4.53 W (heating) • SCP = 0.8 W/g	• Material: NiTi sheets • Regenerative eCE heat pump (single stage, stretching) • Reported from DTU 2016 [67]
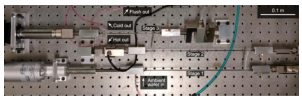	• σ = ∼500 MPa • Tspan = 28.3 K • COP = 0.4–6.0 • $\dot{Q}$ = 0.23 W • SCP = 0.042 W/g	• Material: NiTi wires • Multistage elastocaloric cooler/heater (multi-stage, stretching) • Reported from Cornell 2019 [105]
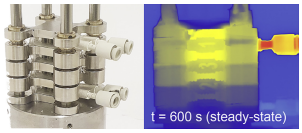	• σ = 775–825 MPa • Tspan = 31.3 K • COP = 1.9–5.7 • $\dot{Q}$ = 60 W • SCP = 4.4 W/g	• Material: NiTi tubes • Fatigue-resistant cooler/heater (paralleled, compression) • Reported from Ljubljana 2022 [21]
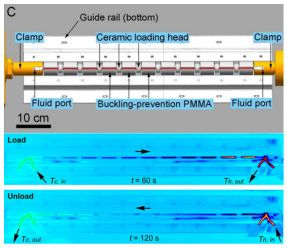	• σ = 900 MPa • Tspan = 50.6 K • COP = 7.1 • $\dot{Q}$ = 203 W • SCP = 1.75 W/g	• Material: Spiral NiTi tubes • Tubular NiTi elastocaloric refrigerator (multi-stage, compression) • Reported from HKUST 2023 [106]
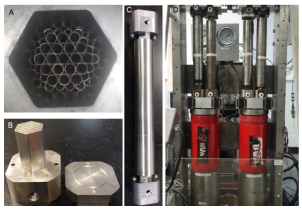	• σ = ∼1000 MPa • Tspan = 22.5 K • COP = 1.03–6.85 • $\dot{Q}$ = 260 W • SCP = NA	• Material: NiTi tubes • Multimode elastocaloric cooler (multi-stage, multi-mode, compression) • Reported from XJTU, Maryland 2023 [22]

1.2.2 Active regeneration

From the listed heat-contact prototypes in Table 1.1, it can be observed that it remains challenging to obtain a high cooling power. In general, the enhanced cooling power requires the adequate thermal mass for the caloric material. For instance, a kilowatt-level prototype for magnetocaloric cooling utilized a total LaFeSiH mass of 1.52 kg [40]. Hence, the heat-contact prototype was limited in the micro-scale cooling and remains challenging to macro-scale. Although a large-size prototype, employed the bundle of NiTi wires from the XJTU in Table 1.1, was constructed [104], the maximum cooling only have 3.1 W, and cannot meet the requirement of the household refrigeration. Fortunately, the active regeneration scheme as Figure 1.5b, involving alternate heat-transfer fluid periods provided by a displacer or pump, allows the prototype design ranging from small to large scale with the enhanced cooling/heating power. Moreover, it can highly extend system temperature span, especially for the caloric materials with the insufficient temperature change, and has been most utilized for the MCE demonstrations. Recently, active regeneration is increasing implemented to the elastocaloric cooling and heating.

Some typical SMAs-based regenerative prototypes are listed in Table 1.2, which contain various constructions differing from loading modes (stretching, compression), connection methods (single-/multi-stage, paralleled). Their performance parameters are also summarized in the table for comparison. Notably, over multiple generation updates and optimization in heat transfer, loading methods, fluidic configurations, and operation modes, active elastocaloric cooling has a significant improvement both in temperature span and cooling power. However, the applied stress in these systems remains remarkably high, often reaching the range of hundreds to thousands of MPa, emphasizing the necessity for mechanically robust systems.

1.2.3 State-of-the-art soft elastocaloric coolers/heat pumps based on elastomers

Recently, soft elastomers, such as natural rubbers, thermoplastic polyurethane, and synthetic polymers, provide a solution for lower-stress elastocaloric cooling at room temperature. It fulfills a comparably high performance in some recent demonstrators based on soft eC elastomers, only driven by several MPa. There are some state-of-the-art soft elastocaloric coolers based on elastomers summarized in Table 1.3. A balloon-like cooler is demonstrated to operate under high-frequency inflation and deflation, in which the natural rubber membrane is subjected to a biaxial tension. It has achieved a remarkably high specific cooling power (SCP) of 20.9 Wg^{-1} and a temperature range of 7.9 K [91].

Table 1.3. State-of-the-art soft elastocaloric coolers and heat pumps based on elastomers. The applied stress (σ), temperature span, COP, cooling/heating power ($\dot{Q}$), and specific cooling power (SCP) of the system are given, in which NA means not observed in the literature.

Elastomer-based prototypes	Performance	Description
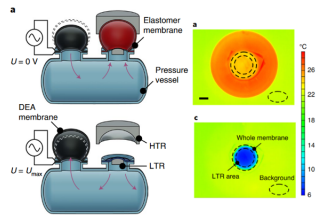	• σ = ∼4.9 MPa • Tspan = 7.9 K • COP = 4.7 • $\dot{Q}$ = 4.53 W • SCP = 20.9 W/g	• Rubber membrane • Inflation-deflation • Heat-contact • Balloon-like eCE cooler • Reported from Linz 2021 [91]
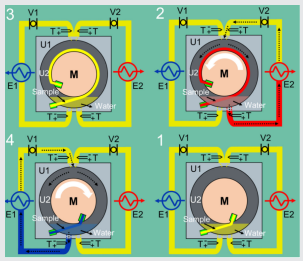	• σ = 9–24 MPa • Tspan = 1.1-5.2 K • COP = 9.3 • $\dot{Q}$ = ∼10 W • SCP = 1.9 W/g	• SEBS thermoplastic elastomers • Rotary motion • Partial active regeneration • Reported from WHUT, THU 2022 [57]
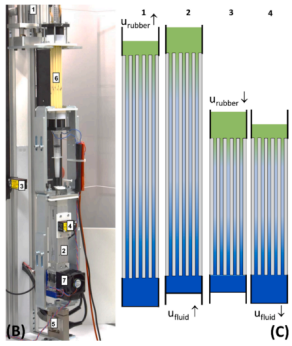	• σ = 1.5–2.0 MPa • Tspan = 8 K • COP = 6.0 • $\dot{Q}$ = 1.5-3.1 W • SCP = 0.23 W/g	• Natural rubber tubes • Uniaxial tension • Active regeneration (paralleled rubber tubes) • Reported from Lyon 2023 [107]

Interestingly, a roller-based prototype by wrapping elastomeric strips has been developed to realize high strains [57], and a maximum of SCP of 1.9 Wg^{-1} and temperature span of 5.2 K are obtained. Among them, the maximum ΔT_{ad} of eCE materials reaches to 15-23 K at 600% strain, yet temperature span of those coolers is relatively low, implying additional space to exert their eC heat towards an improved temperature span.

By comparing the listed SMAs-based eCE coolers, we found that the active regeneration has been successfully implemented to extend the temperature span. Although the roller-based prototype includes some fluids for heat transfer, actually, when the reel stretches the elastomer strip, only part of the elastomer on the bottom is in contact with heat-transfer fluids. And much of elastocaloric effect is absorbed by the roller being as a heat sink. It could be supposed to be a partially regenerative prototype. More recently, a polymer-based elastocaloric cooler using a bundle of rubber tubes is presented in [107], which shows an improved temperature span >8 K. But the assemble of numerous parallel rubber tubes raises complexity of devices, owing to requiring identical length in case nonuniform stretches and compact structure to prevent heat losses.

1.3 Elastocaloric regenerator geometries

Active caloric regenerator acted as a combination of refrigerant and heat exchangers could be a solution for more compact and efficient elastocaloric cooling based on the regenerative scheme. It has been widely implemented in numerous active magnetic regenerators (AMRs), in which magnetocaloric materials were fabricated into various porous structures, typical in spherical or irregular packed beds [108, 109], as well as in parallel-plate, cylindrical, rectangular, honeycomb, triangular, and lamellar micro-channel metrics [110–115]. To maximum exert the caloric materials performance, the regenerator is expected to have a large surface area, thermal mass, and high thermal conductance, meanwhile being less axial conductance to prevent heat exchange between the heat sink and source and lower pressure drops to reduce viscous dissipation [116]. The packed beds mechanically constrained by caloric material particles have high surface area and thermal mass to boost the heat transfer and system cooling power, which has been widely adopted in most large-power AMR demonstrations. But it is difficult to be performed in active elastocaloric regenerators (AER), due to the requirement for uniaxial compression/stretching, which usually applies to an integral structure with continuous axial fluid channels. The structure is also required to have excellent mechanical integrity for long-term operation. The packed beds subjected to cyclic mechanical loading-unloading are prone to cracking and functional failure, as well as increased flow resistance which reduces system efficiency.

Hence, the AER commonly existing in an installation with a bundle of elastocaloric plates, tubes or wires has been constructed and achieved satisfactory performance in

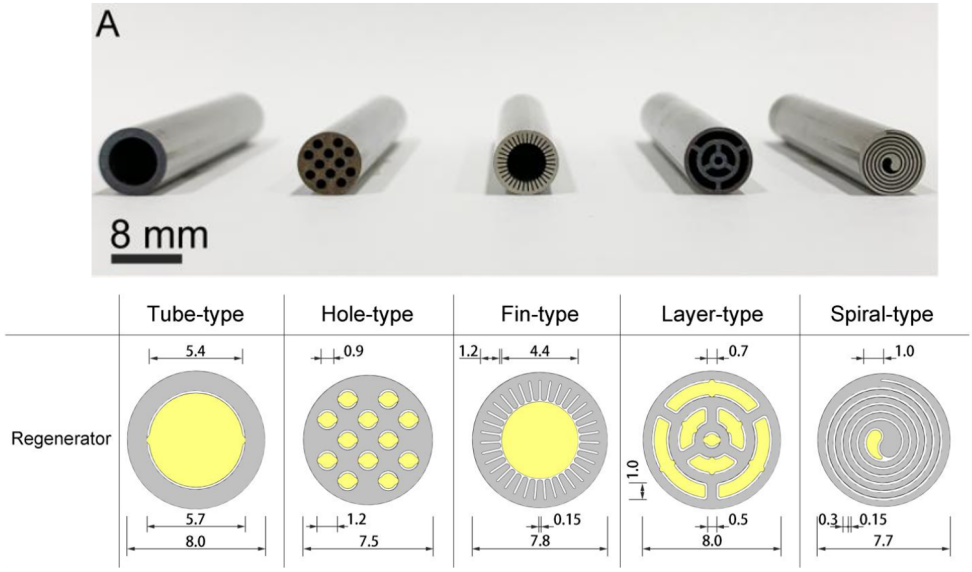

Figure 1.6. Active NiTi regenerators with different fluid microchannels. Images was reproduced from [106].

the aforementioned prototypes. Noteworthily, the high compact demonstration employing cascade-unit AERs has achieved a remarkable elastocaloric cooling performance over 1 million compressive cycles (see Table 1.2), in which the NiTi-based microchannel AERs in various geometries were introduced, as illustrated in Figure 1.6. It allows more efficient heat exchanging due to a high surface area with the optimization of microchannel geometries, especially for the spiral-type channel achieving a good combination of large thermal mass, large surface area, and buckling resistance.

In the fabrication for microchannel regenerators, additive manufacturing (AM) can be an attractive option compared to the traditional machining methods, such as hot/cold pressing, electrical discharge machining, embossing-tape stacking, and extrusion [106, 112, 114, 117, 118]. It is especially adept at fabricating complex 3D structures, capable of increasing freedom of the structural design, and has been increasing to implement to the elastocaloric regenerator fabrication. It shows great potential to construct the full-printed soft active elastocaloric regenerator in high compact configurations integrated the regenerator microchannels and fluid manifolds inside, with distinct low-driven stress and optimized heat-transfer properties.

1.4 Additive manufacturing for caloric regenerators

The implementation of additive manufacturing in engineering applications can add freedom to produce complex geometries, which has been used to produce novel regenerator structures to achieve efficient heat transfer and enhanced functional stability for solid-state cooling [119–122]. For instance, Hou *et al.* made a remarkable advancement in enhancing material fatigue resistance (over one million cycles) for the typical eCM NiTi using laser melting deposition methods as shown in Figure 1.7a. Nevertheless, commonly employed AM techniques such as laser melting deposition and selective beam sintering encounter challenges in producing smooth, intricate regenerator structures and in controlling microstructural changes during printing. Furthermore, there are limitations in the alloy composition and the intricate preparation of raw metallic powders [123, 124].

Using AM for flexible elastomers like fused filament fabrication (FFF) is more cost-effective, versatile, and precise than 3D printing metals, and also more affordable, with a wider range of accessible 3D printers [127–129]. Thermoplastic Elastomers (TPEs) such as TPU which has been observed to have a comparable elastocaloric effect with a 8 K adiabatic temperature change under a 500% strain [93], have been utilized to fabricate flexible 3D components by means of AM technologies [130, 131], often implementing FFF. Manufacturing using FFF consists of depositing successive layers on a build plate by extruding a thermoplastic filament to obtain 3D structures. A fabrication process of FFF is illustrated in Figure 1.7b. Material feeding is controlled by the gear rollers going through a heated nozzle and fabricated into

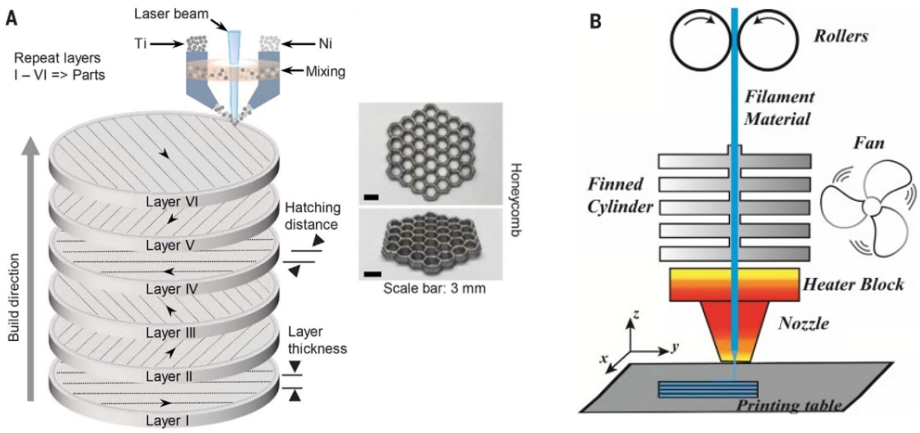

Figure 1.7. Additive manufacturing for caloric materials: a, Laser melting deposition for NiTi alloys. b, Fused filament fabrication for thermoplastic polymers. Images were reproduced from [125, 126].

various complex 3D structures. AM of polymer TPEs is easier to implement, and precise flow channels with improved heat-transfer and flow properties are achievable using more accessible 3D printing devices.

1.5 Motivation and objectives

In this dissertation, we plan to employ soft elastomers to construct a low-stress driven elastocaloric prototype and to study its performance numerically and experimentally. The idea is to implement the FFF method to 3D print the full-scale elastocaloric regenerator using elastocaloric thermoplastic elastomers. The regenerator is expected to be designed in different structures, and the fluid connection ports and clamped ends are directly integrated with the regenerator body by 3D printing. In general, the elastomeric regenerator requires a quite large applied strain to trigger their elastocaloric effect, consequently, leading to a significant fluid channel volume change inside the regenerator associated with the geometry large deformation. A tailored active elastocaloric experimental system has been built to study the regenerator cooling performance and optimize the operation parameters. Moreover, a 1D numerical model involving the large deformation of regenerator length is also developed to numerically investigate the performance of the elastomeric regenerator and the temperature gradients along the regenerator tensile direction, which helps us to seek the optimal operating configuration for the practical application. The motivation and main objectives of this investigation are listed in the form of a questionnaire (see Table 1.4).

Table 1.4. Main motivations and objectives of the dissertation

Motivation 1:	How to construct a low-stress induced elastocaloric cooling prototype in a compact scheme?
Objective	Look for the low-stress driven elastocaloric materials (ECMs) and effective fabrication methods, in which the eCE elastomers can be fabricated into a full-scale active AER by means of additive manufacturing, providing a promising solution.
State-of-the-art	Bending scheme using NiTi plates, several elastomer-based coolers
Article(s)	Article I
Motivation 2:	Which elastocaloric materials could be a candidate for the 3D printed AER?
Objective	Seek the promising eCE materials potential for 3D printing a full-scale regenerator, basically selected from some commercial thermoplastic elastomers.
State-of-the-art	Potential eCE elastomers — Natural rubbers, TPU, SEBS
Article(s)	Article I
Motivation 3:	When subjecting to the required large-strains, there are fluid-channel volume changes observed inside regenerator, and how to account it?

Objective	Capture the mechanical behavior of elastomers and conduct to the explicit FE simulations to calculate the volume changes; the validation experiments should be performed.
State-of-the-art	Has been observed in an active rubber-tube eCE cooler
Article(s)	Article II
Motivation 4:	How to construct an active operation system capable of implementing large-deformation soft eCE regenerators effectively?
Objective	Design a fluidic compensation system which can compensate and expel the increased/decreased volumes during the regenerator loading and unloading; optimize the operation parameters to achieve a satisfactory cooling performance.
State-of-the-art	Haven't been specifically studied with passive volume compensations.
Article(s)	Article III (in preparation)
Motivation 5:	How to numerically investigate and evaluate the cooling performance of a large-deformation soft eCE regenerator?
Objective	Develop a 1D numerical model for the active elastocaloric regenerator when undergoing a large deformation. Combine the FE simulation results for the volume changes to evaluate the its impact on the system performance.
State-of-the-art	Some existing 1D AER models not involving deformed regenerator length and volume changes.
Article(s)	Article IV (in preparation)

1.6 Outline of the dissertation

To fulfill the aforementioned objectives, the specific implementation routes are performed according to the procedures shown in Figure 1.8. The dissertation is presented as follows:

- Chapter 2: The relevant theoretical background, simulation tools, and experiential methods employed in this dissertation are presented.
- Chapter 3: The elastocaloric performance of five commercial thermoplastic filaments are studied to screen the most promising eCE elastomers for 3D printing regenerators. The 3D-printed elastomers properties, including their eCE performance, functional stability, microstructures, are systematically investigated.
- Chapter 4: The large-strain induced volume changes of regenerator fluid channels are studied in different microchannels and loading rates experimentally and numerically.
- Chapter 5: A 1D numerical model is developed to study and optimize the large-deformation elastocaloric regenerator.
- Chapter 6: Experimental investigations are performed for the 3D-printed elastocaloric regenerator, and the impact of volume changes and other typical operating parameters on the regenerator performance is studied.
- Chapter 7: A conclusion related to the corresponding research results and an outlook of future work and ongoing challenges are presented.

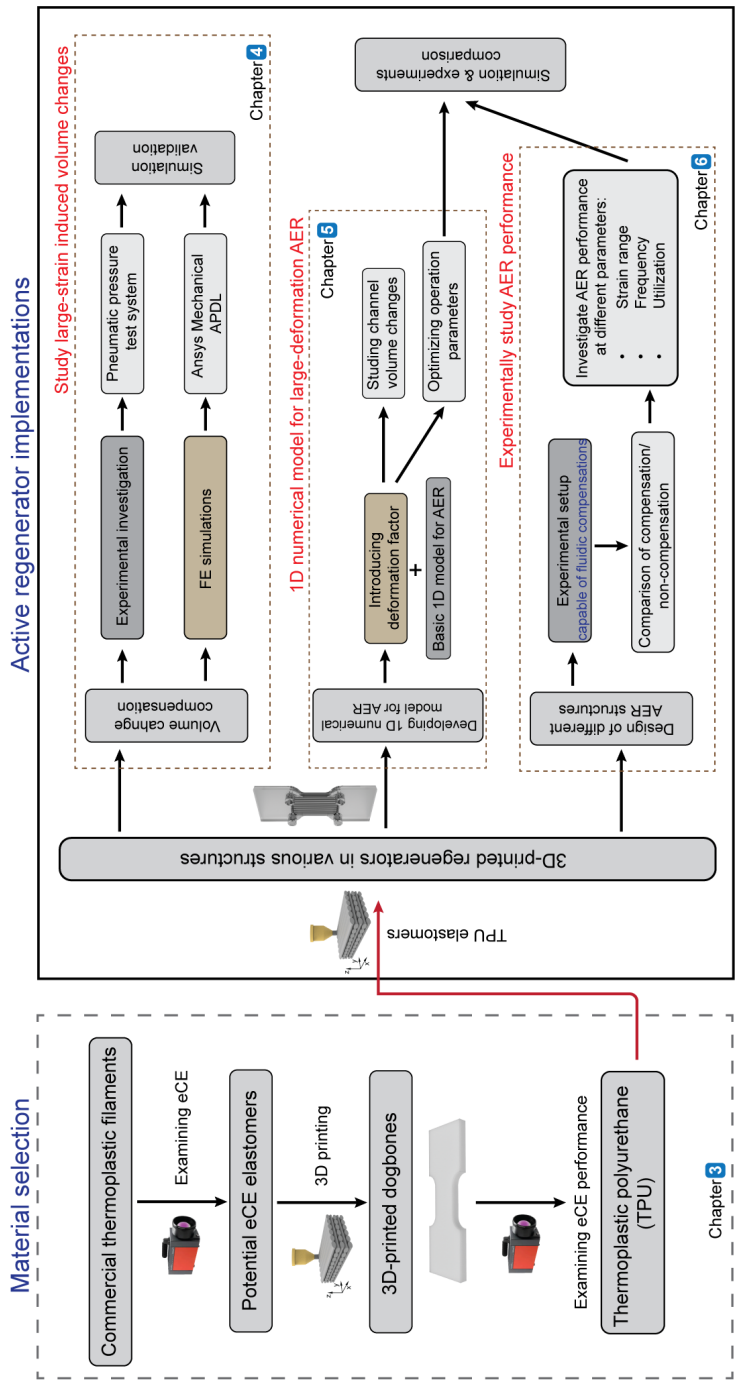

Figure 1.8. Technical procedures for the 3D-printed large-deformation active elastocaloric regenerator investigation, including four steps:
(1) Materials selection; (2) Study regenerator volume change; (3) Develop 1D numerical model for large deformation regenerators; (4) Experimental proof-of-concept.

CHAPTER 2

Theory and methods

"The objective world is, it does not happen. Only to the gaze of my consciousness, crawling along the lifeline of my body, does a section of this world come to life as a fleeting image in space which continuously changes in time."

— Hermann Weyl (German mathematician, 1885−1955)

"Experiment is the only means of knowledge at our disposal. Everything else is poetry, imagination."

— Max Planck (German physicist, 1858−1947)

2.1 Theory

In this part, the basic equations and common concepts implemented in the dissertation are presented. It primarily contains the basic theoretical framework of the following three mostly used parts in the investigations: mechanics for the elastomers (basically implemented in the elastomer mechanical FE simulations); thermodynamics of the eCE elastomers (origin of the elastocaloric effect in elastomers); and energy equations for the active eCE cooling modeling (describing the heat transfer features of the active eCE cooling process and evaluating eCE performance).

2.1.1 Continuum mechanics of elastomers

1. **Basic mechanics parameters**

   a) **Engineering strain and stress**
   Engineering or nominal strain and stress expressions:

$$\varepsilon_{\mathrm{E}} = \frac{l - l_0}{l_0} = \frac{\Delta l}{l_0} \tag{2.1}$$

$$\sigma_{\mathrm{E}} = \frac{F}{A_0} \tag{2.2}$$

where l_0 and l represent the initial and current length of a sample, respectively, as illustrated in a extended 3D beam in Figure 2.1. A_0 is the initial cross section area of a beam.

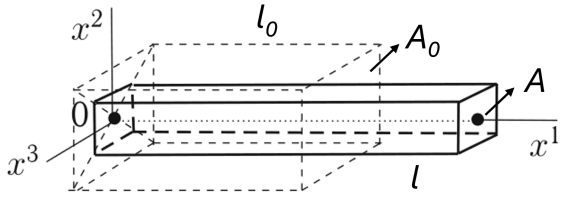

Figure 2.1. Extension diagram of a beam, reproduced from [132].

b) **Elongation or stretches**

Another parameter for describing the deformation is elongation:

$$\lambda = \frac{l}{l_0} = \frac{l_0 + \Delta l}{l_0} = 1 + \varepsilon_{\mathrm{E}} \tag{2.3}$$

c) **True strain and stress**
For large strains, the strain measure can be obtained using the incremental approximation:

$$\varepsilon_T = \int d(\varepsilon_{\mathrm{E}}) = \int_L^l \frac{dl}{l} = \ln \frac{l}{L} = \ln(1 + \varepsilon_{\mathrm{E}}) \tag{2.4}$$

, which leads to the definition of the true or logarithmic strain ε_L, also called Hencky strain.
The true stress is the stress in real time, which can be defined as:

$$\sigma_{\mathrm{T}} = \frac{F}{A} = \frac{F}{A_0}\frac{A_0}{A} = \frac{F}{A_0}\frac{L_0}{L} = \sigma_{\mathrm{E}}(1 + \varepsilon_{\mathrm{E}}) \tag{2.5}$$

d) **Poisson's ratio**
Poisson's ratio (PR) is an important mechanical parameter that associates with the materials geometrical variation when strained elastically. PR shows how the deformation of the cross-section of a body relates to levels of axial deformation. If the lateral contraction is measured, Poisson's ratio can be obtained (for small strains, engineering strain exhibits a good approximation):

$$\nu = -\frac{-\varepsilon_t}{\varepsilon_l} \tag{2.6}$$

where ε_t is the transverse strain and ε_l is the axial strain.

2. Continuum mechanics framework

Continuum mechanics studies the behavior of a continuous three-dimensional material body, such as the Newtonian fluids or the Hookean solids, which are usually used to establish the constitutive theory of the rubber-like elastomers undergoing a large strain. We introduce some basic concepts of the continuum mechanics herein, which are associated with the derivation of hyperelastic models for the large-deformation elastomers.

a) **Invariants of second-order tensor**
The three invariants of a second-order tensor $\mathbf{S} = S_{ij}\mathbf{e}_i \otimes \mathbf{e}_j$ can be obtained by the expansion of the eigen-equation of $\mathbf{S}$. The eigenequation can be expressed as:

$$det(\mathbf{S} - \lambda\mathbf{I}) = \begin{vmatrix} S_{11} - \lambda & S_{12} & S_{13} \\ S_{21} & S_{22} - \lambda & S_{23} \\ S_{31} & S_{32} & S_{33} - \lambda \end{vmatrix} = 0 \tag{2.7}$$

, in which λ is the eigenvalues of $\mathbf{S}$, and $\mathbf{I} = \delta_{ij}\mathbf{e}_i \otimes \mathbf{e}_j$ is the second-order identity tensor. It can be expanded into following equation:

$$\lambda^3 - I_1\lambda^2 + I_2\lambda - I_3 = 0. \tag{2.8}$$

The three invariants I_1, I_2, and I_3 can be obtained from the equation.

$$\begin{aligned} I_1 &= tr\mathbf{S} = S_{ii} \\ I_2 &= \frac{1}{2}(S_{ii}S_{jj} - S_{ij}S_{ji}) = \frac{1}{2}[(tr\mathbf{S})^2 - tr\mathbf{S}^2] \\ I_3 &= det\mathbf{S} = \varepsilon_{ijk}S_{1i}S_{2j}S_{3k} = J^2 \end{aligned} \tag{2.9}$$

J is the Jacobian, which is 0 for incompressible materials and non-zero for compressible materials. If the eigenvalues of $\mathbf{S}$ are λ_1, λ_2, λ_3, the $\mathbf{S}$ can expressed as $\mathbf{S} = \sum_{i=1}^{3} \lambda_i \mathbf{e}_i \otimes \mathbf{e}_i$. The invariants can also be expressed by the eigenvalues:

$$\begin{aligned} I_1 &= tr\mathbf{S} = \lambda_1^2 + \lambda_2^2 + \lambda_3^2 \\ I_2 &= \frac{1}{2}[(tr\mathbf{S})^2 - tr\mathbf{S}^2] \\ &= \lambda_1^2\lambda_2^2 + \lambda_2^2\lambda_3^2 + \lambda_3^2\lambda_1^2 \\ I_3 &= det\mathbf{S} = \lambda_1^2\lambda_2^2\lambda_3^2 = J^2 \end{aligned} \tag{2.10}$$

See more details in the book [133].

b) **Strain measure and stress measure**
The general strain measure in tensor form can be summarized by combining both Lagrangian (**C**) and Eulerian (**B**) strain tensors [134]:

$$\mathbf{e}_n = \begin{cases} \frac{\mathbf{C}^{n/2}-\mathbf{I}}{n} & \text{if } n > 0, \\ \ln \mathbf{C}^{1/2} & \text{if } n = 0, \\ \frac{\mathbf{B}^{n/2}-\mathbf{I}}{n} & \text{if } n < 0. \end{cases} \tag{2.11}$$

Specifically, the Lagrangian (**C**) type represents the right Cauchy-Green tensor and the Eulerian (**B**) type represents the left Cauchy-Green tensor. There are some commonly used strain tensors, for instance, the $n = 0$ for the Hencky (true or logarithmic) strain tensor; the $n = 1$ for the Biot strain tensor; the $n = 2$ for the Green strain tensor; the $n = -2$ for the Almansi strain tensor.

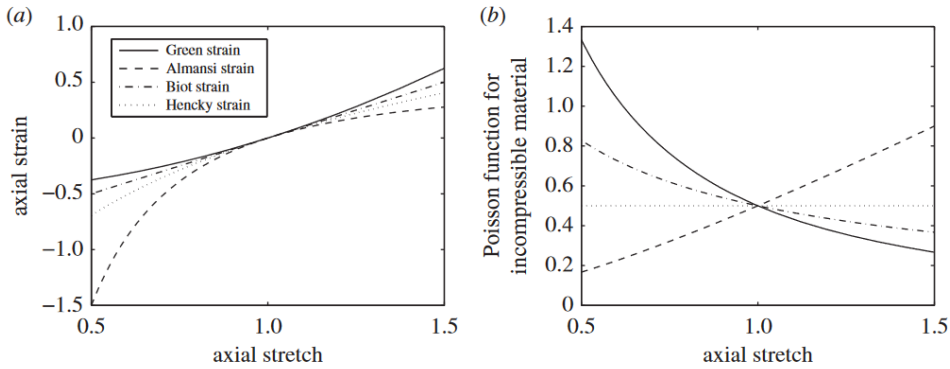

Figure 2.2. Comparison of different strains and Possion's functions (reproduced from [134]): *(a) finite axial strains* $\mathbf{e}_n(a)$ *as a function of stretches* λ*; (b) nonlinear Poisson's ratios of different strains for incompressible materials.*

The first Piola-Kirchhoff (PK1) stress tensor **P**, representing the force per unit area under the reference configuration:

$$\mathbf{P} = J\sigma\mathbf{F}^{-\mathrm{T}} = \frac{\partial \mathcal{W}}{\partial \mathbf{F}} - p\mathbf{F}^{-\mathrm{T}} \tag{2.12}$$

in which **F** is deformation gradient, and $\mathbf{F}^{-\mathrm{T}}$ is the inverse of $\mathbf{F}^{\mathrm{T}}$. T represents the transpose. $J = 1$ indicates incompressible materials, and $p = 0$ indicates compressible materials.
The second Piola-Kirchhoff (PK2) stress tensor **S** is constructed under the symmetric configuration:

$$\mathbf{S} = \mathbf{F}^{-1}\mathbf{P} = J\mathbf{F}^{-1}\sigma\mathbf{F}^{-\mathrm{T}} = 2\frac{\partial \mathcal{W}}{\partial \mathbf{C}} - p\mathbf{C}^{-1} \tag{2.13}$$

where the right Cauchy-Green tensor $\mathbf{C} = \mathbf{F}^{-\mathrm{T}}\mathbf{F}$.

c) **Poisson's function**
For the rubbers and rubber-like elastomers, it is capable of undergoing a large strain. During the large-deformation process, the materials Poisson's ratio is strain-dependent, which can be described by different Poisson's functions $v_{\mathrm{n}}(a)$, defined by different strains as shown in Figure 2.2.

$$v_{\mathrm{n}}(a) = -\frac{\mathbf{e}_{\mathrm{n}}(\lambda(a))}{\mathbf{e}_{\mathrm{n}}(a)} \tag{2.14}$$

where the general strain $\mathbf{e}_n$ in tensor form is used, and a is the current length along axial direction of a hyperelastic body.

Table 2.1. Selected isotropic hyperelastic constitutive models, in which if the J equals to 1, the material is incompressible, otherwise is compressible.

Material models	Strain energy density function $\mathcal{W}(\lambda_1, \lambda_2, \lambda_3)$
neo-Hookean [135]	$\frac{c_1}{2}(\lambda_1^2 + \lambda_2^2 + \lambda_3^2 - 3)$ c_1 independent of deformation
Mooney-Rivlin [136]	$\sum_{i,j=0}^{N} C_{ij}\,(\bar{I}_1 - 3)^i\,(\bar{I}_2 - 3)^j + \sum_{i=1}^{N} \frac{1}{d_i}\,(J-1)^{2i}$ $C_{i,j}$, d independent of deformation
Ogden [137]	$\sum_{i=1}^{N} \frac{\mu_i}{\alpha_i^2}\left(\bar{\lambda}_1^{\alpha_i} + \bar{\lambda}_2^{\alpha_i} + \bar{\lambda}_3^{\alpha_i} - 3\right) + \sum_{i=1}^{N} \frac{1}{d_i}(J-1)^{2i}$ μ, α, d independent of deformation
Gent [138]	$-\frac{\mu J_m}{2} \ln\left(1 - \frac{\overline{I_1}-3}{J_m}\right) + \frac{1}{d}\left(\frac{J^2-1}{2} - \ln J\right)$ J_m, μ, d independent of deformation
Arrunda-Boyce [139]	$\mu\left[\frac{1}{2}(\bar{I}_1 - 3) + \frac{1}{20\lambda_L^2}\left(\bar{I}_1^2 - 9\right) + \frac{11}{1050\lambda_L^4}\left(\bar{I}_1^3 - 27\right) + \right.$ $\left.\frac{19}{7050\lambda_L^6}\left(\bar{I}_1^4 - 81\right) + \frac{519}{673750\lambda_L^8}\left(\bar{I}_1^5 - 243\right)\right] + \frac{1}{d}\left(\frac{J^2-1}{2} - lnJ\right)$ μ, λ_L, d independent of deformation
Yeoh [140]	$\sum_{i=1}^{N} c_{i0}\,(\bar{I}_1 - 3)^i + \sum_{k=1}^{N} \frac{1}{d_k}(J-1)^{2k}$ C_{i0}, N, d independent of deformation

3. **Hyperelastic constitutive models**

Hyperelasticity refers to the large-range elasticity of materials, that can undergo significant deformations and revert to their original shape after unloading. The hyperelastic constitutive models can be implemented to various rubber-like elastomers and biological tissues. The hyperelastic model is developed by different strain potential functions with nonlinear elastic behavior. The constitutive relationship, based on the theory of continuum mechanics, can be described by the strain energy density function $\mathcal{W}$ as follows:

$$\mathcal{W} = \mathcal{W}(I_1, I_2, I_3) = \mathcal{W}(\lambda_1, \lambda_2, \lambda_3), \tag{2.15}$$

in which I_1, I_2, I_3 are the three invariants of the right Cauchy-Green deformation tensor $\mathbf{C}$. These invariants can be obtained from expansion of the eigenequation of deformation tensor, and expressed by the eigenvalues (i.e. stretch ratios, $\lambda_1, \lambda_2, \lambda_3$) of $\mathbf{C}$. We list several typical hyperelastic models in Table 2.1, developed to capture the phenomenological behavior of hyperelastic materials.

In the table, some of the strain energy density functions are expressed by the principle stretches noted by an overline on the top, which is based on the deviatoric-volumetric multiplicative split for compressible material models [141]. For compressible materials, the so-called deviatoric strain invariants are introduced. The strain energy density function consists of the compressible and the hydrostatic terms [141, 142]:

$$W = W_c(I_1, I_2, J) + W_h(J), \tag{2.16}$$

and the deviatoric strain invariants and stretches are defined as:

$$\begin{aligned} \bar{\lambda}_p &= J^{-1/3}\lambda_p \ (p = 1, 2, 3) \\ \bar{I}_p &= J^{-2p/3} I_p \end{aligned} \tag{2.17}$$

The strain energy density function yields:

$$W = W(\bar{I}_1, \bar{I}_2, J) = W(\bar{\lambda}_1, \bar{\lambda}_2, \bar{\lambda}_3, J) \tag{2.18}$$

2.1.2 Thermodynamics of elastocaloric elastomers

In this section, we present the thermodynamics of elastocaloric elastomers and introduce the origin of their elastocaloric effect, mainly associated with the entropic elasticity and strain-induced crystallization (SIC) in the molecular chain. Basically, in thermodynamics, the Helmholtz free energy F of the system can be expressed as:

$$F = U - TS, \tag{2.19}$$

in which the U, T and S are the internal energy, temperature, and entropy, respectively. The differential form of this equation yields:

$$dF = dU - TdS - SdT \tag{2.20}$$

According the first law of thermodynamics, the variation of internal energy is:

$$dU = dQ + dW, \tag{2.21}$$

where the dQ refers to the energy from heat transfer and the dW refers to the work done by the system. It can be written as:

$$\begin{cases} dQ = TdS \\ dW = \vec{F} \cdot d\vec{l} = V\sigma d\varepsilon \end{cases} \tag{2.22}$$

where V is the material volume. By combining equations 2.20 and 2.22, dF yields:

$$dF = V_0 \sigma d\varepsilon - SdT = \left(\frac{\partial F}{\partial \varepsilon}\right)_T d\varepsilon - \left(\frac{\partial F}{\partial T}\right)_\varepsilon \mathrm{d}T \tag{2.23}$$

Considering the Maxwell relation between cross derivatives, we can obtain:

$$\beta = \left(\frac{\partial \sigma}{\partial T}\right)_\varepsilon = \frac{\partial}{\partial T}\left(\frac{\partial F}{\partial \varepsilon}\right)_T = \frac{\partial}{\partial \varepsilon}\left(\frac{\partial F}{\partial T}\right)_\varepsilon = -\rho\left(\frac{\partial S}{\partial \varepsilon}\right)_T \tag{2.24}$$

where ρ is the density, and the constant $\beta = \left(\frac{\partial \sigma}{\partial T}\right)_\varepsilon$ is defined as the Clausius-Clapeyron factor. Accordingly, the isothermal entropy and adiabatic temperature changes can be calculated as follows:

$$\Delta S_{\mathrm{iso}} = -\frac{1}{\rho}\int_0^\varepsilon \left(\frac{\partial \sigma}{\partial T}\right)_\varepsilon d\varepsilon \tag{2.25}$$

$$\Delta T_{ad} = \frac{T_0}{\rho c_{p,\varepsilon=0}}\int_0^\varepsilon \left(\frac{\partial \sigma}{\partial T}\right)_\varepsilon d\varepsilon = -\frac{T_0}{\rho c_{p,\varepsilon=0}}\Delta S_{\mathrm{iso}} \tag{2.26}$$

It is possible to calculate the adiabatic temperature changes at a constant specific heat c_p at T_0. In practical implementations, the adiabatic temperature changes are usually evaluated from a total entropy-temperature ($S - T$) diagram at different applied stresses, which requires the temperature-dependent stress-strain profiles. The total entropy can be evaluated from a zero-field c_p baseline by integration, where a less temperature-dependent c_p should be achieved at the chosen start temperature T_i, specifically as follows:

$$S_{\mathrm{tot}} = S_{\mathrm{tot},\sigma=0} + \Delta s_{\mathrm{iso}} \tag{2.27}$$

$$S_{\mathrm{tot},\varepsilon=0} = \int_{T_i}^{T_2} \frac{c_p}{T}\,\mathrm{d}T. \tag{2.28}$$

It has been demonstrated an effective estimation of temperature-dependent adiabatic temperature changes, for typical SMAs. However, for elastocaloric elastomers [97], this estimation of ΔT_{ad} appears significant uncertainties, probably due to the contribution of strain-induced crystallization (SIC) [143]. There are some improved methods to evaluate the temperature changes, based on statistical mechanics of polymer networks as well as some experimental findings [144–146].

Taking account into the presence of SIC, the Helmholtz free energy density of an incompressible elastomer by introducing the variable crystalline fraction χ can be expressed as [91, 147]:

$$F = c_p T - \chi U_{\mathrm{ac}} - T\left[-\chi \frac{U_{\mathrm{ac}}}{T_{\mathrm{c},0}} + S_{\mathrm{ch}}(\lambda,\chi) + c_p \ln \frac{T}{T_S}\right], \tag{2.29}$$

where c_p refers to the specific volumetric heat capacity, and the term $c_p T - \chi U_{\mathrm{ac}}$ represents the internal energy U. Specifically, the term $-\chi U_{\mathrm{ac}}$ refers to lower energy at the crystalline state. The U_{ac} is the latent heat of crystallization (per unit volume), calculated by the product of density and the crystallization enthalpy ΔH, as follows $U_{\mathrm{ac}} = \rho \Delta H$. In the bracket, the term is the non-equilibrium total entropy, consisting of three parts: the thermal entropy ($c_p \ln \frac{T}{T_S}$); the configurational entropy for the individual structural units ($-\chi S_{ac} = -\chi \frac{U_{\mathrm{ac}}}{T_{\mathrm{c},0}}$); partial crystallization of molecular chains ($S_{\mathrm{ch}}(\lambda,\chi)$), induced by stretching. Thus the total entropy can be written as:

$$\begin{aligned} S &= S_{\mathrm{config}}(\lambda) + S_{\mathrm{thermal}}(T) \\ &= -\chi \frac{U_{\mathrm{ac}}}{T_{\mathrm{c},0}} + S_{\mathrm{ch}}(\lambda,\chi) + c \ln \frac{T}{T_S} \end{aligned} \tag{2.30}$$

Due to the minimize free energy for the system equilibrium, the derivative of Helmholtz free energy equation with respect to χ is zero (i.e. $\frac{\partial F(T,\lambda,\chi)}{\partial \chi}|_{\chi_{\mathrm{eq}}} = 0$), and we can obtain:

$$U_{\mathrm{ac}}\left(\frac{1}{T_{\mathrm{c},0}} - \frac{1}{T}\right) = \frac{\partial S_{\mathrm{ch}}(\lambda,\chi)}{\partial \chi}|_{\chi_{\mathrm{eq}}} = S_{\mathrm{ch},\chi}\left(\lambda,\chi_{\mathrm{eq}}\right), \tag{2.31}$$

in which the $\chi_{\mathrm{eq}}(T,\lambda)$ is the crystalline fraction at equilibrium. Herein, for the adiabatic process $dS = 0$, the full differential of the total entropy at equilibrium, based on equation 2.30 substituted with the equilibrium crystallization expression in Eq. 2.31, can be obtained as follows:

$$\begin{aligned} c_p \frac{dT}{T} &= \left[\frac{U_{\mathrm{ac}}}{T_{\mathrm{c},0}} - S_{\mathrm{ch},\chi}(\lambda,\chi)\right] d\chi - S_{\mathrm{ch},\lambda}(\lambda,\chi) d\lambda \\ &\overset{eq}{=} \frac{U_{\mathrm{ac}}}{T} d\chi - S_{\mathrm{ch},\lambda}(\lambda,\chi_{\mathrm{eq}}) d\lambda \end{aligned} \tag{2.32}$$

Looking into the above equation, the partial derivative of the total configurational entropy with respect to the crystallinity χ yields:

$$\begin{aligned}\frac{\partial S_{\text{config}}(\lambda,\chi)}{\partial \chi} &= S_{\text{config},\chi}(\lambda,\chi) \\ &= -\frac{U_{\text{ac}}}{T_{\text{c},0}} + S_{\text{ch},\chi}(\lambda,\chi) \overset{eq}{=} -\frac{U_{\text{ac}}}{T}\end{aligned} \tag{2.33}$$

At a constant λ, it observed that the total configurational entropy S_{config} decreases with the crystallinity χ and increases with temperature. The last term in Eq 2.32, during the uniaxial tension, is associated with the stress and stretches. As aforementioned the full differential for free energy F, the stress σ can be expressed as $\sigma d\lambda = dF$. In the present of SIC, from the derivation of F, the stress can be obtained:

$$\begin{aligned}\sigma &= \frac{\partial F(\lambda,T)}{\partial \lambda} \\ &= -U_{ac}\frac{\partial \chi}{\partial \lambda} - T\left[-\frac{U_{\text{ac}}}{T_{\text{c},0}}\frac{\partial \chi}{\partial \lambda} + \frac{\partial}{\partial \lambda}S_{\text{ch}}(\lambda,\chi)\right] \\ &\overset{eq}{=} -U_{ac}\frac{\partial \chi_{\text{eq}}(T,\lambda)}{\partial \lambda} - T\left[-\frac{U_{\text{ac}}}{T_{\text{c},0}}\frac{\partial \chi_{\text{eq}}(T,\lambda)}{\partial \lambda} + \frac{\partial}{\partial \lambda}S_{\text{ch}}(\lambda,\chi_{\text{eq}}(T,\lambda))\right]\end{aligned} \tag{2.34}$$

in which the partial derivative of the chain entropy can be deduced by:

$$\frac{\partial}{\partial \lambda}S_{\text{ch}}(\lambda,\chi_{\text{eq}}(T,\lambda)) = \frac{\partial S_{\text{ch}}(\lambda,\chi_{\text{eq}}(T,\lambda))}{\partial \lambda} + \frac{\partial S_{\text{ch}}(\lambda,\chi_{\text{eq}}(T,\lambda))}{\partial \chi}\frac{\partial \chi_{\text{eq}}(T,\lambda)}{\partial \lambda} \tag{2.35}$$

Thus the stress at equilibrium in Eq. 2.34 yields:

$$\begin{aligned}\sigma &\overset{eq}{=} -U_{ac}\frac{\partial \chi_{\text{eq}}(T,\lambda)}{\partial \lambda} + T\frac{U_{\text{ac}}}{T_{\text{c},0}}\frac{\partial \chi_{\text{eq}}(T,\lambda)}{\partial \lambda} \\ &\quad - T\left[\frac{\partial S_{\text{ch}}(\lambda,\chi_{\text{eq}}(T,\lambda))}{\partial \lambda} + \frac{\partial S_{\text{ch}}(\lambda,\chi_{\text{eq}}(T,\lambda))}{\partial \chi}\frac{\partial \chi_{\text{eq}}(T,\lambda)}{\partial \lambda}\right]\Big] \\ &= \left[U_{\text{ac}}\left(\frac{T}{T_{\text{c},0}} - 1\right) - T\frac{\partial S_{\text{ch}}(\lambda,\chi_{\text{eq}}(T,\lambda))}{\partial \chi}\right]\frac{\partial \chi_{\text{eq}}(T,\lambda)}{\partial \lambda} \\ &\quad - T\frac{\partial S_{\text{ch}}(\lambda,\chi_{\text{eq}}(T,\lambda))}{\partial \chi} \\ &= -T\frac{\partial S_{\text{ch}}(\lambda,\chi_{\text{eq}}(T,\lambda))}{\partial \chi} \\ &= -TS_{\text{ch},\lambda}\left[\lambda,\chi_{\text{eq}}(T,\lambda)\right]\end{aligned} \tag{2.36}$$

The equilibrium stress σ is dependent on the variables temperature T, stretches λ, and crystalline fraction χ, and can be expressed as $\sigma\left[T,\lambda,\chi_{\text{eq}}(T,\lambda)\right]$. Accordingly,

the Eq 2.32, replacing the term $S_{\mathrm{ch},\lambda}(\lambda, \chi_{\mathrm{eq}})$ and using the equilibrium stress, can be rewritten as:

$$dT = \frac{U_{\mathrm{ac}}}{c_p} d\chi + \frac{1}{c_p} \sigma \left[T, \lambda, \chi_{\mathrm{eq}}(T, \lambda)\right] d\lambda \tag{2.37}$$

Consequently, the adiabatic temperature changes, including the SIC process, can be calculated by:

$$\Delta T_{\mathrm{ad}} = \frac{U_{\mathrm{ac}} \chi}{c_p} + \frac{1}{V c_p} \int \sigma d\lambda \tag{2.38}$$

in which the U_{ac} can be obtained from the crystallization enthalpy ΔH. The χ is both temperature-dependent and strain-dependent, and the isothermal mechanical behavior for the elastomers is also required to evaluate the temperature-dependent ΔT_{ad}.

2.1.3 1D numerical models for active elastocaloric regenerators

In an active caloric regenerator or heat pump, due to the presence of reciprocating heat-transfer fluids, the heat transfer and heat conversion phenomena are relatively complicated to model. The numerical modelling enables mapping out the theoretical performance of an active caloric regenerator. For instance, the cooling power versus the temperature span, coefficient of performance (COP), and the temperature gradients during an active cycle all can be predicted. The one-dimensional (1D) numerical model has been intensively implemented to predict the AMR performance, which considers several typical thermal connections among the six most important thermal components (see Figure 2.3a) in an active regenerator system, and solves the spatial

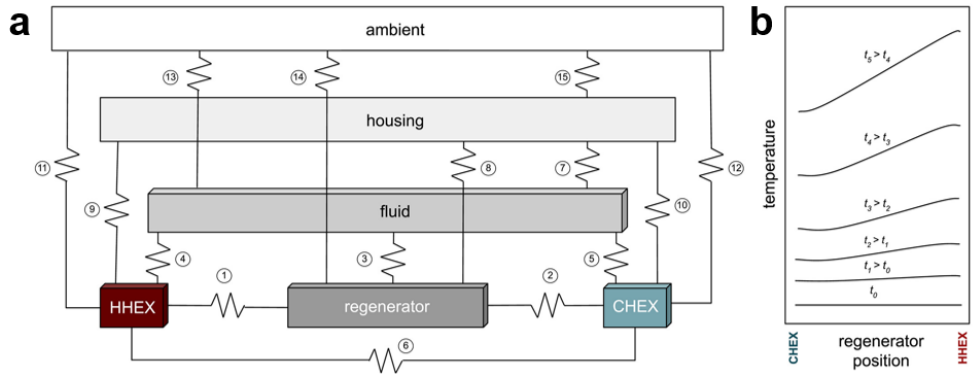

Figure 2.3. a, The 15 possible thermal connections in an active regeneration device, considering the six most significant thermal components regenerator, fluid, cold HEX (CHEX), hot HEX (HHEX), housing and ambient. b, The spatial temperature gradients of the regenerator over the time evolution. Images were reproduced from [148].

temperature gradients (see Figure 2.3b) for the solid and fluid in active cycles. In this dissertation, a one-dimensional (1D) transient model, based on a 1D AMR model by introducing the strain-dependent variables, is developed for the large-deformation active elastocaloric regenerator.

2.1.3.1 Basic governing equations for AER model

A typical active elastocaloric regenerator model based on Ni-Ti alloys has been developed to study the AER performance [18], and has achieved a good prediction for the AER, similar to the 1D AMR models developed by [109, 149, 150]. Here, we expect to develop a typical AER 1D model based on two governing equations for fluids and solids (MCE materials), which can be expressed as:

$$\underbrace{A_c \epsilon \rho_f c_f \frac{\partial T_f}{\partial t}}_{\text{Heat storage}} = \underbrace{\frac{Nuk_f}{D_h} a A_c \left(T_s - T_f\right)}_{\text{Heat convection}} + \underbrace{\frac{\partial}{\partial x}\left(k_{disp} A_c \frac{\partial T_f}{\partial x}\right)}_{\text{Heat conduction}} - \underbrace{\dot{m}_f c_f \frac{\partial T_f}{\partial x}}_{\text{Heat advection}} + \underbrace{\left|\frac{\partial P}{\partial x}\frac{\dot{m}_f}{\rho_f}\right|}_{\text{Viscous dissipation}} \tag{2.39}$$

$$\underbrace{A_c(1-\epsilon)\rho_s c_s \frac{\partial T_s}{\partial t}}_{\text{Heat storage}} = \underbrace{- A_c(1-\epsilon)\rho_s T_s \left(\frac{\partial s_s}{\partial H}\right)_{T_s} \frac{\partial H}{\partial t}}_{\text{Magnetocaloric heat}} + \underbrace{\frac{Nuk_f}{D_h} a A_c \left(T_f - T_s\right)}_{\text{Heat convection}} + \underbrace{\frac{\partial}{\partial x}\left(k_{stat} A_c \frac{\partial T_s}{\partial x}\right)}_{\text{Heat conduction}} \tag{2.40}$$

Actually, the significant difference between the AER and AMR is the applied external field, manifesting itself in the magnetocaloric term in the Eq. 2.40. We can change the magnetocaloric term to the elastocaloric term to obtain an AER model. Practically, when the AER setup is operated for caloric cooling or heat pump, the strain is the controllable parameter. Therefore, the strain was considered as the external field for driving elastocaloric devices. The basic governing equations for the **soft AER model** can be expressed as:

$$\underbrace{A_c \epsilon \rho_f c_f \frac{\partial T_f}{\partial t}}_{\text{Heat storage}} = \underbrace{\frac{Nuk_f}{D_h} a_s A_c \left(T_s - T_f\right)}_{\text{Heat convection}} + \underbrace{\frac{\partial}{\partial x}\left(k_{disp} A_c \frac{\partial T_f}{\partial x}\right)}_{\text{Heat conduction}} - \underbrace{\dot{m}_f c_f \frac{\partial T_f}{\partial x}}_{\text{Heat advection}} + \underbrace{\left|\frac{\partial P}{\partial x}\frac{\dot{m}_f}{\rho_f}\right|}_{\text{Viscous dissipation}} \tag{2.41}$$

$$\underbrace{\frac{\partial T_s}{\partial t}}_{\text{Heat storage}} = \underbrace{- \frac{T_s}{c_{s,\varepsilon}} \left(\frac{\partial s}{\partial \varepsilon}\right)_T \frac{\partial \varepsilon}{\partial t}}_{\text{Elastocaloric heat}} + \underbrace{\frac{Nuk_f a_s}{D_h \rho_s c_{s,\varepsilon}(1-\epsilon)} \left(T_f - T_s\right)}_{\text{Heat convection}} + \underbrace{\frac{1}{\rho_s c_{s,\varepsilon}(1-\epsilon)} \frac{\partial}{\partial x}\left(k_{stat} \frac{\partial T_s}{\partial x}\right)}_{\text{Heat conduction}} \tag{2.42}$$

, in which the T_s, T_f, x, ϵ, Ac, k_{disp}, k_{stat}, $\dot{m}_f$, and a_s are the solid temperature, fluid temperature, axial coordinate (along the regenerator length), porosity, cross-section

area, thermal conductivity of fluid dispersion, static thermal conductivity, mass flow rate of fluids and specific surface area of the regenerator. The subscripts s and f represent the solid matrix (regenerator materials) and the heat-transfer fluids, respectively. The temperature profiles (T_s, T_f) of heat-transfer fluids and regenerator solids can be obtained by solving the energy equations numerically.

However, the soft elastocaloric regenerators require large applied strains, and thus the geometry of regenerators is subjected to a large deformation, which cannot be neglected in the model. A comprehensive explanation of the model improvements for large-deformation regenerators is provided in **Chapter 5**.

2.1.3.2 Performance parameters of active elastocaloric regenerators

The performance of an active elastocaloric regenerator can be influenced by multiple operation parameters, primarily including operating frequency (f), applied strains (ε), working temperature (T_H), mass flow rate $\dot{m}$ (or Utilization, U), and geometrical parameters of the regenerator (porosity, ϵ, channel shapes, etc.). Herein, we first introduce these typical operation parameters and their definitions, and then present several main parameters for evaluating an AER performance.

The definition of typical operating parameters:

- Frequency, f
  The frequency f is determined by an elastocaloric cycle time τ, which is the sum of the field loading/unloading time and the hot/cold blows time in one cycle.

- Applied strains, ε
  In the soft AER operation, the applied strains include not only the strain magnitude but also the operating strain range, because of the existing significant plastic deformation resulting in buckling of the regenerator. It is suggested to operate with a pre-strain to prevent buckling.

- Mass flow rate, $\dot{m}$
  The mass flow rate is associated with the amount of heat transfer fluids displaced by a piston or pump per unit time. In our case, a movable piston is utilized. The $\dot{m}$ can be determined by the piston stroke S_P:

$$\dot{m} = \frac{\pi S_P R_{piston}^2}{t_{piston}} \tag{2.43}$$

- Utilization, U
  Utilization is the thermal mass ratio of the displaced heat exchange medium per blow and the regenerator solid, which is defined as:

$$U = \frac{\int_0^{\tau/2} \dot{m}_f c_f dt}{m_s c_s} = \frac{V_{\text{pump}} \rho_f c_f}{m_s c_s} = \frac{V_{\text{pump}} \rho_f c_f}{(1-\epsilon) V_R \rho_s c_s} \tag{2.44}$$

- Geometrical parameters
  The geometrical parameters are associated with the regenerator structures, which determine how much caloric energy can be extracted from the regenerator to the hot/cold reservoirs by active heat-transfer fluids. In general, AER geometries can be characterized by the following parameters:

  1. Porosity ϵ
  2. Specific surface area a_s
  3. Hydraulic diameter D_h

  With respect to a homogeneous AER structure, these basic geometrical parameters meet a relation:

$$a_s = \frac{4\epsilon}{D_h} \tag{2.45}$$

  We list some most utilized regenerator geometries in state-of-the-art regenerators and the calculation of their corresponding geometrical parameters in Table 2.2.

Table 2.2. Geometrical parameters for different microchannel regenerators

Geometry	Equations of geometrical parameters	Description
Parallel-plate channel	• $\epsilon = \frac{\delta_f}{\delta_s+\delta_f}$ • $D_h = 2\delta_f$ • $a_s = \frac{4\epsilon}{D_h} = \frac{2}{\delta_s+\delta_f}$	Channel thickness (δ_s) and plate thickness (δ_f)
Rectangular microchannels	• $D_h = \frac{2H_{r1}H_{r2}}{H_{r1}+H_{r2}}$ • $a_S = \frac{4\varepsilon}{D_h} = \frac{2\varepsilon(H_{r1}+H_{r2})}{H_{r1}H_{r2}}$	Channel width (H_{r1}) and height (H_{r2})
Circular microchannels	• $D_h = D_c$ • $a_s = \frac{4\varepsilon}{D_h} = \frac{4\varepsilon}{D_c}$	Channel diameter (D_c)

Geometry	Equations of geometrical parameters	Description
Triangular microchannels	• $D_h = \frac{L\sin\theta}{1+\sin\frac{\theta}{2}}$ • $a_S = \frac{4\varepsilon}{D_h} = \frac{4+4\sin\frac{\theta}{2}}{L\sin\theta}$	Triangle length (L) and angle (θ)

There are some important performance parameters for the AERs, subjected to the oscillatory fluids and periodic applied strains in an elastocaloric cycle, including the temperature span, cooling power, specific cooling power, and coefficient of performance. Specifically, they are defined as follows:

- Temperature span between cold and hot reservoirs, T_{span}

$$T_{span} = T_h - T_c \tag{2.46}$$

- Cooling power for elastocaloric cooling, $\dot{Q}_c$

$$\dot{Q}_c = f\int_0^\tau \dot{m}_f c_f \left(T_{f,c,\,\mathrm{out}} - T_{f,c,\,\mathrm{in}}\right) dt. \tag{2.47}$$

- Heating power for elastocaloric heat pumps, $\dot{Q}_h$

$$\dot{Q}_h = f\int_0^\tau \dot{m}_f c_f \left(T_{f,h,\,\mathrm{out}} - T_{f,h,\,\mathrm{in}}\right) dt. \tag{2.48}$$

- Specific cooling power, SCP

$$SCP = \frac{f}{m_s}\int_0^\tau \dot{m}_f c_f \left(T_{f,c,\,\mathrm{out}} - T_{f,c,\,\mathrm{in}}\right) dt. \tag{2.49}$$

- Coefficient of performance of system, COP

  In this dissertation, we need to point out that there are different COPs presented here to distinguish, specifically for eCE materials ($\mathrm{COP_{mat}}$), COP calculated for numerical modeling regenerators, and COP for experimental systems.

  The COP for elastocaloric elastomers can usually be calculated by:

$$\mathrm{COP_{mat}} = \frac{Q/m}{\Delta W/m} = \frac{\int_{T1}^{T_2} c_p dT}{\frac{1}{\rho l_0}\oint \sigma d\varepsilon} = \frac{\Delta T_{\mathrm{ad}} c_p}{\frac{1}{m}\oint F dl} \tag{2.50}$$

  The COP for the experimental system can be calculated by:

$$COP = \frac{Q_c}{W_{mech} + W_{pump}} \tag{2.51}$$

2.2 Methods

2.2.1 FE Simulation

In this dissertation, finite-element (FE) simulations are mainly conducted for the regenerator volume change predication using Ansys Mechanical APDL scripts. The SOLID-187 tetrahedral element type is employed for meshing. Explicit FE methods are implemented in the simulation by inputting the information of a hyperelastic model fitted to the mechanical behavior. There is a related APDL script regarding the FE simulation of a parallel-plate channel regenerator, attached in **Appendix B**. The script is mainly associated with the simulation in **Chapter 4** for investigation of volume compensation of the large deformation eCE regenerator. The APDL scripts are submitted to an **ANSYS®** mechanical solver for the calculation using a MATLAB script, and the data post-processing for the volume change calculation is carried out in **MATLAB®**.

2.2.2 1D AER numerical models

The 1D numerical model for the AER is based on the energy equations, given in Eq. 2.41 and 2.42. Central-difference methods and implicit time schemes are employed to discretize energy equations in both space and time in the simulation, with 500 spatial nodes (Nx) and 2000 temporal nodes (Nt). The difference equations are solved using a sparse matrix decomposition algorithm in **MATLAB®**. The model provides performance parameters once it achieves the thermal steady state within a specified tolerance of 10^{-5}. This model is initially developed by Kurt Engelbrecht [151], and calculated in **MATLAB®**, implementing for an active magnetocaloric device. More detailed information on solving these energy equations can be found in [151–153].

2.2.3 Fabrication

1. **3D printing elastocaloric elastomers**

   In **Chapter 3**, five commercial 3D-printing filaments were employed to screen promising elastocaloric elastomers, namely NinjaFlex, KungFu72A, KungFu98A, Z-Flex and Ultimaker 95A filaments. Most of them are made of thermoplastic polyurethane (TPU), in addition to the Z-Flex filament made of thermoplastic polyester (TPPE). A Zmorph printer with a 0.3 mm nozzle is used to print the NinjaFlex, KungFu98A and Z-Flex elastomers, and the Ultimaker 95A elastomer is printed on an Ultimaker S5 Pro Bundle printer. The G-codes (printing instructions) are generated by Voxelizer2 software and Cura 4.12 for the Zmorph and Ultimaker printers, respectively. More details on materials and printed samples will be presented in **Chapter 3**.

2. **Regenerator fabrication**

The printing quality is important to the regenerator fabrication, which is associated with the material fatigue life, undiminished elastocaloric effect, water tightness, and air tightness of a printed regenerator. Although 3D-printed parts manufactured using the two mentioned 3D printers (Zmorph, Ultimaker S5 Pro) can achieve a satisfactory elastocaloric effect and fatigue life, it is difficult to ensure water tightness for 3D-printed regenerators. When we construct a full-scale 3D-printed AER using NinjaFlex TPU, the regenerator is required to allow the heat-transfer fluids flowing throughout them without leakage, and thus a good water-tightness is essential to the practical implementation. We have tried several methods to make the 3D-printed regenerator watertight, such as gluing, remelting, and chemical treatment. Maintaining effective water tightness remains a challenge when the regenerator undergoes large strains over numerous cycles, as this makes the adhesive on the AER surface prone to peeling off, see some examples of leakage in **Appendix C**.

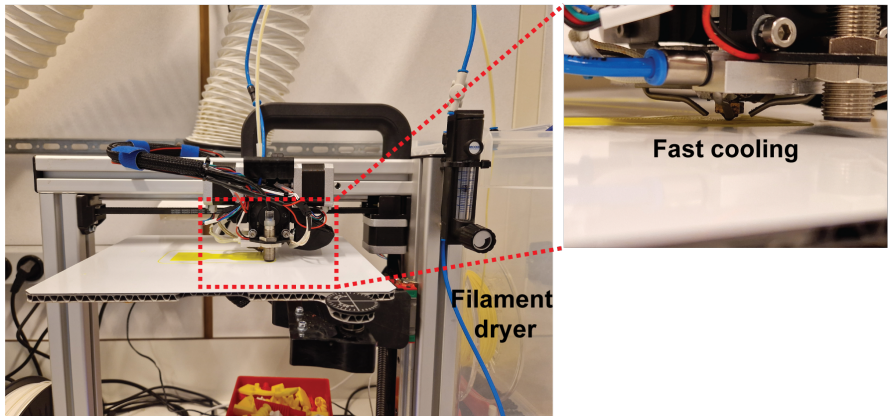

Figure 2.4. A customized Felix Tec 4.1 3D-printer.

To fabricate high-quality active regenerators, enabling water and air tightness, we employed a Felix Tec 4.1 printer as depicted in Figure 2.4, which is located in the research institute AMOLF. This printer has been specially customized with upgrades that include a filament dryer and a pneumatic cooling system. To prevent moisture, the filaments were stored in a ventilation box. The extruding nozzle was surrounded by four air nozzles with an airflow of 3 L/min, allowing for adjustable melts cooling speed to improve deposition quality. The printing G-code was also generated by Cura 5.2. On this printer, another FilaFlex 82A TPU is implemented for the printing. During the printing, the melting material flow can be precisely controlled by a high accurate extruder, and can be fast cooling down with the assistance of a cooling system (see Figure

2.4). Conversely, our Zmorph printer in DTU remains challenging to achieve the precise melt flows and adhesive deposition, for the soft TPU filament. The water tightness of 3D printed regenerators, based on the FilaFlex TPU, are examined in **Appendix C**.

2.2.4 Characterization

1. **Mechanical tests**

Mechanical tests are mainly performed on three different mechanical testers. The mechanical behaviors of the elastomers used in **Chapter 3** and **Chapter 6** are measured on a Zwick/Roell EZ030 mechanical tester, which is equipped with an Xforce K load cell allowing a maximum load of 30 kN with an uncertainty of 1%. The mechanical behavior implemented in **Chapter 4** is tested on a Instron 5965 mechanical tester, equipped with a 5kN load cell with an accuracy of $\pm 0.5\%$, which is located in the research institute AMOLF.

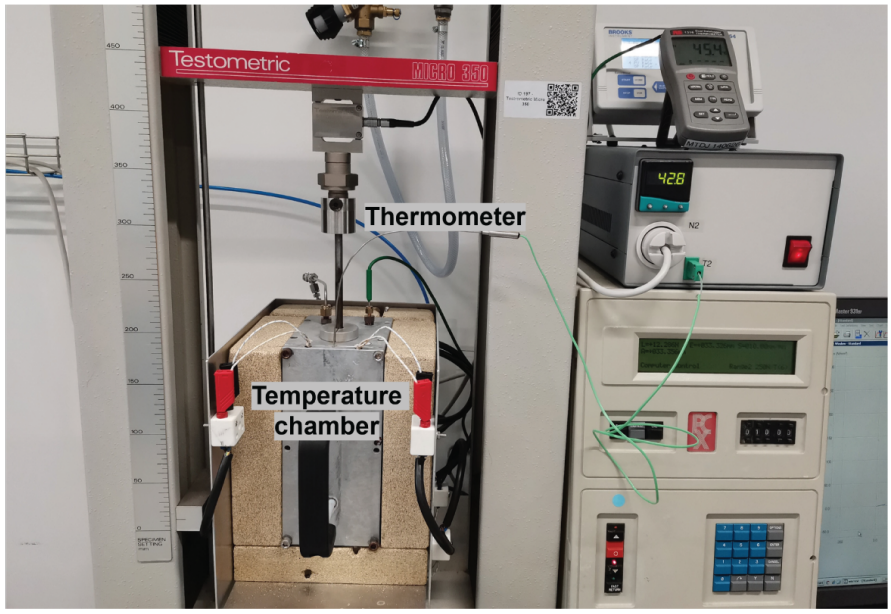

Figure 2.5. A special mechanical tester with a temperature chamber.

In particular, the isothermal mechanical behavior used in **Chapter 5** for capturing the eCE material properties was measured on a Testrometric Micro 350 tester as shown in Figure 2.5, which has a temperature chamber capable of varying test temperatures. The temperature for this apparatus can only increase from room temperature. Here, we put a bag of ice to lower down

the chamber temperature to measure the mechanical behavior at low temperatures. There are also some thermocouples placed in the chamber to monitor inside temperatures and estimate temperature stability during test.

2. **Elastocaloric measurements**

   The direct measuring method based on the thermophotography was used for elastocaloric measurement. Temperature changes were recorded using an infrared (IR) thermographic camera (InfraTec 9400). The spatial resolution and temperature resolution of the IR camera can achieve 0.01 mm/pixel and 0.02 K, respectively.

3. **SEM characterization**

   A Zeiss EVO MA10 Scanning Electron Microscope (SEM) was implemented for the morphological investigation of the 3D printed parts and regenerators as shown in Figure 2.6, which is equipped with energy dispersive X-ray spectroscopic (EDS) spectrophotometry. Our tests were performed at 5kV with a high-sensitive secondary electron detector (SED). The elastomeric sample is required to coat the carbon on the surface to improve the conductivity.

Figure 2.6. Zeiss EVO MA10 SEM with energy dispersive X-ray spectrscopy (EDS).

4. **Thermal analysis**

   Specific heat capacity (c_p) was measured on a custom-built, high-resolution, Peltier element based Differential Scanning Calorimetry (DSC) [154]. The tests

were carried out with heating and cooling rates of 1 K/min in a vacuum of 5×10^{-6} mbar.

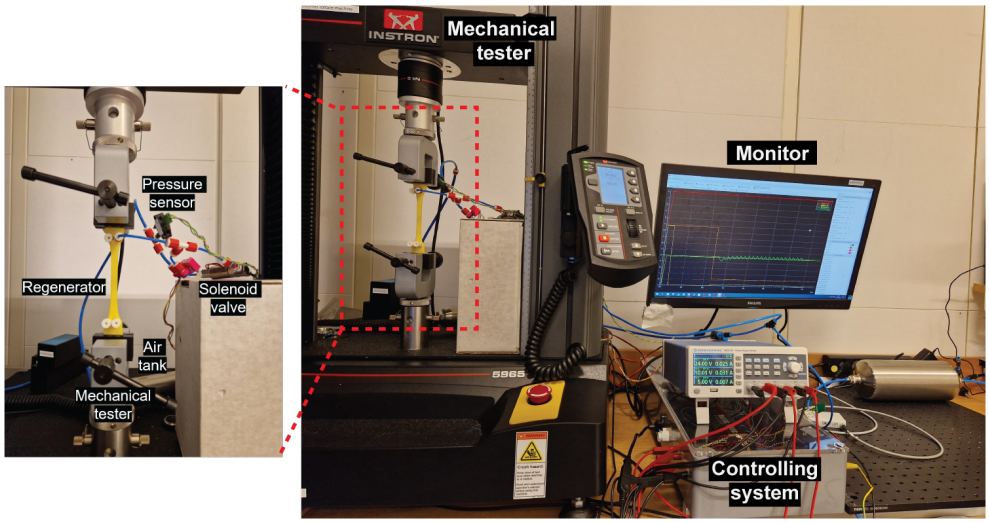

Figure 2.7. Photographs of the fluidic circuit for the volume change test of large-deformation regenerators.

2.2.5 Experimental setups

2.2.5.1 Fluidic circuit for volume-change measurements

The experimental measurements of fluid channel volume changes were performed on a pneumatic fluidic system. It enables to measure the time-dependent pressure difference between the regenerator inside and a reference air tank. This system consists primarily of two air tanks, two pressure sensors, and a pressure regulator, and is controlled by a customized software on the PC as shown in Figure 2.7.

The pressure of the regenerator and the reference pressure were monitored by two pressure sensors: MPX5100DP ($\pm$2.5%) and SSCDRRN005PDAA5 ($\pm$0.25%), respectively. The MPX5100DP pressure sensor was employed for the air tank 2 pressure measurement, in which one port was connected with the air tank and another one was connected to atmosphere. For the second differential pressure, the two ports were connected with the air tank and regenerator to measure the pressure difference. A pressure regulator (Festo, VEAB-L 8067677, 1 bar) with an accuracy of $\pm$0.4% set an initial pressure of 0.5 bar on the regenerator and the reference air tank.

This setup is referred to the context in **Chapter 4**.

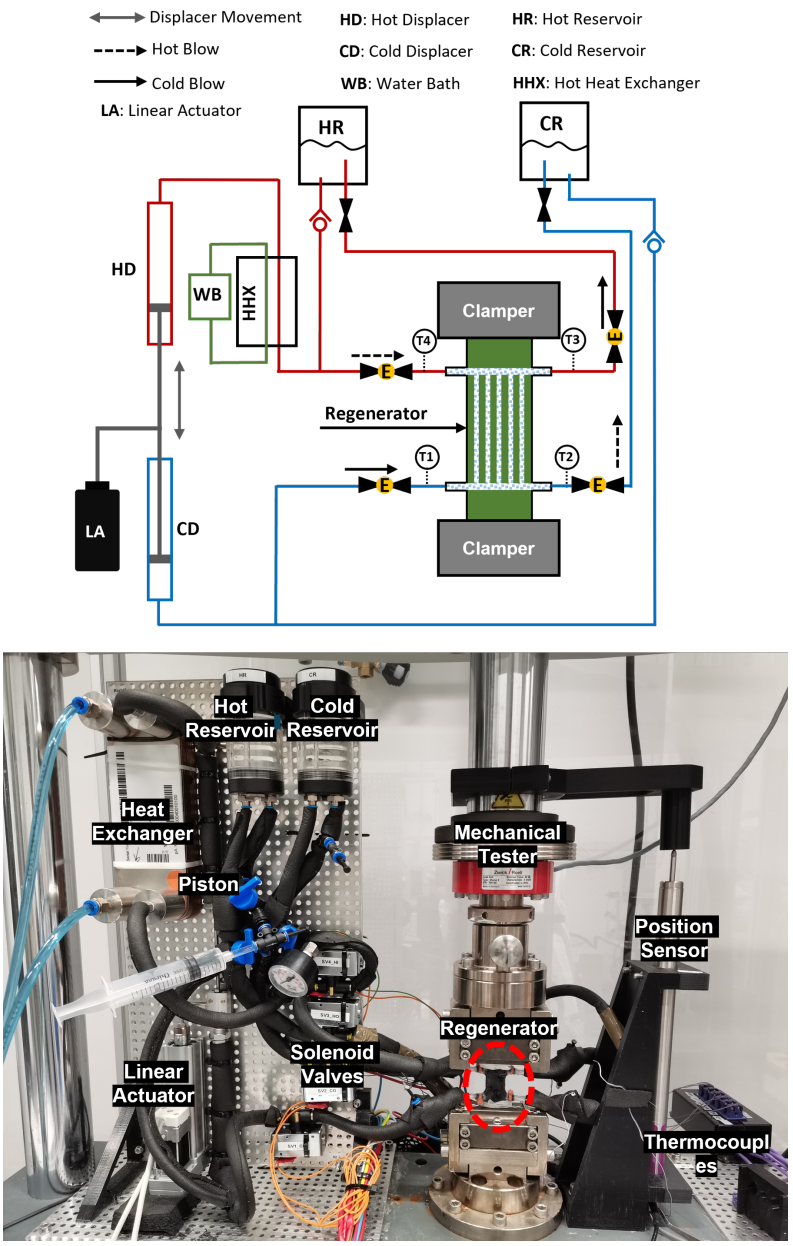

Figure 2.8. Regenerative elastocaloric flow system which is switchable to cooling and heating implementations.

2.2.5.2 Regenerative elastocaloric setup

In this dissertation, a customized active elastocaloric flow system is used in the experimental proof-of-concepts as shown in Figure 2.8. The regenerator was mounted on the Zwick mechanical tester, aside connected with a fluidic flow system. The flow system is consisted of a heat exchanger, two pistons with a linear actuator to control its movement, hot/cold reservoirs, and four solenoid valves. In addition, there is a linear position sensor which indicates the flow system work by the voltage change. The heat-transfer flow paths, including the compensation blow and hot/cold blows, are controlled by the solenoid valves, see a valve indication chart for specific working states in **Appendix C**.

The 3D-printed soft regenerators have four connecting ports, i.e., cold inlet, cold outlet, hot inlet, hot outlet, which are directly connected to the flow system using the 4mm polyurethane pipes. At the each port, the temperatures are recorded by the calibrated E-type thermocouples with a measuring error of ± 0.5 K. The data acquiring and operation parameters for the hardware are controlled by a program based on **LabView®**.

Part II

Investigation and Results

CHAPTER 3

Elastocaloric effect of 3D-printed elastomers

In this chapter, we start with some commercial thermoplastic filaments to study the eCE performance for 3D-printing eCE elastomers. Five filaments of thermoplastic elastomers were chosen to explore their elastocaloric cooling performance. These rubber-like elastomers all exhibit some degree of eCE associated with strain-induced crystallization (SIC), and some of them are shown to be promising for construction of a polymer full-scale active elastocaloric regenerator via additive manufacturing (AM). We screened the promising thermoplastic elastomers in filament form, and fabricated them into printed parts using fused filament fabrication (FFF). The main printing parameters for selected elastomeric materials and their influence on the elastocaloric cooling performance were investigated. As a printed part, NinjaFlex achieved a high material coefficient of performance (COP_{mat}) of 3.2 with 1.74 J/g input work at $\sim$0.1 Hz, driven by a stress of 5.7 MPa. Implementing AM elastocaloric elastomers opens opportunities for full-scale, low-activation-stress regenerative cooling components with optimized flow structures and enhanced heat-transfer performance.

This chapter is mainly based on article **I** in **Appendix A**.

3.1 3D printing elastomers and eCE characterization

3.1.1 Elastomer 3D printing

Commercial 3D-printing filaments were purchased, and the materials are summarized in Table 3.1. Most of them were made of thermoplastic polyurethane, except the Z-Flex filament, which was made of Thermoplastic Polyester (TPPE). The printed 3D parts (NinjaFlex, KungFu98A and Z-Flex) were printed by a Zmorph VX Printer, except the Ultimaker 95A part, which was printed by an Ultimaker S5 Pro Bundle printer. The Zmorph printer used a single extruder with a 0.3 mm nozzle and the Ultimaker S5 Pro used a 0.4 mm nozzle. These FFF based printers deposit a 3D part layer by layer, as shown in the illustration in Figure 3.1(a). The 3D-printed parts for

mechanical tests and elastocaloric measurements are fabricated in dogbone shapes with the same gauge length L_0 of 15 mm and a width of 15 mm. The dogbone 3D geometry is shown in Figure 3.1(a). The thicknesses of the printed dogbones are 1, 2, or 5 mm. Three bead orientations with respect to the x-axis (strain direction) are used to print the dogbones and marked as 0°, 45° and 90°, as shown in Figure 3.1(b). The samples were printed with varying temperatures both for the extruder and build plate and travelling speeds depending on the material. The basic printing parameters for each filament, including printing temperature, bed temperature, and printing speed, are listed in Table 3.1. The infill type used in FFF is line infill (or rectilinear) for all prints. Due to the hygroscopic nature of TPU polymers [155], the filaments will absorb atmospheric moisture and during the printing the wet filament will be melted with the vapor turning to steam which leads to voids in the part and reduces mechanical properties [156]. In order to avoid moisture, they were stored in a filament dryer at 80 °C during and between printing.

3.1.2 Mechanical tests and eCE characterization

Mechanical testing and the experimental characterization of the elastocaloric effect were performed on a Zwick/Roell EZ030 electro-mechanical tester. More detailed information regarding the mechanical tester can be obtained from the literature [157]. The printed parts and filament wires were tightly clamped by T-fatigue grips on the crosshead of the tester. Some rubber protective material was placed between the gripped area of the printed samples and the mechanical grips to protect the sample during the stretching process, which can be seen in Figure 3.1(c). The gauge length of 20 mm and strain rate of 5 s^{-1} are used for the filament elastocaloric measurements, where the large strain rate is implemented to achieve a quasi-adiabatic state which is comparable to the rate reported in the TPU test [93]. This fast-loading strain rate was also implemented for the quasi-adiabatic temperature change measurements in the eCE comparison of different bead orientations (the temperature change as a function of strains). The different samples were employed for different elastocaloric performance tests. Specifically, the thickness of dogbones used for the eCE comparison of different orientations was 5 mm. Dogbones applied for the stability evaluation were printed in 2 mm and the related cyclic mechanical tests were run at a strain rate of

Table 3.1. Information of experimental filaments and the corresponding 3D printing parameters

Filaments	Material	Diameter (mm)	Shore hardness	Nozzle temperature (°C)	Bed temperature (°C)	Print speed (mm/s)
1. NinjaFlex	TPU	2.85	85A	228	40	15
2. Ultimaker95A	TPU	2.85	95A	230	70	20
3. KungFu72D	TPU	1.75	72D	225	45	15
4. KungFu98A	TPU	1.75	98A	225	45	15
5. Z-Flex	TPPE	1.75	83A	220	50	15

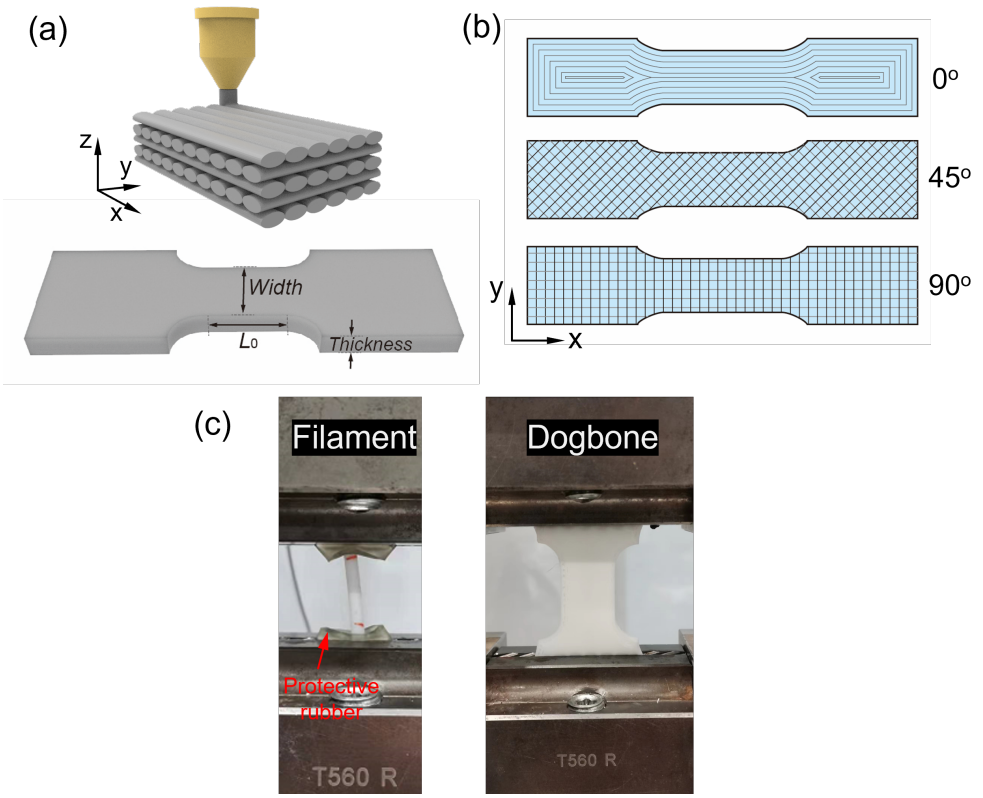

Figure 3.1. FFF printing of elastomeric filaments:
(a) Schematic of FFF 3D printing with cross-stacked layers and geometry of the dogbone part; (b) Three printing orientation for dogbone parts; (c) Physical images for the elastomeric filament and dogbone mechanical tests.

0.33 s^{-1} and operated in a strain range of 150-500%. Dogbones employed for cyclic tests of the material COP calculation were printed with a thickness of 1 mm and the strain rate was 0.67 s^{-1}. The elastocaloric temperature change was measured by the infrared (IR) thermography. In addition, due to the buckling of filaments and printed dogbones during cyclic tests and due to the large applied strains, the middle point of the sample moved during loading. Different middle zones at different states in an elastocaloric cycle were chosen from the sample to obtain the average infrared temperatures, finally combining temperature variation curves of each state into the temperature variation profile of a full cycle. For the cycling tests, a fixed selective zone for infrared temperatures was used to evaluate the adiabatic temperature change, see comments on the cyclic tests in **Scenario 1**.

Scenario 1 Notes on cyclic tests

As observed in filaments as well as the printed dogbone, the elastocaloric effect in elastomers is usually accompanied by a large deformation which leads to buckling during the releasing process. To avoid the buckling in the rubber-like elastomers, some technical tricks can be imposed such as performing pre-elongation of the sample and controlling by going back to zero force instead of zero strain [92, 93]. The cyclic tests performed in the mechanical stability test are controlled by releasing until a strain in the range of when the stress in the material reaches zero in the NinjaFlex filament cyclic test (see, Figure 3.2, which is about $50\% - 150\%$). The pre-strain (strain returns to 150%) approach also applies to the cycled printed samples which are implemented for the SEM analysis, cyclic elastocaloric characterization, and the COP calculations.

3.1.3 SEM and DSC measurements for specific heat capacity

The uncycled printed and cycled specimens, cut at the middle of the active region using a snap-off utility knife (BAHCO KB09-01), were employed for SEM characterization of microstructures. The specimens (about 0.5 mg), cut from the virgin filaments, uncycled printed dogbones and 100 times cycled dogbones, were employed for the specific heat capacity characterization. The tests were performed with heating and cooling rates of 1 K/min in a vacuum of 5×10^{-6} mbar.

The specific heat capacity (c_p) for the materials, including the virgin filaments, uncycled printed samples and cycled printed samples, were investigated and used for materials COP calculations. Due to the weak elastocaloric performance for Kungfu98A, it was not printed for the following studies so its c_p measurement was only mea-

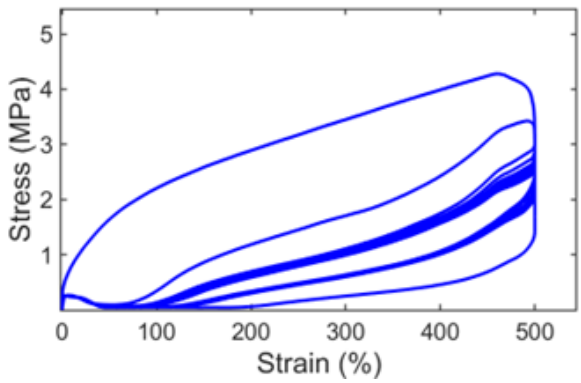

Figure 3.2. Stress-strain curves of the NinjaFlex filament undergoing ten cyclic tests.

Table 3.2. The specific heat capacity values for studied materials in different forms are measured by DSC

Materials	c_p of filament (J/gK)	c_p of uncycled printed specimen (J/gK)	c_p of cycled specimen (J/gK)
1. NinjaFlex	1.707	1.619	1.659
2. Ultimaker95A	1.625	1.560	1.657
3. KungFu72D	1.455	–	–
4. KungFu98A	1.595	1.587	1.618
5. Z-Flex	1.670	1.706	1.686

–: did not measure due to for the sample not being printed.

sured in the filament form. The specific heat capacity of materials, at temperatures within the temperature range of 275-315 K, fully covered the temperature range of operation, is measured. The cycled printed samples are cycled 100 times before the DSC measurements. Eliminating the uncertain values near the test temperature edges, the results of c_p, listed in the Table 3.2, are obtained by averaging c_p within a temperature range of $290 - 310$ K. Here, the values are nearly constant with the temperature increase, and no latent heat is observed in the temperature range. It is noted that the heat capacity of the uncycled printed material has a slight decrease compared to the original filament. Maybe, the reason is that the melting and solidification during the fused filament fabrication process changes its thermal properties, due to the hard segment contents variation [158, 159]. After cyclic tests, the heat capacity of the materials increases, which also happens in natural rubbers, when subjected to a larger uniaxial deformation [160]. The c_p values from the cycled material are closer to the real situation, in which materials are employed for the elastocaloric cooling. Thus these are used for the materials COP calculations.

3.2 Elastocaloric properties in elastomeric filaments

Elastomeric filaments of each material were first characterized for their eCE properties and eCE cooling potential. In Figure 3.3(a), a piece of NinjaFlex filament is mounted in the mechanical tester with two protective rubber gaskets surrounding both gripped ends. The temperature change and filament geometric evolution are recorded by the IR camera. Infrared thermographs present the surface temperature increase and decrease during the stretching and releasing processes (states: *ii* and *iv*, respectively), as well as the temperature equilibrium with ambient temperature T_{amb} = 296 K prior to loading and unloading (states: *i* and *iii*, respectively). In addition to the observed temperature changes, buckling occurs in state *iv* due to the plastic deformation produced by the large deformation. The time-dependent temperature evolution diagram, with the four states, is shown in Figure 3.3(b), which is obtained from the average surface temperature in a selected zone from filament IR images. Notice one interesting phenomenon that the temperature increase during the load-

ing process is higher than the decrease during the unloading process. This may be caused by some intrinsic hysteresis in the loading-unloading process (observed in the cyclic stress-strain curves in Figure 3.3). The asymmetry for temperature increases and decreases has also been observed in other rubbers and rubber-like elastomers due to the large variation of the thermal time constant and the crystallization kinetics [92, 161, 162]. Indeed, the elastic entropy and the SIC both contribute to the elastocaloric effect for natural rubbers. When the applied strain reaches 500-600% for natural rubbers, the crystallization can occur in a few tens of milliseconds upon stretching and the rubber heats up rapidly both from elastic entropy variation and the SIC process [19, 163]. Upon releasing, a fraction of the crystallization will be relaxed due to the holding time in contact with the ambient temperature, and there is a lower contribution for the eCE from the SIC process.

An elastocaloric cooling cycle is illustrated with a temperature-entropy ($T - S$) diagram in Figure 3.3(c) to elucidate the elastomer eCE cooling operating principle, which represents a reversed Brayton thermodynamic cycle. Active elastomers are subject to the four processes in the thermodynamic cycle: adiabatic stretching ($i \rightarrow ii$), fluid flow from cold to hot where heat is rejected from the hot reservoir ($ii \rightarrow iii$), adiabatic releasing ($iii \rightarrow iv$), fluid flow from hot to cold where a cooling load is absorbed in the cold reservoir ($iv \rightarrow i$). While the elastomer undergoes the adiabatic uniaxial stretching, the applied stress leads to a partial phase transition for the elastomer molecular chains from the crimped state to the extended state. Some molecular chains crystallize into ordered phases accompanying with the latent heat and entropy increase [164]. The crystallization of elastomer molecular chains is in-

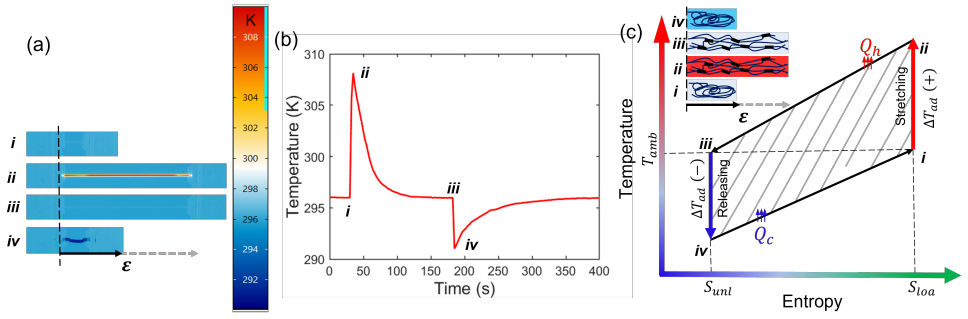

Figure 3.3. Surface temperature variation for the NinjaFlex filament in an eCE cooling cycle: *(a) IR images in each state of the first cycle; (b) Temperature change of the elastocaloric material during an eCE cycle; (c) Schematic temperature-entropy diagram for an eCE cooling cycle, where (+) and (-) represent temperature increase and decrease, respectively; Q_h and Q_c represent the heating and cooling energy, respectively; The inset diagram represents the molecular chain state variation between the disordering and strain-induced crystallization (black blocks) during adiabatic stretching and releasing and the corresponding heating (red) and cooling (blue) of the sample.*

duced by rapidly stretching, i.e., so-called strain-induced crystallization (SIC), which contributes to the elastocaloric effect in elastomers [96, 147]. The consequence is that the surface temperature increases for most of rubbers and soft elastomers. Undergoing an adiabatic releasing process, the recovery to the disordered coil-like state of molecular chains leads to the absorption of heat, and thus a temperature decrease.

Elastocaloric measurements for the five elastomeric filaments were performed under different strains. Figure 3.4(a) shows the stress-strain behavior of the NinjaFlex filament. The measurement was performed using one filament with a sequential strain increase from 0 to 500%. The temperature changes were measured during each loading and unloading process. The system was allowed to equilibrate with ambient after each change in strain, as illustrated in the elastocaloric cycle in Figure 3.3(b). Results of different filaments, for adiabatic temperature increases and decreases, are shown in Figure 3.4(b-c). Regarding the exothermic process, the positive ΔT_{ad} gradually increases as the strain increases to 300%. Subsequently, a ΔT_{ad} plateau was observed for some samples (Ultimaker95A, KungFu98A, Z-Flex) where the adiabatic change increases very little from a strain of 300% to 500%. This indicates that strains above 300% for these materials are less responses for elastocaloric cooling. The adiabatic temperature change of the NinjaFlex filament continues to increase at strains above 300%, and the largest ΔT_{ad} value reaches 12 K at the strain of 500%. The endothermic process, accompanying a negative ΔT_{ad} upon strain releasing, plays a significant role in evaluating the capacity for elastocaloric cooling devices. Since the KungFu72D filament failed mechanically due to its elongation between 300% to 400%, data at 400% is not available and the result for 300% may include significant plastic deformation of the sample. Furthermore, only a negligible elastocaloric effect was observed during the unloading process, which indicates that it is not an attractive material for elastocaloric cooling. During the endothermic process, the remaining four candidates exhibit large elastocaloric effects. The negative ΔT_{ad} of the NinjaFlex filament increases with the strain, and a maximum ΔT_{ad} value as large as 5.55 K at 500% is achieved. The $-\Delta T_{ad}$ values for Ultimaker95A and KungFu98A filaments are similar below 500%, where the adiabatic temperature changes of both are $\sim$2 K. However, within the strains from 400% to 500% in Figure 3.4(c), there is a difference in trend for the Ultimaker95A and KungFu98A filaments. This phenomenon is similar to the behavior for the KungFu72D filament during stretching.

In addition, during stretching, a slight decrease in ΔT_{ad} for KungFu98A is observed in Figure 3.4(b). When the strain increases from 400% to 500%, the stress improvement (8.25%) from 2.91 MPa to 3.15 MPa is less than that (11.31%) of the Ultimaker filament from 6.01 MPa to 6.69 MPa, which results in a $-\Delta T_{ad}$ drop for KungFu98A in Figure 3.4(c). Although the temperature change of the Z-Flex filament was highest among these materials during the adiabatic stretching process, its $-\Delta T_{ad}$ was not as large as the value during the stretching process. A $-\Delta T_{ad}$ value of 1.58 K for the Z-Flex filament was obtained at 500% strain, yet a temperature change of 1.44 K was measured at 300%. Hence, the $-\Delta T_{ad}$ increases slightly as the strain

increases to 500%.

3.3 Softening behavior and reversible elastocaloric effect

When eCE elastomeric filaments undergo several loading-unloading cycles, the stress-strain curve shows significant compliance after the first cycle, and then tends towards a stabilized cycle shown in Figure 3.2. This softening behavior is commonly observed in rubbery materials, the so-called Mullins effect, which contributes to the elastocaloric effect decrease in natural rubbers and elastocaloric elastomers [94, 131]. The eCE performance evolution associated with the softening behavior of elastomeric filaments is investigated by comparing the ΔT_{ad} ratio between the initial cycle and after a small number of cycles ($\sim$10). This relative variation of the adiabatic temperature is shown in Figures 3.5(a) and (b) for strains of 500% and 10 cycles. The tests for each sample were conducted in three procedures: one adiabatic stretching-releasing cycle, with a pause to equilibrate with room temperature in between (initial cycle); cyclical stretching and releasing eight times (cyclic process); and one adiabatic stretching-releasing cycle with pauses for temperature equilibration (10th cycle). After the cyclic process, the values of ΔT_{ad} exhibit a significant decrease between the 1st and 10th cycles for the samples due to the irreversible plastic deformation produced during cycling [92]. However, the degradation of ΔT_{ad} is smaller, and for some samples (Ultimaker, KungFu98A, and Z-Flex) the ΔT_{ad} even increases after the cyclic process. Since the lower value of elongation at the breaking point for the KungFu72D sample, the mechanical fatigue presents after the first stretching. The highest ΔT_{ad} is produced in KungFu72D during the stretching but there is no temperature change observed during the releasing process. The lowest temperature relative variation is observed in the NinjaFlex sample both during the loading and unloading process, manifesting its reversible elastocaloric effect among these elastomeric filaments. Especially, seldom degradation in temperature change appears for NinjaFlex filament during the unloading process.

3.4 Printing orientation and its impacts on elastocaloric properties

To exploit full-scale elastocaloric regenerators printed by these potential elastomeric materials, the manufacturing parameters should be carefully examined to ensure decent elastocaloric and mechanical properties after the printing. Printing parameters such as temperatures and printing patterns can be easily controlled and are directly connected to the mechanical integrity and lifetime of the elastocaloric regenerator.

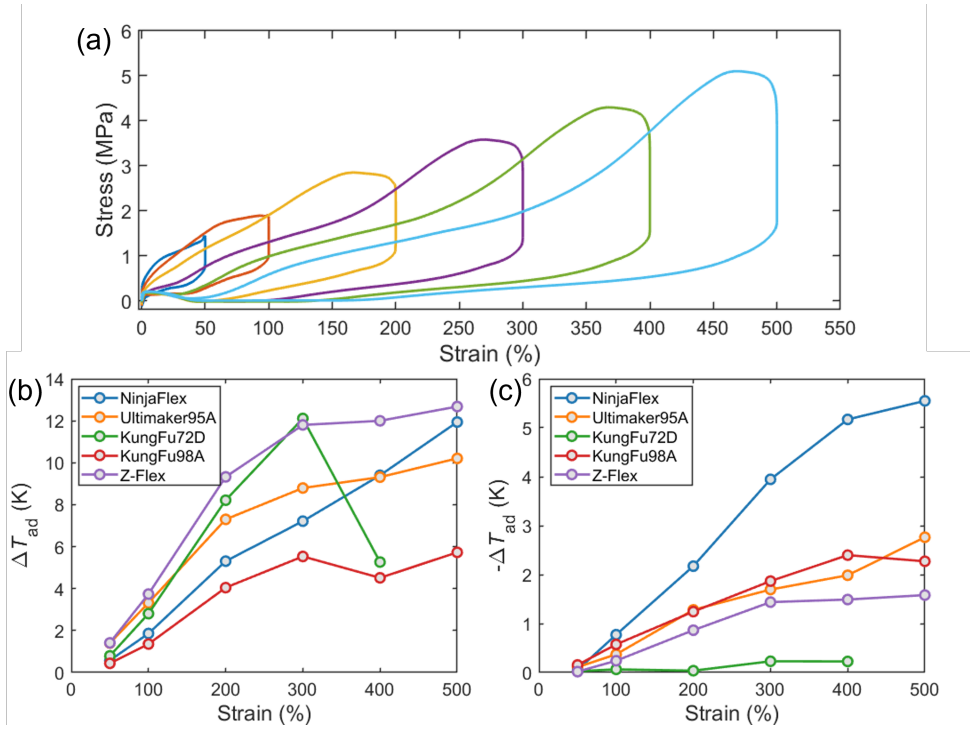

Figure 3.4. Elastocaloric effect comparison for different elastomeric filaments: *(a) Stress-strain profiles for the NinjaFlex filament; (b) Temperature change as a function of strain for different filaments during the filament stretching; (c) Temperature change as a function of strain for different filaments during the filament releasing.*

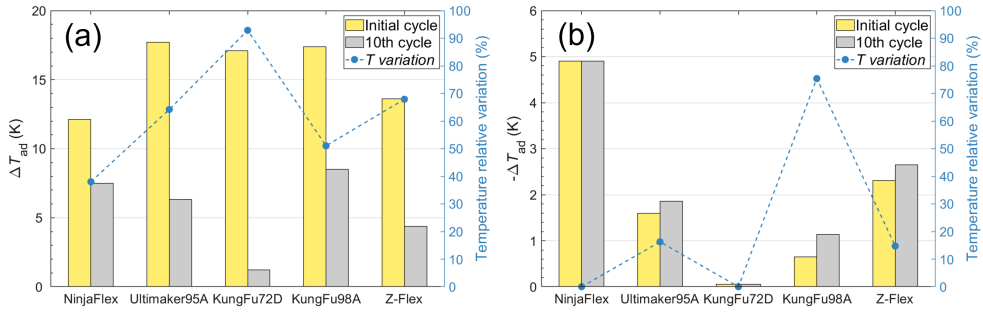

Figure 3.5. Adiabatic temperature change comparison for different samples undergoing the initial cycle and 10th cycle during the stretching (a) and releasing (b) processes, and the corresponding temperature variation ratio.

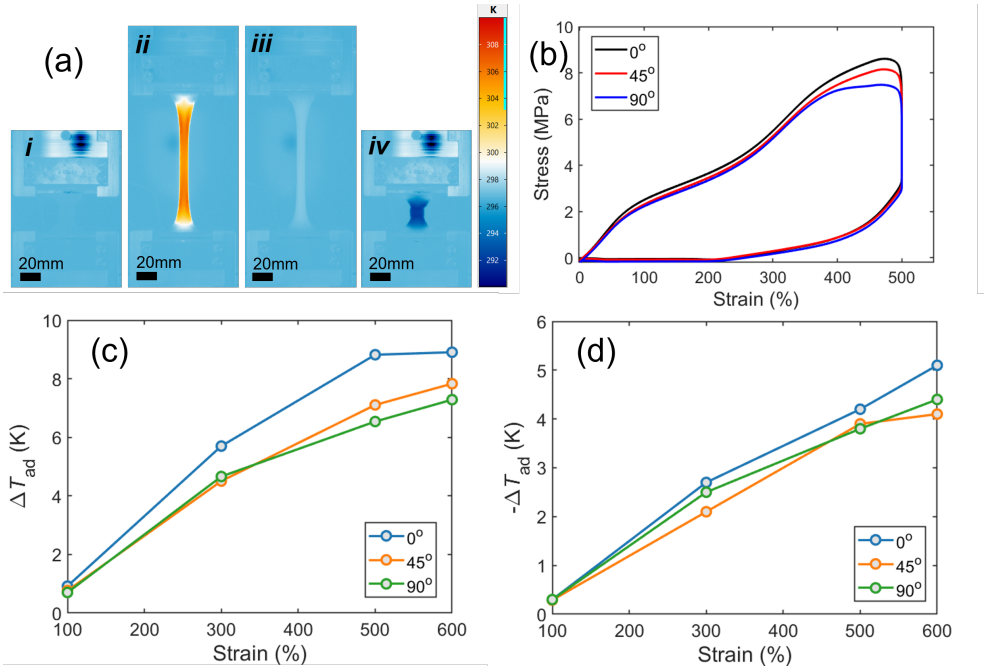

Figure 3.6. Elastocaloric properties of different oriented parts:
(a) IR images of printed NinjaFlex dogbone part at different states in an elastocaloric cycle; (b) Stress-strain profiles of printed NinjaFlex dogbones with different orientations; (c) Temperature change as a function of strain for different printing orientations during stretching; (d) Temperature change as a function of strain for different printing orientations during releasing.

For FFF, the 3D part is deposited layer by layer. Extruded beads within each layer could be aligned in different directions. The orientation of extruded beads and layers is essential to the mechanical properties of printed parts. Another parameter, solidity ratio (SR), given by the distance between beads, and thus representing the printed density, is also crucial for printing mechanical properties [165]. The highest infilled-pattern quality (95%) is applied for each printing to obtain samples with as high a density as possible. Therefore, the effect of the spacing between beads is not considered here. Printed parts employed for eCE cooling are subjected to uniaxial stretching, which means that stacked layers inside of the sample should be able to endure the large cyclical uniaxial stress. Three printing profiles for the dogbone-shape parts with different orientations were chosen, as illustrated in Figure 3.1(b). In the 0° orientation the layers are stacked with the same printing pattern as the diagram shown. The dogbones with 45° and 90° orientations are printed with a cross-hatched structure in the stacked layers.

Elastocaloric effect measurements for each orientation were conducted with samples printed from the NinjaFlex filament as this was found to have the most promis-

ing properties. The surface temperature variation of the 0° dogbone undergoing the four states of an elastocaloric cycle measured by IR thermography is shown in Figure 3.6(a). The temperature distribution is uniform in the middle rectangular area of the dogbone, but some higher temperatures are observed at the two ends of the active area owing to the uneven stress distribution. The measured adiabatic temperature changes during loading and unloading as a function of strain are obtained from the average temperature in the middle of the active area of each dogbone. Mechanical tests return to zero strain (the original length) at the end of every cycle. Buckling occurs due to the large deformation that occurs in stage iv of the dogbone test. The stress-strain behavior for the different printing orientations is compared in Figure 3.6(b). The tensile modulus of differently oriented dogbones is 7.9±0.6 MPa for 0°, 7.4±0.8 MPa for 45°, and 6.8±0.7 MPa for 90°. These are evaluated in an elastic strain range of 0-10%. The value of stress and tensile modulus decrease with an increase in orientation angle, during the loading process. This is in agreement with the results observed in various studies for FFF parts, where beads oriented parallel to the load direction (0° orientation) are always stronger than beads oriented perpendicular to the load direction [165, 166].

For the 0° orientation dogbone the larger tensile modulus indicates a higher stiffness and tighter bead attachment, and thus a denser part as well as good mechanical properties are expected. Adiabatic temperature changes during loading and unloading are shown in Figures 3.6(c) and Elastocaloric effect measurements for each orientation were conducted with samples printed from the NinjaFlex filament as this was found to have the most promising properties. The surface temperature variation of the 0° dogbone undergoing the four states of an elastocaloric cycle measured by IR thermography is shown in Figure 3.6(a). The temperature distribution is uniform in the middle rectangular area of the dogbone, but some higher temperatures are observed at the two ends of the active area owing to the uneven stress distribution. The measured adiabatic temperature changes during loading and unloading as a function of strain are obtained from the average temperature in the middle of the active area of each dogbone. Mechanical tests return to zero strain (the original length) at the end of every cycle. Buckling occurs due to the large deformation that occurs in stage iv of the dogbone test. The stress-strain behavior for the different printing orientations is compared in Figure 3.6(b). The tensile modulus of differently oriented dogbones is 7.9±0.6 MPa for 0°, 7.4±0.8 MPa for 45°, and 6.8±0.7 MPa for 90°. These are evaluated in an elastic strain range of 0-10%. The value of stress and tensile modulus decrease with an increase in orientation angle, during the loading process. This is in agreement with the results observed in various studies for FFF parts, where beads oriented parallel to the load direction (0° orientation) are always stronger than beads oriented perpendicular to the load direction [165, 166]. For the 0° orientation dogbone the larger tensile modulus indicates a higher stiffness and tighter bead attachment, and thus a denser part as well as good mechanical properties are expected.

Adiabatic temperature changes during loading and unloading are shown in Figures 3.6(c) and 5(d), respectively. The results of ΔT_{ad} for different dogbone orienta-

tions confirm that the 0° orientation dogbone maintains a significant elastocaloric effect in 3D printed parts. From the perspective 3D printing elastocaloric regenerators, the orientation of beads and stacked layers should be aligned parallel to the loading direction to realize the largest lifetime and eCE.(d), respectively. The results of ΔT_{ad} for different dogbone orientations confirm that the 0° orientation dogbone maintains a significant elastocaloric effect in 3D printed parts. From the perspective 3D printing elastocaloric regenerators, the orientation of beads and stacked layers should be aligned parallel to the loading direction to realize the largest lifetime and eCE.

Scenario 2 Solidify ratio evaluation for printed samples

For the fused filament fabrication (FFF) printed part, the sample density is associated with the solidity ratio (SR) which can be calculated theoretically via the area of the ellipsoid bead divided by the potential maximum area between the beads (the rectangle area with the nozzle diameter and layer height) [165], written as the following equation:

$$SR = \frac{S_{\text{ellipsoid}}}{S_{\text{Rectangle}}} = \frac{ab\pi}{hD} \tag{3.1}$$

where the a, b, h and D are the semi-major, semi-minor axes of the ellipsoid bead and the layer height and the nozzle diameter. The SR is a normalized density for the printed part. The layer height is 0.0943 mm, obtained from the printed part height divided by the layer number generated in the printing G-code, and D is 0.3 mm for the printing. The parameters a and b are obtained from the measurement on the SEM images.

3.5 Microstructures of printed parts

The microstructures of the printed parts with different bead orientations were studied in uncycled and cycled 3D-printed parts. Figures 3.7(a) and (b) show profile and cross-section views of the 0° dogbone. Good attachment between the ellipsoid beads stacked along the z-direction is achieved by the FFF printing. Interbead voids between the extruded beads are produced during the deposition process. The printed 0° dogbone was subjected to 100 cyclic tests to study the microstructural evolution after plastic deformation. From the cross-section view in Figure 3.7(c), it can be observed that the plastic deformation leads to a reduced mean width of the ellipsoid beads from 248±13 μm to 189±8 μm measured from the SEM images. Figures 3.7(d-e) show the cross-section view from the 90° dogbone before stretching and after periodic stretching and releasing. The net-like connection between the extruded beads in the 90° dogbone differs from the bonding connection in the 0° dogbone, which is a parallel-stacked architecture. The size of the interbead void in the 90° uncycled dogbone is larger than that of the 0° one and the bead width decreases to 221±14

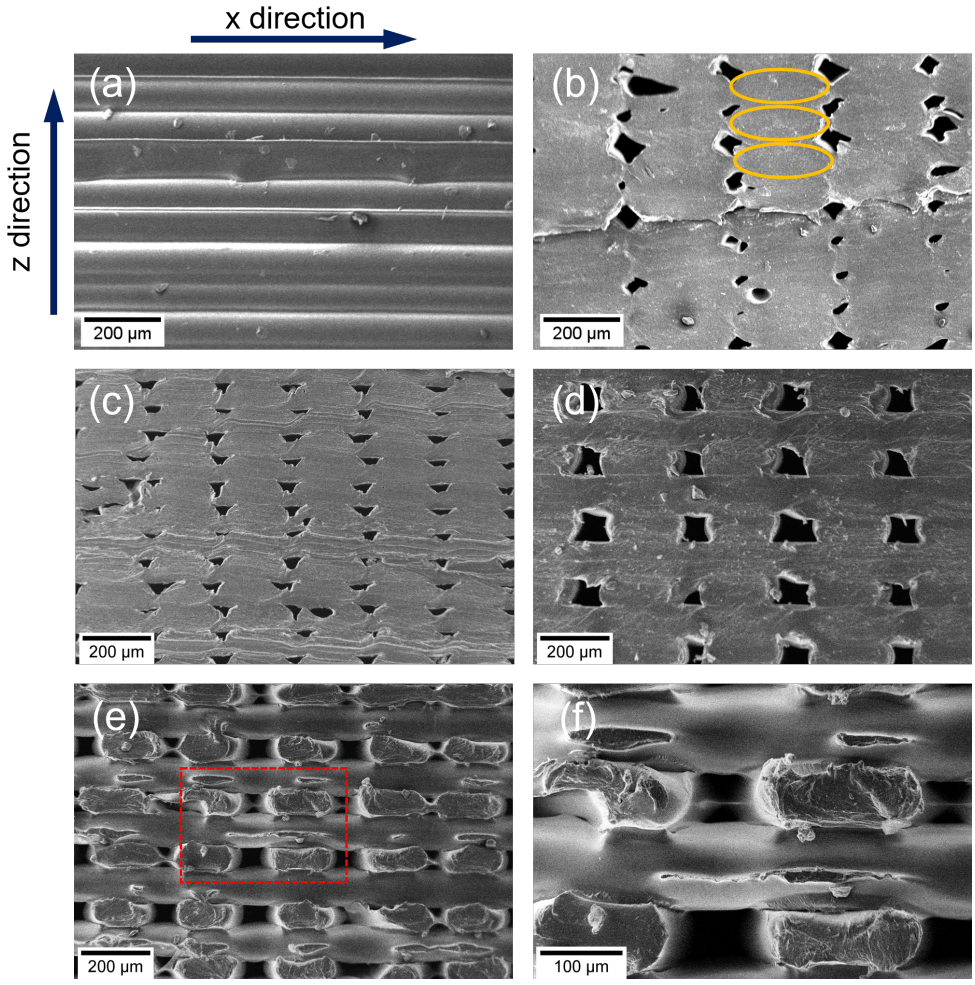

Figure 3.7. Microstructures of printed parts:
(a) and (b) are SEM images of the profile and cross-section views for a printed dogbone with the 0° *printing orientation, respectively; (c) is a cross-section view after cycling. (d) and (e) are SEM images of profile and cross-section views for a* 90° *printed dogbone before and after training, respectively; (f) magnified SEM image from the red rectangular zone in (e).*

μm. After deformation, the ellipsoid bead width further diminishes to 177$\pm$10 μm. From Figure 3.7(e), it can be observed that the beads parallel to the stretching direction are plastically deformed and constrained by the beads perpendicular to the stretching direction. Because the transverse beads are not subjected to the stretching, they experience no plastic deformation, which causes dimensional mismatches with the longitudinal beads that are deformed. This mismatch causes cracks on the transverse bead due to the alternating mechanical interaction between the longitudinal and transverse beads.

One of the representative areas is magnified and shown in Figure 3.7(f) to accentuate the crack. It can be deduced that the mechanical interaction will also produce cracks on the longitudinal bead, thereby reducing the mechanical properties of the part. To evaluate the density of a printed FFF part quantitatively, the SR can be calculated by the area of the bead divided by the potential maximum area between the beads, indicated by a box around each bead [165]. The maximum area is determined by the layer height and the width of the bead, which is typically the nozzle diameter. A SR value of 0.79 is obtained for the printing at different orientations (see **Scenario 2**). The actual normalized density is evaluated by calculating the area ratio between the solid and pore regimes from cross-section SEM images. The values for the uncycled and cycled parts in 0° orientation are 0.97 and 0.95, respectively. For the 90° orientation one, the results are 0.93 and 0.89, respectively. All these values are higher than the theoretical value because the real bead shape is not a perfect ellipsoid and it changes during the melting and depositing process. The quantitative result for the printing density also indicates that the 0° dogbone is denser than the 90° dogbone, both before and after undergoing the cyclic loading and unloading. This is further substantiated by the higher tensile modulus obtained in the 0° dogbone. The voids caused by the 90° printing will be enlarged in the longitudinal and transverse direction during the stretching. When this part is employed in an active elastocaloric regenerator, these voids inside the regenerator can absorb the liquid heat-transfer fluid during the loading and unloading processes, resulting in parasitic heat losses. However, the voids in the 0° dogbone are disconnected, smaller, and maintain their shape under cycling. Additionally, the connection between the extruded beads in the 0° dogbone remains tight after cyclic tests. Therefore, the 0° orientation seems best for fabricating a full-scale elastocaloric regenerator, due to advantages both in elastocaloric properties and density stability.

3.6 Mechanical and elastocaloric stability

The stability of the mechanical properties and eCE of elastocaloric materials is an essential characteristic for evaluating the potential for caloric cooling applications, as it determines the lifetime of the device employing the given eCE materials. Figure 3.8(a) shows 100 loading-unloading cycles for the parts printed with different orientations. Similar to the foregoing discussed on the printing orientation impacts

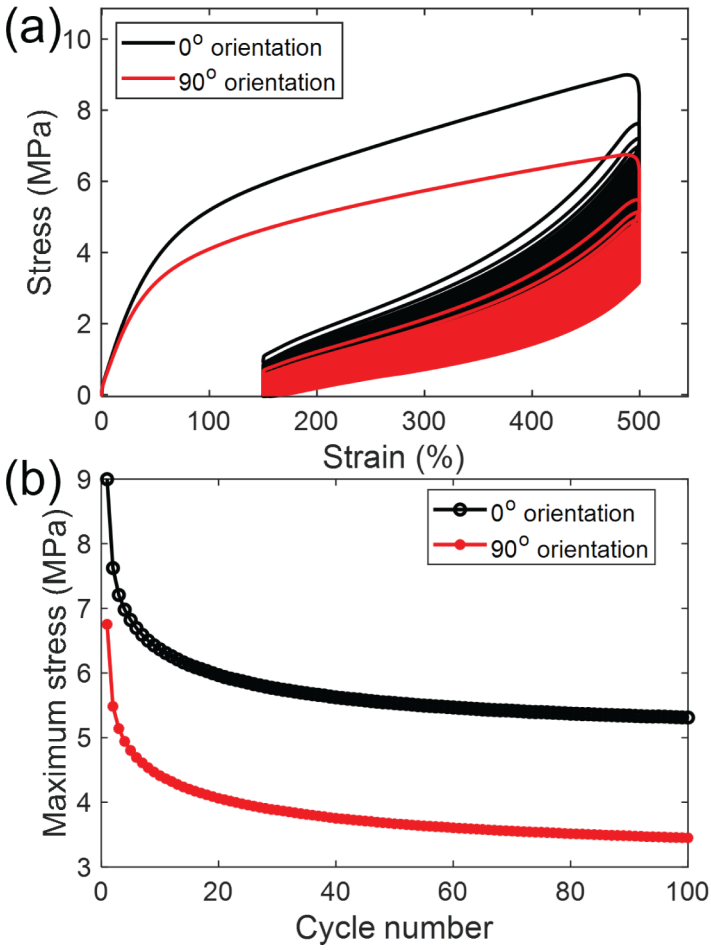

Figure 3.8. **(a) Stress-strain profiles of printed NinjaFlex dogbones for 100 loading-unloading cycles; (b) Evolution of the maximum stress achieved in each cycle as a function of the cycle number**

on the eCE, the tensile modulus and the maximum stress also decreased with the printing orientation, increasing to 90° during the cyclic tests. As shown in Figure 3.8(b), when increasing the cycle number, the stabilized stress can reach to 5.31 MPa for the 0° dogbone, and 3.45 MPa for the 90° dogbone. This can be explained by the higher alignment along the tensile direction for the 0° dogbone, as observed in the microstructural distribution for the extruded beads. The printed layers of the 0° dogbone maintain a good mechanical stability and therefore favor a higher uniaxial stress.

A 0° dogbone with a thickness of 2 mm is subjected to over 1000 cycles to examine the stability of the eCE and its mechanical properties. To avoid any buckling caused by the plastic deformation, the strain is set back to 150% instead of 0% during the releasing process. A slow strain rate of 0.33 s^{-1} is applied throughout the test. The stress-strain profiles of some cycles are selected and shown in Figure 3.9(a). It was observed that the maximum loading stress decreases as the cycle number increases. The temperature evolution profile of the first 85 cycles is recorded by the IR camera as shown in Figure 3.9(b). After the first several cycles, the temperature variation tends to stabilize, and the detailed temperature variation for cycles 50-56 is given in Figure 3.9(c). The average cyclic temperature for the 0° dogbone reaches 3.92 K. Later, the temperature profiles for cycles 955-1015 were captured, as show in Figure 3.9(d). The average cyclic temperature change from cycles 1000-1006 is 3.09 K, which indicates a good functional stability for the eCE of the 3D-printed NinjaFlex.

3.7 Elastocaloric cooling performance of the printed elastomers

The material coefficient of performance (COP_{mat}) is defined for evaluating and comparing potential caloric materials to be employed in caloric cooling [167], calculated by the cooling energy per unit mass divided by the input work per unit mass as shown in Eq. 3.2. In a Brayton-based cycle, the cooling energy can be expressed as an integral of the specific heat capacity c_p from T_1 to T_{amb}, where the T_1 is the cold temperature obtained during the loading process and the T_{amb} is the ambient temperature. The input work is obtained from the area of the stress-strain curve.

The measurements of c_p for the elastomeric materials show a weak temperature dependence and can be considered to be constant. The average c_p values near room temperature are listed in Table 3.2. Thus, the COP_{mat} calculation is simplified to the measured values of ΔT_{ad}, c_p divided by the input work per unit mass:

$$COP_{mat} = \frac{Q/m}{\Delta W/m} = \frac{\int_{T1}^{T_{amb}} c_p dT}{\frac{1}{\rho l_0} \oint \sigma d\varepsilon} \tag{3.2}$$

Figure 3.10(a) shows the cyclic temperature variation in a stable loading-unloading state. The adiabatic temperature change for the cyclic mode is defined as the dis-

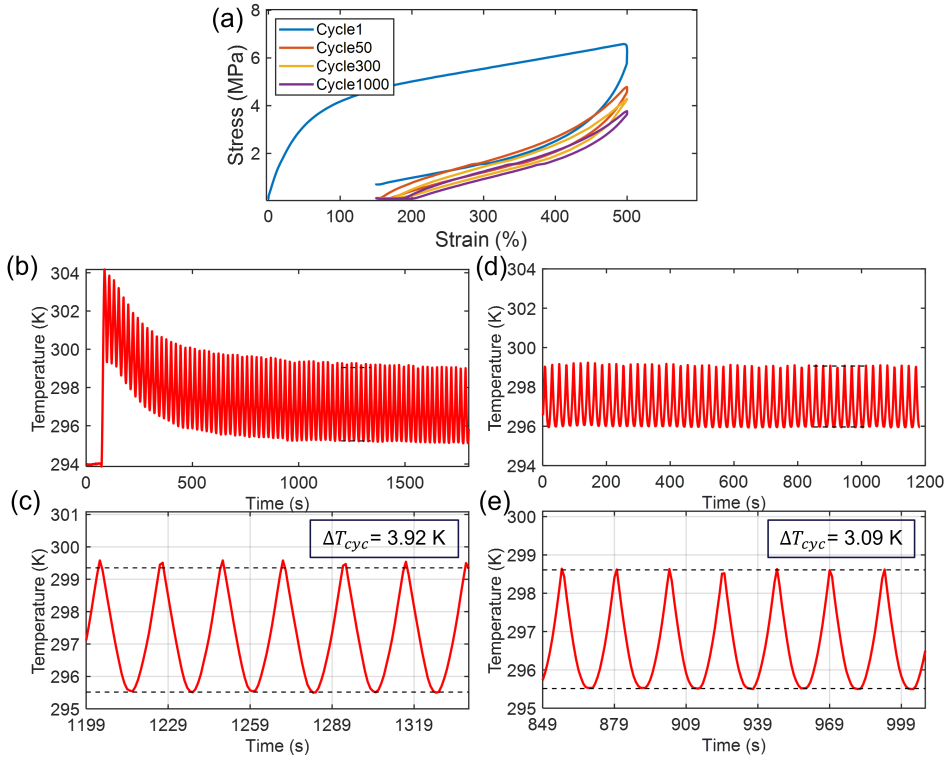

Figure 3.9. Functional stability for the 2 mm printed parts over 1000 loading/unloading cycles:
(a) Stress-strain behavior for the selected cycles; (b) Cyclic temperature changes for the first 85 cycles at a strain rate of 0.33 s^{-1}; (c) Stabilized temperature change evolution in cycle numbers 50 to 56 selected from (b); (d) Cyclic temperature changes for cycles 955-1015 at a strain rate of 0.33 s^{-1}; (e) Stabilized temperature change evolution in cycle numbers 1000 to 1006 selected from (d).

tance between the top and bottom peaks during loading and unloading. When the loading-unloading process reaches equilibrium, the adiabatic temperature change will be stable and remains constant for the following cycles, reflecting its prominent and stabilized cycling performance. The ΔT_{cyc} for different materials during cycles 60-100 are shown in Figure 3.10(b). The 0° NinjaFlex dogbone produces the largest average ΔT_{cyc} value of 3.24 K during these 40 cycles. However, we noticed that the ΔT_{cyc} for the 1 mm dogbone is less than the ΔT_{cyc} of 3.92 K obtained for the 2 mm NinjaFlex dogbone in Section 3.5. That is because the cyclic test in the stability evaluation is operated at a much lower strain rate, which would favor a higher temperature change as the results shown in Figure 3.10(b). The temperature change for the Z-Flex sample is also able to reach a considerable value of 2.84 K. COP_{mat} and the input work (ΔW) as a function of the cycle number for the NinjaFlex Ultimaker95A,

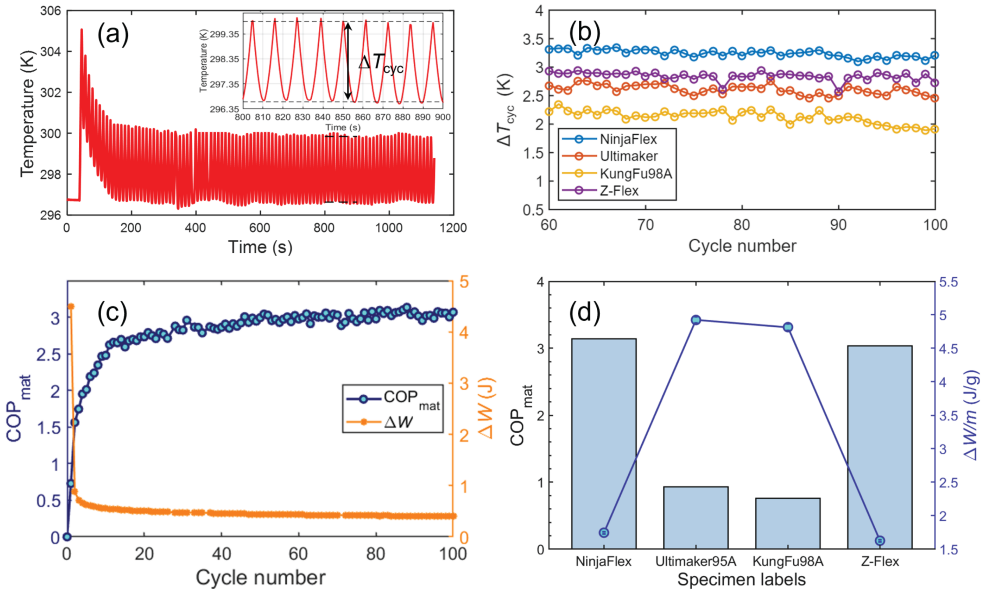

Figure 3.10. Cyclic temperature characteristics and material COP_{mat} for different elastomers:
(a) Time-dependent surface temperature for cyclic tests and the detailed temperature oscillation of a NinjaFlex 0o dogbone stretched at 500% strain and 0.67 s^{-1} strain rate; (b) Stabilized temperature change evolution in cycle numbers 60 to100 for different materials; (c) COP_{mat} and input work evolution as a function of the number of cycles for NinjaFlex dogbone; (d) Average COP_{mat} and input work per unit mass during cycles 80-100 for different materials as printed parts in 0o orientation.

KungFu98A, Z-Flex materials rapidly increase during the first ten cycles and tend to stabilize in the following cycles, see Figure 3.10(c) for NinjaFlex. The temperature changes and the input work per unit mass in each cycle for different materials are also obtained from temperature profiles listed in Table 3.3, which exhibit a rapid decrease over the first several cycles, ending in a stable state. The average COP_{mat} and input work per unit mass during the stabilized cycles ($80^{th} - 100^{th}$) for different materials are compared in Figure 3.10(d). The highest COP_{mat} of 3.14 with 1.74 J/g input work is observed in the NinjaFlex part at an operating frequency of $\sim$0.1 Hz. From the stress-strain behavior of the Z-Flex printed part, it can be noticed that the input work is significantly reduced as the number of cycles is increased (among proposed materials the lowest input work of 1.63 J/g is required). Therefore, a considerable COP_{mat} of 3.04 with an input work of 1.63 J/g for Z-Flex is obtained when cycling 100 times despite its small temperature change.

The comparison of the COP_{mat} for some common elastocaloric SMAs and polymers is summarized in the Table1. Compared to the commonly used SMAs materials, the studied 3D printed NinjaFlex and Z-Flex polymer elastomers are superior

Table 3.3. The specific heat capacity values for studied materials in different forms are measured by DSC

Materials	$\lvert\Delta T_{ad}\rvert$ (K)	ΔT_{cyc}(K)	$\Delta\sigma$(MPa)	ε(%)	COP_{mat}	Refs.
NinjaFlex	12	$3.24-3.92$	5.7	500	3.14	This work
Ultimaker95A	17.8	2.84	11.7	500	0.93	
KungFu98A	17.2	2.62	11.3	500	0.76	
Z-Flex	13.5	2.28	6.4	500	3.04	
$Ni-Ti$	22	$10-29$	800	5	7.5	[18, 27, 168]
$(Ni_{50}Mn_{31.5}Ti_{18.5})_{99.8}$ $B_{0.2}$	31.5	–	700	7	–	[20]
$Cu_{68.3}Al_{27.1}Ni_{4.6}$	13.6	4.6	400	7.5	9.5	[72]
$Cu_{68.2}Zn_{15.7}Al_{16.1}$	15.3	–	118	8	10.6	[169]
$Ni_{50.0}Fe_{19.0}Ga_{27.1}Co_{3.9}$	11	7.2	130	3.8	4 (system)	[170]
NR	$3.5-12$	2	$1-4.2$	$600-800$	2.08	[19, 89, 94]
Synthetic rubbers	$1.7-2.1$	–	$5.8-10$	$300-600$	$0.23-0.3$	[94]
SEBS	15.3	–	12	600	16.2	[57]
TPU	8	$3.3-4.5$	6.5	400	8	[93]

–: did not find; system: COP obtained from cooling system

in considerably lower driving stress (∼6 MPa, 500%) and provide a desirable elastocaloric performance. It can be observed that the cyclic temperature change for the NinjaFlex reaches 3.92 K which is lower than several Ni-Ti alloys but comparable to the ΔT_{cyc} of 4.6 K for $Cu_{68.3}Al_{27.1}Ni_{4.6}$ SMA. There is some variation in the material COP calculation presented in literature. For the shape memory alloys, the COP_{mat} are obtained with a correction for the irreversibility of the phase transformation process [171, 172]. For rubber-like materials due to less hysteresis, equation 3.2 was used for the COP_{mat} calculation [57, 93]. Here, the NinjaFlex, Ultimaker 95A, and Kungfu 98A filaments both consist of the thermoplastic polyurethane, but there are differences in the elastocaloric effect and COP_{mat} when comparing to the reported elastocaloric TPU [93]. That results from different types of TPU being used and a maximum temperature change employed for the COP_{mat} calculations in literature.

3.8 Prospects for an operation system for large deformation eCE regenerators

In comparison to the experimental system for elastocaloric cooling/heat pumping using SMAs, soft elastomeric eCE regenerators require much larger deformations (300-500%) to achieve a considerable eCE. At present, some related elastocaloric coolers based on the elastomers have been designed by inflation/deflation devices or by rolling onto a rotational wheel to trigger the eCE of polymer elastomers subjected to a large deformation [91, 97]. These designs give inspiration to apply the elastomeric eCE polymers in the solid-state cooling/heat pumping field. However, when considering the construction of an experimental active elastocaloric cooling/heat-pumping system for polymer elastomers, the large deformation raises several issues, including buckling, and fluid channels volume change. It can be predicted that the fluid-channel volume inside the 3D-printed regenerator changes when the regenerator undergoes a larger deformation due to the Poisson's ratio and strain-induced material volume change [173–175]. The fluid channel volume is expected to increase during the stretching process and decrease during the releasing process, which will lead to asymmetric fluid-flow volumes between the hot/cold blows. Therefore, operating a large deformation regenerator in a flow system, the empty volume from the stretching process needs to be compensated by the flow system. On the other hand, the compensated fluid from the stretching process should be expelled back to the flow system during the releasing process, otherwise, the extra fluid can increase the pressure and may cause leakage. Future work could include a tailored fluid network configuration and operation strategy capable of handling the change of fluid channel volume in an elastomeric regenerator.

3.9 Summary

We explored the elastocaloric cooling performance of five thermoplastic elastomers and demonstrated the potential for fabricating the soft elastomers directly into full-scale elastocaloric regenerators via additive manufacturing technologies. The elastocaloric effect in the five elastomeric filaments were initially investigated before manufacturing the filaments into 3D parts using FFF. Except for KungFu72D, the studied filaments show a satisfactory reversible elastocaloric effect. We found that the 3D-printed parts with the extruded beads aligned in parallel to the uniaxial strain direction can achieve an elastocaloric effect similar to the raw filament with stable mechanical behavior. NinjaFlex and Z-Flex dogbones exhibited a COP_{mat} of 3.14 and 3.04, respectively, at a low required stress of $\sim$6 MPa, which makes them potentially attractive for elastocaloric devices. Combining AM technologies with printable elastocaloric elastomer can result in full-scale elastocaloric regenerator that can be printed directly and actuated at significantly lower forces than comparable SMA systems. Several challenges need to be overcome for AM elastocaloric regenerator systems to achieve high performance. Since the heat-transfer fluid will flow through internal channels inside the regenerator, the AM parameters should be optimized to achieve fine regenerator geometries as well as being watertight. These would improve the fluid channel quality that could lower the flow pressure drop and enhance the heat-transfer performance. Another challenge is the large elongation required to achieve a high eCE for elastomeric regenerators, which will require special design of external equipment. There are also a number of issues that stem from the large required strains, including: softening behavior (Mullins effect), which occurs during the first cycle, and buckling during strain release caused by plastic deformation, which will bend/twist the fluid channels and influence the heat exchange. A certain number of training cycles until reaching the equilibrium could be a solution for the softening issue of these soft elastomers. Similar to the suggested pre-elongation method implemented in natural rubbers [92], the buckling can be avoided by applying the pre-strain approach, performed by unloading to a given strain. Additionally, manipulating the pre-elongation to the eve of SIC enables higher efficient elastocaloric cooling resulting from less mechanical energy input. Overall, these achievements show a great potential to construct the soft active elastocaloric regenerator with distinct low-driven stress, opening the opportunity to develop high-performance elastocaloric cooling regenerators with optimized heat-transfer properties and structures by means of additive manufacturing.

CHAPTER 4

Fluidic compensations of large-deformation regenerators

As aforementioned issues in the elastomeric eCE cooling system design, the large deformation is required to trigger a satisfactory eCE, however, which will produce a series of nonlinear behaviors for elastomers, both in the structural and mechanical aspects. When operating as an active eCE regenerator, elastomer-based regenerators are subjected to four steps: adiabatic loading, the cold-to-hot blow (cold blow), adiabatic unloading, and and hot-to-cold blow (hot blow). The large strains cause the volume of fluid channels to change in a unclear manner which results in asymmetric hot and cold blows as well as the energy imbalance in an eCE thermodynamic cycle. This volume change has been observed in the rubber-tube eCE cooler and elastomers [176, 177], yet it has never been specifically investigated.

In this chapter, to better understand how to realize a regenerative elastocaloric cooling system with continuous fluid compensations, we study the volume change produced by the large deformation in elastomeric regenerators experimentally and numerically. We study different fluid channels to investigate the geometrical impacts on volume changes as well as the strain-dependent volume change. Hyperelastic models are implemented for mechanical behavior fitting and employed for the volume change prediction of eCE regenerators. The corresponding regenerators are 3D-printed for validation of volume changes under large deformations.

This chapter is mainly based on article II in **Appendix A**.

4.1 Volume compensation of the large deformation regenerator and two typical regenerators

Operating as an active eCE regenerator, elastomer-based regenerators are subjected to four steps: loading, the cold-to-hot blow (cold blow), unloading, and hot-to-cold

blow (hot blow). Figure 4.1 **a** illustrates the fluid-channel volume change evolution over an elastocaloric thermodynamic cycle. The temperature variation associated with corresponding loading-unloading steps of elastocaloric elastomers is shown in Figure 4.1 **b** as obtained from our previous work [101]. During the first process 1 to 2, the regenerator is stretched resulting in a temperature increase. At the same time the fluid-channel volume increases as the regenerator undergoes large strains, as shown in Figure 4.1 **a**. The volume change is expressed as $V_f - V_i$ indicating the difference of the final and initial fluid-channel volume.

Importantly, it can been observed in a rubber-tube eCE cooler and in elastomers[176, 177] that large strains cause the volume of fluid channels to change in an unclear manner which results in asymmetric hot and cold blows as well as potentially unwanted heat transfer between the fluid and eCM during the loading and unloading processes. However, this effect has never been specifically investigated.

Here, we investigate the volume change produced by the large deformation in elastomeric regenerators both experimentally and numerically to understand how to realize a regenerative elastocaloric cooling system with continuous fluid compensations. We study different fluid channels to investigate the geometrical impacts on volume changes, as illustrated in Figure 4.1. Hyperelastic models are implemented in finite element (FE) simulations to predict volume changes of eCE regenerators. The corresponding regenerators are 3D-printed for validation of volume changes under large deformations.

The extra increased volume should be compensated to ensure the best-possible fluid flow profile throughout the cycle. In continuous flow systems, compensating for volume increases of the channel is typically inevitable due to the resulting negative pressure. Accordingly, a tailored fluidic compensation strategy can be devised to accommodate this volume change. The strategy involves managing compensations from the hot or cold reservoirs during the loading process and returning them to the reservoirs during the unloading process, depending on the specific cooling or heating implementations. Quantifying the amount of compensation volume is necessary for the development of high-performance regenerative elastomeric eCE regenerators.

We consider two typical regenerator fluid channels, namely parallel-plates (PP) and square channels, as shown in Figure 4.1 **c**. For both regenerator geometries, the external regenerator shape is a dogbone to avoid stress concentrations. The PP regenerator comprises 18 identical channels with a height of 4 mm while the square channel regenerator consists of 18×5 channels uniformly distributed in the regenerator. Both the PP channel and the square channel have a channel length of 36 mm in the same regenerator shape.

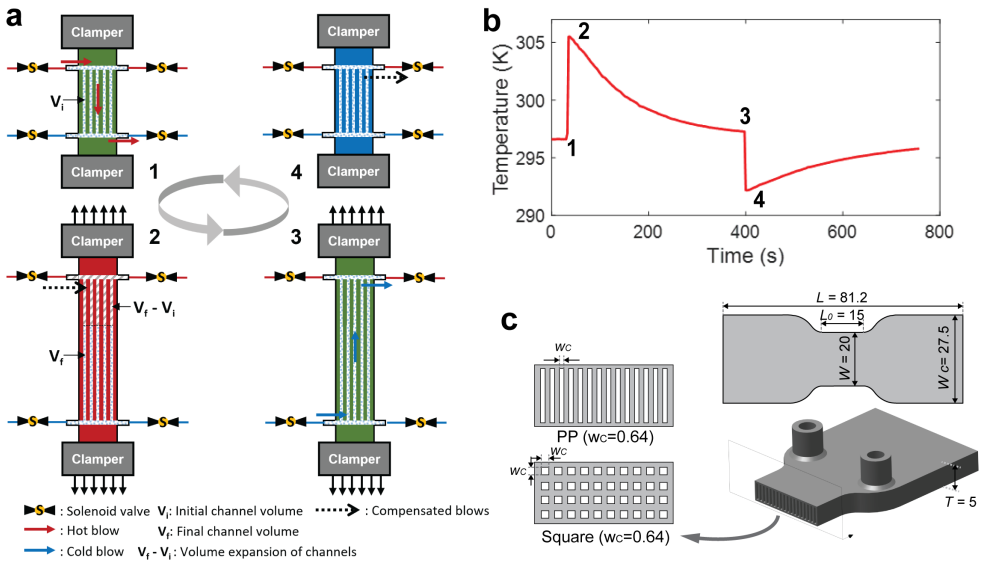

Figure 4.1. Schematic illustration of the volume change induced by large deformation and the corresponding steps in an elastocaloric cycle, a and b; schematic regenerator and two selected fluid channels labeled with the related geometric dimension (unit in mm), c. Note that the schematic channels differ from the real numbers of channels, which are 18 for PP channels and 18×5 for square channels.

4.2 Fitting of hyperelastic models

TPU possesses various complex mechanical properties such as hysteresis, softening, Mullins effect, time dependence, and equilibrium paths [87, 178–180]. In this study, we have simplified the constitutive model based on the actual operating conditions of eCE regenerators. These regenerators undergo alternating loading and unloading at a constant strain rate, ultimately reaching a steady thermal exchange status and mechanical equilibrium. To accurately capture the fluid-channel volume change during cyclic loading, we start with FE simulations by employing hyperelastic constitutive models to fit the equilibrium stress-strain response for large-deformation eCE regenerators. Explicit FE methods are implemented in the simulation for the volume change predication. Hyperelasticity is also commonly employed to simplify phenomenological models for rubber-like materials [181–183].

We use a hyperelastic constitutive models to fit uniaxial stress-strain response of the elastocaloric TPUs. The hyperelastic model is based on different strain potential density functions W. We assume that our printed elastomers are isotropic. The constitutive relationship based on the theory of continuum mechanics can then be expressed by the three invariants of the right Cauchy-Green deformation tensor $\mathbf{C}$

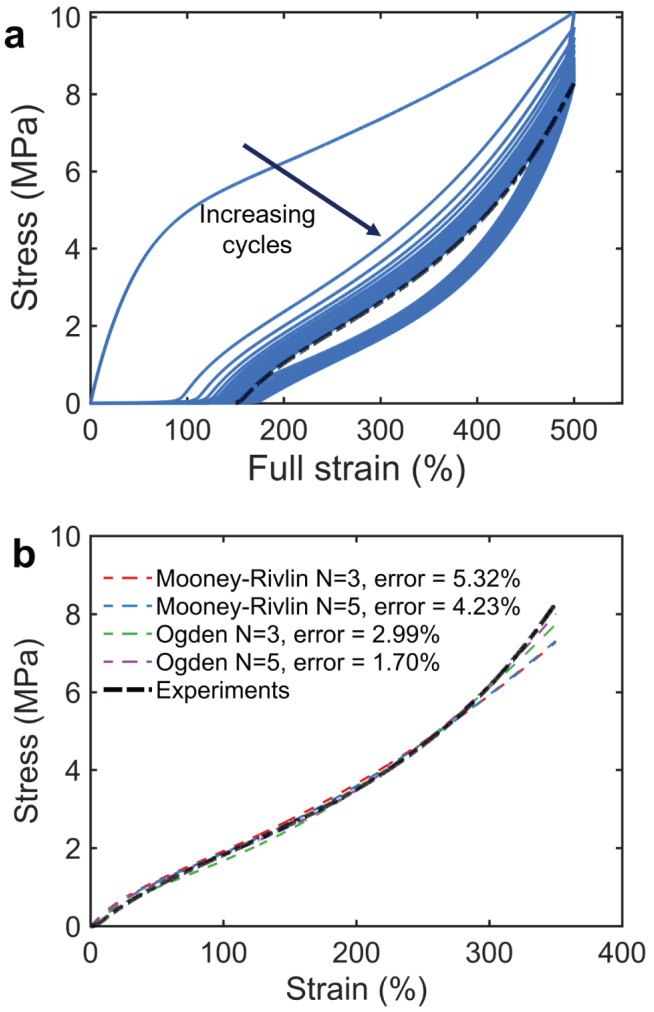

Figure 4.2. Hyperelastic model fitting for the stress-strain response of TPU elastomers: ***a*** *20 tensile cycles (blue) with the equilibrium curve for fitting (black);* ***b*** *Comparison of hyperelastic fittings.*

[184, 185]:

$$W = W\left(I_1, I_2, I_3\right) \tag{4.1}$$

These invariants can be obtained from expansion of the eigen-equation of deformation tensor and expressed by eigenvalues (i.e. stretch ratios, $\lambda_1, \lambda_2, \lambda_3$) of $\mathbf{C}$ as follows:

$$\begin{aligned} I_1 &= tr\mathbf{C} = \lambda_1^2 + \lambda_2^2 + \lambda_3^2 \\ I_2 &= \frac{1}{2}[(tr\mathbf{C})^2 - tr\mathbf{C}^2] \\ &= \lambda_1^2\lambda_2^2 + \lambda_2^2\lambda_3^2 + \lambda_3^2\lambda_1^2 \\ I_3 &= det\mathbf{C} = \lambda_1^2\lambda_2^2\lambda_3^2 = J^2. \end{aligned} \tag{4.2}$$

Here J is the Jacobian denoting the volume ratio of TPU before and after deformation. For rubber-like elastomers during uniaxial tensile tests, the mechanical response is close to incompressibility ($J = 1$) under small stretches. However, when applying large strains, Poisson's ratio and mechanical responses will be highly strain-dependent [185, 186]. For our cases, the applied strain reaches 500-600% which means the nonlinear Poisson's ratio and compressible conditions need to be accounted for in the regenerator volume change prediction. Here we choose the Mooney-Rivlin model and Ogden model to fit the stress-strain response of TPU elastomers. The Mooney-Rivlin strain energy function can be expressed as [187]:

$$W = \sum_{i,j=0}^{N} C_{ij}\left(\bar{I}_1 - 3\right)^i \left(\bar{I}_2 - 3\right)^j + \sum_{i=1}^{N} \frac{1}{d_i}\left(J-1\right)^{2i}, \tag{4.3}$$

and the Ogden strain energy function can be expressed as [188]:

$$W = \sum_{i=1}^{N} \frac{\mu_i}{\alpha_i^2}\left(\bar{\lambda}_1^{\alpha_i} + \bar{\lambda}_2^{\alpha_i} + \bar{\lambda}_3^{\alpha_i} - 3\right) + \sum_{i=1}^{N} \frac{1}{d_i}(J-1)^{2i}. \tag{4.4}$$

In these strain energy function expressions, the invariants are modified in principal stretches (marked with the overline) form based on the deviatoric-volumetric multiplicative split for compressible material models [141, 185], see details in the theory of **Chapter 2**.

To approach stabilized mechanical behavior, the standard sample was loaded for 20 cycles at a strain rate of 1 s^{-1} which reaches equilibrium, as shown in Figure 4.2 **a**. The performed strain range 0-500% is based on our desired operating range for a prototype. The equilibrium stress-strain response of loading process of the 20th cycle is employed for the hyperelastic model fitting by removing the creep regime. Basically, this bucking is always observed due to creep caused extension, even upon full contraction of the loading conditions. The fitting results are shown in Figure 4.2

Table 4.1. The fitting results list of the different hyperelastic models with different parameter numbers

Hyperelastic models	Number	List of parameters										
Mooney model	N=3	C10	C01	C11	d_1							
		0.205	0.458	0.051	5.385e-05							
	N=5	C10	C01	C20	C11	C02	d_1					
		0.414	0.228	0.041	0.048	5.994e-4	0.159					
Ogden model	N=3	μ_1	α_1	μ_2	α_2	μ_3	α_3	d_1				
		50.515	0.048	0.048	4.796	-0.052	-0.382	0.167				
	N=5	μ_1	α_1	μ_2	α_2	μ_3	α_3	μ_4	α_4	μ_5	α_5	d_1
		1.556	0.397	0.397	2.835	0.005	7.489	2.835	0.326	2.285	0.035	1.003

b. The fitting error can be evaluated as:

$$\text{error } (\%) = \frac{\int_{\varepsilon_0}^{\varepsilon} \left|\sigma_{\text{sim}} - \sigma_{\text{exp}}\right| d\varepsilon}{\int_{\varepsilon_0}^{\varepsilon} \sigma_{\text{exp}} d\varepsilon} \times 100\% \tag{4.5}$$

The fitting parameters for these four models are summarized in the table 4.1. Comparing the fitting results, the N=5 Ogden model achieves the best fitting and is therefore implemented in the FE simulation for the 3D-printed regenerator fluid-channel volume change prediction.

Scenario 3 Calibrations for the pressure change measurement

Temperature calibration: The temperature changes were recorded during the cyclic loading-unloading process of the volume change measurement for temperature calibration. The temperature ratio (C) is defined as:

$$\frac{P_f V_f}{P_i V_i} = \frac{T_f}{T_i} = C \tag{4.6}$$

The pressure change ratio can be modified according to the following equation:

$$\begin{aligned} \delta V = \frac{V_f - V_i}{V_i} &= \frac{\frac{C P_i V_i}{P_f} - V_i}{V_i} \\ &= C\frac{P_i}{P_f} - 1 \end{aligned} \tag{4.7}$$

Volume calibration: The volume ratio between regenerator channels and connection tubes is define as α,

$$\alpha = \frac{V_R}{V_{\text{tube}}}. \tag{4.8}$$

The volume change can be calibrated by following way:

$$\begin{aligned} \delta V = \frac{V_f - V_i}{V_i} &= \frac{V_{R,f} + V_{\text{tube}} - (V_{R,i} + V_{\text{tube}})}{V_{R,i} + V_{\text{tube}}} \\ &= \frac{V_{R,f} - V_{R,i}}{V_{R,i} + V_{\text{tube}}} = \frac{\Delta V_R}{(1 + \frac{1}{\alpha}) V_R} = \frac{1}{1 + 1/\alpha} \delta V_R \end{aligned} \tag{4.9}$$

Thus, the actual volume change of regenerator channel itself is:

$$\delta V_R = (1 + \frac{1}{\alpha}) \delta V. \tag{4.10}$$

4.3 Simulations for different regenerator channels

Next, a FE modeling of the regenerator to find the volume change was conducted. Half of the regenerator was modelled due to the symmetry and the inlet structures were also neglected in the simulation. We applied a strain in a sequence from 0 to 600% and the volume change ratio ($\delta V = \frac{V_f - V_i}{V_i} \times 100\%$) calculated is shown in Figure 4.3 **a** and **c**. It can be seen that the volume change ratio in the PP-channel regenerator is higher than that of the square channel. Furthermore, the PP channel has a higher stress in the middle active region of the regenerator due to its smaller cross-sectional area. In principle, the stress should be similar. But this section is softer due to less material, thus more deformation goes there, so it should experience a higher stress. To visualize the fluid channels geometry variation under large deformation, the fluid channels of the initial and final states at a strain of 600% are shown in Figure 4.3 **b** and **d** for PP channels and square channels, respectively. Comparing the deformed channels in Figure 4.3 **a** and **b**, we observe that the PP channels are subject to a buckling along the Z-axis (thickness direction) which is significant at the boundary channels while this is not observed for the square channels. This buckling might be the reason of the observed reduction in stability in the Z-axis of thin plate walls between the channels when undergoing a large uniaxial strain[189]. As a consequence, the PP channel buckling contributes to an increased volume change ratio in the PP channels. In addition, higher strains ($\sim$53 mm, 600%) are obtained by PP channels.

4.4 Volume-change measurements and validation

To validate the simulation results, experimental measurements were conducted to determine the actual volume change of the fluid channels during the stabilized mechanical process. The experimental setup was designed based on pressure difference measurements (see details in **Scenario 3**). The idea is to apply the same pressure to the regenerator and the air tank 2 (reference pressure) when the pressure gets stabilized to seal the regenerator as a closed volume. During the loading process, the volume change can be determined by monitoring pressure changes between the regenerator and air tank 2. The experimental fluidic system shown in Figure 4.4 **a** and Figure 4.4 **b** is the physical setup, where the regenerator pressure is denoted as $P1$ and the reference pressure from air tank 2 is denoted as $P2$. The volume change ratio can be calculated based on the ideal gas law equation ($PV = nRT$):

$$\delta V = \frac{V_f - V_i}{V_i} = \frac{P_i}{P_f} - 1 = \frac{P_2}{P_1} - 1. \tag{4.11}$$

Taking into account impacts from the temperature changes of the regenerator and the connected tubes volume between the regenerator and the pressure sensor, the

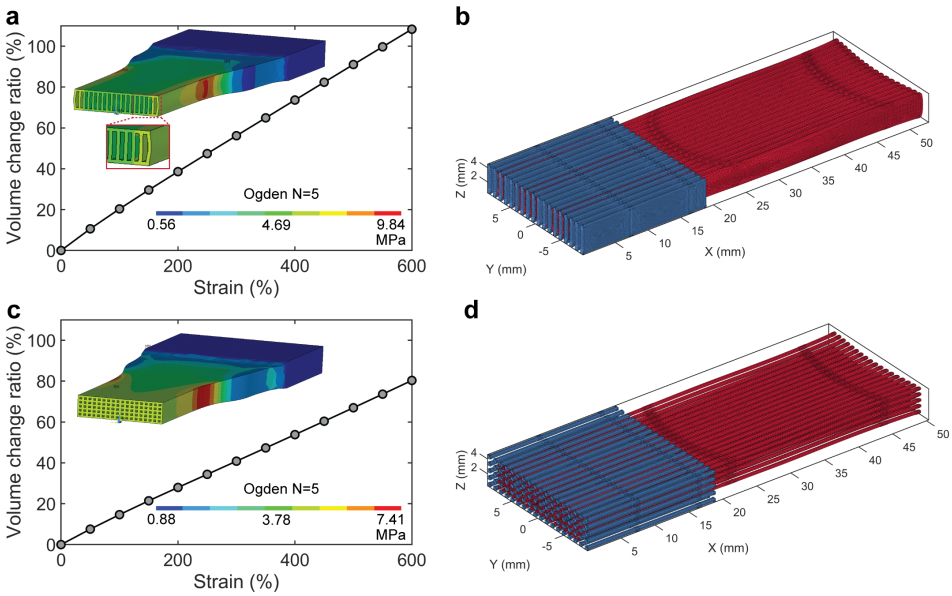

Figure 4.3. Simulation results for PP channels a and square channels c volume change prediction as a function of strain (Von Mises stress at 600% for the insets), and corresponding 3D-fluid channels b and d under 600% strain where X = 0 mm is symmetric plane (Y-Z) and the clamped area is at X = 25.5 mm and X = 85.5 mm for initial (blue) and deformed (red) channels (there is a 7.5 mm distance between the channel end and clamped area before loading).

actual volume change ratio of the regenerator can be calibrated to be (see details in **Scenario 3**):

$$\delta V_R = (1 + \frac{1}{\alpha})(C\frac{P_i}{P_f} - 1), \tag{4.12}$$

in which α and C are the temperature and volume calibration ratio, respectively. The α value is 0.985 for PP channels and the C value is 1.01 at 600%.

The PP regenerator is employed for the volume-change validation experimentally. Before measurements, the airtightness of the device and the regenerator need to be ensured. We applied a 0.5 bar pressure to tank 2 and the regenerator and closed the two solenoid valves (at 20 min in Figure 4.4 **c**) and waited for 30 min to confirm the pressure maintenance. The results of pressure differences ($P1-P2$) is stabilized approaching to zero indicating no air leakage in the regenerator and thus a good airtightness of the sample. The volume change measurements are performed under cyclic operation along X-axis at different strain rates for a strain range of 200-600% to avoid creep. The volume change ratio as a function of strain at rates of 0.1 s^{-1} and 1 s^{-1} is shown in Figure 4.4 **d** along with the simulation results normalized to 200% strain to remove the creep regime. From the experimental results at different

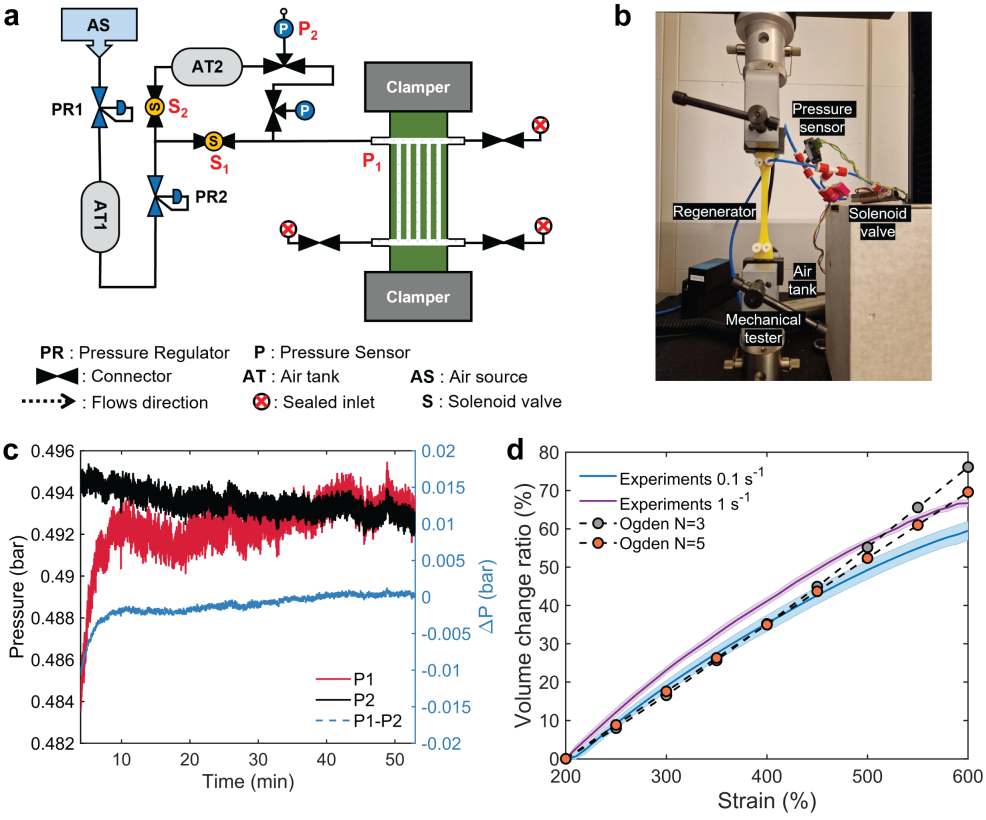

Figure 4.4. Pneumatic experimental setup and simulation validation:
a. *Fluidic circuit for pressure difference measurements (P1: regenerator pressure, P2: air tank 2 pressure);* ***b***. *Physical picture for the setup;* ***c***. *Airtight examination by monitoring pressure holding;* ***d***. *Comparison of volume change ratio as a function of strains at different loading rates (simulations performed at 1* s^{-1} *loading rate).*

loading rates, the higher loading rate shows a larger volume change ratio. From the experimental results, we noticed that the regenerator subjected to a higher loading rate exhibited a larger volume change ratio. This is because the lower loading rate allows more creep deformation to occur [87, 190]. The simulation results at 1 s^{-1} were slightly lower than the experimental results overall. This difference could be because the simulations did not include certain connecting structures between the regenerator fluid channels and the fluid inlet and outlet, which were present in the experiments, and could also be that in experiments the cross-section is different due to the printing. Here the Ogden model was applied to the simulation for comparison. It is noteworthy that the Ogden 3 and 5 models provide satisfactory predictions for the regenerator volume change in our desired operating range. When strains exceed 500%, there is an over estimation for Ogden 3 due to the constrained strain range (500%) employed for the hyperelastic fittings in Figure 4.2. It can be anticipated that by employing a larger strain range during the hyperelastic model fitting, more accurate predictions can be obtained.

Operating in an eCE cycle, the ratio (V^*) of displaced fluid volume (V_{disp}) and regenerator volume (V_R) or Utilization are one of evaluating factors for the eCE regenerator performance to measure how much heat extracted from the regenerator by heat-transfer fluids [18, 22, 67]. The V^* shows to be 1 for the best COP in a NiTi-based prototype at 1.7% [67], which means the same V_{disp} and V_R. In this volume increased case, the V^* can be rewritten as:

$$V^* = \frac{V_{disp}}{0.5 \times (V_{R,i} + V_{R,f})} = \frac{V_{disp}}{V_{R,i} + 0.5 V_{R,i} \delta V_R}. \tag{4.13}$$

For the PP regenerator, with a δV_R of 66.7% the equivalent V^* will be 0.74, indicating decrease in V^* when the fluidic channel volume increases by large deformation. In previous regenerative coolers [22, 176], it has been demonstrated that the optimized V^*/Utilization ratio provides enhanced cooling power and temperature span. However, this strain-induced volume change leads to the deviatoric V^* and asymmetric hot-cold blows and further will reduce the temperature span. It suggests a tailored flow system allowing compensating this volume change to maintain a satisfactory temperature span during practical operation.

4.5 Position-dependent volume changes in the tensile direction

In an actual 3D printed elastocaloric regenerator, the volume change also may be position-dependent. Simulation results can quantify the volume change distribution along the tensile direction. We consider the fluid channels segmented into 15 segments to examine the volume change distribution along the tensile axis. Figure 4.5 **a** and **c** show the results for the PP channels and square channels under 600%

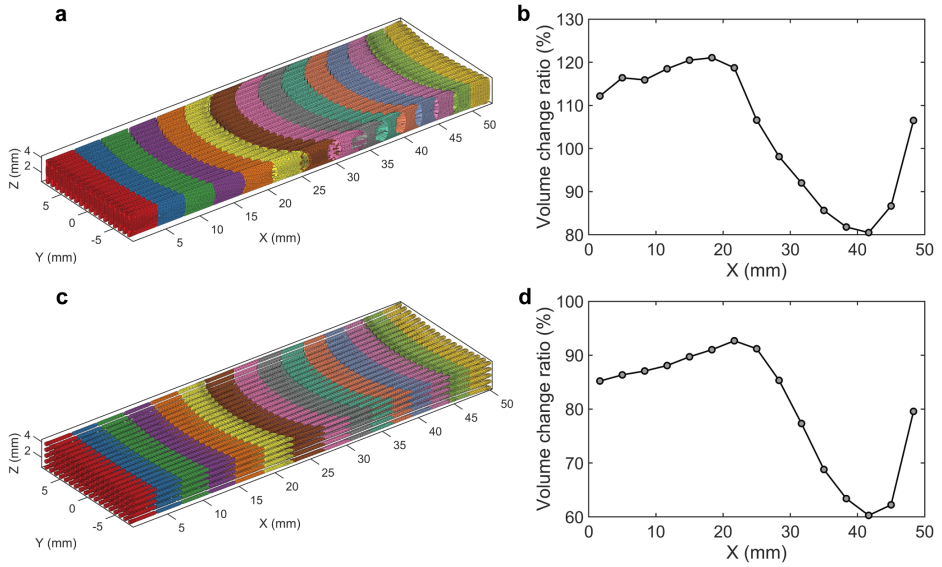

Figure 4.5. Volume change distribution (volume change as a function of the X coordinate at 600%) along the tensile direction for the different volume channels:
a *and* ***b*** *for the parallel-plate channel;* ***c*** *and* ***d*** *for the square channel; in the figure of 3D-fluid channels Y-Z is symmetric plane and X = 85.5 mm is clamped area (actually, there is a 7.5 mm distance between the channel end and clamped area).*

strain and the volume change ratio of each segment is plotted in Figure 4.5 **b** and **d**. We observed after 20 mm of regenerator length the volume change ratio gradually decreases in a certain coordinate range for both PP channels (up to 48 mm) and square channels (up to 40 mm) and then slightly increases. This decrease in volume change along the regenerator length direction is due to the compression exerted by the rounded section of the dogbone-shaped regenerator, by observing deformed structures in Figure 4.3 **a** and **c**. The volume change ratio increases at the channel end could be attributed to the boundary effect near the clamped side. In an actual regenerator, we can understand that the significant volume changes of fluid channels occur in the active zone, i.e., the middle of a dogbone regenerator, which is supposed to the regenerator length. The average volume changes in this zone are expected to conduct to the AER numerical modelling. It is more approaching to the real status of our simulated regenerators.

4.6 Summary

In summary, Ogden hyperelastic constitutive models successfully achieve a good fit for the stress-strain response of eCE TPU elastomers and corresponding FE simulations for the prediction of regenerator volume compensations exhibit excellent agreement with experimental results. The PP regenerator shows higher volume change compared to the square-channel regenerator under significant deformation, due to thin-plate buckling instability. Subjecting the PP regenerator to a 200-600% strain results in a 66.7% volume change ratio. A nonuniform volume change behavior is observed along the stretching direction, particularly in the rounded region of the dogbone-shaped regenerators. These results hold promise for accurately predicting volume compensation in soft, large-deformation eCE regenerators and inspiring the design and modeling of active large-deformation regenerators.

The model and underlying data are accessible from the online database [191].

CHAPTER 5

1D numerical model for large-deformation elastocaloric regenerators

The numerical models are universally implemented for the evaluation and optimization of regenerative caloric regenerators [149, 192–194]. Moreover, it also insights on the development and design of the corresponding active cooling or heat-pumping system. To better understand the implementation of our 3D-printed soft active elastocaloric regenerators, in this chapter, we developed an improved 1D AER numerical model which adapts to the regenerator undergoing large deformations and involving volume change issues. This large-deformation AER model is based on the 1D AMR and elastocaloric models, which rarely relates to the significant volume change of heat-transfer fluidic channels when operating in an active caloric thermodynamic cycle and the significant evolution in the spatial length of the model. Prior to the model construction, we notice that there are several challenges for these polymeric eCE regenerators modelling to address:

- Evaluating the volume compensations (already studied in the previous chapter) to consider into the model during the loading and unloading processes;
- Consideration for the regenerator length elongation (usually 200-600% applied strains) in the model;
- The cross-section area geometry changes (including the fluid channel, regenerator materials) with the uniaxial elongation, especially for the large deformation which shows nonlinear behavior.
- The spatial grids of the numerical model should be updated according to the applied strains due to the significant elongation of the regenerator length.

This chapter is related to article **IV** in **Appendix A**.

5.1 Temperature gradients for large-deformation elastocaloric regenerators

The significant volume change of the regenerator fluid channels has been observed for large-deformation AERs. The potential temperature gradients of the fluid inside the regenerator are shown in Figure 5.1. For the purpose of cooling, the fluidic compensation is expected to come from the hot reservoir (HR) where the temperature is fixed by a heat exchanger. The Figure 5.1 illustrates the temperature gradients over an active thermodynamic cycle. Meanwhile, the compensation and expelling processes, denoted by dash line, are provided. The evolution of the temperature gradients is indicated by the change of the initial temperature (T_i, dash line) to the final temperature (T_f, solid line) in each process.

Upon adiabatic loading, the regenerator temperature gradually increases and the fluid channels are subjected to a significant deformation when the regenerator goes to a large stretch. The fluid channel volume increases as we found in the last chapter. During this process, there are passive compensation fluids flowing into the regenerator from the hot reservoir (here, we assumed the regenerator was placed vertically with the hot reservoir on the top.) owing to the gravity. And the temperature on the upper channels is equal to the T_H (temperature of HR). Ideally, the volume of this part of channels filled with compensated fluids is identical to the volume changes induced by large strains. This compensated volume will be accounted into the 1D numerical model for AERs. Afterward, when the loading is finished, the piston displaces the heat transfer fluids from the cold reservoir (CR) to the HR (the cold blow in Figure 5.1), and the initial temperature of fluids is decreased.

Upon adiabatic unloading, the regenerator temperature is decreasing, meanwhile the fluid channel volume is reducing. During this process, the extra fluids need to be expelled out, where it is operated to flow back to the HR. As shown in the expelling blow in Figure 5.1, the temperature of the upper channels decreases as they are cut off from the main flow, as this portion is expected to be completely expelled into the HR. When the strain is fully released, the regenerator temperature drops, resulting in the cooling of the fluids. This cooling process is marked by the hot blow of fluids from the hot side (HR) to cold side (CR), where the elastocaloric cooling load is extracted from the regenerator the cold side.

Actually, the temperature gradient distribution in the regenerator is complicated, which depends on the regenerator structures, operation frequency, working temperature (T_H), mass flow rate, and high-strain induced volume changes. To comprehend the possible temperature gradient within the large-deformation soft regenerator, we introduce a 1D numerical AER model in this chapter. This model considers both the significant deformation of the regenerator's length and fluid compensation, which can predict the performance parameters of the AER.

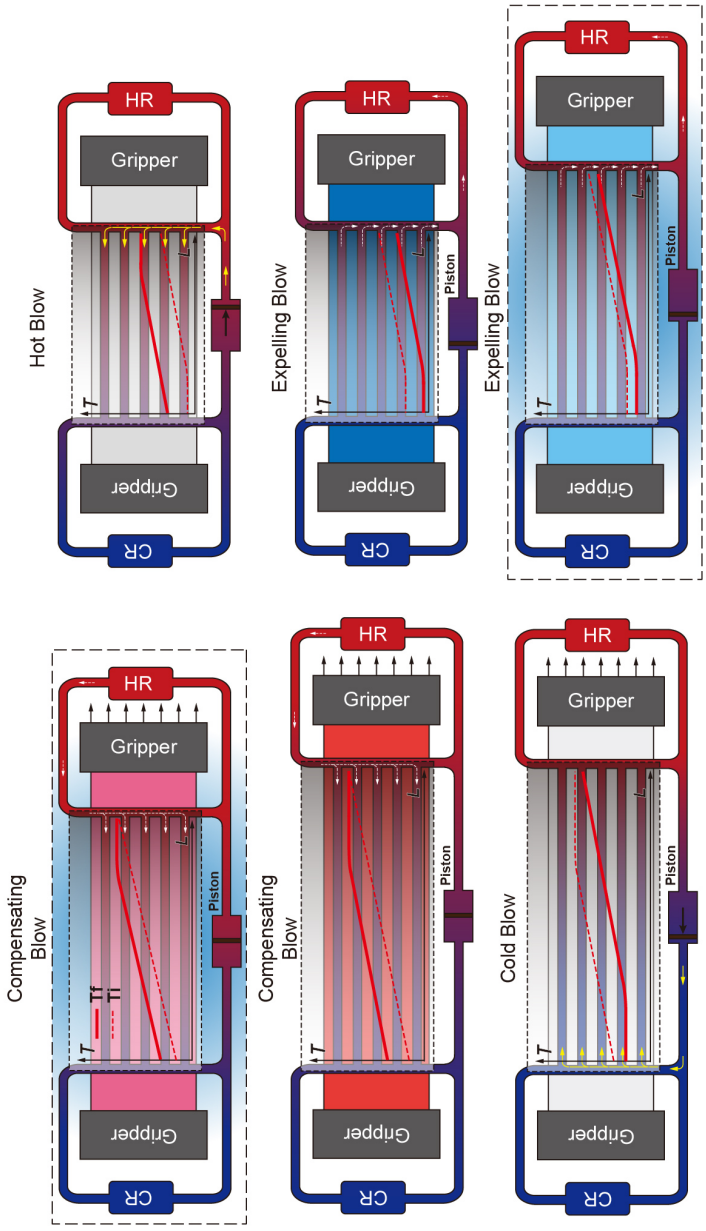

Figure 5.1. Potential temperature gradients evolution with fluidic volume compensation inside the large-deformation elastocaloric regenerator.

5.2 1D elastocaloric numerical models

In general, to develop the 1D elastocaloric model, the two basic governing equations based on the AMR and the Ni-Ti based elastocaloric regenerator models can be obtained from the literature, which have been described in **Chapter 2** as follows:

$$\underbrace{A_c\phi\rho_f c_f\frac{\partial T_f}{\partial t}}_{\text{Heat storage}} = \underbrace{\frac{Nuk_f}{D_h}a_s A_c\left(T_s - T_f\right)}_{\text{Heat convection}} + \underbrace{\frac{\partial}{\partial x}\left(k_{disp}A_c\frac{\partial T_f}{\partial x}\right)}_{\text{Heat conduction}} - \underbrace{\dot{m}_f c_f\frac{\partial T_f}{\partial x}}_{\text{Heat advection}} + \underbrace{\left|\frac{\partial P}{\partial x}\frac{\dot{m}_f}{\rho_f}\right|}_{\text{Viscous dissipation}} \tag{5.1}$$

$$\underbrace{\frac{\partial T_s}{\partial t}}_{\text{Heat storage}} = \underbrace{\frac{T_s}{c_{s,\varepsilon}}\left(\frac{\partial s}{\partial \varepsilon}\right)_T\frac{\partial \varepsilon}{\partial t}}_{\text{Elastocaloric heat}} + \underbrace{\frac{Nuk_f a_s}{D_h\rho_s c_{s,\varepsilon}(1-\phi)}\left(T_f - T_s\right)}_{\text{Heat convection}} + \underbrace{\frac{1}{\rho_s c_{s,\varepsilon}(1-\phi)}\frac{\partial}{\partial x}\left(k_{stat}\frac{\partial T_s}{\partial x}\right)}_{\text{Heat conduction}} \tag{5.2}$$

When an AER system is configured for cooling or heat-pumping applications, the strain serves as a controllable parameter. Therefore, we treat the strain as the external field which is responsible for driving the elastocaloric devices in the solid equation 5.2.

5.2.1 Spatial nodes adjustment

When dealing with the two partial differential equations (PDEs) mentioned above, numerical calculations employ a central differential scheme and implicit temporal discretization. It is noteworthy that the large-deformation AER model differs from previous AMR or AER models, where spatial dimensions remain fixed during the heat transfer process. In the case of the Ni-Ti regenerator, the strain is relatively small compared to the spatial length of the regenerator, enabling us to neglect geometrical changes. However, in the case of soft elastomer regenerators, significant deformations lead to notable changes in the geometry and fluid channel volume (accounted for 69%), influencing the flow direction of heat transfer fluids. Moreover, heat conduction is also affected by these geometry changes. Therefore, it becomes necessary to modify the fundamental governing equations by introducing modifications for the spatial nodes and corresponding volume changes.

When operating an elastomeric regenerator to prevent buckling which is resulted from irreversible deformation, the regenerator will return to a pre-strain (ε_0). In this context, we define the regenerator's length at this strain as the initial length (L_0). Assuming that the actual initial length is denoted as (l_0), and given the relationship $L_0 = (1+\varepsilon_0)l_0$, the length at the final strain is represented as L. To discretize the elongated axial length, we employ a simplifying assumption for the extended nodes. We assume that each node undergoes proportional stretching, as illustrated in Figure

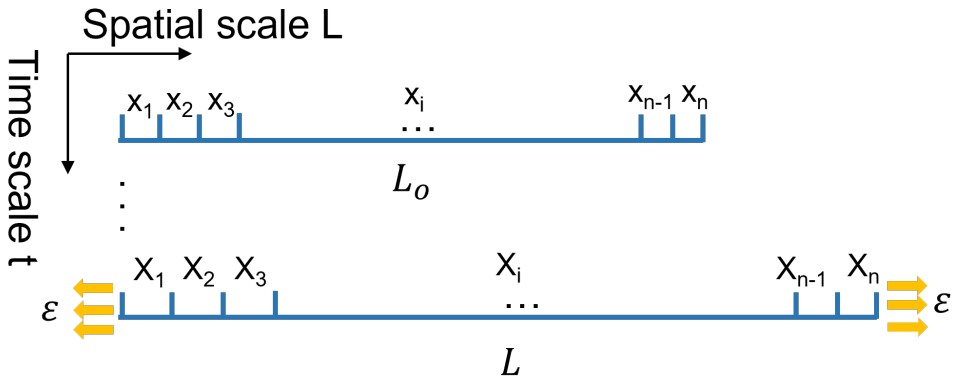

Figure 5.2. Spatial discretization for releasing and stretching length.

5.2. The initial spatial coordinate and the stretched spatial coordinate are denoted as x and X, respectively. The spatial length is discretized into an equal number of nodes. Each unit grid can be expressed as follows:

$$X_i = \lambda x_i \tag{5.3}$$

, where the λ is the elongation ratio. For 1D model the differential operators in the PDEs can be written as:

$$\begin{aligned} \nabla &= \frac{\partial}{\partial x} = \frac{1}{\lambda}\frac{\partial}{\partial X} \\ \nabla^2 &= \frac{\partial^2}{\partial x^2} = \frac{1}{\lambda^2}\frac{\partial^2}{\partial X^2} \end{aligned} \tag{5.4}$$

5.2.2 Modifications for the geometrical and fluidic parameters

In the basic governing equations, several parameters are dependent on the spatial length and undergo alterations after stretching. Below, we list a few key geometric parameters that play an important role in determining fluid properties, and have a significant impact on heat transfer within the elastocaloric regenerator. The star superscript (*) on the variables represents the parameter undergoing deformation.

- **Cross-section area** Ac
  The cross-section area is the product of the width (W) and the thickness (δ) of the regenerator. The width and the thickness stretching to a strain ε can be expressed using Poisson's ratio:

$$\begin{aligned} W^* &= (1 - \nu\varepsilon)W_0 \\ \delta^* &= (1 - \nu\varepsilon)\delta_0 \end{aligned} \tag{5.5}$$

in which W_0 and δ_0 represent the initial width and thickness, respectively.

We define the $(1-\nu\varepsilon) = \varphi$ as the **deformation factor** for the regenerator solid. Thus, the current cross-section area becomes:

$$A_c^* = (1-\nu\varepsilon)^2 A_{c,0} = \varphi^2 A_{c,0} \tag{5.6}$$

- **Porosity of the regenerators** ϕ
  Porosity calculations depend on the type of packed beds. Here we used the parallel plate regenerator as an example shown in Figure 5.3. The solid regenerator height and the fluid channel height are h_1 and h_2. The deformation factor for the regenerator solid, as mentioned earlier, is represented as φ. However, it is important to note that the deformation factor for the fluid channel is not the same and varies depending on the geometry changes of the channel. We define it as φ^* for the channel deformation factor, which can be deduced from the channel volume change and will be provided in the subsequent discussion. The porosity after stretching can be written as:

$$\phi^* = \frac{\varphi^* h_2}{\varphi h_1 + \varphi^* h_2} \tag{5.7}$$

- **Specific surface area of the regenerators** a_s
  For the parallel-plate regenerators the specific surface area is expressed as:

$$a_s^* = \frac{2}{\varphi h_1 + \varphi^* h_2} \tag{5.8}$$

- **Hydraulic diameter** D_h
  For parallel-plate regenerators the hydraulic diameter is expressed as:

$$D_h^* = 2\varphi^* h_2 \tag{5.9}$$

It is noteworthy that if we have data set for the volume change of fluid channels, actually which is attainable from the finite element (FE) simulations which has been discussed in the **Chapter 4**, we can directly calculate the deformation factor of fluid

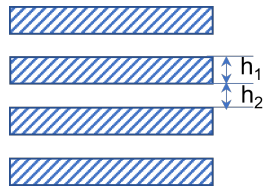

Figure 5.3. Parallel-plate regenerators.

channels φ^* using equation 5.6 for the deformed cross-section area. The calculation of the volume change can be expressed by:

$$\begin{aligned}\Delta V &= A^*_{c,f} L - A_{c,f} l_0 = A^*_{c,f} \lambda l_0 - A_{c,f} l_0 \\ &= \varphi^{*2} A_{c,f} \lambda l_0 - A_{c,f} l_0 \\ &= (\varphi^{*2} \lambda - 1) A_{c,f} l_0\end{aligned} \tag{5.10}$$

in which L, l_0, $A_{c,f}$, λ represent the final regenerator length, initial regenerator length, final regenerator cross-section area, elongation ratio, respectively. Consequently, the deformation factor φ^* of fluid channels yields:

$$\varphi^* = \sqrt{\frac{\Delta V + A_{c,f} l_0}{\lambda A_{c,f} l_0}} \tag{5.11}$$

The geometric relationship can also be generalized to versatile cross-section structures. If the two spatial scales of the cross-section area are considered as two differential elements dy and dz in y and z direction (where x is defined as the axial direction), the initial cross-section area A_c can be expressed in integral form using the following equations. Similarly, we employ the same expression for the deformed regenerator's cross-section area A^*_c.

$$\begin{aligned}A_{c,0} &= \iint dydz = \oint da \\ dY &= (1 - \nu\varepsilon) dy \\ dZ &= (1 - \nu\varepsilon) dz \\ dA &= dY dZ = (1 - \nu\varepsilon)^2 da \\ A^*_c &= \oint dA = (1 - \nu\varepsilon)^2 A_c = \varphi^2 A_{c,0}\end{aligned} \tag{5.12}$$

Analogously, we represent other geometric parameters using φ and φ^* under different strains. However, for different channel structures, the specific surface area and hydraulic diameter need to be calibrated based on the corresponding expressions, in which its characteristic length can be scaled by the deformation factors φ and φ^*.

5.2.3 1D elastocaloric model for the large deformation regenerator

In addition to aforementioned geometric variables, some other related variables in the partial differential equations can also be modified based on the geometric deformation. Here, we modified the differential operators from the spatial deformation relations and denoted the corresponding revised parameters using the star superscript, and the governing equation for the large-deformation regenerator yields:

$$\underbrace{A_c^*\phi^*\rho_f c_f\frac{\partial T_f}{\partial t}}_{\text{Heat storage}}=\underbrace{\frac{Nu^*k_f^*}{D_h^*}a_s^*A_c^*\left(T_s-T_f\right)}_{\text{Heat convection}}+\underbrace{\frac{\partial}{\lambda\partial X}\left(k_{disp}^*A_c^*\frac{\partial T_f}{\lambda\partial X}\right)}_{\text{Heat conduction}}-\underbrace{\dot{m}_f c_f\frac{\partial T_f}{\lambda\partial X}}_{\text{Heat advection}}+\underbrace{\left|\frac{\partial P^*}{\lambda\partial X}\frac{\dot{m}_f}{\rho_f}\right|}_{\text{Viscous dissipation}} \tag{5.13}$$

$$\underbrace{\frac{\partial T_s}{\partial t}}_{\text{Heat storage}}=\underbrace{\frac{T_s}{c_{s,\varepsilon}}\left(\frac{\partial s}{\partial\varepsilon}\right)_T\frac{\partial\varepsilon}{\partial t}}_{\text{Elastocaloric heat}}+\underbrace{\frac{Nu^*k_f^*a_s^*}{D_h^*\rho_s c_{s,\varepsilon}(1-\phi^*)}\left(T_f-T_s\right)}_{\text{Heat convection}}+\underbrace{\frac{1}{\rho_s c_{s,\varepsilon}(1-\phi^*)}\frac{\partial}{\lambda\partial X}\left(k_{stat}^*\frac{\partial T_s}{\lambda\partial X}\right)}_{\text{Heat conduction}} \tag{5.14}$$

5.2.4 Model discretization and numerical solution process

The numerical model of AER is based on the solver implemented for the previous AMR 1D models [150, 152, 195]. The governing equations are discretized using the center differential method, and the energy equations can be rewritten as discretized equations:

$$\begin{aligned} A_{i,i}T_{f,i,j+1} &+ A_{i,N_x+i}T_{s,i,j+1} &&= B_i \\ A_{N_x+i,i}T_{f,i,j+1} &+ A_{N_x+i,N_x+i}T_{s,i,j+1} &&= B_{N_x+i} \end{aligned} \tag{5.15}$$

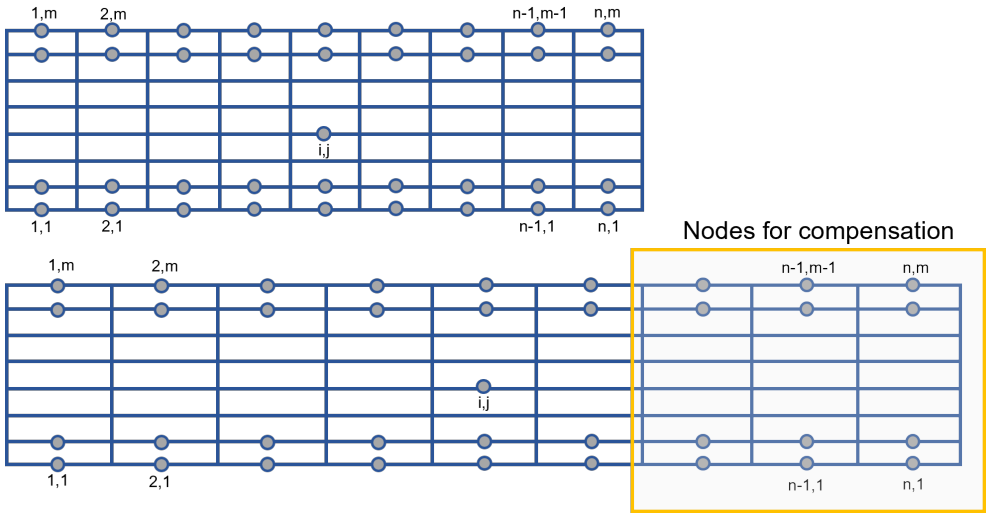

Figure 5.4. Discretized nodes for fluidic compensations.

Afterward, the two discretized equations can be combined as a matrix equation:

$$\begin{bmatrix} \mathbf{A_{i,i}} & \mathbf{A_{i,N_x+i}} \\ \mathbf{A_{N_x+i,i}} & \mathbf{A_{N_x+i,N_x+i}} \end{bmatrix} \times \begin{bmatrix} \mathbf{T_{f,i,j+1}} \\ \mathbf{T_{s,i,j+1}} \end{bmatrix} = \begin{bmatrix} \mathbf{B_i} \\ \mathbf{B_{N_x+i}} \end{bmatrix} \tag{5.16}$$

$$[\mathbf{A}] \cdot [\vec{\mathbf{T}}] = [\vec{\mathbf{B}}], \tag{5.17}$$

in which **A** is a tridiagonal matrix of the coefficients of the discretized equations, **B** is a vector of the constant terms (the temperatures from the previous time step, the boundary conditions, etc.), and **T** is a vector of the unknown temperatures (T_f, T_s) in the next time step. See details of the discretization of the governing equations from [150, 195].

The temperature profiles T for the regenerator solid (T_s) and fluids (T_f) can be calculated by inverse solution of matrix equation $[\mathbf{T}] = [\mathbf{A}]^{-1} \cdot [\mathbf{B}]$. In practice, the **A** is a 2Nx*2Nx sparse matrix and the **T** and **B** are two 2Nx vectors when solving in the MATLAB. Nx and Nt are the spatial node number and time node number for discretization, respectively. The spatial node coordinate is updating dynamically at each time node according to the real-time stretch (λ). A schematic discretized network for time and space from the initial length to stretching length is shown in Figure 5.4, in which the n and m equal to Nx and Nt, repectively. The node network is stretched along the axial (tensile) direction. During this process, the other geometric parameters, such across section area, hydraulic diameter, and porosity, etc., are also updated with respect to time steps. As previously postulated, compensation for the cooling application was supplied from the hot reservoir, and the regenerator was vertically positioned. As a result, compensation nodes can be obtained from one side of the spatial nodes, marked with a yellow rectangle in Figure 5.4. These nodes are determined by assessing the volume changes of fluid channels, which are accessible from **Chapter 4**.

From our FE simulation, we obtain the strain-dependent volume changes and across section area. Due to the large deformation, volume changes play an important role and the Poisson's ratio (ν) is no longer a constant, which is also strain dependent. The ν as a function of strains can be obtained from the FE model. Accordingly, it will be possible to update the deformation factors (φ, φ^*) with respect to the strain. The specific implementation for cooling is performed referring the pseudocode in **Scenario 4**. The sparse matrix **A** and vector **B** in each operation step were filled with the corresponding values according to the sign of mass flow rate (`mdot`) of fluids and the applied strain profiles (`Fapp`). The while sentence controls the main loop, and when the calculation error less than the target value it will jump out the loop and save the final result of performance parameters.

Scenario 4 Algorithm: Large-deformation AER algorithm for cooling in pseudocode

Initialize variables
Input the parameter set **D**, compensation modes **Mode**
Create mass flow `mdot` and applied strain field profiles `Fapp`
Create time-dependent volume change profiles, `Vtnode`
Calling *FindCompenPoint.m* to obtain the compensation spatial nodes set, N_{Com}
do while (`err` $>$ Target)
  Time steps, j=j+1
  Bed geometry
  Calling *DeformingPara.m* to obtain deformation factors φ, φ^*
  if $\dot{Fapp} > 0$ **(compensation blow, upon loading)**
    Assign the fluid temperature on N_{Com} as the hot side temperature $T_{f,h,end}$, solve temperature matrix equation, $AT = B$
  else if $\dot{Fapp} = 0$ and `mdot` > 0 **(cold-to-hot blow)**
    Solve $T = A^{-1}B$, obtain $T_{i,f}$, $T_{i,r}$
  else if $\dot{Fapp} < 0$ **(expelling blow, upon unloading)**
    Regenerate the temperature gradient for T_f, T_r between the temperature T_1 and $T_{N_{1,Com}}$, solve temperature matrix equation, $AT = B$
  else if $\dot{Fapp} = 0$ and `mdot` < 0 **(hot-to-cold blow)**
    Solve $T = A^{-1}B$, obtain $T_{i,f}$, $T_{i,r}$
  end
  if j = `Nx` **(check for convergence)**
    Calculate the energy balance for previous cycle, `Ebalacyc`
    Calculate the numerical error for previous cycle, `err`
    Calculate system performance for previous cycle, `COP, Pcool, Pheat`
    Initialize the time node, j=0
  end
end
Calculate dimensionless parameters, effectiveness, `Nuf, U, Qloss`
Save the results into an array of structures, `S`

5.3 Temperature-dependent elastocaloric behavior

5.3.1 Isothermal tests

In order to include the eCE elastomer material properties into the numerical model (the eCE term in Eq. 5.14), we need to calculate the temperature-dependent ΔT_{ad} and isothermal entropy changes ΔS_{iso} of the elastomers. In general, it can be ob-

tained from temperature-dependent stress-strain profiles. The isothermal mechanical behavior of 3D printed elastomers was measured on a Testrometric Micro 350 tester for 287 to 321 K. The ISO 37 type III standard dogbone printed using NinjaFlex TPU is implemented to the test. Before the isothermal test, dogbone samples were stretched 20 cycles to avoid the Mullins effect and irreversible strains.

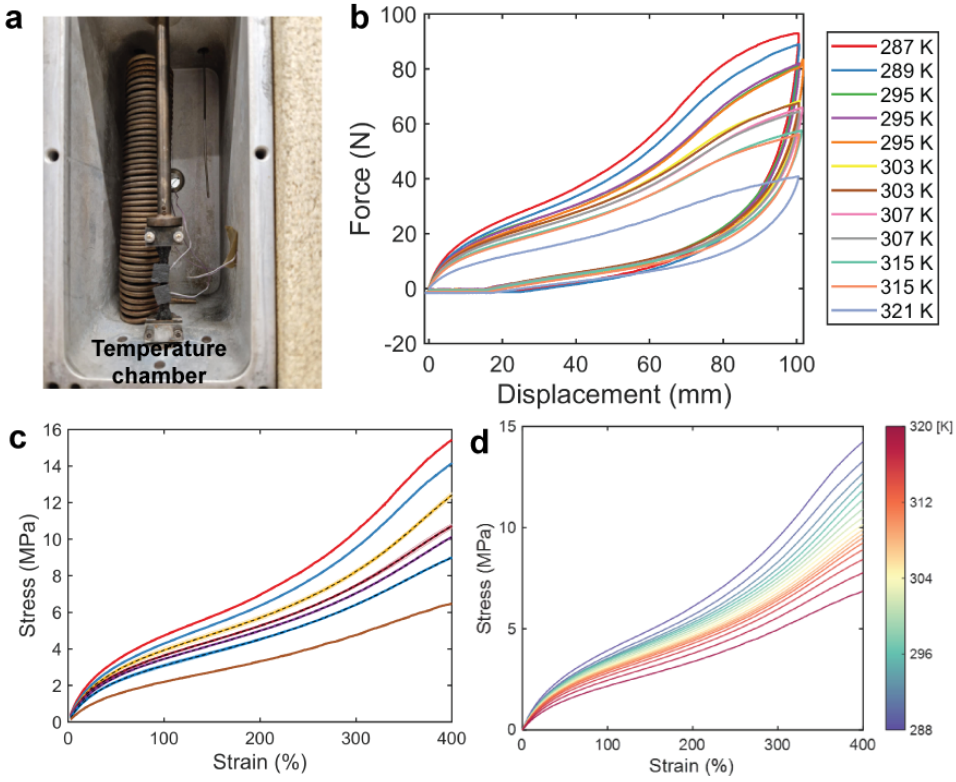

Figure 5.5. Isothermal mechanical test and temperature-dependent mechanical behaviors: ***a****, A mounted sample with the thermocouples stuck on the surface to measure their temperature changes during stretching.* ***b****, Force-displacement curves at different ambient temperatures.* ***c****, Stress-strain curves for the loading process at each temperature.* ***d****, isothermal mechanical behavior profiles in the temperature range of 288-320 K with an identical increment interpolated from* ***c****.*

Figure 5.5a shows the photograph of a 3D printed sample mounted on the tester. We attached some thermocouples on the sample to record the temperature changes. In addition, a thermocouple is placed in the atmosphere close to the sample, which is implemented to monitor the ambient temperature. Mechanical behaviors at different temperatures during a sample loading-unloading process are shown in Figure 5.5b. The stress-strain curves for the loading process are used in the calculation of en-

tropy change and temperature change in a strain range of 0-400%, extracted shown in Figure 5.5c. And then we implemented the linear interpolation for the isothermal stress-strain profiles to obtain more curves for the calculation.

From the isothermal mechanical characterization, a significant hysteresis was observed in the stress-strain curves, which is probably resulting from the strain-induced SIC in polymers. There is no stress plateau observed in both the loading and unloading processes, which is commonly presented in SAMs owing to the austenitic-martensitic transformation [18]. For the TPU loading process, the stress-strain curves exhibit a significant temperature dependence. However, for the unloading process, the curves show almost temperature independent and some crossover curves are observed, leading to the positive adiabatic temperature changes, which is in opposite sign compared to the real measurements for eCE. This might be a result of the complicated mechanical behavior of TPU, such as creep, relaxation, and softening. It has also been observed in other isothermal tests for natural rubbers [97], and some of them are less temperature dependent for the loading process. Therefore, we only employed the stress-strain behavior of the loading process for the following calculation.

5.3.2 Isothermal entropy changes and adiabatic temperature changes

According to the Maxwell relations, the isothermal entropy change from the initial strain to the final strain can be calculated by:

$$\Delta S_{\text{iso}} = -\frac{1}{\rho}\int_{\varepsilon_0}^{\varepsilon}\left(\frac{\partial\sigma}{\partial T}\right)_{\varepsilon} d\varepsilon \tag{5.18}$$

In analogy to the methods implemented to calculate the adiabatic temperature changes in SAMs, the ΔT_{ad} as a function of temperature can be obtained from a total entropy-temperature diagram. The temperature-dependent isothermal entropy changes at different strains of TPU are calculated using the Eq. 5.18, as shown in Figure 5.6a. We can employ the total entropy at zero applied strain as a baseline to deduce the entropy-temperature profiles under different strains as follows (see details of the method [196]):

$$S_{\text{tot}}\left(T_0\right)_{\varepsilon=0} = \int_{T_0}^{T}\frac{c_{p,\varepsilon=0}(T)}{T}dT, \tag{5.19}$$

$$\begin{aligned} S_{\text{tot}}(T)_{\varepsilon} &= \int_{T_0}^{T}\frac{c_{p,\varepsilon}(T)}{T}dT + S_{\text{tot}}\left(T_0\right)_{\varepsilon=0} \\ &= \Delta S_{\text{iso}}\left(T\right)_{\varepsilon} + S_{\text{tot}}\left(T_0\right)_{\varepsilon=0}, \end{aligned} \tag{5.20}$$

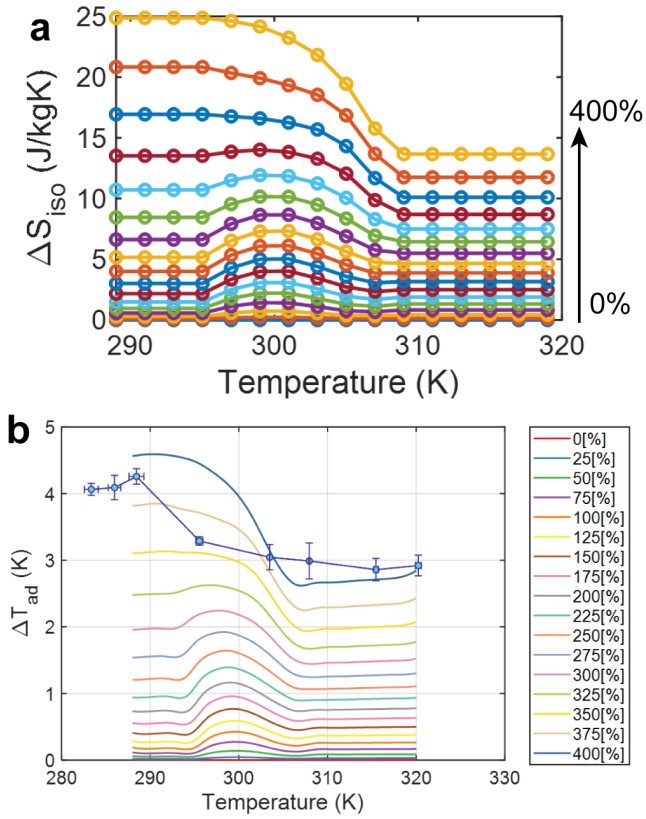

Figure 5.6. Temperature-dependent entropy changes and adiabatic temperature changes of 3D-printed NinjaFlex TPU:
***a**, Temperature-dependent Isothermal entropy changes at different applied strains. **b**, Calculated adiabatic temperature change profiles from the total entropy-temperature diagram and the experimental measured temperature changes at 400%.*

And the corresponding adiabatic temperature changes as a function of temperature can be calculated by:

$$\Delta T_{\mathrm{ad}} = T_2\left(S_{\mathrm{tot}}, \varepsilon\right) - T_1\left(S_{\mathrm{tot}}, \varepsilon = 0\right), \tag{5.21}$$

from the entropy-temperature diagram, as shown in Figure 5.6b. Compared to the measured temperature change at 400% strain, the calculated ΔT_{ad} at 400% shows a good agreement with the experiments.

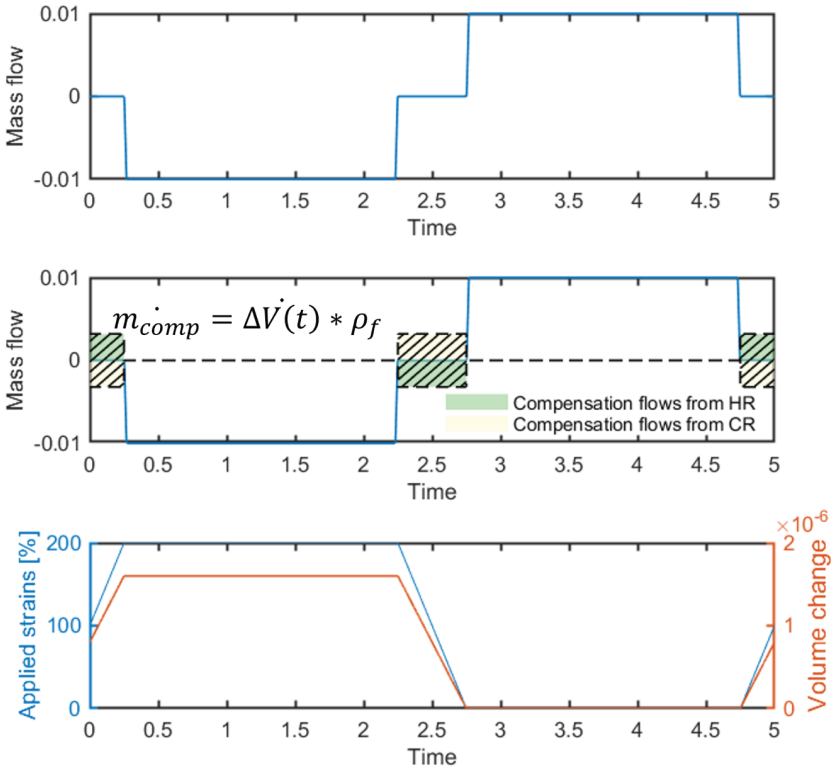

Figure 5.7. Schematic phases for the mass flow rate, compensation flow rate, and the applied strain over a thermodynamic cycle.

5.4 Mass flow rate diagram and analysis for the volume-varied regenerators

The fluid mass flow rate is a crucial variable in the energy equations, and it can be implemented, to indicate the states of the hot/cold heat-transfer blows. It acts as an indicator for the numerical AER model to identify the compensation process and to perform the corresponding compensation-blow calculations, which have been implemented in the above pseudocode. A typical fluid mass flow rate profile in an active cycle period is shown in Figure 5.7. Moreover, we establish a distinct mass flow rate profile for compensation blows, which is synchronized with the loading and unloading processes of the strains, as shown in the second graph in Figure 5.7, which is synchronized with the loading and unloading processes of strains. If compensation

is operated from the hot reservoir (green), during the loading process, the sign of mass flow rate is positive, which indicates compensation blow from HR. During the unloading process, the sign is negative, which indicates expelling blow to HR. If it compensates from cold side, it will be in the opposite sign (yellow). The last graph is about the applied strain as a function of time. According to the simulation for the volume change of fluid channels, we can obtain the relationship of volume changes and strains as shown in **Figure 4.4d**. The simulated results are approaching to linear, therefore, we can obtain the volume change at each strain shown in Figure 5.7 and the time-dependent volume change. Here, we neglect the rate dependence and relaxation properties of TPU, as we found the volume change has less rate dependence among the a loading rate range of 0.1-1 s^{-1} and the experimental operation is expected within these loading rate range.

We constructed two types of microchannel regenerators for the numerical simulation, which are the same regenerators implemented in the FE simulation in **Chapter 4**. One is the parallel-plate (PP) channel and another one is the square channel. The main parameters of large-deformation AER, implemented in the numerical modelling, are listed in Table 5.1. The applied strain inputted to the model is normalized by subtracting the irreversible strain. Because this irreversible strain causes the mechanical buckling for the regenerator. During the practical operation, we operate a regenerator in a higher strain range. For instance, a 3D printed regenerator was operated in a strain range of 200-600%, and the normalized strain was determined to 400%.

Table 5.1. Main input parameters for 3D-printed soft regenerator simulations.

Parameter	Values
Regenerator1	Parallel-plate microchannel
Regenerator2	Square microchannel
Material	TPU (NinjaFlex)
Ambient temperature, T_{amb}, [K]	296
Hot side temperature, T_H, [K]	296
Material density, ρ_s, $[kg/m^3]$	1235
Applied strain (normalized), ε, $[-]$	400%
Regenerator volume, V_R, $[mm^3]$	913.65 (parallel-plate), 1091.5 (square)
Regenerator width, d_R, [mm]	20
Regenerator height, d_R, [mm]	5
Total initial length, L_0, [mm]	15
Channel size, D_c, [mm]	0.64 (thickness, parallel-plate), 0.64 (square)
Temperature span, ΔT, [K]	$2-5$
Operating frequency, f, [Hz]	$0.0833-0.2$
Hydraulic diameter, d_h, [mm]	1.28 (parallel-plate), 0.64 (square)
Porosity, ε, $[-]$	39.1% (parallel-plate), 27.23%(square)
Thermal conductivity, k_s, $[W/(m \cdot K)]$	0.2

5.5 Comparison of volume compensation mechanism

To determine the suitable direction for compensation in elastocaloric cooling, we compare two schemes: 1) hot reservoir compensation (HR scheme); 2) cold reservoir compensation (CR scheme). The comparison is based on a PP channel regenerator, which has significant volume changes induced by large strains.

The numerical modeling was carried out under a series of mass flow rates at a frequency of 0.1 Hz. The volume change of PP channels at 400% was determined to 69% from FE simulation and was inputted into the model. The temperature span (temperature difference between the HR and CR) was set as 2 K. The simulated results of the cooling power and COP are shown in Figure 5.8. In the numerical model the cooling power and COP are calculated as follows:

$$\dot{Q}_c = f \int_0^\tau \dot{m}_f c_f \left(T_{f,c,\,\mathrm{out}} - T_{f,c,\,\mathrm{in}} \right) dt \tag{5.22}$$

$$COP = \frac{\dot{Q}_c}{\dot{Q}_h - \dot{Q}_c} \tag{5.23}$$

Under identical operating conditions, it is evident that the cooling power and COP of the CR scheme are consistently negative. This signifies its inability to reach a 2 K temperature span. However, the HR scheme exhibits a 2 K temperature span for elastocaloric cooling at a lower mass flow rate, as indicated by the red circles. The maximum cooling power, reaching 0.69 W, occurs at a mass flow rate of 0.15×10^{-3} kg/s. As a result, this indicates the preference for selecting the hot reservoir for fluid compensation in elastocaloric cooling applications. Subsequently, our numerical modeling and experimental design are based on the HR scheme.

5.6 Parametric investigation of the regenerator

When operating an active regenerator as a cooling device, its cooling performance can be influenced by multiple parameters, such as operating frequency, mass flow rate (or Utilization), hot reservoir temperature (T_H), applied strain, etc. The presented numerical model encompasses the mentioned parameters, enabling a comprehensive examination of their effects on regenerator performance. Two typical regenerators, featuring PP and square channels, are chosen for analysis. The large-strain induced volume changes, calculated as 69% and 41% based on finite-element simulations for the PP and square regenerators, respectively, are input into the numerical model. In this context, the hot side temperature T_H is set equal to the ambient temperature at 296 K. Our main objective is to explore regenerator performance under varying frequencies, mass flow rates, and temperature spans, with the aim of identifying the optimal operational conditions. Examining the cooling power depen-

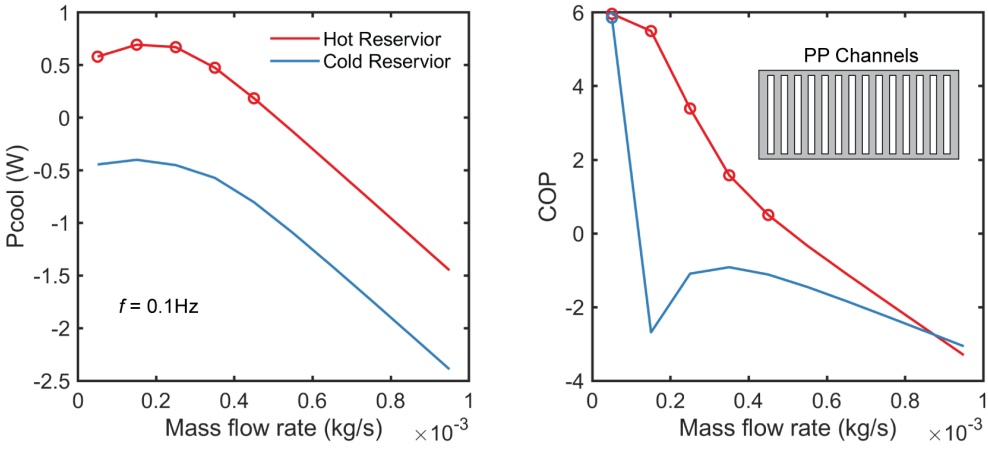

Figure 5.8. Comparison of the cooling power and COP for compensating from hot reservoir and cold reservoir at a 2 K temperature span based on a PP channel regenerator.

dence on temperature span enables us to predict the attainable maximum temperature span by the regenerator during elastocaloric cooling.

Figure 5.9 displays the cooling power and COP results of a PP channel regenerator operating at two frequencies of 0.06 and 0.1 Hz. The mass flow rate is varied for each frequency across different temperature spans to assess the performance. As the mass flow rate increases, the COP decreases, while the cooling power initially rises and subsequently decreases. If the set temperature span cannot be achieved, there will be a negative cooling power or COP which has been removed from the figure. As a result, an increase in the temperature span corresponds to a decrease in both the maximum cooling power and COP. Furthermore, a higher frequency is found to achieve a higher maximum cooing power at the optimal mass flow rates. For instance, at a same temperature span 3 K, the maximum cooling powers at frequencies of 0.06 Hz and 0.1 Hz are 0.12 W and 0.31 W, respectively. Notably, the maximum COP at 0.1 Hz is 1.8, surpassing the value of 1.0 attained at 0.06 Hz.

Figure 5.10 shows the results of the square channel regenerator that was simulated at different temperature spans from 0.5 K to 5 K. Based on the maximum cooling power, the optimal mass flow rate for the lower frequency is about 0.175×10^{-3} kg/s, which is increasing to 0.3×10^{-3} kg/s for the frequencies of 0.1 Hz and 0.13 Hz. It is because the higher frequency requires more fluid to extract heat from the regenerator. The predicted maximum cooling power is decreasing with temperature span increase, and in a same manner if the temperature span is not achievable the cooling power and COP will be negative. At an identical temperature span at 3.2 K, the maximum cooling power is obtained to be 0.43 W, 0.51 W and 0.65 W for the frequency from 0.08 Hz to 0.13 Hz. When the frequency increases from 0.08 Hz to 0.13 Hz, the maximum COP is also increasing from 4.58 to 5.25. At this temperature span,

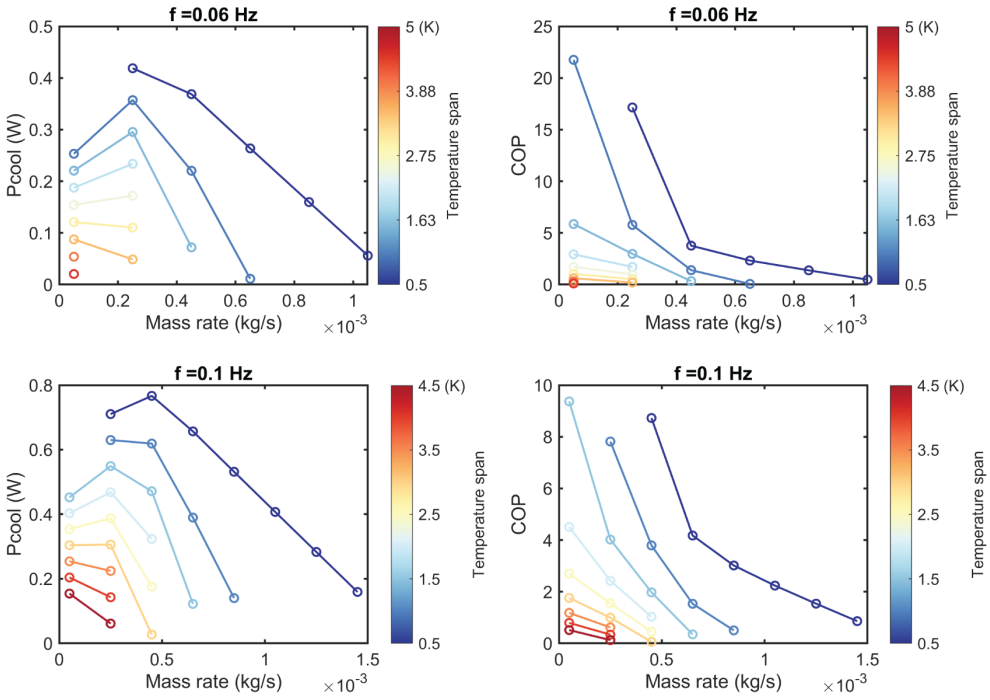

Figure 5.9. Cooling power and COP results of the PP regenerator operating under different frequencies and mass flow rates at varying temperature spans.

it indicates that the higher frequency favors to an improved cooling performance of the regenerator. However, we noted that the optimal mass flow rate for the COP is at a lower value of 0.175×10^{-3} kg/s for the frequencies of 0.1 Hz and 0.13 Hz. It maybe the reason that displacing the more heat transfer fluid probably improves the cooling power, whereas it requires more pump work which reduces the efficiency.

5.7 Predication of maximum temperature span

Both the maximum cooling power and temperature span serve as equally important indicators of the prototype's performance. The cooling power of the PP and square regenerators at varying temperature spans has been mapping out under different operating parameters, which allows us to predict the potential maximum temperature span that can be achieved by the optimization for Utilization. The simulation results provide information on the cooling power in relation to the temperature span. Typically, a linear relationship exists, allowing for linear extrapolation of the results to obtain the maximum temperature span and cooling power. As illustrated in Fig-

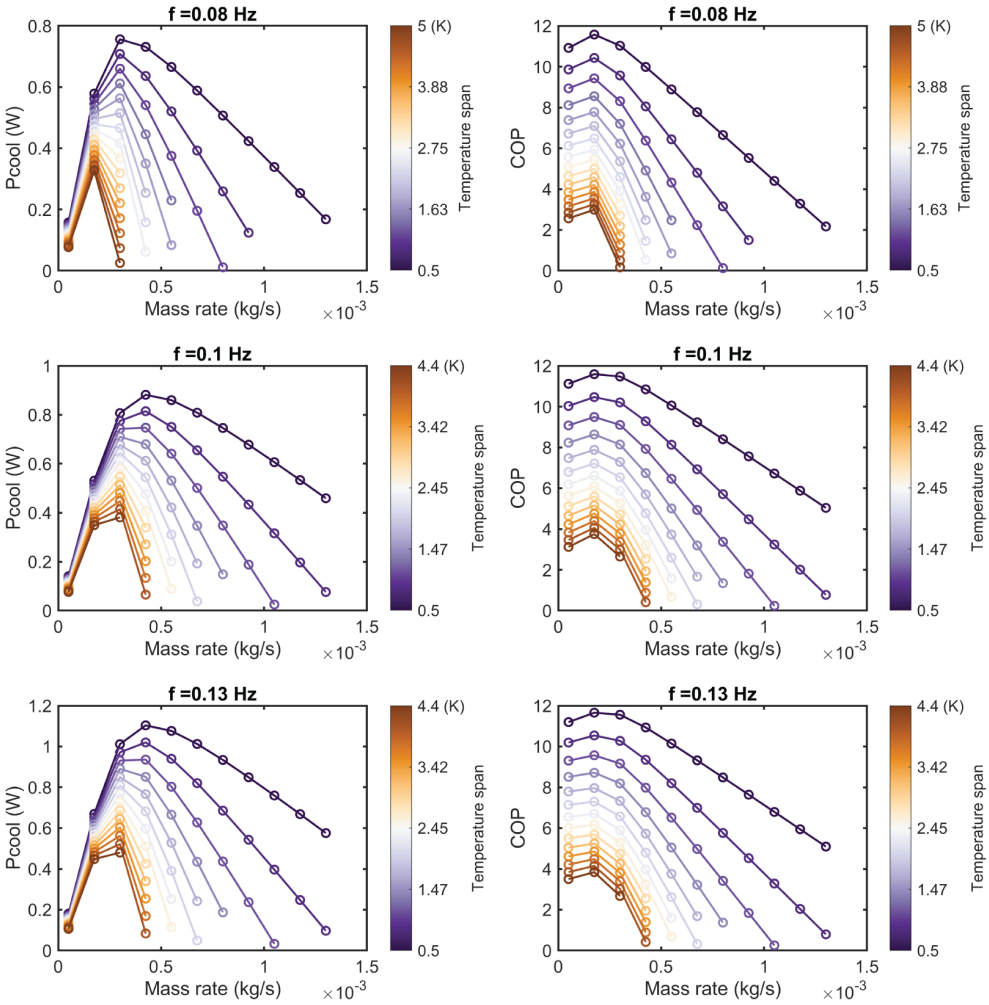

Figure 5.10. Cooling power and COP results of the square regenerator operating under different frequencies and mass flow rates at varying temperature spans.

ure 5.11, the cooling power is displayed as a function of temperature span under different Utilization at an operating frequency of 0.1 Hz for the square channel regenerator. The data exhibits a suitable linear fit. This linear fitting enables the determination of the maximum cooling power $\dot{Q}_{c,max}$ at zero temperature span and the temperature span $\Delta T_{span,max}$ at zero cooling power. The method of linear extrapolation has also been applied in the evaluation of $\dot{Q}_{c,max}$ and $\Delta T_{span,max}$ in the study by Qian et al. [22]. For the active regeneration, Utilization is generally related to

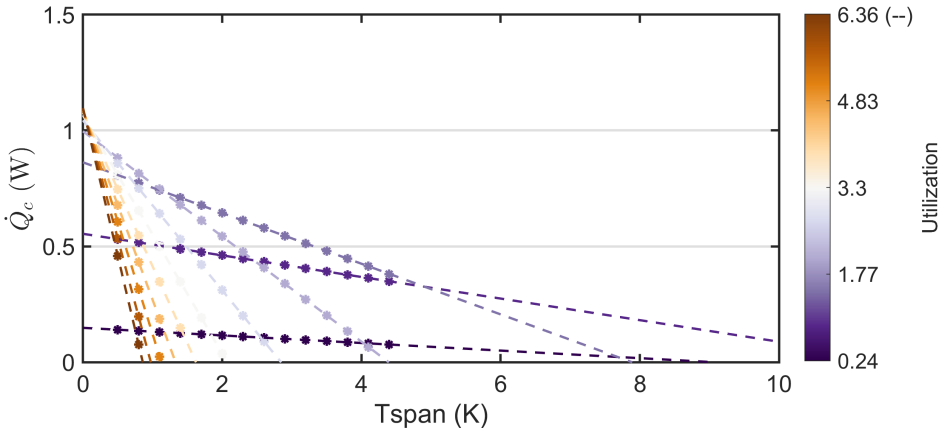

Figure 5.11. Linear fitting for the cooling power and temperature span (dots) under different Utilization in which the maximum cooling power $\dot{Q}_{\mathbf{c,max}}$ and temperature span $\Delta T_{\mathbf{span,max}}$ can be obtained by linear extrapolation.

the fraction of elastocaloric heat extracted from the regenerator by the fluid, which is defined as:

$$U_0 = \frac{\int_0^{\tau/2} \dot{m}_f c_f dt}{m_s c_s} = \frac{V_{\text{pump}} \rho_f c_f}{m_s c_s}. \tag{5.24}$$

where $\dot{m}_f$ is the mass flow rate of the heat transfer fluid, and τ represents the period of an active cycle. Due to the same duration implemented for the heat rejection and heat absorption processes, the half of period time is used for the integration. The volume change of regenerator channels is not accounted in this definition, which can avoid the variation in determining the optimal Utilization associated with the volume changes, mentioned in **Chapter 4**. Yet, the corresponding volume changes are included into the model at each given applied strain. In this way, we can assess the optimal Utilization for achieving the maximum temperature span. Here, we also define another Utilization which takes account compensation fluids into the heat transfer fluid periods, which can be expressed as:

$$\begin{aligned} U &= \frac{\int_0^{\tau/2} \dot{m}_f c_f dt + \frac{1}{2} \int_0^{\tau/2} \dot{m}_{comp} c_f dt}{m_s c_s} \\ &= \frac{(V_{\text{pump}} + 0.5 V_{\text{chan},0} \delta V) \rho_f c_f}{m_s c_s}, \end{aligned} \tag{5.25}$$

in which the $V_{chan,0}$ is the initial fluid channel volume and the δV is the volume change ratio which has been defined in **equation 4.11**. As the compensation fluid

participate the heat transfer only during the cold blow, extracting eCE heat to the hot side, a half amount of compensation fluids contributes to the heat transfer in an active cycle. It is similar to the definition for the heat transfer volume ratio of active regeneration in **equation 4.13** in **Chapter 4**. For the predication of maximum temperature span, we neglect the volume change effect on the Utilization, where the U_0 is employed.

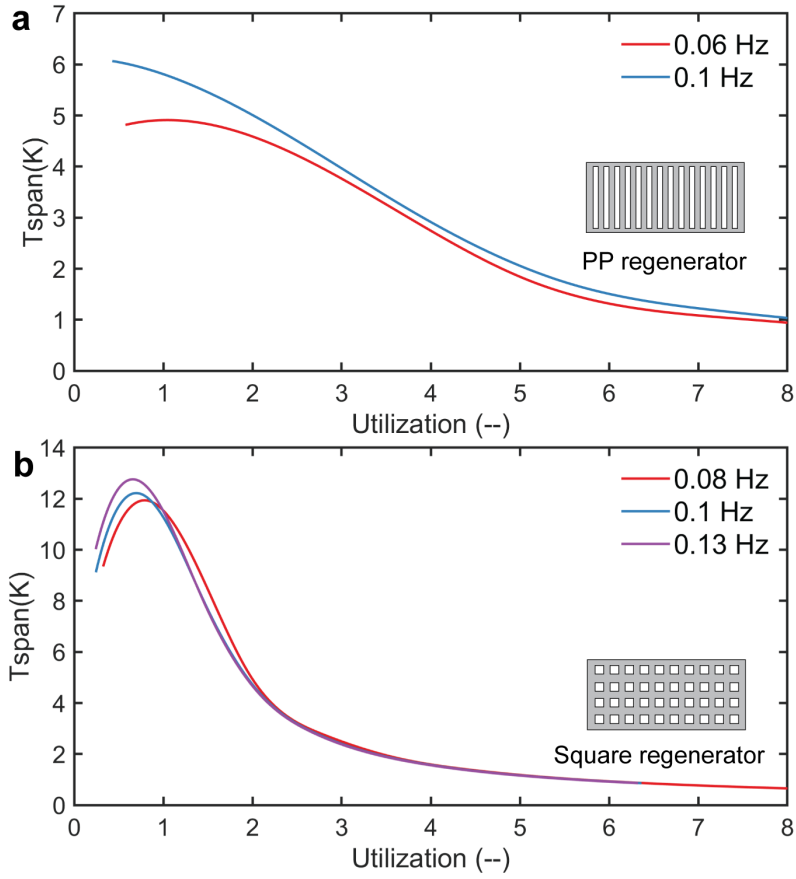

Figure 5.12. Predicted maximum temperature span as a function of Utilization operating under different frequencies for the PP and square regenerators.

Figure 5.12 **a** and **b** depict the temperature span as a function of Utilization for the PP and square regenerators, respectively. These plots are obtained from linear fitting for the relationship of the cooling power and temperature span. For the PP regenerator, the maximum temperature span of 6.1 K can be attained at a Utilization of 0.43 at 0.1 Hz. However, at a lower operating frequency of 0.06 Hz, the maximum

temperature span of 4.9 K is achieved with a higher U_0 of 1.1. For the square regenerator, the maximum temperature span is improved to 12.8 K which is operated under a Utilization of 0.65 and frequency of 0.13 Hz. The observation indicates that an increase in frequency results in a higher temperature span, and correspondingly, the optimal Utilization should be reduced. For instance, when the frequency is 0.08 Hz, the optimal U_0 is 0.70, achieving a maximum temperature span of 11.9 K.

5.8 Summary

In this chapter, the 1D modelling for the large-deformation elastocaloric regenerator has been developed. In this numerical model, introducing the stretch ratio λ and deformation factors φ, associated with the varied spatial length of the regenerator and the large-strain induced volume changes, facilitates the study of large-deformation active elastocaloric regenerators. The relationship between λ and φ of a regenerator can be determined by FE simulations, which provides the information of the deformed geometries and associated volume changes of regenerators.

For cooling implementation, the volume compensation from the hot and cold sides is compared. The results indicate that the compensation from the hot reservoir is more suitable for cooling applications. This finding guides the construction of our experimental setup, emphasizing the need to manage compensation flow from the hot side to the regenerator, during the loading process. Furthermore, a comparison between two regenerator geometries, one with PP channels and the other with square channels, was conducted. The square regenerator exhibited superior cooling performance, manifesting in a higher temperature span and cooling power after parametric optimization. This superiority may be attributed to the square regenerator having more elastocaloric material (eCM) mass, even though its porosity is comparatively lower than the PP regenerator. This suggests the importance of balancing regenerator porosity with sufficient eCM mass during the regenerator design.

CHAPTER 6

Active elastocaloric cooling system based on 3D-printed soft regenerators

In order to experimentally explore the performance of 3D-printed regenerators with significant deformations, we designed a regenerative elastocaloric system capable of passive compensation for volume changes in regenerator channels during stretching. Three regenerators with distinct microchannels were employed for this investigation. The significant volume changes in fluid channels, which lead to asymmetry in fluid exchange during an active cycle, were numerically studied and analyzed in previous chapters. This phenomenon has the potential to diminish the cooling performance of the active regenerator.

This chapter focuses on the experimental study of the impact of volume changes induced by large deformation on regenerator performance. Additionally, we conducted optimization of operating parameters, including strain ranges, frequency, and Utilization. The influence of geometry on regenerator performance was investigated by comparing different types of regenerators under varying Utilization conditions.

This chapter is related to article III in **Appendix A**.

6.1 Regenerator preparation

The regenerator used in the experimental study is 3D printed using commercial FilaFlex TPU, which is the same type of TPU utilized for the volume change measurements in **Chapter 4**. As shown in Figure 6.1, we designed three distinct active elastocaloric regenerators with different microchannels, namely REG1, REG2, and

REG3. These regenerators are expected to be fully 3D printed, including the heat-transfer channels, connection ports (the extruded short tubes) and clamped heads in a dogbone-like shape, avoiding stress concentration during stretching. REG1 and REG2 have the same dogbone shape with porosities of 39.1% and 27.2%, respectively, which is consistent with the regenerators used in the 1D numerical modeling and volume change investigation. In contrast, REG3 is designed with a thicker regenerator wall and a lower porosity of 19.4%. Typically, the dogbone regenerator REG3 has a gauge length of 20 mm and a width of 15 mm, while the other two regenerators each have a length of 15 mm and a width of 20 mm. All regenerators have an identical thickness of 5 mm, ensuring they have the same volume in the middle active zone of the dogbone regenerator but only differ in their aspect ratios. Afterwards, the elastocaloric regenerators based on these 3D models are manufactured using 3D printing and Cura 5.2 to generate the required printing G-code. In addition, the samples employed in the mechanical tests are 3D-printed into the geometry of a standard ISO 37 Type III sample, with a thickness of 3 mm.

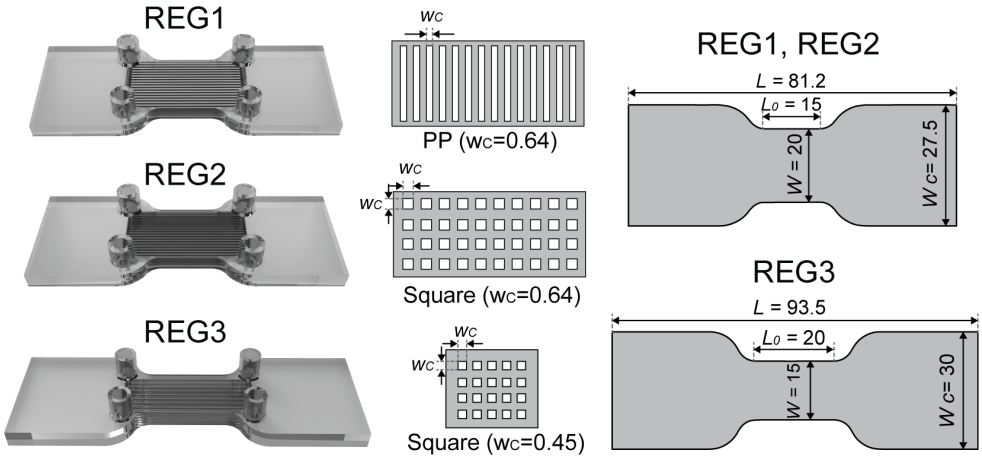

Figure 6.1. 3D-printed elastocaloric regenerators with different microchannels, namely REG1 (parallel-plate channel), REG2 (square channel), REG3 (square channel with wider surrounding thickness). The dimensions are denoted in millimeters. Note that the actual channel numbers for REG1, REG2, and REG3 are 18, 18×5, and 18×4, respectively.

6.2 3D printed elastomers and mechanical stability

We study the elastocaloric performance of the 3D printed TPU elastomers associated with the evolution steps of molecular chain strain-induced crystallization (SIC), as

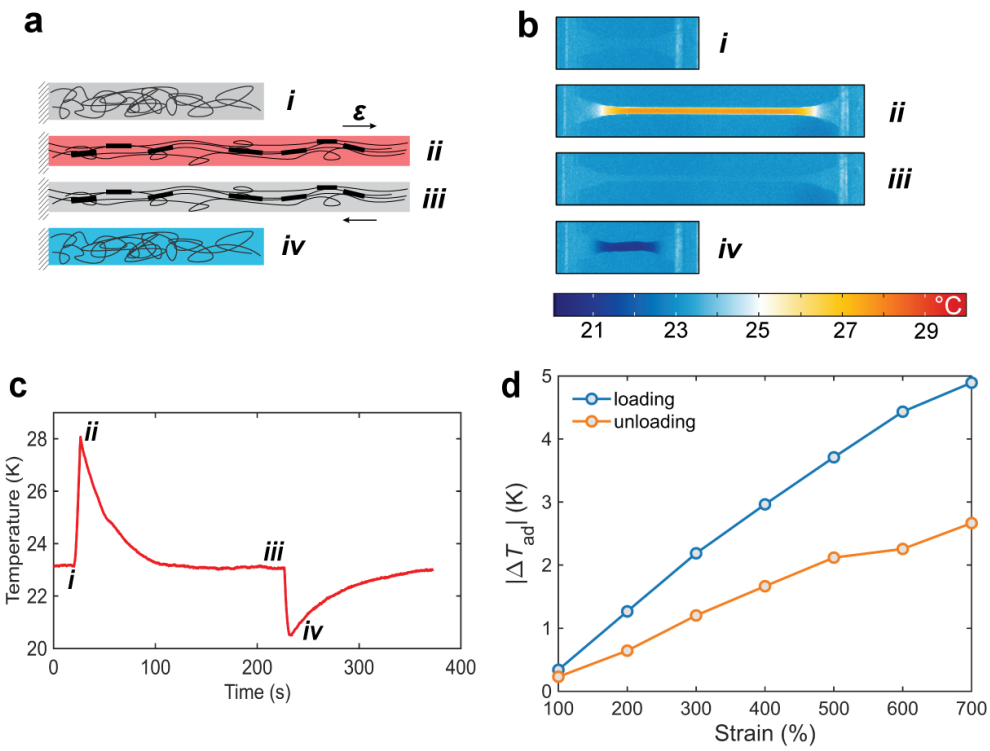

Figure 6.2. Elastocaloric properties for the 3D-printed eCE elastomers:
***a**, Schematic molecular chain state evolution over four states, between the disordering and strain-induced crystallization (black blocks) during adiabatic loading and unloading. Different colors refer to the heating (red) and cooling (blue) of polymers driven by SIC, and grey represents ambient temperature. **b**, IR images of counterpart SIC states from i to iv for 3D-printed elastomeric samples; **c**, Temperature change of 3D-printed elastomers over an eCE cycle. **d**, Adiabatic temperature change as a function of strain for 3D-printed elastomers during the loading and unloading process in relation to the measuring method in **c**.*

shown in Figure 6.2a, which has been discussed in Chapter 3. The infrared images in Figure 6.2b and the corresponding temperature-time profile in Figure 6.2c illustrate the temperature increase and decrease in response to adiabatic loading and unloading for the printed elastomers under a 600% strain. Following the loading process ($i \rightarrow ii$), the temperature reaches equilibrium with the ambient ($ii \rightarrow iii$). Subsequently, upon releasing the applied strain, a temperature decrease is observed ($iii \rightarrow iv$). The temperature change as a function of strains is measured from 100% to 700%, as shown in Figure 6.2d. The temperature change of printed elastomers at 600% during loading is 4.43 K, whereas upon unloading, it is lower (2.26 K) due to

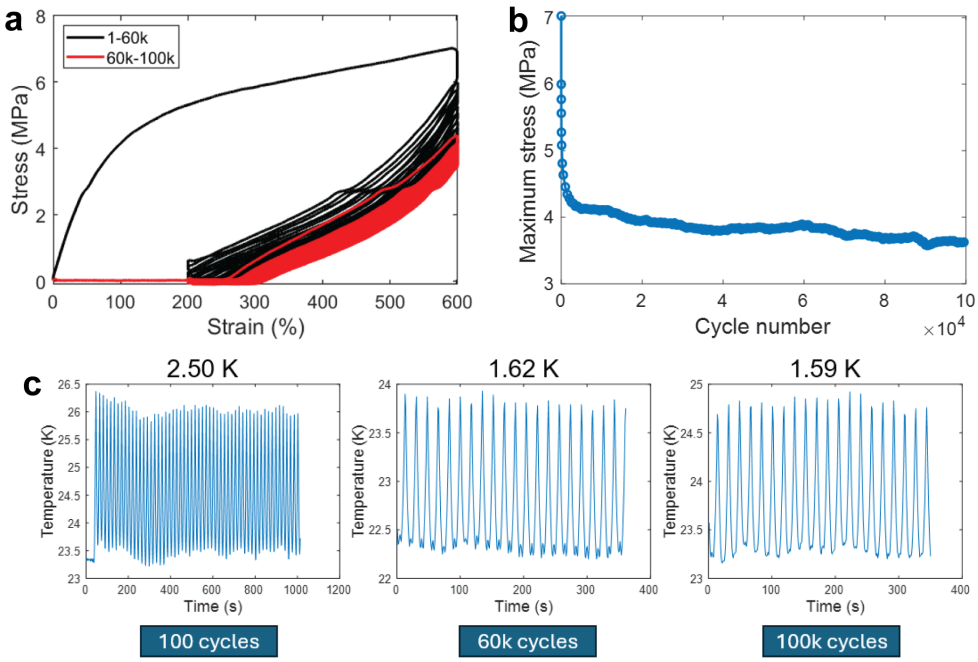

Figure 6.3. Mechanical and elastocaloric stability of the 3D-printed eCE elastomers: ***a****, Stress-strain behavior of 3D printed elastomer over* 10^5 *cycles in the strain range of 200-600%;* ***b****, The maximum applied stress as a function of cycle numbers obtained from a strain range of 200-600%;* ***c****, Cyclic temperature changes of 3D-printed elastomers at different cycle numbers.*

the partial relaxation/creep of SIC, which is also observed in other eC elastomers [57, 157]. Due to the existing irreversible deformation, the applied strains return to a pre-strain 200% , which remains within the realm of the SIC phase transition.

Additionally, the fatigue life and mechanical stability are crucial for constructing an active elastocaloric regenerator based on these 3D printed elastomers. The 3D printed dogbone undergoes a long-term cyclic test, as shown in Figure 6.3a. Here over 10^5 cycles are endured without mechanical failure within a 200-600% strain range at 1 s^{-1} strain rate. The maximum applied stress decreases with the cycle number increase, as depicted in Figure 6.3b, which is decreased from 7 MPa at the first cycle to 3.7 MPa by the 10^5 cycle. Moreover, the elastocaloric stability over this large number of cycles is also investigated. The corresponding cyclic temperature changes are recorded after 100, 6×10^4, and 10^5 cycles. The results show a $\sim$0.9 K decrease in cyclic temperature change after 10^5 cycles, probably resulting from a decrease in applied stress. Nevertheless, this 3D-printed elastomer maintains a temperature change of 1.59 K, which is comparable to some magnetocaloric materials.

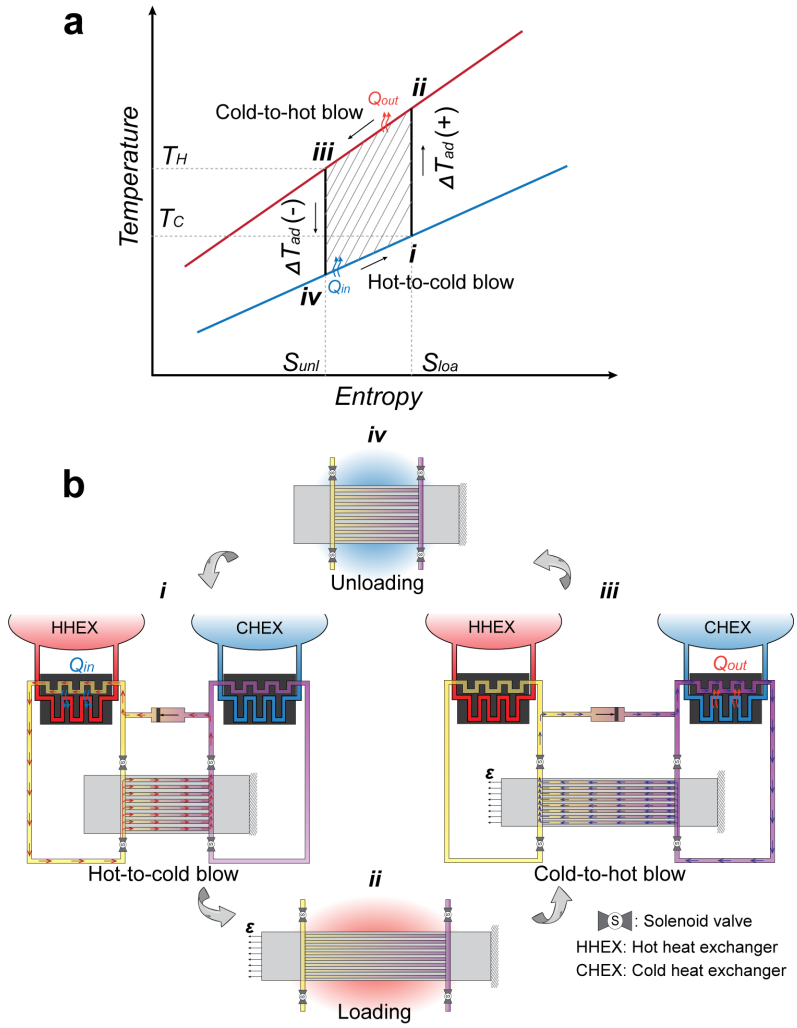

Figure 6.4. Illustration for the 3D-printed soft regenerative eC cooling:
***a**, A Brayton-based temperature-entropy diagram for a regenerative elastocaloric cycle from i to iv, where (+) and (-) represent temperature increase and decrease; Q_h and Q_c represent the rejected heat and absorbed heat, respectively. T_h and T_c are the temperatures of the hot side (heat sink) and cold side (heat source), respectively. The enclosed area denoted by the infilled line refers to the input mechanical energy. The ii→iii (cold blow) and iv→i (hot blow) processes involve active fluid flow periods for heat transfer. **b**, Schematic operation of an active elastocaloric regenerator subjected to the four processes shown in **a**. There are fluid channels inside the regenerator, and the regenerator is heating and cooling with the strain loading and unloading accordingly. A movable piston pumps the heat-transfer fluid, and the flow path is controlled by solenoid valves. The warmed fluid from the cold blow rejects heat to the hot side heat exchanger (HHEX), and the cold fluid from the hot blow absorbs heat from the cold side heat exchanger (CHEX).*

6.3 Active elastocaloric cooling system

A regenerative elastocaloric thermodynamic cycle based on a reversible Brayton-based cycle is illustrated using the temperature-entropy (*T*-*S*) diagram in Figure 6.4a. The steps from *i* to *iv* are analogous to the steps of a material cycle in Figure 6.2. Upon stretching, the regenerator temperature increases for $i \rightarrow ii$, related to the state *ii* in Figure 6.4b, which shows an active elastocaloric regenerator operating during a regenerative cycle associated with the *T*-*S* diagram. When the strain is released, the regenerator temperature decreases for $iii \rightarrow iv$, related to the state *iv* in Figure 6.4b. Steps of $ii \rightarrow iii$ and $iii \rightarrow iv$ in a material cycle take place through natural convection with surroundings. In contrast, the active regeneration contains reciprocating fluid flows for heat transfer during these two processes, which are provided by a fluidic displacer or a pump. The $ii \rightarrow iii$ process (cold-to-hot blow) refers to an active heat transfer fluid flow from the cold side (heat source) to the hot side (heat sink), and the $iii \rightarrow iv$ process (hot-to-cold blow) refers to fluid flow from the hot side to the cold side, simply named cold blow and hot blow, respectively. Afterward, the heated fluid from the cold blow passes through the hot heat exchanger (HHEX), absorbing heat from the heat sink. Similarly, the cooled fluid from hot blow passes through the cold heat exchanger (CHEX), releaseing heat to the heat resource. The T_H and T_C represent the temperatures of hot and cold sides.

6.4 Volume compensation system for regenerative elastocaloric cooling

Soft elastocaloric regenerators undergo significant volume changes in their fluid channels due to the required large deformation. As shown in Figure 6.5a, during the loading process $i \rightarrow ii$, the fully-filled fluid channels after the hot blow are subjected to a large strain. The increased volume inside the channel equals $V_f - V_i$, which is compensated from the hot side. The compensating blow is illustrated using the dash arrows. The regenerator warms up due to the elastocaloric effect, and hence, the cold blow extracts the eCE heat from the regenerator. For the unloading process $iii \rightarrow iv$, the extract volume produced by the loading process is passively expelled out to the hot side. Operating the compensation blows to the hot reservoir is according to the numerical results obtained in **Chapter 5**, which suggests a higher performance for the cooling application.

Based on our previous FE model for the volume change predication, we conduct the FE modelling for these three regenerators to predict their fluid channel volume changes at different applied strains. The volume change ratio is implemented to describe the volume changes defined as:

$$\delta V = \frac{V_f - V_i}{V_i} \times 100\% \tag{6.1}$$

The predicted results for REG1, REG2, and REG3 are shown in Figure 6.5b and the inset shows the deformation of parallel-plate channels undergoing stretches. The δV of REG1 fluid channels is superior to the others, which results from the transverse buckling of the parallel plate channels under a large axial elongation. This phenomenon has been discussed in **Chapter 4**. At a 600% strain, the δV of REG1 reaches 101.7%, and the values for REG2 and REG3 are 71.4% and 76.3%, respectively. If the regenerator is operated in a 200-600% strain range, the volume change ratio can be normalized by subtracting the δV at 200%. In fact, the amount of volume change depends on their initial volume. Among them, the REG3 has a smallest initial fluid channel volume due to its lowest porosity. The volume change amount associated with their initial volumes under a strain range from 200% to 600% can be calculated for REG1, REG2, and REG3 from Figure 6.5b, respectively.

Accordingly, we construct a elastocaloric cooling flow system capable of compensating these large-strain induced volume changes, as shown in Figure 6.6. In the flow system, the active heat transfer fluid is provided by two displacers, specifically, the hot displacer for hot blow and the cold displacer for cold blow. The movement is controlled by a linear actuator. The piston stroke of the displacers is related to the mass flow rate of the heat transfer fluid. The hot reservoir temperature is fixed by a heat exchanger, which is connected with a water bath. In the experiments, we set the water bath temperature to 23 °C, and the hot inlet temperature is fixed at 23 °C. For the cooling application, the system can control the compensation from the hot reservoir, which is implemented as follows: during loading, the solenoid valve 4 is open, and the other valves are all sealed, allowing the compensation fluid to passively flow into the regenerator from HR by gravity (because the hot reservoir is mounted at a higher position, see **Figure 2.8**). During unloading, only the solenoid valve 3 is open, and the extra fluid is forced to expel back into the HR. More detailed information regarding this flow system operation is in **Appendix C**. Additionally, to investigate the impact of this volume change on the elastocaloric regenerator performance, the other operation scheme, without the volume compensation, is also performed for comparison. The non-compensation scheme is operated by closing all the valves during the loading and unloading processes, and the hot and cold blows are kept same. There are four thermocouples, namely T1, T2, T3, T4, which are mounted by sequence in relation to the cold inlet, cold outlet, hot outlet, and out inlet, respectively. During the active cycle, the thermocouples can record the temperature profiles at these four ports.

6.5 Impacts of fluid channel volume change on cooling performance

The impact of volume changes on the regenerative cooling performance has been investigated based on a PP regenerator (REG1), which has a significant volume changes under large strains. REG1 is operated under the two above-mentioned

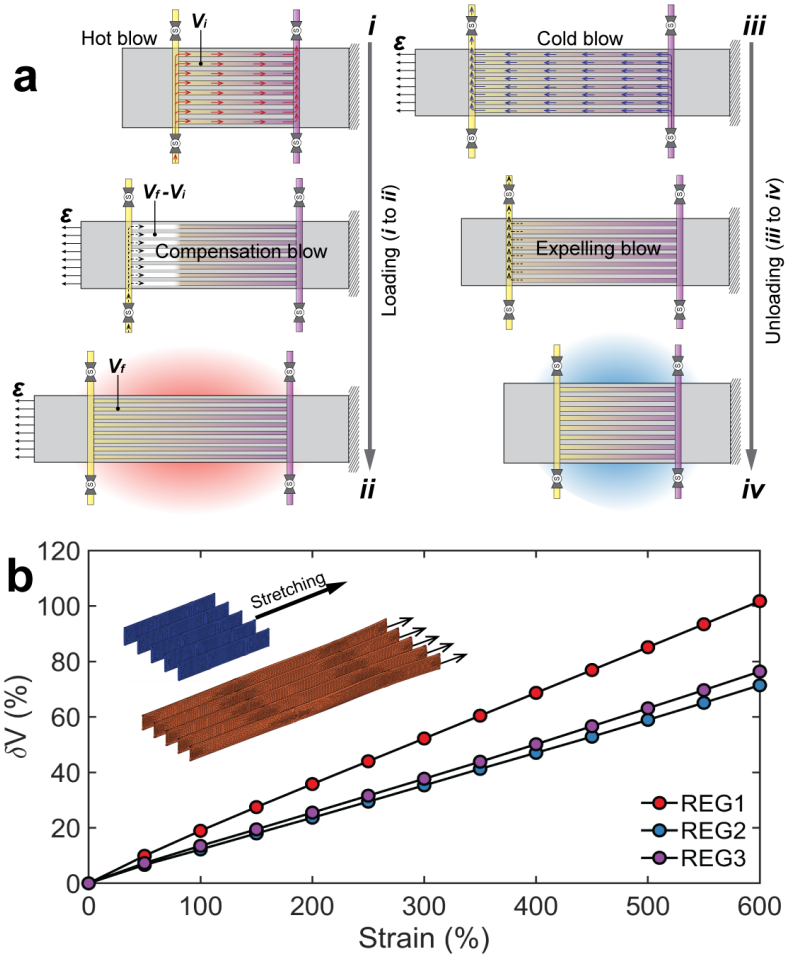

Figure 6.5. High-strain induced volume changes in eC regenerators and impacts on active regeneration:
***a**, Schematic production of fluid channel volume changes and associated volume compensation scheme during an active elastocaloric cycle. **b**, Numerical results of volume change ratio vs applied strains for different regenerator types. The inset shows some selective channels before (blue) and after (orange) deformation for REG1.*

schemes: with and without volume compensation. The temperature profiles for the compensation and noncompensation schemes, when they reach a steady state under a strain range of 200-600%, are plotted in Figure 6.7a. Specifically, one active cycle is utilized to compare the temperature profiles of compensation and noncompensation, in which the loading and unloading zones are highlighted in a cycle. The

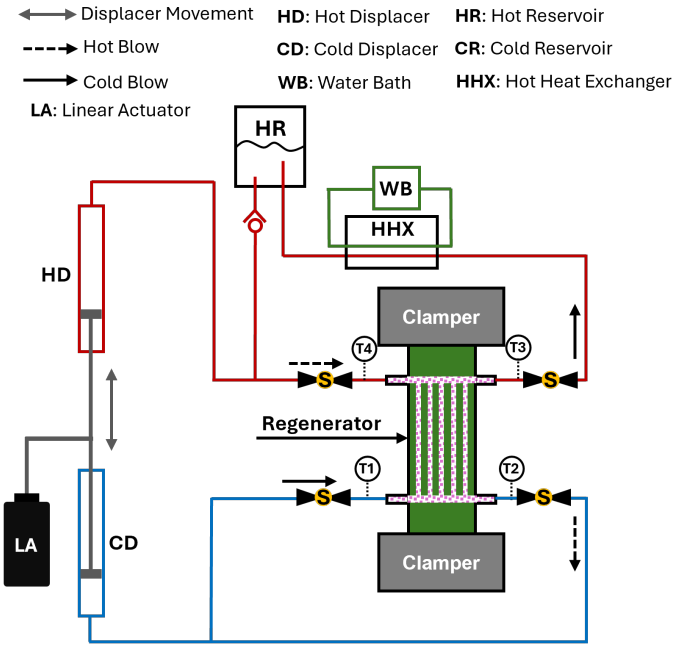

Figure 6.6. A special elastocaloric flow system for the large deformation regenerator with the fluidic compensation.
In the flow system, hot reservoir temperature is determined by the heat exchanger temperature and the hot blow and cold blow are provided by the hot displacer (HD) and cold displacer (CD), respectively. Four thermocouples are mounted separately at the cold inlet (T1), cold outlet (T2), hot outlet (T3), hot inlet (T4). The opening and closing of the corresponding fluid ports are controlled by the four solenoid valves (SVs). In addition, there is a position sensor, which is not shown in this picture, that monitors the regenerator applied strain to trigger the flow system for active hot/cold blows or compensation blows.

associated steps (i, ii, iii, iv) in an active cycle are marked using different color points for the compensation (blue) and noncompensation (grey) temperature profiles. In some time points, they overlap, notably observed at point i in the hot outlet profile (detailed in the inset of Figure 6.7a), represented by the blue point at the top. The primary distinction between these two operation schemes becomes evident during the loading (yellow) and unloading (purple) processes, where volume changes occur.

In the noncompensation scheme, during loading (process $i \rightarrow ii$), the temperature at the hot outlet experiences a sudden decrease (indicated by the dashed line). This decrease is attributed to backflow on the channel top due to the volume increase of channels. In contrast, the temperature remains stable in the compensation scheme, facilitated by the continuous flow of compensation fluid into the regenerator for the hot inlet. During unloading (process $iii \rightarrow iv$), the extra volume in the

fluid channels is expelled into the hot reservoir through the hot outlet for the compensation scheme, where the temperature of hot outlet decreases from the process *iii* to *iv* (see the blue points on the red solid line in the inset of Figure 6.7a). However, for the noncompensation scheme, the temperature from *iii* to *iv* maintains constant, but at the time point *iv* when the valve is open for the hot blow, the temperature of *iv* suddenly drops to the same temperature marked on the compensation temperature curve (blue point), denoted using a brown arrow in the inset. This rapid drop for the noncompensation scheme results from the extra fluid inside the regenerator after unloading, expelling out into the flow system through the hot outlet. The same phenomenon also happens to the hot inlet, where a significant temperature peak is observed at *iv* (orange dash line). Consequently, these unstable fluids produced by the volume change during the loading and unloading processes lead to a comparably lower temperature span in the noncompensation scheme.

Figure 6.7b is a comparison of the elastocaloric cooling temperature span for the compensation and noncompensation schemes under different Utilizations at a frequency of 0.1 Hz in a 200-600% strain range. Here, the temperature span is obtained by averaging temperature difference between the temperature ($T_{h,o}$) of hot outlet and the temperature ($T_{c,o}$) of cold outlet in 10 selected steady cycles.

$$T_{span} = \overline{T_{h,o}} - \overline{T_{c,o}} \tag{6.2}$$

in which $\overline{T_{c,o}}$ and $\overline{T_{c,o}}$ are the average temperature of cold outlet and cold outlet, respectively.

The Utilization with the modification of fluid channel volume changes is implemented with the equation:

$$U = \frac{(V_{\text{pump}} + 0.5V_{\text{chan},0}\delta V)\rho_f c_f}{m_s c_s}, \tag{6.3}$$

in which $V_{\text{chan},0}$ is the initial regenerator channel volume, and V_{pump} is the displaced fluid volume. The discussion on the comparison of this Utilization and a normal Utilization (U_0), given in Eq. 5.24 without volume changes, has been conducted in **Chapter 5**. For the compensation scheme, the temperature span has a less Utilization dependence when U is from 1.4 to 5.7. The temperature span is obtained about 2.1 K. For the noncompensation scheme, the maximum temperature span 1.74 K is obtained under a Utilization of 1.34. It can be seen that the overall temperature span of noncompensation is lower than that of the compensation scheme. Therefore, we conclude that the volume compensation scheme can avoid the imbalanced heat-transfer fluid flow during regenerative elastocaloric cooling, which facilitates an improved cooling performance with a higher temperature span.

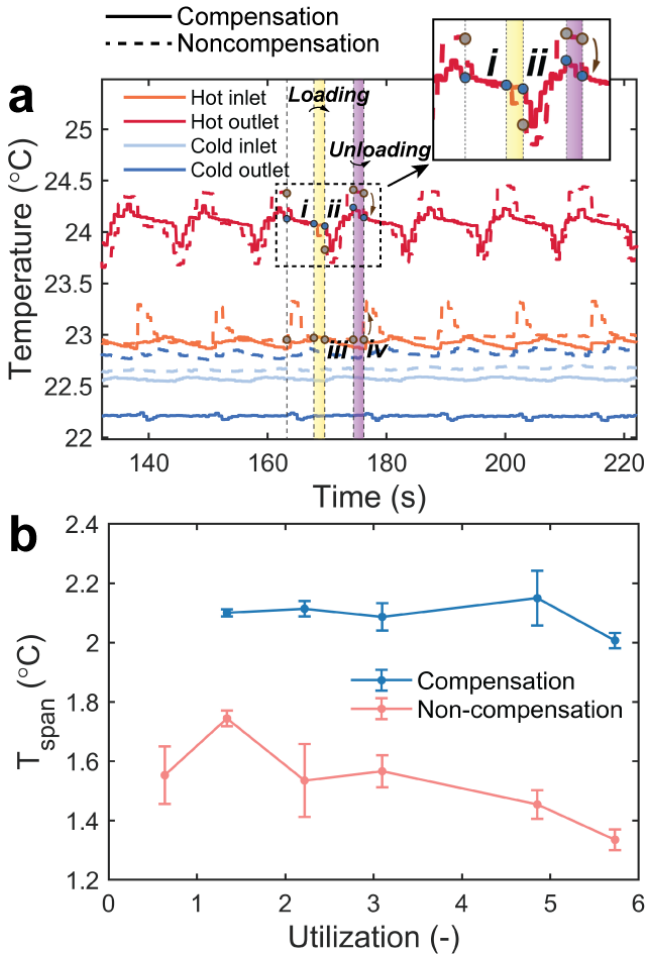

Figure 6.7. Comparison of the active elastocaloric temperature span under the compensation and non-compensation schemes in the REG1:
a, *Comparison of temperature profiles during steady cycles running with volume compensation (solid line) and without volume compensation (dash line) for REG1. Over an active cycle, the corresponding steps i to iv are denoted by the different color dots for compensation scheme (grey) and non-compensation scheme (blue), and the loading (yellow) and unloading (purple) zones are highlighted by colors. The inset shows the zoomed in hot-inlet temperature profile comparison.* ***b***, *Comparison of temperature span under different utilization for REG1 operating with the compensation scheme and non-compensation scheme.*

6.6 Different operating strain ranges

Operating these soft elastomeric regenerators as an active cooling device requires a large applied strain, which risks the significant irreversible deformation to the regenerator. When the regenerator is stretched over several cycles, if it is recovered to the initial length, the regenerator will be bent, kinking the microchannels inside the regenerator. Therefore, it is necessary to set a pre-strain back to which the regenerator reverts without structural buckling, which is also utilized in the rubber-based regenerators undergoing large deformation [107, 197]. It has been observed that the 3D printed elastomer can resist buckling when returning to a 200% strain over 10^4 times from the mechanical stability examination, which is determined by the obtained strain at the zero stress in Figure 6.3a. However, this irreversible strain increases with the cycling number. The pre-strain can be increased to around 300% at the 10^5 cycle due to the special mechanical properties of TPU, such as creep and softening [87].

To compare the impact of applied strain range on the regenerator performance, a set of strain ranges 200-500%, 200-600%, and 300-700% are employed to operate a REG2 regenerator under different Utilization at a frequency of 0.1 Hz. The obtained temperature span for these three strain ranges is shown in Figure 6.8a, and there is no buckling observed when operating under these strain ranges. The REG2 regenerator exhibits a superior performance at a 200-600% strain range, and the maximum temperature span 3.6 K is obtained at a 2.2 Utilization. The 200-500% regenerator displays the reduced performance, probably due to its lowest the normalized strain ($\varepsilon_{max} - \varepsilon_{pre}$) of 300%. For the 200-600% and 300-700%, their normalized strains both are 400%. For the strain range 300-700%, the relatively lower temperature span may be the reason that more volume changes occur in a higher strain range, but the smaller ΔT_{ad} improvement can be achieved by increasing applied strain at that strain range.

6.7 Cooling performance of different regenerator structures

6.7.1 Temperature span under different Utilization

Here, we choose the 200-600% strain range to compare the regenerative cooling performance for the three different regenerators REG1, REG2, REG3. The results are shown in Figure 6.8b for the temperature span under different Utilization. The steady state temperature profiles for REG1, REG2, REG3 at their optimal Utilization in Figure 6.8b are shown in Figure 6.9. The hot side temperature for each is set at 23 °C, and the operating frequency is 0.1 Hz. The error bands are obtained from the several thermocouples mounted at each fluid port. A significant fluctuation at

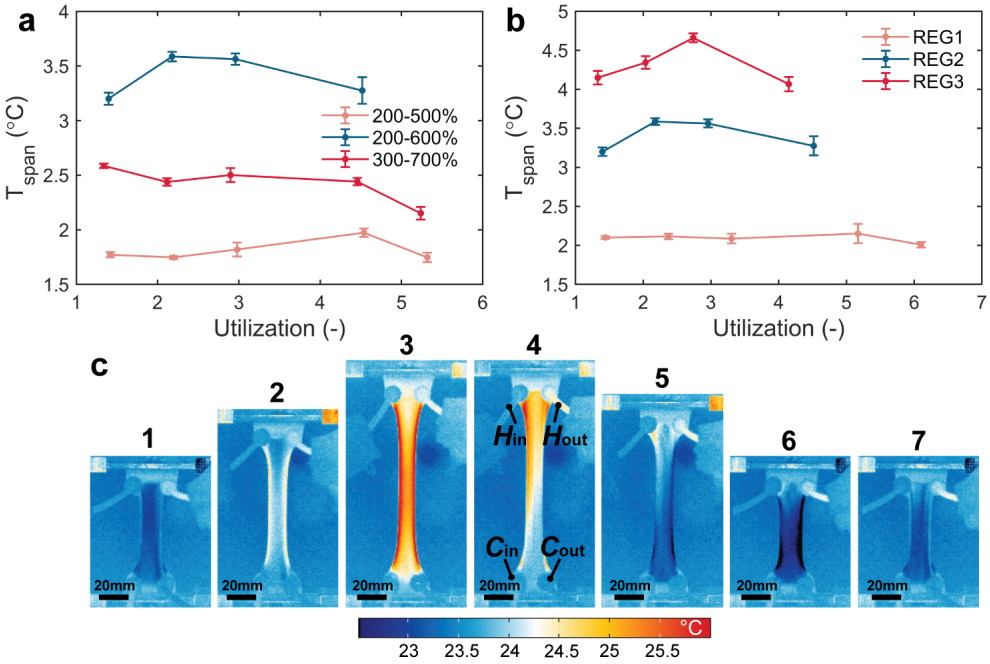

Figure 6.8. Temperature span of the three regenerators operating under different parameters:
***a**, Temperature span with respect to Utilization operating in different strain ranges for REG2 at a frequency of 0.1 Hz; **b**, Temperature span for different regenerators under a frequency of 0.1 Hz and a 200-600% strain range; **c**, IR images for the REG2 in an active cycle under a strain range of 200-600% during steady state, in which the hot inlet (H_{in}), hot outlet (H_{out}), cold outlet (C_{out}), cold inlet (C_{in}) are denoted.*

the hot outlet temperature can be observed, which probably results from the effect of compensation blows or the measurement error of thermocouples.

The maximum temperature span 4.7 K is obtained in the REG3 regenerator under a Utilization of 2.7. REG3 has a higher optimal Utilization compared to the Utilization of 2.2 to achieve the maximum temperature span of REG2, due to the smaller porosity (19.4%) of REG3 compared to REG2 (27.2 %), indicating a higher eCM mass of REG3. It requires more heat transfer fluid to extract the eCE heat from the regenerator, leading to a higher optimal Utilization. However, for REG1, which shows the near flat temperature span with respect to Utilization about 2 K, and also a larger Utilization more than 6, this phenomenon could be attributed to its significant volume changes and the inherently lower thermal conductivity of TPU (∼0.2 W/mK) compared to the benchmark eCE material NiTi (10 W/mK) [198] and MCE material Gd (8 W/mK) [199]. The large volume change of regenerator channels favors a

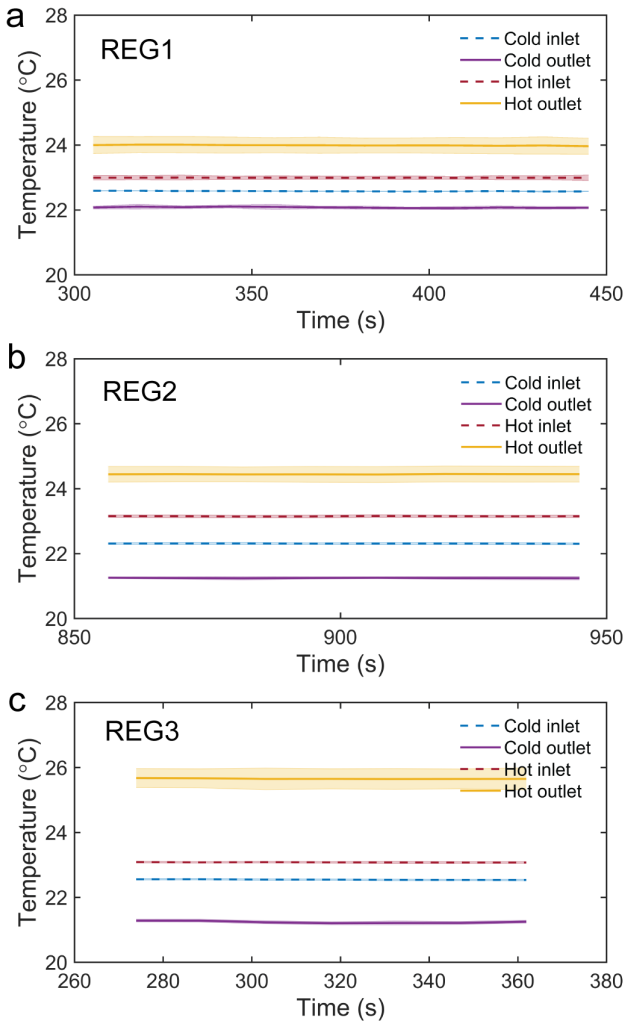

Figure 6.9. Temperature profiles of REG1, REG2, REG3 under the optimized Utilization at a frequency of 0.1 Hz during steady state.

higher Utilization value, as described in Eq. 6.3. Small thermal conductivity is associated with a reduced heat-exchange efficiency between the regenerator and fluids, emphasizing the need for more heat transfer fluids and heat exchange time. In the AMR prototypes, the regenerators with a poor thermal conductivity, such as epoxy bonded regenerator [109, 200] and ceramic-based regenerator [201], also exhibited a relatively high optimal Utilization.

The infrared image in Figure 6.8c displays the temperature distribution of a REG2 regenerator during an active cycle when reaching to steady state at a frequency of 0.1 Hz. Steps 1 to 3 refer to the loading process. The regenerator warms up at 3, and then at step 4, the cold blow is carried out, where the active heat transfer fluid from C_{in} to H_{out} extracts eCE heat to the hot outlet. The temperature gradients along the tensile direction can be observed, moreover, the temperature gradients also exist in the horizoned direction, due to the side-by-side distribution of the cold inlet and hot outlet. Steps 4 to 6 refer to the unloading process, in which the regenerator is cooling down. At step 7, the fluid is displaced from H_{in} to C_{out}, pumping the cooling load to the cold side. The compensation blows during the loading and unloading processes are difficult to observe in these images because the loading process is comparably fast. These images are recorded under an optimal U of 2.2.

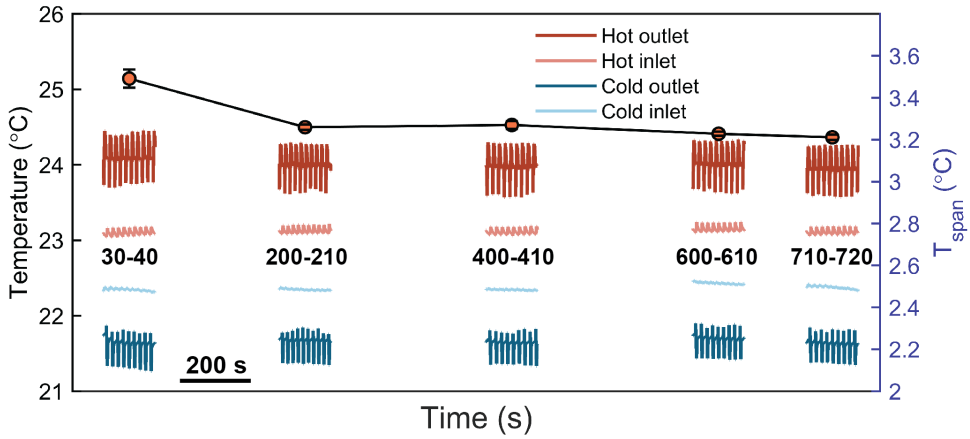

Figure 6.10. The variation in temperature span corresponding to the cycle number for a REG2 regenerator operating at 0.1 Hz under a 200-600% strain range.

6.7.2 Stability of the active regeneration

The stability of 3D printed elastomers has been investigated, revealing a robust fatigue life exceeding 10^5 cycles and satisfactory eCE stability. However, when the elastomer was fabricated into different regenerators, which contain microchannels, the mechanical properties and cyclic stability may be different. A REG2 regenerator is employed to examine the cyclic stability during active cooling cycles. Figure 6.10 shows the temperature profiles when the REG2 regenerator is operated at its maximum temperature span. The operation parameters at this temperature span have been obtained from Figure 6.8a, with a Utilization of 2.2 and strain range of 200-600% at 0.1 Hz. The temperature span of REG2 deceases from 3.6 K to 3.3 K

when reaching to 200 cycles, and then REG2 maintains a 3.2 K temperature span over 700 cycles. At the 720th cycle, a small crack emerges on the regenerator surface, leading to fluid leakage. This is due to the thin 0.5 mm thickness of the regenerator wall, measured from the inside boundary channel to the regenerator surface. With an increasing number of cycles, the thin regenerator wall becomes more prone to failure, resulting in leakage. Notably, imperfections introduced during 3D printing, which cause stress concentration, raise the risk of structural failure. If a failure occurs on the regenerator surface, leakage could lead to an immediate operational breakdown. Hence, in practice, implementing a thicker regenerator wall to better withstand structural failures and leakage on the surface is suggested.

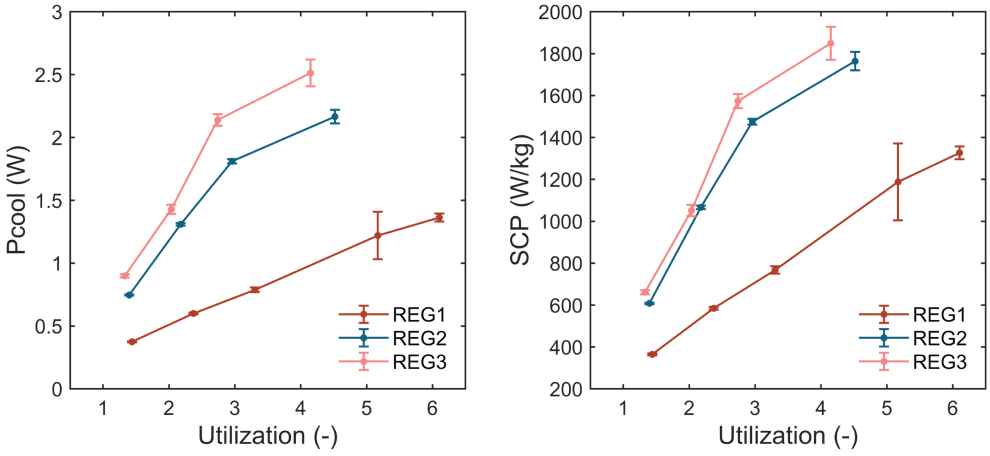

Figure 6.11. Cooling power and specific cooling power as a function of Utilization for the regenerator REG1, REG2, REG3, operating under a 0.1 Hz frequency and a 200-600% strain range.

6.7.3 Cooling power and specific cooling power

The system cooling power ($Pcool$, $\dot{Q}_c$) and specific cooling power (SCP) were evaluated when the steady state was reached for the three regenerators, as follows:

$$\dot{Q}_c = \dot{m}_f \cdot c_{p,f} \cdot \left(\overline{T_{c,i}} - \overline{T_{c,o}}\right) \tag{6.4}$$

$$SCP = \frac{\dot{Q}_c}{m_s}, \tag{6.5}$$

in which $\overline{T_{c,i}}$ and $\overline{T_{c,o}}$ are the average temperature of cold inlet and cold outlet obtained from 10 steady-state cycles, respectively. m_s is the effective regenerator mass,

determined by the middle zone of the dogbone regenerator with the microchannels inside. The regenerator mass m_s for REG1, REG2, REG3 are 1.027 g, 1.228 g, and 1.359 g, respectively.

Figure 6.11 shows the calculated cooling power and specific cooling power as a function of Utilization of our regenerators, operating under 0.1 Hz and a 200-600% strain range. The maximum cooling power for each regenerator is 1.3 W (REG1, $U = 6.1$), 2.2 W (REG2, $U = 4.5$), 2.5 W (REG3, $U = 4.1$) and the maximum specific cooling power 1850 W/kg is obtained in the REG3. For all of the regenerators, the cooling power and SCP increases with the Utilization, as these elastomeric regenerators can achieve a temperature span in a large Utilization range without a significant drop (see Figure 6.8b). The Utilization value is almost proportional to the displaced fluid volume, which means the more heat-transfer fluids were displaced over the cycle, and a higher cooling power is achieved in a wide Utilization range. This specific cooling power of 1850 W/kg achieved in REG3 at a frequency of 0.1 Hz, is comparable to a magnetocaloric regenerator prototype proposed by Jacobs et al. [40] which has a 2001 W/kg SCP at 0.2 Hz. Meanwhile, our REG3 SCP is superior to a SPC of 360 W/kg at 0.1 Hz obtained in a rubber-based regenerative cooling device [107].

6.7.4 COP of the regenerative cooling system

The coefficient of performance (COP) of the cooling system can be calculated based on the fraction of cooling power and system input power:

$$\begin{aligned} \mathrm{COP} &= \frac{\dot{Q}_c}{\dot{W}_{\mathrm{sys}}} \\ \dot{W}_{\mathrm{sys}} &= f \cdot W_{sys} \\ W_{sys} &= W_{\mathrm{mech}} + W_{\mathrm{pump}} \end{aligned} \tag{6.6}$$

in which f is the frequency of an active cooling cycle. The system input work W_{sys} includes two parts:
1) mechanical input work, responsible for driving the regenerator to stretch and release, which can be obtained from the enclosed area of stress-strain curves during steady state:

$$W_{\mathrm{mech}} = V_{\mathrm{s}} \oint \sigma d\varepsilon, \tag{6.7}$$

where V_{s} is the regenerator volume.
2) pump work, responsible for the oscillating heat transfer fluid flow periods provided by a displacer, shown in the flow system in Figure 6.6:

$$W_{\mathrm{pump}} = \int_0^{\tau} \frac{\dot{m}_f \cdot \Delta p}{\rho_f} dt. \tag{6.8}$$

The Δp is the pressure drop between the hot side and cold side. In our case, we didn't have a hydraulic pressure meter to record the pressure drop during the cycles. Here,

the pressure drop for different microchannel regenerators is evaluated according to their channel geometries, as discussed in the **Scenario 5**.

Scenario 5 Calculation for the pressure drop of parallel-plate and square channels

There are two typical fluid channels designed in the regenerators: parallel-plate channels and square channels. The pressure drop of the parallel plate channel and square can be both calculated by:

$$\Delta p = \int_0^\tau L(t)\frac{dp}{dx}dt = \int_0^\tau 4L(t)f_F\left[\frac{\dot{m}_f^2}{2\rho_f D_h\left(A_c\epsilon\right)^2}\right]dt \tag{6.9}$$

$L(t)$ is the regenerator length as a function of time, which is related to the strain-time profile. τ is the cycle time and A_c is the cross section area of the regenerator. The friction factor (f_F) for the parallel-plate channel is [202]:

$$f_F = 24/\,\mathrm{Re} \tag{6.10}$$

The friction factor for the square channel ($\alpha = 1$) is [203]:

$$f_F = 24\left(1 - 1.3553\alpha + 1.9467\alpha^2 - 1.7012\alpha^3 + 0.9564\alpha^4 - 0.2537\alpha^5\right)/\,\mathrm{Re} \tag{6.11}$$

where the Reynolds number can be calculated by:

$$\mathrm{Re} = \frac{\dot{m}_f D_h}{\epsilon\mu_f} \tag{6.12}$$

The hydraulic diameter D_h for different microchannels is listed in Table 2.2. ϵ is the porosity of the regenerator, and μ_f is the fluid viscosity (0.0016 Ns/m^2 for water).

Figure 6.12 shows the comparison for the total input work and COP for the cooling system. The total system work and pump work of REG1 and REG2 are closely aligned, while REG3 shows a higher pump work, reaching 5.7 J at a Utilization of 4.1, as illustrated in Figure 6.12a. This discrepancy is attributed to REG3 having a smaller square channel size (0.45 mm) and lower porosity of 19.4 %, resulting in an improved pressure drop compared to REG1 and REG2. Consequently, REG3 exhibits a notably higher total system work. Examining the system COP in Figure 6.12b, REG2 displays a remarkable COP, reaching a maximum of 1.7 at a Utilization of 4.5. Conversely, REG3 reaches its maximum COP at a Utilization of 2.7, experiencing a subsequent decline due to a significant contribution of pump work W_{pump}. The comparison of the maximum COP for each regenerator is presented in Figure 6.12c. Notably, REG3 exhibits the lowest COP, despite achieving a maximum temperature span. However, REG2 demonstrates an efficient implementation for regenerative cooling, with a maximum COP of 1.7.

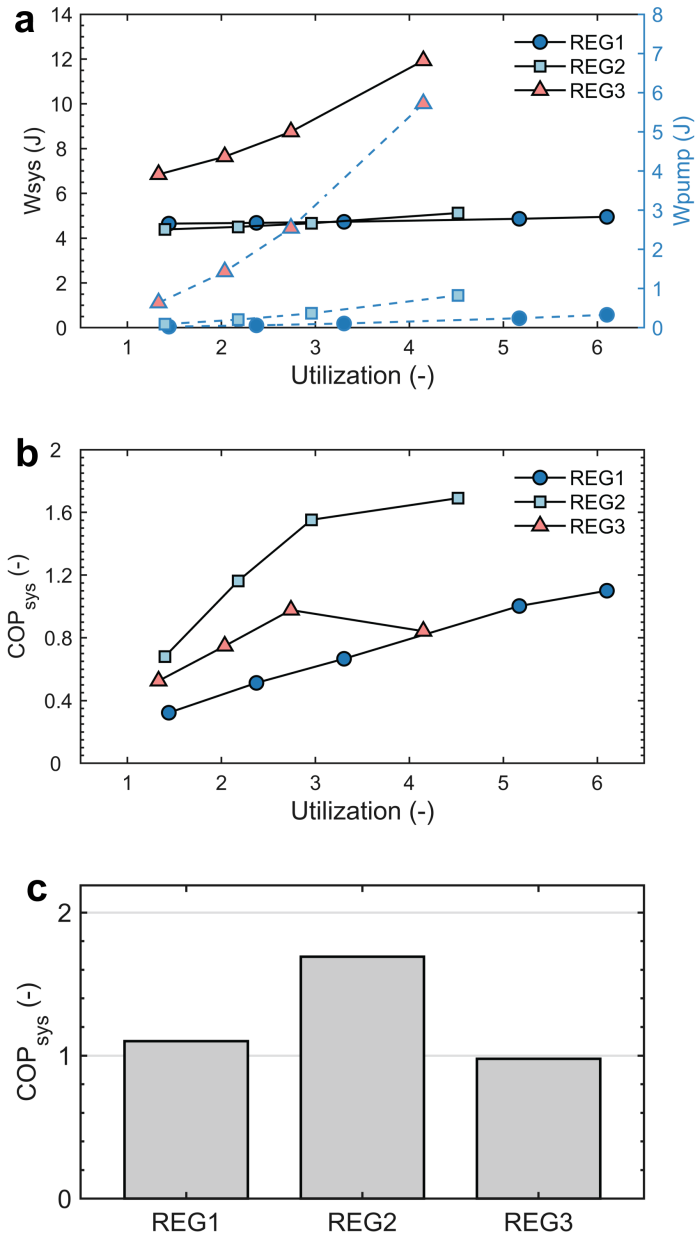

Figure 6.12. Comparison of system COP and input work:
***a**, The total system work (black) and pump work (blue) as a function of Utilization for REG1, REG2, REG3; **b**, COP of the cooling system under different Utilization; **c**, Maximum COP of REG1, REG2, REG3.*

6.8 Comparison with the state-of-the-art elastocaloric prototypes

As a performance metric for the regenerator design, the regeneration ratio has been defined as [204]:

$$\zeta = \frac{\Delta T_{\text{span}}}{\Delta T_{\text{ad}}} \tag{6.13}$$

in which ΔT_{span} is the regenerator temperature span and ΔT_{ad} is the adiabatic temperature change of the regenerator material. ζ can be employed to evaluate the effectiveness of an active regeneration system in extending the temperature change of the elastocaloric material. When ζ exceeds 1, the regenerator temperature surpasses the material's adiabatic temperature change, leading to an expanded temperature span. Otherwise, if ζ is less than 1, it implies inadequate regeneration.

In Figure 6.13, several typical elastocaloric prototypes employing polymers or NiTi-based shape-memory alloys are selected for comparison with the presented 3D printed TPU-based regenerator. The maximum regenerator ratio ζ of 1.84 is obtained in our 3D-printed regenerator, which is superior to the first three polymer-based prototypes with a < 1 regenerator ratio, although the active regeneration has been performed in a rubber-tube based regenerator from Lyon [107] and in a roller-strip device from WHUT [57]. Our regeneration ratio is also comparable to some NiTi-based regenerative prototypes, but an up-to-date prototype in the cascaded scheme integrated with 11 regenerator units can achieve a high ζ of 3.67 [106]. Additionally, in the figure, the specific cooling power (SCP) is also compared. It can observe that the SCP of our 3D-printed regenerators is higher than most alloy-based regenerators, but lower than the other two polymer based prototypes. It is attributed to their elastomers being employed in the form of a thin film or membrane, which favors more efficient heat exchange. In particular, the balloon-like prototype [91], exploiting fast inflation and deflation of a rubber membrane (0.036 g), allows the operation at a high frequency of 1.1 Hz and achieves a remarkable SCP of 20.9×10^3 W/kg. By operating at a higher frequency, our regenerative cooling system can be expected to obtain an improved SCP. Such an effect has been demonstrated in an active magnetic regenerator when operating in a 20 Hz frequency, resulting in a 12.5 $\times 10^3$ W/kg SCP [205].

6.9 Summary

In summary, the full-scale 3D printed soft active elastocaloric regenerator (AER) has been successfully demonstrated for regenerative elastocaloric cooling in a volume compensation setup. As the first milestone, the 3D printing for elastocaloric elastomers is improved to fabricate durable 3D printed parts (mechanical stability over

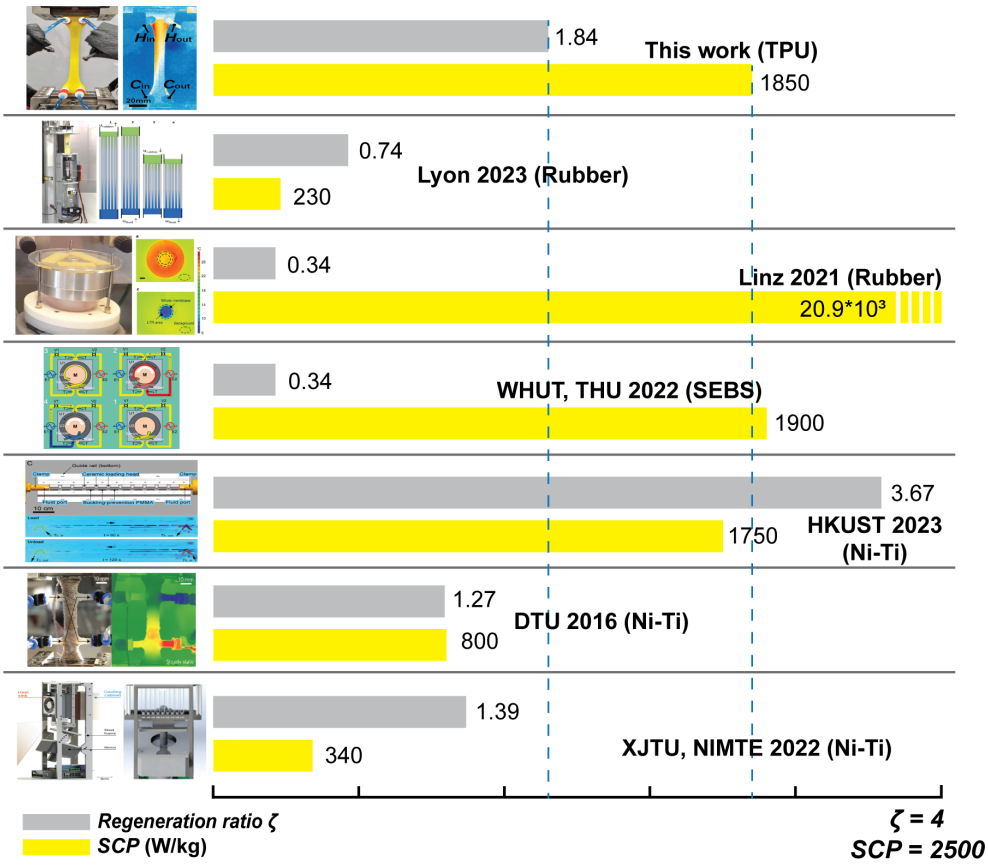

Figure 6.13. Comparison of the obtained maximum specific coolling power (*SCP*, yellow) and regeneration ratio (ζ, grey) in selected prototypes with our 3D-printed active regenerators [57, 67, 91, 104, 106, 107]. Note the *SCP* of Linz 2021 exceeds the coordinate range, as indicated by the dashed yellow bar, representing an external extension.

10^5 cycles) and high quality regenerators (watertight, airtight, see **Appendix C**), ensuring the implementation of regenerative cooling.

To address the issues in operating these soft elastomeric regenerators, such as large applied strains and large-strain induced volume changes in microchannels, a tailored regenerative flow system is developed. With this apparatus, the continuous heat-transfer fluid flow periods during the active cycle, capable of compensation for the volume changes in fluid channels, is ensured. The effect of these unusual volume changes on the cooling performance has been studied by a comparison of the two operation schemes with and without fluid compensation in a REG1 regenerator. The noncompensation scheme exhibits a lower temperature span compared to the compensation scheme, due to the imbalanced fluid flow periods produced by volume changes.

Different operating strain ranges are compared in a REG2 regenerator, which suggests a 200-600% strain range for the regenerator operation. The three regenerators with different microchannels have been studied under various Utilization. The results show a REG3 regenerator achieving a maximum temperature span of 4.7 K and a cooling power of 2.5 W, while a REG2 regenerator attains a maximum COP of 1.7. The 3D printed regenerator achieves a remarkable regeneration ratio of 1.84 compared to state-of-the-art polymer-based prototypes. Furthermore, REG3 demonstrates a specific cooling power of 1850 W/kg, comparable to the latest Ni-Ti-based coolers. These 3D-printed soft active elastocaloric regenerators bring forth promising prospects for the future commercialization of regenerative elastocaloric cooling, exploiting cost-effective and flexible eCE elastomers.

Part III

Conclusions and Outlook

CHAPTER 7

Conclusion and outlook

"Available energy is the main object at stake in the struggle for existence and the evolution of the world"

— Ludwig Boltzmann (Austrian physicist, 1844−1906)

"Ceaseless work, analysis, reflection, writing much, endless self-correction, that is my secret."

— Johann S. Bach (German composer, 1685−1750)

This dissertation investigated the 3D printing of soft elastocaloric regenerators and its regenerative cooling performance numerically and experimentally. A regenerative elastocaloric cooling system has been realized, employing soft full-printed elastocaloric regenerators, which exhibits a comparable cooling performance with expanded temperature span to 4.7 K. Nevertheless, aiming to enhanced system performance, the optimization of the regenerator design and the operational apparatus is ongoing. In this chapter, we summarize the notable achievements in relation to each chapter and present the existing challenges for future investigations.

7.1 Conclusion

In the first Chapter 1, the main motivations and objectives have been listed, reflecting in the investigation of each chapter. Here, to conclude the main achievements of this dissertation, we summarize the related findings in response to associated questions in Table 7.1.

Table 7.1. Conclusion in relation to each chapter of the dissertation

Motivation 1:	How to construct a low-stress induced elastocaloric cooling prototype in a compact scheme?
Chapter 3 Article I **Chapter 6** Article III	Rubber-like elastomers hold the nature of softness and elasticity to mechanically deform under a small force. There are some soft elastomers, exhibiting notable elastocaloric effect with an adiabatic temperature change more than 15 K at a stress of ∼10 MPa. Some of them, such as thermoplastic polyurethane (TPU), are capable of 3D printing to construct a compact elastocaloric regenerator, integrating the heat transfer microchannels and fluidic manifolds. Implementing additive manufacturing to fabricate elastocaloric regenerators, using soft elastocaloric elastomers, has been demonstrated. The 3D printed parts show an excellent fatigue life and cyclic stability over 10^5 cycles in FilaFlex 82A TPU, and a high printing quality is achieved, ensuring the water tightness of the regenerator to operate in an active cooling system.
Motivation 2:	Which elastocaloric materials could be a candidate for the 3D printed AER?
Chapter 3 Article I **Chapter 6** Article III	In the **Chapter 3**, the TPU is screened out from five commercial thermoplastic elastomers, with a superior temperature decrease of 5.6 K upon unloading at 5.7 MPa in the NinjaFlex TPU. However, 3D printing elastocaloric regenerators, employing the NinjaFlex TPU, confronts leakage issues, as depicted in **Appendix C**. Although different glues attempt to seal the regenerator, the regenerators are struggled to maintain a long-term water tightness during the testing. Fortunately, a customized 3D printer Felix Tec 4.1, developed in the research institute AMOLF where I was doing my external visiting, can achieve a good printing quality for the elastocaloric regenerator fabrication. Yet, the material FilaFlex 82A TPU, with a smaller ΔT_{ad} of 2.5 K, is employed on this printer. Hence, the experimental tests for regenerative cooling performance and volume change measurement are all based on the FilaFlex TPU.
Motivation 3:	When subjecting to the required large-strains, there are fluid-channel volume changes observed inside regenerator, and how to account it?
Chapter 4 Article II	When the elastomer-based regenerator is subjected to large deformation (600%), We observe significant volume changes in the regenerator fluid channels. This volume change results in an asymmetric fluid exchange as well as discontinuous heat transfer fluid flow periods. A finite-element (FE) model, capturing the mechanical behavior of the elastomer based on hyperelastic model, facilities the predication of the regenerator volume change. The predicted results are validated by experimental measurements, exhibiting good agreement.
Motivation 4:	How to numerically investigate and evaluate the cooling performance of a large-deformation soft eCE regenerator?

Chapter 5 Article **IV**	A 1D numerical model for active large-deformation elastocaloric regenerators has been developed, with the volume compensation and dynamic spatial nodes. The strain-dependent geometrical information and volume changes are available from FE simulations, which is input to the numerical model. The temperature-dependent entropy changes and temperature changes are obtained from a NinjaFlex TPU for the simulation. The volume compensation schemes, from hot or cold reservoir, are compared for elastocaloric cooling. A better cooling performance is achieved when compensating from hot reservoir, suggesting the hot-reservoir compensation scheme for cooling applications. In addition, the maximum temperature span can be achieved in a square-channel regenerator, reaching 11.9 K at a frequency of 0.13 Hz. An optimal Utilization of 0.65 for this regenerator is obtained.
Motivation 5:	How to construct an active operation system capable of implementing large-deformation soft eCE regenerators effectively?
Chapter 6 Article **III**	We construct a fluidic compensation system to test 3D-printed elastocaloric regenerators, which can compensate and expel the increased/decreased volumes during the regenerator loading and unloading. The effect of large-strain induced volume changes is studied with the comparison of two operating schemes with and without volume compensation. The results show the non-compensation scheme leads to discontinuous heat transfer fluid flow periods, consequently, reducing the system temperature span. The compensation scheme, allowing continuous volume compensation during active cycles, favors a higher temperature span. The operating parameters are optimized in three different 3D-printed regenerators with distinct microchannels. The results show a REG3 regenerator achieving a maximum temperature span of 4.7 K and a cooling power of 2.5 W, while a REG2 regenerator attains a maximum COP of 1.7. The 3D printed regenerator achieves a remarkable regeneration ratio of 1.84 compared to state-of-the-art polymer-based prototypes. Furthermore, REG3 demonstrates a specific cooling power of 1850 W/kg, comparable to the latest Ni-Ti-based coolers.

7.2 Outlook

The low-stress regenerative elastocaloric cooling, based on fully 3D-printed soft regenerators, has been demonstrated with a satisfactory cooling performance. Moreover, the findings and insights from the investigation of these active 3D-printed soft regenerators, ranging from numerical modelling to experimental proof-of-concepts, present an exciting prospect to implement additive manufacturing in producing fantastic elastocaloric regenerators. Yet, the challenge is always ceaseless. Here, we provide an outlook on ongoing challenges and further exploration based on this dissertation.

The ongoing challenges encompass the following issues:

- **Improving the 3D-printing reliability**
  Even though the watertight regenerator is printed on an improved 3D printer employing FilaFlex TPU and a good mechanical stability has been achieved, the yield rate of the regenerator printing remains low. Moreover, the printing nozzle is prone to blocking after printing a few parts. Hence, improving the reliability of 3D printers and and exploring superior elastocaloric filaments are essential for the high-efficiency production of a large number of elastocaloric regenerators.

- **Effective models to capture the thermo-mechanical properties of soft elastomers**
  In relation to Chapter 5, simulating the temperature gradients during active cycles using a 1D numerical model, the temperature-dependent mechanical behavior of NinjaFlex TPU are implemented. Actually, in the isothermal entropy change calculation, there are divergences of the calculation, existing at the low (<290 K) and high (>320 K) temperatures. The calculated results in the middle temperature zone, exhibiting good agreement with the experimental results, are taking out for the 1D model. If a high temperature is achieved in the regenerator, for example a more than 10 K cooling temperature span at a hot side temperature of 300 K, the simulation results may be less reliable. Because, the material data at <290 K is obtained by extrapolation, which results in predication errors. Directly based on isothermal stress-strain curves, the prediction of material temperature-dependent properties is also observed with a significant discrepancy in elastocaloric rubbers [97]. Therefore, to obtain accurate isothermal entropy changes and ΔT_{ad}, it is necessary to develop an effective thermo-mechanical model to capture the isothermal mechanical behavior of elastocaloric elastomers.

- **Geometrical optimization for heat transfer fluid channels**
  In the regenerative cooling testing, we observed the regenerator with smaller square channels favors a better cooling temperature span. It can be expected to achieve improved cooling performance by geometrical optimization for the

regenerator channels. The optimization can be implemented, in relation to enhanced heat-transfer properties (higher specific surface area) and reduced volume changes in fluid channels based on topological optimization. Furthermore, additive manufacturing ensures the fabrication of complex channel structures after geometrical optimization.

- **Improving the operational configuration of the active flow system**
  In fact, the active flow system lacks effectively thermal isolation for large deformation regenerators. During active cycles, the regenerator exchanges heat with ambient, leading to thermal losses. The effective thermal isolation for the regenerator should be considered. Moreover,for our flow system, it is challenging to operate at a high frequency and lower Utilization. Specifically, the frequency is restricted by the fluid flow speed, provided by two movable pistons in our apparatus, and the fast movement of them is not attainable by present actuator. When the regenerator thermal mass is fixed, the Utilization value depends on the piston stroke and diameter. To achieve a lower Utilization requires a reduced piston diameter at a small stroke.

The further exploration is expected to continue in these aspects:

- **Enhancing the heat transfer performance**
  As known that these elastomers have a lower thermal conductivity compared to elastocaloric alloys, seeking the elastocaloric elastomers with high thermal conductivity has significant impact on developing more efficient elastomeric regenerators. These elastocaloric regenerators are expected to achieve enhanced heat transfer and efficient energy conversion at a high frequency.

- **Heat pump applications**
  In addition to regenerative cooling, our flow system is also possible for the heat-pumping application employing these 3D printed soft regenerators. The system only needs to fix the cold side temperature. Moreover, using our 1D numerical model, the compensation direction and regenerator performance can also be investigated for the heat pump. Actually, the elastocaloric elastomer shows a higher temperature increase upon loading, compared to the temperature decrease upon unloading. These soft elastomers are probably more suitable for the heat-pumping application. Thus, we expect to employ our 3D printed regenerators for heat pump in the future exploration.

Bibliography

[1] Iea is cooling the future of heating? `https://www.iea.org/commentaries/is-cooling-the-future-of-heating` (2020).

[2] Davis, L. W. & Gertler, P. J. Contribution of air conditioning adoption to future energy use under global warming. *Proceedings of the National Academy of Sciences* **112**, 5962–5967 (2015).

[3] Isaac, M. & Van Vuuren, D. P. Modeling global residential sector energy demand for heating and air conditioning in the context of climate change. *Energy policy* **37**, 507–521 (2009).

[4] Gi, K., Sano, F., Hayashi, A., Tomoda, T. & Akimoto, K. A global analysis of residential heating and cooling service demand and cost-effective energy consumption under different climate change scenarios up to 2050. *Mitig. Adapt. Strateg. Glob. Chang.* **23**, 51–79 (2018).

[5] Iea the future of cooling. `https://www.iea.org/reports/the-future-of-cooling` (2018).

[6] Coulomb, D., Dupont, J. & Pichard, A. The role of refrigeration in the global economy. *International Institute of Refrigeration: Paris, France* (2015).

[7] Velders, G. J., Fahey, D. W., Daniel, J. S., McFarland, M. & Andersen, S. O. The large contribution of projected hfc emissions to future climate forcing. *Proceedings of the National Academy of Sciences* **106**, 10949–10954 (2009).

[8] Velders, G. J. *et al.* Preserving montreal protocol climate benefits by limiting hfcs. *Science* **335**, 922–923 (2012).

[9] Pecharsky, V. K. & Gschneidner Jr, K. A. Giant magnetocaloric effect in gd5(si2ge2). *Physical review letters* **78**, 4494 (1997).

[10] Pecharsky, V. K. & Gschneidner Jr, K. A. Magnetocaloric effect and magnetic refrigeration. *Journal of magnetism and magnetic materials* **200**, 44–56 (1999).

[11] Wada, H. & Tanabe, Y. Giant magnetocaloric effect of mnas 1- x sb x. *Applied physics letters* **79**, 3302–3304 (2001).

[12] Tegus, O., Brück, E., Buschow, K. & De Boer, F. Transition-metal-based magnetic refrigerants for room-temperature applications. *Nature* **415**, 150–152 (2002).

[13] Liu, J., Gottschall, T., Skokov, K. P., Moore, J. D. & Gutfleisch, O. Giant magnetocaloric effect driven by structural transitions. *Nature materials* **11**, 620–626 (2012).

[14] Mischenko, A., Zhang, Q., Scott, J., Whatmore, R. & Mathur, N. Giant electrocaloric effect in thin-film pbzr0. 95ti0. 05o3. *Science* **311**, 1270–1271 (2006).

[15] Neese, B. *et al.* Large electrocaloric effect in ferroelectric polymers near room temperature. *Science* **321**, 821–823 (2008).

[16] Qian, X. *et al.* High-entropy polymer produces a giant electrocaloric effect at low fields. *Nature* **600**, 664–669 (2021).

[17] Bonnot, E., Romero, R., Mañosa, L., Vives, E. & Planes, A. Elastocaloric effect associated with the martensitic transition in shape-memory alloys. *Phys. Rev. Lett* **100**, 125901 (2008).

[18] Tušek, J., Engelbrecht, K., Mikkelsen, L. P. & Pryds, N. Elastocaloric effect of ni-ti wire for application in a cooling device. *Journal of Applied Physics* **117** (2015).

[19] Candau, N., Vives, E., Fernández, A. I. & Maspoch, M. L. Elastocaloric effect in vulcanized natural rubber and natural/wastes rubber blends. *Polymer* **236**, 124309 (2021).

[20] Cong, D. *et al.* Colossal elastocaloric effect in ferroelastic ni-mn-ti alloys. *Phys. Rev. Lett* **122**, 255703 (2019).

[21] Ahčin, Ž. *et al.* High-performance cooling and heat pumping based on fatigue-resistant elastocaloric effect in compression. *Joule* **6**, 2338–2357 (2022).

[22] Qian, S. *et al.* High-performance multimode elastocaloric cooling system. *Science* **380**, 722–727 (2023).

[23] Matsunami, D., Fujita, A., Takenaka, K. & Kano, M. Giant barocaloric effect enhanced by the frustration of the antiferromagnetic phase in mn3gan. *Nat. Mater.* **14**, 73–78 (2015).

[24] Li, B. *et al.* Colossal barocaloric effects in plastic crystals. *Nature* **567**, 506–510 (2019).

[25] Romanini, M. *et al.* Giant and reversible barocaloric effect in trinuclear spin-crossover complex fe3 (bntrz) 6 (tcnset) 6. *Advanced Materials* **33**, 2008076 (2021).

[26] Zhang, Z. *et al.* Thermal batteries based on inverse barocaloric effects. *Science Advances* **9**, eadd0374 (2023).

[27] Hou, H., Qian, S. & Takeuchi, I. Materials, physics and systems for multicaloric cooling. *Nat. Rev. Mater.* **7**, 633–652 (2022).

[28] Sawyer, C. B. & Tower, C. Rochelle salt as a dielectric. *Physical review* **35**, 269 (1930).

[29] Cui, J. *et al.* Demonstration of high efficiency elastocaloric cooling with large δt using niti wires. *Applied Physics Letters* **101** (2012).

[30] Müller, K. A. *et al.* Cooling by adiabatic pressure application in pr 1-x la x nio 3. *Applied physics letters* **73**, 1056–1058 (1998).

[31] Strässle, T., Furrer, A., Lacorre, P. & Müller, K. A. A novel principle for cooling by adiabatic pressure application in rare-earth compounds. *Journal of Alloys and Compounds* **303**, 228–231 (2000).

[32] Gschneidner Jr, K. & Pecharsky, V. K. Magnetocaloric materials. *Annual review of materials science* **30**, 387–429 (2000).

[33] Brück, E., Ilyn, M., Tishin, A. & Tegus, O. Magnetocaloric effects in mnfep1-xasx-based compounds. *Journal of magnetism and magnetic materials* **290**, 8–13 (2005).

[34] Moya, X., Kar-Narayan, S. & Mathur, N. D. Caloric materials near ferroic phase transitions. *Nat. Mater.* **13**, 439–450 (2014).

[35] Gottschall, T., Skokov, K. P., Burriel, R. & Gutfleisch, O. On the s (t) diagram of magnetocaloric materials with first-order transition: Kinetic and cyclic effects of heusler alloys. *Acta Materialia* **107**, 1–8 (2016).

[36] Greco, A., Aprea, C., Maiorino, A. & Masselli, C. A review of the state of the art of solid-state caloric cooling processes at room-temperature before 2019. *International Journal of Refrigeration* **106**, 66–88 (2019).

[37] Zhang, H. *et al.* Large magnetocaloric effects of rfesi (r= tb and dy) compounds for magnetic refrigeration in nitrogen and natural gas liquefaction. *Applied Physics Letters* **103** (2013).

[38] Numazawa, T., Kamiya, K., Utaki, T. & Matsumoto, K. Magnetic refrigerator for hydrogen liquefaction. *Cryogenics* **62**, 185–192 (2014).

[39] Beckmann, B. *et al.* Dissipation losses limiting first-order phase transition materials in cryogenic caloric cooling: A case study on all-d-metal ni (-co)-mn-ti heusler alloys. *Acta Materialia* **246**, 118695 (2023).

[40] Jacobs, S. *et al.* The performance of a large-scale rotary magnetic refrigerator. *International journal of refrigeration* **37**, 84–91 (2014).

[41] Dall'Olio, S. *et al.* Novel design of a high efficiency multi-bed active magnetic regenerator heat pump. *International Journal of Refrigeration* **132**, 243–254 (2021).

[42] Alves Dias, P., Bobba, S., Carrara, S. & Plazzotta, B. The role of rare earth elements in wind energy and electric mobility. *European Commission: Luxembourg* (2020).

[43] Kitanovski, A. Energy applications of magnetocaloric materials. *Advanced Energy Materials* **10**, 1903741 (2020).

[44] Torelló, A. *et al.* Giant temperature span in electrocaloric regenerator. *Science* **370**, 125–129 (2020).

[45] Wang, Y. *et al.* A high-performance solid-state electrocaloric cooling system. *Science* **370**, 129–133 (2020).

[46] Ma, R. *et al.* Highly efficient electrocaloric cooling with electrostatic actuation. *Science* **357**, 1130–1134 (2017).

[47] Aznar, A. *et al.* Giant barocaloric effects over a wide temperature range in superionic conductor agi. *Nature communications* **8**, 1851 (2017).

[48] Vallone, S. P. *et al.* Giant barocaloric effect at the spin crossover transition of a molecular crystal. *Advanced Materials* **31**, 1807334 (2019).

[49] Czernuszewicz, A., Kaleta, J., Lewandowski, D. & Przybylski, M. An idea of the test stand for studies of magnetobarocaloric materials properties and possibilities of their application. *physica status solidi (c)* **11**, 995–999 (2014).

[50] Stern-Taulats, E., D'Ammaro, A., Avramenko, A., Robinson, A. & Moya, X. First steps towards barocaloric refrigeration. In *International Conference on Caloric Coolig, Thermag VIII, Darmstadt (Germany)* (2018).

[51] Wang, R. *et al.* Torsional refrigeration by twisted, coiled, and supercoiled fibers. *Science* **366**, 216–221 (2019).

[52] Czernuszewicz, A., Griffith, L., Slaughter, J. & Pecharsky, V. Low-force compressive and tensile actuation for elastocaloric heat pumps. *Applied Materials Today* **19**, 100557 (2020).

[53] Sharar, D. J., Radice, J., Warzoha, R., Hanrahan, B. & Smith, A. Low-force elastocaloric refrigeration via bending. *Applied Physics Letters* **118** (2021).

[54] Gough, J. A description of a property of caoutchouc, or indian rubber. *Memories of the Literacy and Philosophical Society of Manchester* **1**, 288–295 (1805).

[55] Joule, J. P. V. on some thermo-dynamic properties of solids. *Philosophical Transactions of the Royal Society of London* 91–131 (1859).

[56] Guyomar, D. *et al.* Elastocaloric modeling of natural rubber. *Appl. Therm. Eng.* **57**, 33–38 (2013).

[57] Zhang, S. *et al.* Solid-state cooling by elastocaloric polymer with uniform chain-lengths. *Nat. Commun.* **13**, 9 (2022).

[58] Ding, L. *et al.* Learning from superelasticity data to search for ti-ni alloys with large elastocaloric effect. *Acta Materialia* **218**, 117200 (2021).

[59] of Energy, U. D. Energy savings potential and rd&d opportunities for non-vapor-compression hvac technologies. Tech. Rep. (2014).

[60] Technology roadmap in preparatory/review study on commission regulation (ec) no. 643/2009 with regard to ecodesign requirements for household refrigeration appliances and commission delegated regulation (eu). *VHK and armines* (2016).

[61] Ossmer, H., Miyazaki, S. & Kohl, M. The elastocaloric effect in tini-based foils. *Materials Today: Proceedings* **2**, S971–S974 (2015).

[62] Chen, H. *et al.* Improvement of the stability of superelasticity and elastocaloric effect of a ni-rich ti-ni alloy by precipitation and grain refinement. *Scripta Materialia* **162**, 230–234 (2019).

[63] Chen, J., Zhang, K., Kan, Q., Yin, H. & Sun, Q. Ultra-high fatigue life of niti cylinders for compression-based elastocaloric cooling. *Applied Physics Letters* **115** (2019).

[64] Mañosa, L., Jarque-Farnos, S., Vives, E. & Planes, A. Large temperature span and giant refrigerant capacity in elastocaloric cu-zn-al shape memory alloys. *Applied Physics Letters* **103** (2013).

[65] Yuan, B., Qian, M., Zhang, X., Imran, M. & Geng, L. Enhanced cyclic stability of elastocaloric effect in oligocrystalline cu–al–mn microwires via cold-drawing. *International Journal of Refrigeration* **114**, 54–61 (2020).

[66] Sun, W., Liu, J., Zhao, D. & Zhang, M. Directional solidification and elastocaloric effect in a ni45mn44sn11 magnetic shape memory alloy. *Journal of Physics D: Applied Physics* **50**, 444001 (2017).

[67] Tušek, J. *et al.* A regenerative elastocaloric heat pump. *Nature Energy* **1**, 1–6 (2016).

[68] Qian, S., Yuan, L., Yu, J. & Yan, G. Numerical modeling of an active elastocaloric regenerator refrigerator with phase transformation kinetics and the matching principle for materials selection. *Energy* **141**, 744–756 (2017).

[69] Qian, S., Wang, Y., Yuan, L. & Yu, J. A heat driven elastocaloric cooling system. *Energy* **182**, 881–899 (2019).

[70] Ianniciello, L., Bartholome, K., Fitger, A. & Engelbrecht, K. Long life elastocaloric regenerator operating under compression. *Applied Thermal Engineering* **202**, 117838 (2022).

[71] Chluba, C. *et al.* Ultralow-fatigue shape memory alloy films. *Science* **348**, 1004–1007 (2015).

[72] Bechtold, C., Chluba, C., Lima de Miranda, R. & Quandt, E. High cyclic stability of the elastocaloric effect in sputtered tinicu shape memory films. *Applied Physics Letters* **101** (2012).

[73] Ossmer, H. *et al.* Evolution of temperature profiles in tini films for elastocaloric cooling. *Acta materialia* **81**, 9–20 (2014).

[74] Chluba, C., Ossmer, H., Zamponi, C., Kohl, M. & Quandt, E. Ultra-low fatigue quaternary tini-based films for elastocaloric cooling. *Shape Memory and Superelasticity* **2**, 95–103 (2016).

[75] Xiao, F. *et al.* Martensitic transformation and elastocaloric effect of ti–ni–cu–al microwire. *Materialia* **9**, 100547 (2020).

[76] Liang, X. *et al.* Elastocaloric effect induced by the rubber-like behavior of nanocrystalline wires of a ti-50.8 ni (at.%) alloy. *Scripta Materialia* **134**, 42–46 (2017).

[77] Schmidt, M., Schütze, A. & Seelecke, S. Elastocaloric cooling processes: The influence of material strain and strain rate on efficiency and temperature span. *APL Materials* **4** (2016).

[78] Fedotov, S. Y., Morozov, E., Koledov, V., Shavrov, V. & Shelyakov, A. Studying the elastocaloric effect in a fast-quenched ti 2 nicu ribbon with the shape memory effect. *Bulletin of the Russian Academy of Sciences: Physics* **81**, 1374–1376 (2017).

[79] Villa, E. *et al.* Tailoring thermomechanical treatment of ni-fe-ga melt-spun ribbons for elastocaloric applications. *Journal of Materials Research and Technology* **8**, 4540–4546 (2019).

[80] Xiao, F., Jin, M., Liu, J. & Jin, X. Elastocaloric effect in ni50fe19ga27co4 single crystals. *Acta Materialia* **96**, 292–300 (2015).

[81] Yang, Z., Cong, D., Sun, X., Nie, Z. & Wang, Y. Enhanced cyclability of elastocaloric effect in boron-microalloyed ni-mn-in magnetic shape memory alloys. *Acta Materialia* **127**, 33–42 (2017).

[82] Zhang, K., Kang, G. & Sun, Q. High fatigue life and cooling efficiency of niti shape memory alloy under cyclic compression. *Scripta Materialia* **159**, 62–67 (2019).

[83] Wu, Y., Ertekin, E. & Sehitoglu, H. Elastocaloric cooling capacity of shape memory alloys–role of deformation temperatures, mechanical cycling, stress hysteresis and inhomogeneity of transformation. *Acta Materialia* **135**, 158–176 (2017).

[84] Imran, M. & Zhang, X. Elastocaloric effects in polycrystalline ni-fe-ga foams with hierarchical pore architecture. *Physical Review Materials* **4**, 065403 (2020).

[85] Imran, M., Zhang, X., Qian, M. & Geng, L. Enhancing the elastocaloric cooling stability of nifega alloys via introducing pores. *Advanced Engineering Materials* **22**, 1901140 (2020).

[86] Imran, M. & Zhang, X. Ferromagnetic shape memory ni-fe-ga alloy foams for elastocaloric cooling. *Journal of Physics D: Applied Physics* **53**, 245503 (2020).

[87] Qi, H. J. & Boyce, M. C. Stress–strain behavior of thermoplastic polyurethanes. *Mechanics of materials* **37**, 817–839 (2005).

[88] Sui, T., Baimpas, N., Dolbnya, I. P., Prisacariu, C. & Korsunsky, A. M. Multiple-length-scale deformation analysis in a thermoplastic polyurethane. *Nature communications* **6**, 6583 (2015).

[89] Guyomar, D. *et al.* Elastocaloric modeling of natural rubber. *Applied thermal engineering* **57**, 33–38 (2013).

[90] Yoshida, Y., Yuse, K., Guyomar, D., Capsal, J.-F. & Sebald, G. Elastocaloric effect in poly (vinylidene fluoride-trifluoroethylene-chlorotrifluoroethylene) terpolymer. *Applied Physics Letters* **108** (2016).

[91] Greibich, F. *et al.* Elastocaloric heat pump with specific cooling power of 20.9 w g–1 exploiting snap-through instability and strain-induced crystallization. *Nature Energy* **6**, 260–267 (2021).

[92] Xie, Z., Sebald, G. & Guyomar, D. Elastocaloric effect dependence on pre-elongation in natural rubber. *Applied Physics Letters* **107** (2015).

[93] Coativy, G. *et al.* Elastocaloric properties of thermoplastic polyurethane. *Applied Physics Letters* **117** (2020).

[94] Bennacer, R., Liu, B., Yang, M. & Chen, A. Refrigeration performance and the elastocaloric effect in natural and synthetic rubbers. *Applied Thermal Engineering* **204**, 117938 (2022).

[95] Dart, S. & Guth, E. Rise of temperature on fast stretching of butyl rubber. *The Journal of Chemical Physics* **13**, 28–36 (1945).

[96] Tosaka, M. Strain-induced crystallization of crosslinked natural rubber as revealed by x-ray diffraction using synchrotron radiation. *Polymer journal* **39**, 1207–1220 (2007).

[97] Xie, Z., Sebald, G. & Guyomar, D. Comparison of direct and indirect measurement of the elastocaloric effect in natural rubber. *Applied Physics Letters* **108** (2016).

[98] Kitanovski, A. & Egolf, P. W. Thermodynamics of magnetic refrigeration. *International Journal of Refrigeration* **29**, 3–21 (2006).

[99] Ossmer, H., Chluba, C., Kauffmann-Weiss, S., Quandt, E. & Kohl, M. Tini-based films for elastocaloric microcooling—fatigue life and device performance. *APL Materials* **4** (2016).

[100] Johra, H. & Bahl, C. Innovative heating and cooling systems based on caloric effects: A review. In *CLIMA 2022 conference* (2022).

[101] Wang, K., Engelbrecht, K. & Bahl, C. R. Additive manufactured thermoplastic elastomers for low-stress driven elastocaloric cooling. *Appl. Mater. Today* **30**, 101711 (2023).

[102] Ossmer, H. & Kohl, M. Elastocaloric cooling: Stretch to actively cool. *Nature Energy* **1**, 1–2 (2016).

[103] Bruederlin, F., Bumke, L., Quandt, E. & Kohl, M. Cascaded sma-film based elastocaloric cooling. In *2019 20th International Conference on Solid-State Sensors, Actuators and Microsystems & Eurosensors XXXIII (TRANSDUCERS & EUROSENSORS XXXIII)*, 1467–1470 (IEEE, 2019).

[104] Chen, Y., Wang, Y., Sun, W., Qian, S. & Liu, J. A compact elastocaloric refrigerator. *The Innovation* **3** (2022).

[105] Snodgrass, R. & Erickson, D. A multistage elastocaloric refrigerator and heat pump with 28 k temperature span. *Scientific reports* **9**, 18532 (2019).

[106] Zhou, G., Zhu, Y., Yao, S. & Sun, Q. Giant temperature span and cooling power in elastocaloric regenerator. *Joule* **7**, 2003–2015 (2023).

[107] Sebald, G. *et al.* High-performance polymer-based regenerative elastocaloric cooler. *Applied Thermal Engineering* **223**, 120016 (2023).

[108] Huang, B. *et al.* Development of an experimental rotary magnetic refrigerator prototype. *International Journal of Refrigeration* **104**, 42–50 (2019).

[109] Lei, T. *et al.* Passive characterization and active testing of epoxy bonded regenerators for room temperature magnetic refrigeration. *Applied Thermal Engineering* **128**, 10–19 (2018).

[110] Tušek, J., Kitanovski, A. & Poredoš, A. Geometrical optimization of packed-bed and parallel-plate active magnetic regenerators. *International Journal of Refrigeration* **36**, 1456–1464 (2013).

[111] Kamran, M. S. *et al.* Numerical investigation of room temperature magnetic refrigerator using microchannel regenerators. *Applied Thermal Engineering* **102**, 1126–1140 (2016).

[112] Pryds, N. *et al.* A monolithic perovskite structure for use as a magnetic regenerator. *Journal of the American Ceramic Society* **94**, 2549–2555 (2011).

[113] Wang, C. *et al.* Novel fabrication of honeycomb-like magnetocaloric regenerators via a self-organization process. *Scripta Materialia* **223**, 115067 (2023).

[114] Liang, J. *et al.* Performance assessment of a triangular microchannel active magnetic regenerator. *Appl. Therm. Eng.* **186**, 116519 (2021).

[115] Christiansen, C. D., Nielsen, K. K. & Bjørk, R. Functionally graded multi-material freeze-cast structures with continuous microchannels. *Journal of the European Ceramic Society* **40**, 1398–1406 (2020).

[116] Trevizoli, P. V. & Barbosa Jr, J. R. Entropy generation minimization analysis of oscillating-flow regenerators. *International Journal of Heat and Mass Transfer* **87**, 347–358 (2015).

[117] Shao, Y., Liu, Y., Wang, K., Zhang, M. & Liu, J. Impact of interface structure on functionality in hot-pressed la-fe-si/fe magnetocaloric composites. *Acta Materialia* **195**, 163–171 (2020).

[118] Radulov, I. A., Skokov, K. P., Karpenkov, D. Y., Braun, T. & Gutfleisch, O. Polymer-bonded la (fe, mn, si) 13 h x plates for heat exchangers. *IEEE Transactions on Magnetics* **51**, 1–4 (2015).

[119] Hou, H. *et al.* Elastocaloric cooling of additive manufactured shape memory alloys with large latent heat. *Journal of Physics D: Applied Physics* **50**, 404001 (2017).

[120] Navickaitė, K. *et al.* Experimental characterization of active magnetic regenerators constructed using laser beam melting technique. *Appl. Therm. Eng.* **174**, 115297 (2020).

[121] Stevens, E. *et al.* Mastering a 1.2 k hysteresis for martensitic para-ferromagnetic partial transformation in ni-mn (cu)-ga magnetocaloric material via binder jet 3d printing. *Additive Manufacturing* **37**, 101560 (2021).

[122] Sun, W. *et al.* Multicaloric effect in ni–mn–sn metamagnetic shape memory alloys by laser powder bed fusion. *Additive Manufacturing* **59**, 103125 (2022).

[123] Herzog, D., Seyda, V., Wycisk, E. & Emmelmann, C. Additive manufacturing of metals. *Acta Materialia* **117**, 371–392 (2016).

[124] Liu, Z. *et al.* Additive manufacturing of metals: Microstructure evolution and multistage control. *Journal of Materials Science & Technology* **100**, 224–236 (2022).

[125] Hou, H. *et al.* Fatigue-resistant high-performance elastocaloric materials made by additive manufacturing. *Science* **366**, 1116–1121 (2019).

[126] Wu, H. *et al.* Multi-functional ultem 1010 composite filaments for additive manufacturing using fused filament fabrication (fff). *Additive Manufacturing* **24**, 298–306 (2018).

[127] Tanikella, N. G., Wittbrodt, B. & Pearce, J. M. Tensile strength of commercial polymer materials for fused filament fabrication 3d printing. *Additive Manufacturing* **15**, 40–47 (2017).

[128] Gao, X. *et al.* Fused filament fabrication of polymer materials: A review of interlayer bond. *Additive Manufacturing* **37**, 101658 (2021).

[129] Fico, D., Rizzo, D., Casciaro, R. & Esposito Corcione, C. A review of polymer-based materials for fused filament fabrication (fff): focus on sustainability and recycled materials. *Polymers* **14**, 465 (2022).

[130] Valentine, A. D. *et al.* Hybrid 3d printing of soft electronics. *advanced Materials* **29**, 1703817 (2017).

[131] Adams, R. *et al.* A novel pathway for efficient characterisation of additively manufactured thermoplastic elastomers. *Mater. Des.* **180**, 107917 (2019).

[132] Dimitrienko, Y. I. *Nonlinear continuum mechanics and large inelastic deformations*, vol. 174 (Springer Science & Business Media, 2010).

[133] Bonet, J. & Wood, R. D. *Nonlinear continuum mechanics for finite element analysis* (Cambridge university press, 1997).

[134] Mihai, L. A. & Goriely, A. How to characterize a nonlinear elastic material? a review on nonlinear constitutive parameters in isotropic finite elasticity. *Proceedings of the Royal Society A: Mathematical, Physical and Engineering Sciences* **473**, 20170607 (2017).

[135] Treloar, L. R. Stress-strain data for vulcanized rubber under various types of deformation. *Rubber Chemistry and Technology* **17**, 813–825 (1944).

[136] Mooney, M. A theory of large elastic deformation. *Journal of applied physics* **11**, 582–592 (1940).

[137] Ogden, R. W. Large deformation isotropic elasticity–on the correlation of theory and experiment for incompressible rubberlike solids. *Proceedings of the Royal Society of London. A. Mathematical and Physical Sciences* **326**, 565–584 (1972).

[138] Gent, A. N. A new constitutive relation for rubber. *Rubber chemistry and technology* **69**, 59–61 (1996).

[139] Arruda, E. M. & Boyce, M. C. A three-dimensional constitutive model for the large stretch behavior of rubber elastic materials. *Journal of the Mechanics and Physics of Solids* **41**, 389–412 (1993).

[140] Yeoh, O. H. Some forms of the strain energy function for rubber. *Rubber Chemistry and technology* **66**, 754–771 (1993).

[141] Simo, J. C. & Hughes, T. J. *Computational inelasticity*, vol. 7 (Springer Science & Business Media, 2006).

[142] Chaves, E. W. *Notes on continuum mechanics* (Springer Science & Business Media, 2013).

[143] Alfonso, G. C. & Bras, W. *Polymer Crystallization II: From Chain Microstructure to Processing* (Springer International Publishing AG., 2017).

[144] Bruning, K., Schneider, K., Roth, S. V. & Heinrich, G. Kinetics of strain-induced crystallization in natural rubber studied by waxd: dynamic and impact tensile experiments. *Macromolecules* **45**, 7914–7919 (2012).

[145] Murakami, S., Senoo, K., Toki, S. & Kohjiya, S. Structural development of natural rubber during uniaxial stretching by in situ wide angle x-ray diffraction using a synchrotron radiation. *Polymer* **43**, 2117–2120 (2002).

[146] Toki, S. *et al.* Strain-induced molecular orientation and crystallization in natural and synthetic rubbers under uniaxial deformation by in-situ synchrotron x-ray study. *Rubber chemistry and technology* **77**, 317–335 (2004).

[147] Khiêm, V. N. & Itskov, M. Analytical network-averaging of the tube model: Strain-induced crystallization in natural rubber. *Journal of the Mechanics and Physics of Solids* **116**, 350–369 (2018).

[148] Silva, D. J., Ventura, J. & Araujo, J. P. Caloric devices: A review on numerical modeling and optimization strategies. *International Journal of Energy Research* **45**, 18498–18539 (2021).

[149] Nielsen, K. K. *et al.* Review on numerical modeling of active magnetic regenerators for room temperature applications. *International Journal of Refrigeration* **34**, 603–616 (2011).

[150] Engelbrecht, K. L., Nellis, G. F. & Klein, S. A. Predicting the performance of an active magnetic regenerator refrigerator used for space cooling and refrigeration. *Hvac&R Research* **12**, 1077–1095 (2006).

[151] Engelbrecht, K., Nellis, G. & Klein, S. *A numerical model of an active magnetic regenerator refrigeration system* (Springer, 2005).

[152] Lei, T. Modeling of active magnetic regenerators and experimental investigation of passive regenerators with oscillating flow. *Technical University of Denmark* (2016).

[153] Liang, J. Experimental and analytical study of active magnetic regenerators (2021).

[154] Nielsen, K. K. *et al.* Direct measurements of the magnetic entropy change. *Rev. Sci. Instrum.* **86** (2015).

[155] Jasmee, S. *et al.* Hydrophobicity performance of polyethylene terephthalate (pet) and thermoplastic polyurethane (tpu) with thermal effect. *Mater. Res. Express.* **5**, 096304 (2018).

[156] Bruère, V., Lion, A., Holtmannspoetter, J. & Johlitz, M. Under-extrusion challenges for elastic filaments: The influence of moisture on additive manufacturing. *Prog. Addit. Manuf.* **7**, 445–452 (2022).

[157] Greibich, F. *et al.* Elastocaloric heat pump with specific cooling power of 20.9 w g–1 exploiting snap-through instability and strain-induced crystallization. *Nat. Energy* **6**, 260–267 (2021).

[158] Zdrahala, R., Gerkin, R., Hager, S. & Critchfield, F. Polyether-based thermoplastic polyurethanes. i. effect of the hard-segment content. *Journal of Applied Polymer Science* **24**, 2041–2050 (1979).

[159] Stribeck, A., Eling, B., Pöselt, E., Malfois, M. & Schander, E. Melting, solidification, and crystallization of a thermoplastic polyurethane as a function of hard segment content. *Macromolecular Chemistry and Physics* **220**, 1900074 (2019).

[160] Nieto Simavilla, D., Schieber, J. D. & Venerus, D. C. Evidence of deformation-dependent heat capacity and energetic elasticity in a cross-linked elastomer subjected to uniaxial elongation. *Macromolecules* **51**, 589–597 (2018).

[161] Gent, A. & Zhang, L.-Q. Strain-induced crystallization and strength of rubber. *Rubber chemistry and technology* **75**, 923–934 (2002).

[162] Brüning, K., Schneider, K., Roth, S. V. & Heinrich, G. Kinetics of strain-induced crystallization in natural rubber: A diffusion-controlled rate law. *Polymer* **72**, 52–58 (2015).

[163] Candau, N. *et al.* Characteristic time of strain induced crystallization of crosslinked natural rubber. *Polymer* **53**, 2540–2543 (2012).

[164] Holzapfel, G. A. & Simo, J. Entropy elasticity of isotropic rubber-like solids at finite strains. *Comput. Methods Appl. Mech. Eng.* **132**, 17–44 (1996).

[165] Koch, C., Van Hulle, L. & Rudolph, N. Investigation of mechanical anisotropy of the fused filament fabrication process via customized tool path generation. *Addit. Manuf.* **16**, 138–145 (2017).

[166] Nasirov, A. & Fidan, I. Prediction of mechanical properties of fused filament fabricated structures via asymptotic homogenization. *Mechanics of Materials* **145**, 103372 (2020).

[167] Qian, S. *et al.* A review of elastocaloric cooling: Materials, cycles and system integrations. *International journal of refrigeration* **64**, 1–19 (2016).

[168] He, Y. & Sun, Q. Frequency-dependent temperature evolution in niti shape memory alloy under cyclic loading. *Smart Materials and Structures* **19**, 115014 (2010).

[169] Manosa, L., Planes, A., Vives, E., Bonnot, E. & Romero, R. The use of shape-memory alloys for mechanical refrigeration. *Functional Materials Letters* **2**, 73–78 (2009).

[170] Li, Y. *et al.* Energy-efficient elastocaloric cooling by flexibly and reversibly transferring interface in magnetic shape-memory alloys. *ACS applied materials & interfaces* **10**, 25438–25445 (2018).

[171] Qian, S., Ling, J., Hwang, Y., Radermacher, R. & Takeuchi, I. Thermodynamics cycle analysis and numerical modeling of thermoelastic cooling systems. *International Journal of Refrigeration* **56**, 65–80 (2015).

[172] Kabirifar, P. *et al.* Elastocaloric cooling: state-of-the-art and future challenges in designing regenerative elastocaloric devices. *Strojniski Vestnik/Journal of Mechanical Engineering* **65** (2019).

[173] Smith, T. L. Volume changes and dewetting in glass bead-polyvinyl chloride elastomeric composites under large deformations. *Transactions of the Society of Rheology* **3**, 113–136 (1959).

[174] Greaves, G. N., Greer, A. L., Lakes, R. S. & Rouxel, T. Poisson's ratio and modern materials. *Nature materials* **10**, 823–837 (2011).

[175] Clausen, A., Wang, F., Jensen, J. S., Sigmund, O. & Lewis, J. A. Topology optimized architectures with programmable poisson ' s ratio over large deformations. *Adv. Mater* **27**, 5523–5527 (2015).

[176] Sebald, G. *et al.* High-performance polymer-based regenerative elastocaloric cooler. *Appl. Therm. Eng.* 120016 (2023).

[177] Candau, N., Pradille, C., Bouvard, J.-L. & Billon, N. On the use of a four-cameras stereovision system to characterize large 3d deformation in elastomers. *Polymer Testing* **56**, 314–320 (2016).

[178] Prisacariu, C. *Polyurethane elastomers: from morphology to mechanical aspects* (Springer Science & Business Media, 2011).

[179] Chattopadhyay, D. & Webster, D. C. Thermal stability and flame retardancy of polyurethanes. *Progress in Polymer Science* **34**, 1068–1133 (2009).

[180] Yu, K., Xin, A., Feng, Z., Lee, K. H. & Wang, Q. Mechanics of self-healing thermoplastic elastomers. *Journal of the Mechanics and Physics of Solids* **137**, 103831 (2020).

[181] Rivlin, R. S. & Saunders, D. Large elastic deformations of isotropic materials vii. experiments on the deformation of rubber. *Philos. Trans. R. Soc.* **243**, 251–288 (1951).

[182] Haines, D. & Wilson, W. Strain-energy density function for rubberlike materials. *J. Mech. Phys. Solids* **27**, 345–360 (1979).

[183] Wang, Y. *et al.* Simplification of hyperelastic constitutive model and finite element analysis of thermoplastic polyurethane elastomers. *Macromol. Theory Simul.* **29**, 2000009 (2020).

[184] Upadhyay, K., Subhash, G. & Spearot, D. Thermodynamics-based stability criteria for constitutive equations of isotropic hyperelastic solids. *J. Mech. Phys. Solids* **124**, 115–142 (2019).

[185] Pelliciari, M., Sirotti, S. & Tarantino, A. M. A strain energy function for large deformations of compressible elastomers. *J. Mech. Phys. Solids* **176**, 105308 (2023).

[186] Beatty, M. F. & Stalnaker, D. O. The poisson function of finite elasticity. *J. Appl. Mech.* **53**, 807–813 (1986).

[187] Rivlin, R. S. Large elastic deformations of isotropic materials iv. further developments of the general theory. *Trans. R. Soc. Lond. Ser. A Math. Phys. Sci.* **241**, 379–397 (1948).

[188] Ogden, R. W. *Non-linear elastic deformations* (Courier Corporation, 1997).

[189] Brighenti, R. Numerical buckling analysis of compressed or tensioned cracked thin plates. *Eng. Struct.* **27**, 265–276 (2005).

[190] Bergström, J. S. & Boyce, M. C. Constitutive modeling of the large strain time-dependent behavior of elastomers. *J. Mech. Phys. Solids* **46**, 931–954 (1998).

[191] Wang, K., Overvelde, J. T. B., Engelbrecht, K., Bjørk, R. & Bahl, C. R. H. Data set for "volume compensation of large-deformation 3d-printed soft elastomeric elastocaloric regenerators". *data.dtu.dk* (2023).

[192] Petersen, T. F. *et al.* Comparison between a 1d and a 2d numerical model of an active magnetic regenerative refrigerator. *Journal of Physics D: Applied Physics* **41**, 105002 (2008).

[193] Kalizan, J. & Tušek, J. Caloric micro-cooling: Numerical modelling and parametric investigation. *Energy conversion and management* **225**, 113421 (2020).

[194] Zhu, Y., Zhou, G., Cheng, S., Sun, Q. & Yao, S. A numerical study of elastocaloric regenerators of tubular structures. *Applied Energy* **339**, 120990 (2023).

[195] Tušek, J., Kitanovski, A., Prebil, I. & Poredoš, A. Dynamic operation of an active magnetic regenerator (amr): Numerical optimization of a packed-bed amr. *International Journal of Refrigeration* **34**, 1507–1517 (2011).

[196] Tušek, J., Engelbrecht, K., Mañosa, L., Vives, E. & Pryds, N. Understanding the thermodynamic properties of the elastocaloric effect through experimentation and modelling. *Shape Memory and Superelasticity* **2**, 317–329 (2016).

[197] Xie, Z., Sebald, G. & Guyomar, D. Comparison of elastocaloric effect of natural rubber with other caloric effects on different-scale cooling application cases. *Applied Thermal Engineering* **111**, 914–926 (2017).

[198] Huang, W. On the selection of shape memory alloys for actuators. *Materials & design* **23**, 11–19 (2002).

[199] Jacobsson, P. & Sundqvist, B. Thermal conductivity and electrical resistivity of gadolinium as functions of pressure and temperature. *Physical Review B* **40**, 9541 (1989).

[200] Bahl, C. R. *et al.* Operational test of bonded magnetocaloric plates. *International Journal of Refrigeration* **76**, 245–251 (2017).

[201] Legait, U., Guillou, F., Kedous-Lebouc, A., Hardy, V. & Almanza, M. An experimental comparison of four magnetocaloric regenerators using three different materials. *International journal of refrigeration* **37**, 147–155 (2014).

[202] Bejan, A. *Entropy generation minimization: the method of thermodynamic optimization of finite-size systems and finite-time processes* (CRC press, 2013).

[203] Shah, R. K. & London, A. L. *Laminar flow forced convection in ducts: a source book for compact heat exchanger analytical data* (Academic press, 2014).

[204] Engelbrecht, K., Bahl, C. R. H. & Nielsen, K. K. Experimental results for a magnetic refrigerator using three different types of magnetocaloric material regenerators. *International Journal of refrigeration* **34**, 1132–1140 (2011).

[205] Maier, L. M. *et al.* Active magnetocaloric heat pipes provide enhanced specific power of caloric refrigeration. *Communications Physics* **3**, 186 (2020).

APPENDIX A

List of publications

The following articles are published or under preparation during the period of this PhD project. For easier reference, the status of the articles has been updated in 2023 after the end of the PhD project. The articles are divided into different sections based on their status and content. The roman numbers enumerate the scientific articles in chronological order and they are used as references in the main text.

A.1 Articles published or under preparation

I **K. Wang**, K. Engelbrecht, and C. R. H. Bahl. Additive manufactured thermoplastic elastomers for low-stress driven elastocaloric cooling. *Applied Materials Today*, 30, 101711, (2023).

II **K. Wang**, J. T. B. Overvelde, K. Engelbrecht, R. Bjørk, and C. R. H. Bahl. Volume compensation of large-deformation 3D-printed soft elastomeric elastocaloric regenerators. *Applied Physics Letters*, 123, 223904, (2023).

III **K. Wang**, K. Engelbrecht, C. R.H. Bahl, and R. Bjørk. Full-scale 3D-printed soft regenerative elastocaloric cooling. Under preparation (2023).

IV **K. Wang**, K. Engelbrecht, C. R.H. Bahl, and R. Bjørk. Numerical modelling for soft regenerative elastocaloric cooling with volume compensation. Under preparation (2023).

A.2 Other published peer-reviewed articles

V B. G. F. Eggert, **K. Wang**, S. Jafarzadeh, C. R. H. Bahl, B. C. Hauback, C. Frommen. Study of the magnetostructural transition in critical-element free Mn1-xNi1-xFe2xSi0.95Al0.05. *AIP Advances*, 13, (2), (2023).

A.3 Conference presentations

VI **K. Wang**, K. Engelbrecht, C. R. H. Bahl, R. Bjørk. 3D-printed soft regenerators for low-stress elastocaloric cooling. *Dresden Days on Magnetocalorics*, Oral presentation, 2023, Dresden, Germany.

VII **K. Wang**, K. Engelbrecht, C. R. H. Bahl. 3D-printed Elastocaloric Regenerator . *DTU PhD symposium*, Poster, 2022, Copenhagen, Denmark.

APPENDIX B

Scripts

The scripts implemented in this PhD thesis are mainly based the APDL scripts for FE simulations, and the MATLAB scripts for numerical AER simulations.

The MATLAB scripts are improved by defining some functions to include the regenerator volume changes and time-dependent spatial nodes. In this PhD thesis, the main calculation parts for the sparse matrix solving and heat transfer functions are based on the MATLAB codes, developed by my supervisor Kurt Engelbrecht for the Active Magnetic Regenerative Refrigerator [151], at the University of Wisconsin - Madison.

The APDL scripts for FE simulations used in this PhD thesis are inspired by the scripts for a 2D rubber HoleySheet compression example, developed by Johannes T. B. Overvelde. The scripts are created when the author was external-staying in the soft robotic matter group at the AMOLF institute, Netherlands.

B.1 APDL scripts for FE simulations

Here, an example of the APDL codes for the fluid channel volume change simulations of a parallel-plates regenerator is given in the attached PDF.

C:\Programs\APDL_Workspace\MyModels\PP2Chan18.srm

```
!This is the ANSYS APDL codes for the fluid channel volume change simulations of the parallel-plates regenerator;
!The deformed and initial fluidic channels are exported to matlab for the volume change calculations;
!The material information are obtained by the fitting for the TPU mechanical behavior;
!The scripts are created when the author was external-staying in the soft robotic matter group in AMOLF institute, Netherlands,
!which is inspired by the scripts for a 2D rubber HoleySheet compression example by J.T.B. Overvelde.

!Created by Kun Wang, May 2023

/clear
Finish,
!/INQUIRE, maindir, DIRECTORY ! gets main directory name
!srm ! initializes macro
l
!!!!!!!!!!!!!!!!!!!!!!!!
! PARAMETER DEFINITION !
!!!!!!!!!!!!!!!!!!!!!!!!

! material parameters (using same material properties)


! Define geometric parameters
pi = 3.141592653589793 ! universal ratio circle perimeter to radius

LL=15 !dogbone gauge length
L0=81.2 !dogbone total length
DD=L0-44 !dogbone length included the arc zone
W=20 !width of the middle rectangular area
W0=27.41 !width of the dogbone clamped area
R1=5 !first radius of the arc close to the middle area
R2=8 !second radius of the arc close to the clamped area
T=5 !dogbone thickness

!for the honeycomb and cylinder channel
!d_hole=0.6 !circular channel diameter

CUTX=0 !offset along x direction
CUTY=0 !offset ablong Y direction
n=18 !circle num along x
m=1 !circle num along y
Edgex_t=0.5 !the thickness between the channel and the wall outside x axis
Edgey_t=0.5 !the thickness between the channel and the wall outside y axis


!calculate x and y by number
!for the rectangurlar channel define the width XX, and height YY
*IF, n, EQ, 1, THEN
   XX = W-Edgex_t*2
   Offet_x = W !set x increment to width
   Wx_edge=Edgex_t !set x initial coordinate
```

```
*ELSE
   XX = (W-Edgex_t*2)/(2*n-1)
   Wx_edge=Edgex_t !set x initial coordinate
   Offet_x = XX*2 !set x increment
*ENDIF

*IF, m, EQ, 1, THEN
   YY = T-Edgey_t*2
   Offet_y = T !set y increment to thickness
   Wy_edge=Edgey_t !set y initial coordinate
*ELSE
   YY = (T-Edgey_t*2)/(2*m-1)
   Wy_edge=Edgey_t !set y initial coordinate
   Offet_y = YY*2 !set y increment
*ENDIF


!loading parameters
Strain = 6 !600% strain, can be input

! meshing parameters
Middle_element = 0.8
Round_element = 0.5
Clamped_element = 2

! solver parameters
nb_steps = 60

! general
filename = 'dogbone3D_PP'
!/inp,parameter,inp ! if commented, parameter values defined hereabove are used. Otherwise,
parameter values defined in parameter.inp are used

!Inverse colors (white background)
/RGB,INDEX,100,100,100, 0
/RGB,INDEX, 80, 80, 80,13
/RGB,INDEX, 60, 60, 60,14
/RGB,INDEX, 0, 0, 0,15

/PREP7

!!!!!!!!!!!!!!!!!!!!!!!!!!!!!!!!!!!!!!!!!!
! MATERIAL AND ELEMENT TYPE DEFINITION !
!!!!!!!!!!!!!!!!!!!!!!!!!!!!!!!!!!!!!!!!!!

! define elements type
ET, 1, 187 ! solid 3D 10-node element (quadratic)

! hyperelastic material
TB, HYPER, matid, 1, 3, OGDEN
TBDATA, 1, 1.15874
TBDATA, 2, 1.42562
TBDATA, 3, 0.00980809
TBDATA, 4, 5.8589
TBDATA, 5, -0.167398
TBDATA, 6, -2.67747
```

```
TBDATA, 7, 0.04
TBDATA, 8, 0
TBDATA, 9, 0

!!!!!!!!!!!!!!!!!!!!!!
! GEOMETRY DEFINITION !
!!!!!!!!!!!!!!!!!!!!!!

! auxiliary geometric parameters (see meaning from drawing)
xx03=LL/2 !x of K3
yy03=W/2
!xx05=DD/2 !x of K5
yy05=W0/2
px1=xx03 !x of P1(center of the arc 1)
py1=yy03+R1
!px2=xx05 !x of P2(center of the arc 2)
py2=yy05-R2

deltaY=py1-py2 !y distance between two arc centers
!deltaX=px2-px1 !x distance between two arc centers
deltaX=sqrt((R1+R2)*(R1+R2)-deltaY*deltaY) !x distance between two arc centers
px2=px1+deltaX
xx05=px2
sinAlpha=deltaY/(R1+R2)
cosAlpha=deltaX/(R1+R2)

xx04=px1+R1*cosAlpha
yy04=py1-R1*sinAlpha

! keypoints (see drawing)
K, 1, 0, 0
K, 2, 0, W/2
K, 3, xx03, yy03
K, 4, xx04, yy04
K, 5, xx05, yy05
K, 6, L0/2, W0/2
K, 7, L0/2, 0
K, 8, px1, py1
K, 9, px2, py2


! lines (arcs and straight lines)
LARC, 3, 4, 8, R1
LARC, 4, 5, 9, R2
L, 1, 2
L, 2, 3
L, 5, 6
L, 6, 7
L, 7, 1

!AREA
AL, 1, 2, 3, 4, 5, 6, 7
ARSYM,Y,ALL !(select the normal axis of the symmetry plane)
!ARSYM,X,ALL

NUMCMP, LINE !renumbering the lines
```

```
NUMCMP, AREA !renumbering the lines
AADD,ALL
ASEL,ALL
CM, dogbone_draw, AREA
!Selecting all area for extruding
VEXT, dogbone_draw,,,0,0,T

!Create channels
!K, 200, 0, W/4, T/2
Extendx=15
WPROTA,,,-90, !working planes rontating -90 degree
WPOFFS,,W/2,, !WP offset y W/2
WPROTA,-90,,, !working planes rontating -90 degree using z-axis
!!!!!now the work plane move to left-bottom
!Create circles
i=0
*do, x, Wx_edge, W, Offet_x
     *do, y, Wy_edge, T, Offet_y
        !CYL4, x, y, d_hole/2, , , ,-(LL/2+10)
        BLC4, x, y, XX, YY, -(LL/2+Extendx)
    *enddo
*enddo

!Remove channels from dogbone
FLST,3,n*m,5,ORDE,2
FITEM,3,2
FITEM,3,-(n*m+1)

!substract volume from volume
VSBV,1,P51X

!VSYMM,X,ALL !create volumes via symmetry (select the normal axis of the symmetric plane)
!VADD,ALL !combining all volumes into one entity
NUMCMP, LINE !renumbering the lines
NUMCMP, AREA !renumbering the areas
NUMCMP, VOLU !renumbering the volume

!partition the volume before meshing (Scheme 1)
WPOFFS,,,-LL/2 !working planes offset along Z
VSBW, ALL !partition volume by YX
WPOFFS,,,-(xx05-LL/2) !working planes offset along Z
VSBW, ALL !partition volume by YX
WPOFFS,,,xx05 !back to initial position (center)

!combing the areas of middle and ends
VSEL, ALL
ASEL, S, LOC, X, 0
AADD, ALL

VSEL, ALL
ASEL, S, LOC, X, L0/2
AADD, ALL

!!!!partition the volume before meshing (Scheme2)
!WPOFFS,,,-(xx05) !working planes offset along Z
!VSBW, ALL !partition volume by YX
```

```
!WPOFFS,,,(xx05)*2 !working planes offset along Z
!VSBW, ALL !partition volume by YX
!WPOFFS,,,-(xx05) !back to initial position (center)

!!!!!!!!!!!!!!!!!!!!!!
!!!!!!! Meshing !!!!!!!
!!!!!!!!!!!!!!!!!!!!!!
VSEL,S, LOC, X, 0, LL/2
CM, MidVol, VOLU
VSEL,S, LOC, X, LL/2, xx05
CM, RoundVol, VOLU

!!!!Define the channel surface
VSEL, ALL
ASEL, S, LOC, X, 0, LL/2+Extendx !select the areas for the channels in longitudinal dirction
!CM, MidArea, AREA
ASEL, R, LOC, Y, -(W-0.001*Edgex_t)/2, (W-0.001*Edgex_t)/2 !among those, select the channels
surfaces in y direction
ASEL, R, LOC, Z, 0.001*Edgey_t, T-0.001*Edgey_t !among those, select the channels surfaces in
y direction
ASEL, U, LOC, X, LL/2 !unselect the two interface between the middle/round volumes
ASEL, U, LOC, X, LL/2+Extendx !unselect the two interface between the middle/round volumes
ASEL, U, LOC, X, xx05 !unselect the two interface between the middle/round volumes
ASEL, U, LOC, X, 0 !unselect the two interface between the middle/round volumes

CM, ChannelSurf, AREA
!CMPLOT, ChannelSurf, ,'ONLY' !show the user defined channel surface to check

VATT, 1,,1,, !associate material #1 and element type #1 to unmeshed volumes
MSHKEY, 0 !Specifies whether free meshing or mapped meshing
          !0: free, 1: mapped
MSHAPE, 1,3D !0:Cuadrilat 1:Trianglar

! mesh control for Channels
CMSEL, S, ChannelSurf, AREA
AESIZE, ALL, XX/1.5
!SMRTSIZE, 1

CMSEL, S, MidVol, VOLU
!SMRTSIZE, 3
ESIZE, Middle_element
VMESH, MidVol
!AREFINE, ALL, 3, SMOOTH, OFF

!!!!!!!!!!!!!!!!!!!!!!!!!!!!!
CMSEL, S, RoundVol, VOLU
ESIZE, Round_element
!!!!!CHKMSH,'VOLU'
VMESH,RoundVol
VSEL,ALL
ESIZE, Clamped_element !element size
VMESH,ALL !Meshing all

!define the channel's nodes for postprocessing
CMSEL, S, ChannelSurf, AREA
NSLA, S, 0
CM, Channel_nodes, NODE
```

```
272
273 CMSEL, S, ChannelSurf, AREA
274 NSLA, S, 0
275 CM, Channel_elements, ELEM
276
277
278
279 !!!!!!!!!!!!!!!!!!!!!!!!!!!!!!!!
280 ! BOUNDARY CONDITION DEFINITION !
281 !!!!!!!!!!!!!!!!!!!!!!!!!!!!!!!!
282
283 !Constrains (Clamped side, fixed all the DOF)
284 NSEL, S, LOC, X, 0
285 CM, Cross_Section, NODE
286 D, ALL, UX, 0.0
287
288 ! x-displacement constraint for left side
289 NSEL, S, LOC, X,(LL/2+Extendx+2), (L0/2)
290 CM, Stretched_body_nodes, NODE
291 D, ALL, UY, 0.0
292 D, ALL, UZ, 0.0
293
294
295 NSEL, S, LOC, X, (L0/2)
296 CM, Stretched_edge_nodes, NODE
297 D, ALL, UX, LL*2*0.5
298
299 !!!!!!!!!!!!
300 ! SOLUTION !
301 !!!!!!!!!!!!
302
303 /SOLU
304 ANTYPE, STATIC ! static analysis
305
306 ! taking geometric nonlinearities into account
307 ! in this case: large displacement and large strains because hyperelastic elements are used
308 NLGEOM, ON
309
310 NSUBST, nb_steps ! number of substeps
311 OUTRES, ALL, ALL
312 ALLSEL, ALL
313 SOLVE
314
315
316
317 /POST1
318 ! computing total reaction force and displacement and saving them in files
319 !*USE,OUTPUT_RF,'Stretched_edge_nodes'
320
321 !extract channel nodes
322 CMSEL, S, Channel_nodes, NODE
323 *GET,nNodes,NODE,ALL,COUNT   ! Number of nodes
324 iNode = 0
325 *CFOPEN, %filename%_Results_step1_strain600, csv
326 *DO, j, 0, nNodes-1
327    iNode = NDNEXT(iNode)   ! Select next node
```

```
   *GET,locX,NODE,iNode,LOC,X
   *GET,locY,NODE,iNode,LOC,Y
   *GET,locZ,NODE,iNode,LOC,Z
   *GET,dispX,NODE,iNode,U,X
   *GET,dispY,NODE,iNode,U,Y
   *GET,dispZ,NODE,iNode,U,Z
    ! ('Node Num X Y Z UX UY UZ')
   *VWRITE,locX,locY,locZ,dispX,dispY,dispZ,forceX,forceY,forceZ
   %G, %G, %G, %G, %G, %G, %G, %G, %G
*ENDDO
*CFCLOSE
FINISH
```

APPENDIX C

Experiment Instructions

C.1 Watertight Treatment for Regenerators

The water tightness of the regenerator is crucial to the regenerator operating on a regenerative flow system. Our preliminary regenerators were fabricated using NinjaFlex 85A TPU, which is 3D printed on a Zmorph printer. However, when displacing oscillating fluid (water) periods inside regenerators, the printing deficiency leads to leakage of the regenerator. Several different type glues were implement to seal the 3D-printed regenerator. Among them, a polyurethane based glue exhibits a satisfactory attachment with the TPU regenerator. Figure C.1 shows a glued regenerator. Prior to gluing, the regenerator underwent 20 cycles of training. Unfortunately, owing to glue rupture after hundreds of cycles and fractures on the regenerator surface, leakage occurs easily.

The water tightness is achieved in 3D-printed regenerators based on FilaFlex TPU fabricated on a Flix Tex 3D-printer, as depicted in Figure C.2. The tightness is tested by inflating a sealed regenerator in the water using a syringe, to see if there

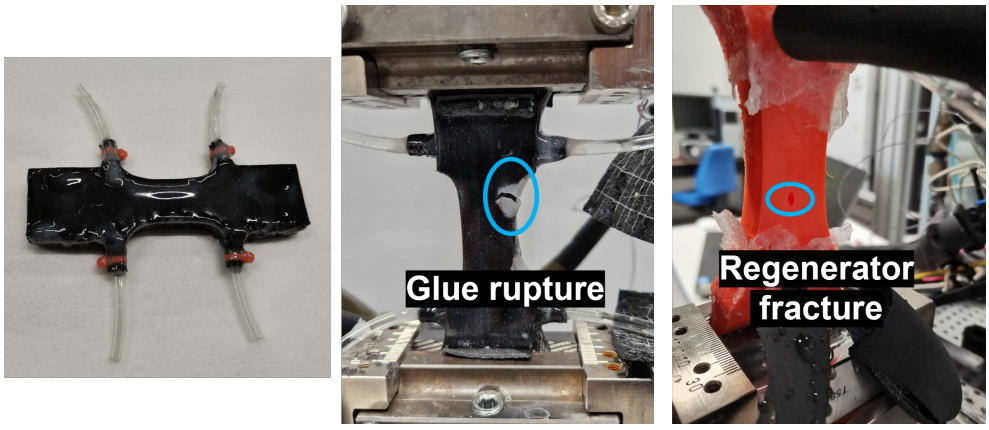

Figure C.1. A glued 3D-printed regenerator based on NinjaFlex TPU and the associated challenges of leakage

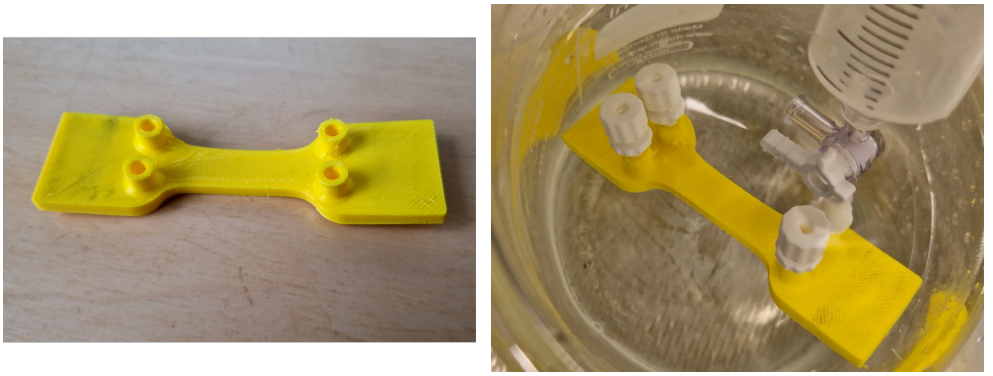

Figure C.2. A 3D-printed regenerator based FilaFlex TPU and tightness examination

are leaking bubbles.

C.2 Regenerator Processing

Figure C.3 shows the process of 3D printing on a Flix Tex 3D-printer and a top view for the heat transfer microchannels.

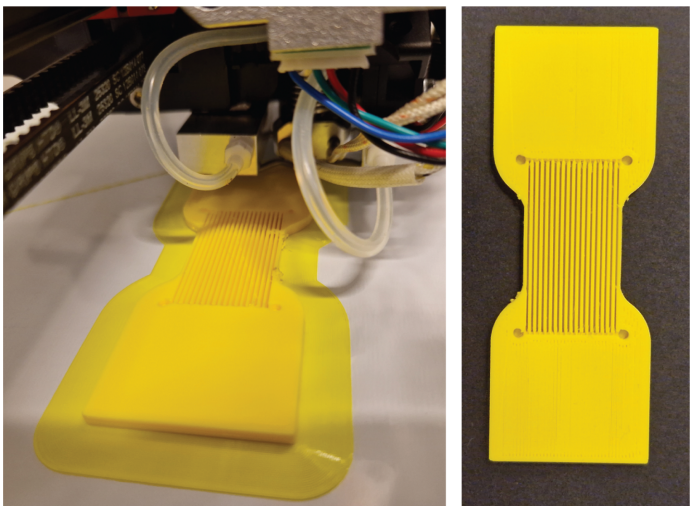

Figure C.3. 3D printing for a parallel plate regenerator

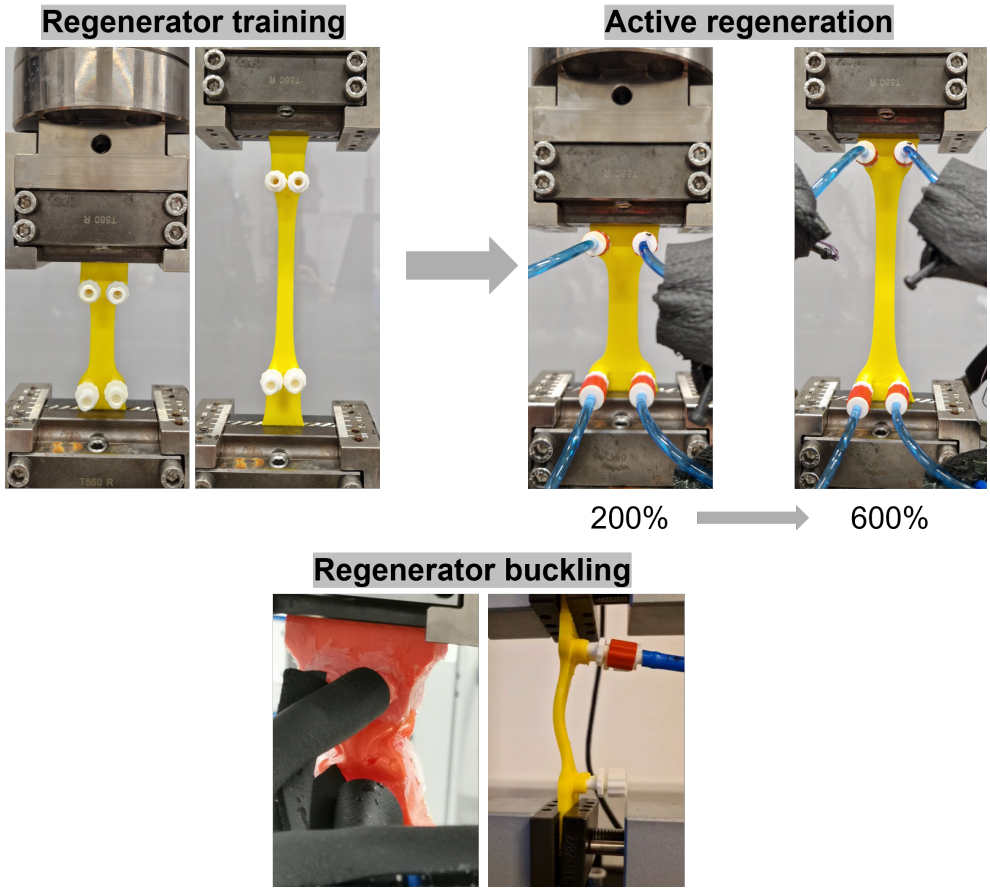

Figure C.4. Operation for large-deformation soft regenerators, including prior mechanical training, active regeneration, and potential buckling

C.3 Large-deformation regenerator operation

Before regenerators are implemented for active elastocaloric applications, the 3D printed regenerator is subjected to more than 20 time mechanical training to introducing the irreversible deformation and avoiding the Mullins effect, as dipected in Figure C.4. A pre-strain is introduced during the active regeneration. The regenerator buckling from irreversible deformation can be avoided (see the buckling due to insufficient pre-strain in Figure C.4).

C.4 Active elastocaloric Flow System Instructions

The specific working principles of the compensation flow system are shown in Figure C.5, associated with the four operation steps in an active cycle.

At step 1, in relation to the hot-to-cold blow, the solenoid valves (SV) T2 and T4 are open. The linear actuator drives the hot displacer moving up, to extract the eCE cooling load generated inside the regenerator to the cold side. At step 2, in relation to the loading process, the non-compensation scheme refuses the fluids flowing into the regenerator from the flow system, where all the SVs are closed. In contrast, the compensation scheme, opening the SV T4, allows the passive fluids from the hot reservoir to compensate the regenerator volume changes.

At step 3, in relation to the cold-to-hot blow, the solenoid valves (SV) T1 and T3 are open. The linear actuator drives the cold displacer moving down, to extract the eCE heating load generated inside the regenerator to the hot side. At step 4, in relation to the unloading process, the non-compensation scheme refuses the fluids flowing from the flow system, where all the SVs are closed. In contrast, the compensation scheme, opening the SV T3, allows the extra fluids passively expelling into the hot reservoir. See details from the SV indication chart in Figure C.5.

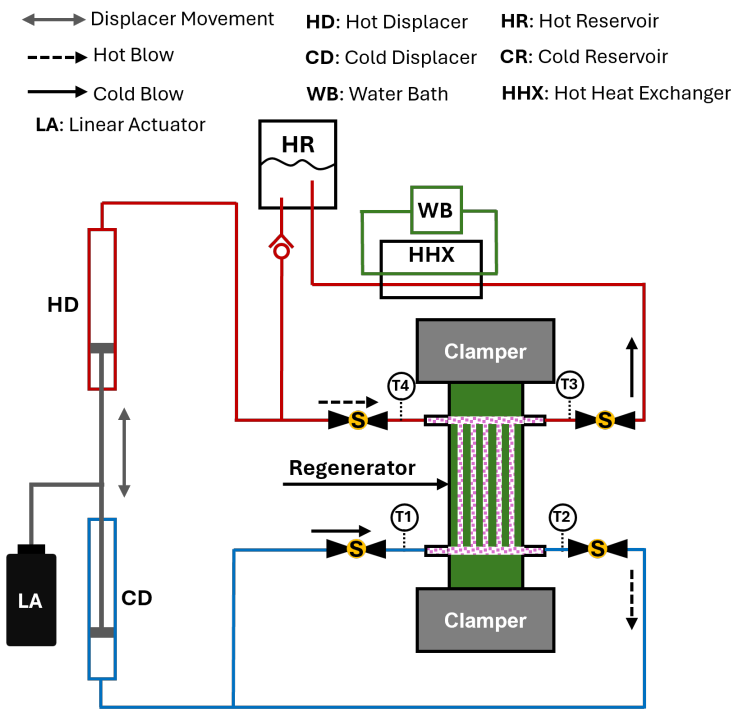

Steps	Actions	Material temperature	Channel volume	Heat-transfer flows (solid arrows) & valve states	Compensation flows (dash arrows) & valve states
1	—	↑ (convection)	V_i	T4 to T2 T1 T2 T3 T4 ● ○ ● ○	—
2	Loading	↑ (eCE)	V_f	—	Non-compensation (close all) T1 T2 T3 T4 ● ● ● ● Compensated $V_f - V_i$ from T4 T1 T2 T3 T4 ● ● ● ○
3	—	↓ (convection)	V_f	T1 to T3 T1 T2 T3 T4 ○ ● ○ ●	—
4	Unloading	↓ (eCE)	V_i	—	Non-compensation (close all) T1 T2 T3 T4 ● ● ● ● Expelled Vf – Vi to T3 T1 T2 T3 T4 ● ● ○ ●

Figure C.5. Valve indications for the compensation/non-compensation cooling flow system. In the chart, the black circle indicates the valve open, and the black dot indicates the valve close.

APPENDIX D

Journal articles

The following contains published articles supporting this PhD thesis. For a full list of publications, see **Appendix A**. The supplementary material is only appended for the articles where it is relevant for the thesis. Instead, I refer to the website of the publisher for supplementary material.

I

ARTICLE

D.1 Articles I

K. Wang *et al.*
Additive manufactured thermoplastic elastomers for low-stress driven elastocaloric cooling
Appl. Mater. Today (2023), https://doi.org/10.1016/j.apmt.2022.101711

Applied Materials Today 30 (2023) 101711

Contents lists available at ScienceDirect

Applied Materials Today

journal homepage: www.elsevier.com/locate/apmt

Additive manufactured thermoplastic elastomers for low-stress driven elastocaloric cooling

Kun Wang *, Kurt Engelbrecht, Christian R.H. Bahl

Department of Energy Conversion and Storage, Technical University of Denmark, Anker Engelunds Vej 301, Kongens Lyngby 2800, Denmark

ARTICLE INFO

Keywords:
Elastocaloric cooling
Additive manufacturing
Elastomers
Low-stress
Strain-induced crystallization (SIC)

ABSTRACT

Exploiting the strain-induced crystallization of soft elastomeric polymers elastocaloric cooling has recently been explored as an environmental-friendly alternative to conventional refrigeration. Elastomers require a much lower applied stress to induce the elastocaloric effect compared to shape memory alloys. Several prototype coolers employing these soft polymers have been demonstrated to achieve a moderate temperature span under lower stresses. Here, we investigate the elastocaloric properties and potential cooling performance of five thermoplastic elastomers that can be 3D printed, both in the form of filaments and as Additive Manufactured (AM) parts. The materials were first characterized as filaments to screen for the elastomers with the highest elastocaloric effects. A large adiabatic temperature change of 17.8 K was obtained in the Ultimaker98A filament. AM parameters were optimized to achieve parts with satisfactory functional stability while maintaining their elastocaloric effect. As a printed part, NinjaFlex achieved a high material coefficient of performance (COP_{mat}) of 3.2 with 1.74 J/g input work at ~0.1 Hz, driven by a stress of 5.7 MPa. Implementing AM elastocaloric elastomers creates opportunities for the development of full-scale low-activation-stress regenerative elastocaloric cooling components that enable optimizing flow structures and enhanced heat-transfer performance.

1. Introduction

Current cooling and heating devices consume significant amounts of the electricity used worldwide and are largely dominated by conventional vapor-compression refrigeration technologies [1,2]. These technologies are based on cycles in which a refrigerant is alternately compressed and expanded to achieve a cooling cycle. Vapor compression systems can have significant environmental impact associated with leakage of their working refrigerant as well as system losses that reduce efficiency [1]. Therefore, substantial efforts have been devoted to the development of more efficient, greenhouse-gas-free refrigerants, as well as novel and alternative cooling technologies. Solid-state cooling technologies based on caloric materials, employing so-called caloric effects; (magnetocaloric [3,4], electrocaloric [5], elastocaloric [6,7], barocaloric [8]), are found to be promising, environmentally-friendly, and efficient alternatives to vapor-compression refrigeration. The caloric effects of the materials are induced by different external fields, namely a magnetic field for the magnetocaloric effect, an electric field for the electrocaloric effect, a uniaxial strain for the Elastocaloric Effect (eCE), and an isostatic pressure for the barocaloric effect.

Elastocaloric materials are attracting increasing attention and have been recommended as the most promising alternative for non-vapor-compression technology by the US Department of Energy [9]. These materials exhibit an increase in temperature when a uniaxial strain is applied and a decrease in temperature when the strain is released adiabatically. Devices based on these materials usually operate by applying a linear strain either in tension or compression to the material, but several novel driving methods such as bending and torsion have also been demonstrated [10–13]. In recent years, Shape Memory Alloys (SMAs) with a austenitic–martensitic phase transformation at room temperature have been intensively explored, among these NiTi-based SMAs [14–16], Cu-based SMAs [17,18], and NiMn-based Heusler-type magnetic SMAs [19–21]. Particularly, the NiTi-based SMAs are most commonly employed for solid-state cooling/heat-pumping system demonstration both in numerical simulation and experimental aspects [22–26]. However, driving the eCE of SMAs requires large tensile stresses as high as several hundreds of MPa, which remains a troublesome engineering challenge for practical applications [27]. For instance, commonly used Ni-Ti alloys when developed as a cooling device require large stresses reaching 1000 MPa under compression [28].

Polymer elastomers such as Natural Rubber (NR) were initially

* Corresponding author.
E-mail address: kunwa@dtu.dk (K. Wang).

https://doi.org/10.1016/j.apmt.2022.101711
Received 12 September 2022; Received in revised form 13 November 2022; Accepted 27 November 2022
Available online 7 December 2022

Nomenclature

Abbreviations

AM	additive manufacturing
FFF	fused filament fabrication
TPU	thermoplastic polyurethane
TPPE	thermoplastic polyester
TPEs	thermoplastic elastomers
NR	natural rubber
eCE	elastocaloric effect
SIC	strain-induced crystallization
SMAs	shape memory alloys
SEM	scanning electron microscope
IR	infrared radiation
DSC	differential scanning calorimetry

Variables

COP	coefficient of performance, [-]
ΔW	input work, [J]
c_p	specific heat capacity, [J kg^{-1} K^{-1}]
ΔT	temperature change
SR	solidity ratio, [-]
ε	strain, [-]
σ	stress, [MPa]
ρ	density, [kg m^{-3}]
S	entropy, [J K^{-1}]
ω	fitting time constant, [s]
Q	cooling/heating work, [W]
L	length, [m]
m	mass, [kg]
T	temperature, [K]
t	time, [s]

Subscripts

ad	adiabatic
cyc	cyclic
mat	material
amb	ambient
loa	loading
unl	unloading
c	cooling
h	heating

reported to have elastocaloric properties by Joule in 1859, namely having the Gough-Joule effect [29]. Compared to most SMAs, the stress to trigger the eCE in the elastomers is one or two orders of magnitude less than for SMAs. Additionally, the advantages of elastomer materials include softness, low cost, sustainability, and lack of toxic materials. This has driven increasing research into exploiting various elastomers in recent years, which opens new avenues for eCE refrigeration [30–34]. The eCE in rubbers and Thermoplastic Polyurethane (TPU) elastomers has been increasingly studied and the softening effect (namely, the Mullins effect) on its caloric cooling application was elucidated as well [32,35–37]. TPU elastomers have been observed with considerable eCE at room temperature due to Strain-Induced Crystallization (SIC), which is associated with a partial crystallization of the elastomer caused by deformation [38,39]. The inherent SIC in elastomers can enhance their mechanical functionality and improve the eCE cooling performance [34, 35,40]. More recently, a novel elastocaloric cooler based on SIC using an inflating-deflating rubber membrane was developed with an attractive specific cooling power of 20.9 W/g, showing that elastomers can absorb a high cooling load per mass [34]. High cooling power has been demonstrated in vulcanized NR fibers and polyethylene wires by means of twisting, untwisting, and stretching simultaneously [12]. Thermoplastic elastomers with uniform molecular chain lengths were synthesized, and the elastocaloric effect was shown to improve [41]. These achievements in the search for eCE elastomers and in developing practical cooling prototypes based on them demonstrate the promise of regenerative elastocaloric cooling/heat-pumping systems based on elastomers.

Implementing Additive Manufacturing (AM) to engineering applications can add freedom to produce complex geometries, which has been used to develop novel regenerator structures to achieve efficient heat transfer and enhanced functional stability for solid-state cooling [42–44]. Thermoplastic Elastomers (TPEs) such as TPU, have been utilized for fabricating flexible 3D components by means of AM technologies [45,46], often using Fused Filament Fabrication (FFF). Manufacturing using FFF consists of depositing successive layers on a build plate by extruding a thermoplastic filament to obtain 3D structures. FFF is a low-cost, commercialized technology [47–50]. Commonly used AM techniques for metallic caloric materials, including selective laser melting and selective beam sintering, cannot produce smooth, fine regenerator structures and struggle to control the microstructure evolution during printing. There are also limitations in the alloy composition, as well as the complex preparation for the raw powders [51,52]. AM of polymer TPEs is easier to implement, and precise flow channels with improved heat-transfer and flow properties are achievable using more accessible 3D printing devices.

In this work, five filaments of thermoplastic elastomers were chosen to explore their elastocaloric cooling performance. These rubber-like elastomers all exhibit some degree of eCE associated with SIC and some are shown to be promising for construction of a polymer full-scale active elastocaloric regenerator produced by additive manufacturing. We screened the possible thermoplastic elastomers in filament form and fabricated the most promising into printed parts using FFF. The main printing parameters for selected elastomeric materials and their influence on the elastocaloric cooling performance were investigated.

2. Materials and methods

2.1. Elastomeric filaments and printing parameters

Commercial 3D-printing filaments were purchased, and the materials are summarized in Supplementary Table 1. Most of them were made of thermoplastic polyurethane, except the Z-Flex filament, which was made of Thermoplastic Polyester (TPPE). The printed 3D parts (NinjaFlex, KungFu98A and Z-Flex) were printed by a Zmorph VX Printer, except the Ultimaker 95A part, which was printed by an Ultimaker S5 Pro Bundle printer. The Zmorph printer used a single extruder with a 0.3 mm nozzle and the Ultimaker S5 Pro used a 0.4 mm nozzle. The G-codes (printing instructions) were generated by Voxelizer2.0 software and Cura 4.12 for the Zmorph and Ultimaker printers, respectively. These FFF based printers deposit a 3D part layer by layer, as shown in the illustration in Fig. 1(a). The 3D-printed parts for mechanical tests and elastocaloric measurements are fabricated in dogbone shapes with the same gauge length L_0 of 15 mm and a width of 15 mm. The dogbone 3D geometry is shown in Fig. 1(a). The thicknesses of the printed dogbones are 1, 2, or 5 mm. Three bead orientations with respect to the x-axis (applied strain direction) are used to print the dogbones and marked as 0°, 45° and 90°, as shown in Fig. 1(b). The samples were printed with varying temperatures both for the extruder and build plate and travelling speeds depending on the material. The basic printing parameters for each filament, including printing temperature, bed temperature, and printing speed, are listed in Supplementary Table 1. The infill type used in FFF is line infill (or rectilinear) for all prints. Due

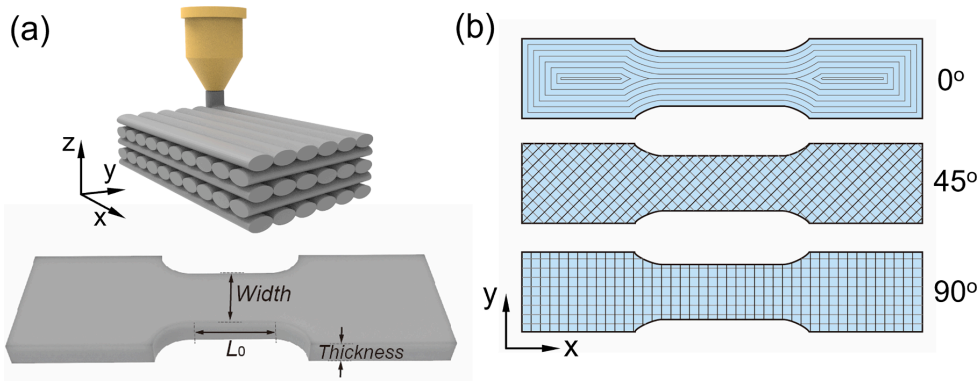

Fig. 1. FFF printing of elastomeric filaments: (a) Schematic of FFF 3D printing with cross-stacked layers and geometry of the dogbone part; (b) Three printing orientation for dogbone parts.

to the hygroscopic nature of TPU polymers [53], the filaments will absorb atmospheric moisture and during the printing the wet filament will be melted with the vapor turning to steam which leads to voids in the part and reduces mechanical properties [24]. Thus, they were stored in a filament dryer at 80 °C during and between printing in order to avoid moisture.

2.2. Mechanical tests and infrared temperature measurements for elastomers

Mechanical testing and experimental characterization of the elastocaloric effect were performed on a Zwick/Roell EZ030 electromechanical tester. An Xforce K load cell enabling a maximum load of 30 kN with an uncertainty of 1% was used for the tests. More detailed information regarding the mechanical tester can be obtained from the literature [34]. The printed parts and filament wires were tightly clamped by T-fatigue grips on the crosshead of the tester. Some rubber protective material was placed between the gripped area of the printed samples and the mechanical grips to protect the sample during the stretching process, which can be seen in Supplementary Fig. 1. The gauge length of 20 mm and strain rate of 5 s^{-1} are used for the filament elastocaloric measurements, where the large strain rate is implemented to achieve a quasi-adiabatic state which is comparable to the rate reported in the TPU test [36]. This fast-loading strain rate was also implemented for the quasi-adiabatic temperature change measurements in the eCE comparison of different bead orientations (the temperature change as a function of strains). The different samples were employed for different elastocaloric performance tests. Specifically, the thickness of dogbones used for the eCE comparison of different orientations was 5 mm. Dogbones applied for the stability evaluation were printed in 2 mm and the related cyclic mechanical tests were run at a strain rate of 0.33 s^{-1} and operated in a strain range of 150–500%. Dogbones employed for cyclic tests of the material COP calculation were printed with a thickness of 1 mm and the strain rate was 0.67 s^{-1}. The elastocaloric temperature change was measured using an infrared (IR) thermographic camera (InfraTec 9400). The spatial resolution and temperature resolution of the IR camera can achieve 0.01 mm/pixel and 0.02 K, respectively. In addition, due to the buckling of filaments and printed dogbones during cyclic tests and due to the large applied strains, the middle point of the sample moved during loading/unloading. Different middle zones at different states in an elastocaloric cycle were chosen from the sample to obtain the average infrared temperatures, finally combining temperature variation curves of each state into the temperature variation profile of a full cycle. For the cycling tests, a fixed selective zone for infrared temperatures was used to evaluate the adiabatic temperature change.

2.3. SEM characterization and thermal analysis

Surface microstructures of the printed parts were characterized by a Zeiss EVO MA10 Scanning Electron Microscope (SEM). The uncycled printed and cycled specimens for SEM were cut at the middle of the active region using a snap-off utility knife (BAHCO KB09-01). Before the SEM imaging, polymer specimens were processed by carbon coating on the surface to improve the conductivity. Specific heat capacity was measured on a custom built, high-resolution, Peltier element based Differential Scanning Calorimetry (DSC) [54]. The measured specimens (~0.5 mg) were cut from the virgin filaments, uncycled printed dogbones and 100 times cycled dogbones. The tests were performed with heating and cooling rates of 1 K/min in a vacuum of 5×10^{-6} mbar.

3. Results & discussion

3.1. Elastocaloric properties in elastomeric filaments

Elastomeric filaments of each material were first characterized for their eCE properties and eCE cooling potential. In Fig. 2(a), a piece of NinjaFlex filament is mounted in the mechanical tester with two protective rubber gaskets surrounding both gripped ends. The temperature change and filament geometric evolution are recorded by the IR camera. Infrared thermographs present the surface temperature increase and decrease during the stretching and releasing processes (states: *ii* and *iv*, respectively), as well as the temperature equilibrium with ambient temperature $T_{amb} = 296$ K prior to loading and unloading (states: *i* and *iii*, respectively). In addition to the observed temperature changes, buckling occurs in state *iv* due to the plastic deformation produced by the large deformation. The time-dependent temperature evolution diagram, with the four states, is shown in Fig. 2(b), which is obtained from the average surface temperature in a selected zone from filament IR images. Notice one interesting phenomenon that the temperature increase during the loading process is higher than the decrease during the unloading process. This may be caused by some intrinsic hysteresis in the loading-unloading process (observed in the cyclic stress-strain curves in Supplementary Fig. 2). The asymmetry for temperature increases and decreases has also been observed in other rubbers and rubber-like elastomers due to the large variation of the thermal time constant and the crystallization kinetics [36,40]. Indeed, the elastic entropy and the SIC both contribute to the elastocaloric effect for natural rubbers. When the applied strain reaches 500–600% for natural rubbers, the crystallization can occur in a few tens of milliseconds upon stretching and the rubber heats up rapidly both from elastic entropy variation and the SIC process [55,56]. Upon releasing, a fraction of the crystallization will be relaxed due to the holding time in contact with the

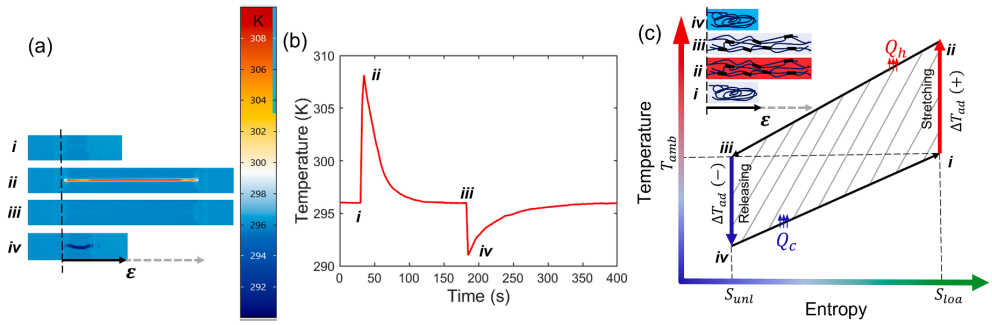

Fig. 2. Surface temperature variation for the NinjaFlex filament in an eCE cooling cycle: (a) IR images in each state of the first cycle; (b) Temperature changes of the elastocaloric material during an eCE cycle; (c) Schematic temperature-entropy diagram for an eCE cooling cycle, where (+) and (−) represent temperature increase and decrease, respectively; Q_h and Q_c represent the heating and cooling energy, respectively; The inset diagram gives a representation of the molecular chain state variation between the disordering and strain-induced crystallization (black blocks) during adiabatic stretching and releasing and the corresponding heating (red), cooling (blue), and ambient (grey) of the sample.

ambient temperature, and there is a lower contribution for the eCE from the SIC process.

An elastocaloric cooling cycle is illustrated with a temperature-entropy (*T*-*S*) diagram in Fig. 2(c) to elucidate the elastomer eCE cooling operating principle, which represents a reversed Brayton-based thermodynamic cycle. Active elastomers are subject to the four processes in the thermodynamic cycle: adiabatic stretching (*i*→*ii*), fluid flow from cold to hot where heat is rejected from the hot reservoir (*ii*→*iii*), adiabatic releasing (*iii*→*iv*), fluid flow from hot to cold where a cooling load is absorbed in the cold reservoir (*iv*→*i*). While the elastomer undergoes the adiabatic uniaxial stretching, the applied stress leads to a partial phase transition for the elastomer molecular chains from the crimped state to the extended state. Some molecular chains crystallize into ordered phases accompanying with the latent heat and entropy increase [57]. The crystallization of elastomer molecular chains is induced by rapidly stretching, i.e., so-called strain-induced crystallization (SIC), which is the reason for the elastocaloric effect in elastomers [39,58]. The consequence is that the surface temperature increases for most of rubbers and soft elastomers. Undergoing an adiabatic releasing process, the recovery to the disordered coil-like state of SIC molecular

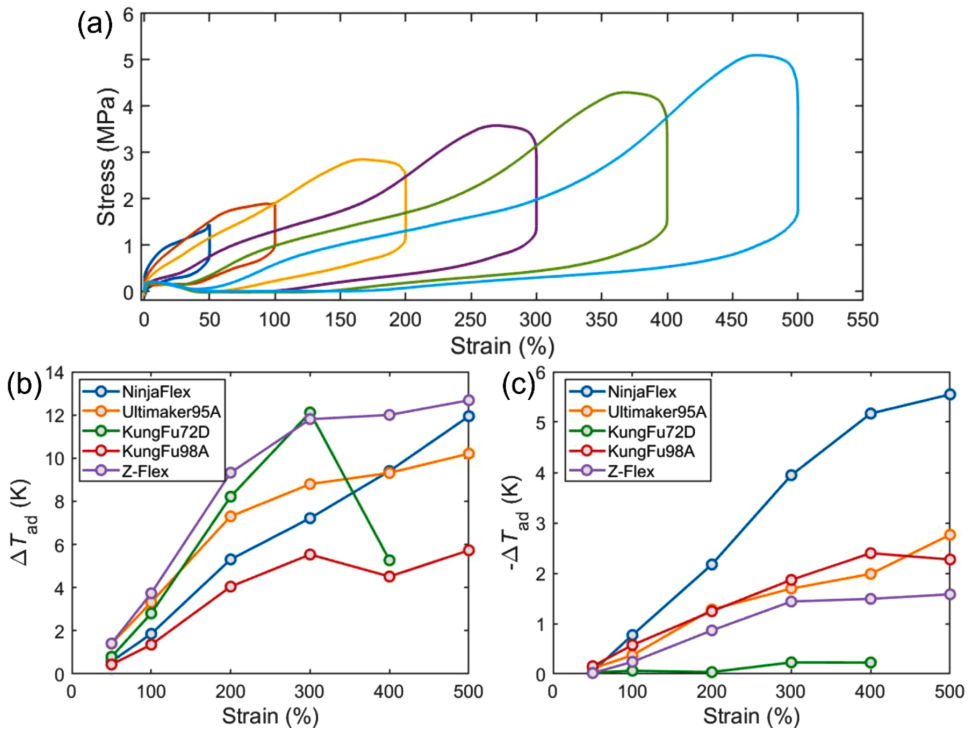

Fig. 3. Elastocaloric effect comparison for different elastomeric filaments: (a) Stress-strain profiles for the NinjaFlex filament; (b) Temperature change as a function of strain for different filaments during the filament stretching; (c) Temperature change as a function of strain for different filaments during the filament releasing.

chains leads to the absorption of heat and thus a temperature decrease.

Elastocaloric measurements for the five elastomeric filaments were performed under different strains. Fig. 3(a) shows the stress-strain behavior of the NinjaFlex filament. The measurement was performed using one filament with a sequential strain increase from 0 to 500%. The stress-strain curves and time-dependent temperatures for the other samples are given in Supplementary Figs. 3–7. The temperature changes were measured during each loading and unloading process. The system was allowed to equilibrate with ambient after each change in strain, as illustrated in the elastocaloric cycle in Fig. 2(b). Results for adiabatic temperature increases and decreases of different filaments are shown in Fig. 3(b and c). Regarding the exothermic process, the positive ΔT_{ad} gradually increases as the strain increases to 300%. Subsequently, a ΔT_{ad} plateau was observed for some samples (Ultimaker95A, KungFu98A, Z-Flex) where the adiabatic change increases very little from a strain of 300–500%. This indicates that strains above 300% for these materials are less elastocaloric responses. The adiabatic temperature change of the NinjaFlex filament continues to increase at strains above 300%, and the largest ΔT_{ad} value reaches 12 K at the strain of 500%. The endothermic process accompanying a negative ΔT_{ad} upon releasing the strain plays a significant role in evaluating the capacity for elastocaloric cooling devices. Since the KungFu72D filament failed mechanically due to its elongation between 300 and 400%, data at 400% is not available and the result for 300% may include significant plastic deformation of the sample. Furthermore, only a negligible elastocaloric effect was observed during the unloading process, which indicates that it is not an attractive material for elastocaloric cooling applications. The remaining four candidates exhibit large elastocaloric effects during the endothermic process. The negative ΔT_{ad} of the NinjaFlex filament increases with the strain increase and a maximum $-\Delta T_{ad}$ value as large as 5.55 K at 500% is achieved. The $-\Delta T_{ad}$ values for Ultimaker95A and KungFu98A filaments are similar below 500% where the adiabatic temperature changes of both are ~2 K. However, there is a difference in trend for the Ultimaker95A and KungFu98A filaments between the strains of 400 and 500% in Fig. 3(c). This phenomenon is similar to the behavior for the KungFu72D filament during stretching. In addition, a slight decrease in ΔT_{ad} for KungFu98A during stretching is observed in Fig. 3(b). The stress improvement (8.25%) from 2.91 to 3.15 MPa due to the strain increase from 400 to 500% is less than that (11.31%) of the Ultimaker filament from 6.01 to 6.69 MPa, (the corresponding stress-strain behavior is given in the Supplementary Figs. 4 and 6), which results in a $-\Delta T_{ad}$ drop for KungFu98A in Fig. 3(c). Although the temperature change of the Z-Flex filament was highest among these materials during the adiabatic stretching process, its $-\Delta T_{ad}$ was not as large as the value during the stretching process. A $-\Delta T_{ad}$ value of 1.58 K for the Z-Flex filament was obtained at 500% strain but a temperature change of 1.44 K was measured at 300% and thus the $-\Delta T_{ad}$ increased slightly as the strain increased to 500%.

3.2. Softening behavior and reversible elastocaloric effect

When eCE elastomeric filaments undergo several loading-unloading cycles, the stress-strain curve shows significant compliance after the first cycle and then tends towards a stabilized cycle (Supplementary Fig. 2). This softening behavior is commonly observed in rubbery materials, the so-called Mullins effect, which contributes to the elastocaloric effect decrease in natural rubbers and elastocaloric elastomers [37,46]. The eCE performance evolution associated with the softening behavior of elastomeric filaments is investigated by comparing the ΔT_{ad} ratio between the initial cycle and after a small number of cycles (~10). This relative variation of the adiabatic temperature is shown in Fig. 4(a) and (b) for strains of 500% and 10 cycles. The tests for each sample were conducted in three procedures: one adiabatic stretching-releasing cycle, with a pause to equilibrate with room temperature in between (initial cycle); cyclical stretching and releasing eight times (cyclic process); and one adiabatic stretching-releasing cycle with pauses for temperature equilibration (10th cycle). After the cyclic process, the values of ΔT_{ad} exhibit a significant decrease between the 1st and 10th cycles for the samples due to the irreversible plastic deformation produced during cycling [35,41]. However, the degradation of $-\Delta T_{ad}$ is smaller, and for some samples (Ultimaker, KungFu98A, and Z-Flex) the $-\Delta T_{ad}$ even increases after the cyclic process. Since the lower value of elongation at the breaking point for the KungFu72D sample, the mechanical fatigue presents after the first stretching. The highest ΔT_{ad} is produced in KungFu72D during the stretching but there is no temperature change observed during the releasing process. The lowest temperature relative variation is observed in the NinjaFlex sample both during the loading and unloading process, manifesting its reversible elastocaloric effect among these elastomeric filaments. Especially, seldom degradation in temperature change appears for NinjaFlex filament during the unloading process.

3.3. Printing orientation and its impacts on elastocaloric properties

To exploit full-scale elastocaloric regenerators printed by these potential elastomeric materials, the manufacturing parameters should be carefully examined to ensure decent elastocaloric and mechanical properties after the printing. Printing parameters such as temperatures and printing patterns can be easily controlled and are directly connected to the mechanical integrity and lifetime of the elastocaloric regenerator. For FFF, the 3D part is deposited layer by layer. Extruded beads within each layer could be aligned in different directions. The orientation of extruded beads and layers is essential to the mechanical properties of printed parts. Another parameter, solidity ratio (SR), given by the distance between beads, and thus representing the printed density, is also crucial for printing mechanical properties [59]. The highest infilled-pattern quality (95%) is applied for each printing to obtain

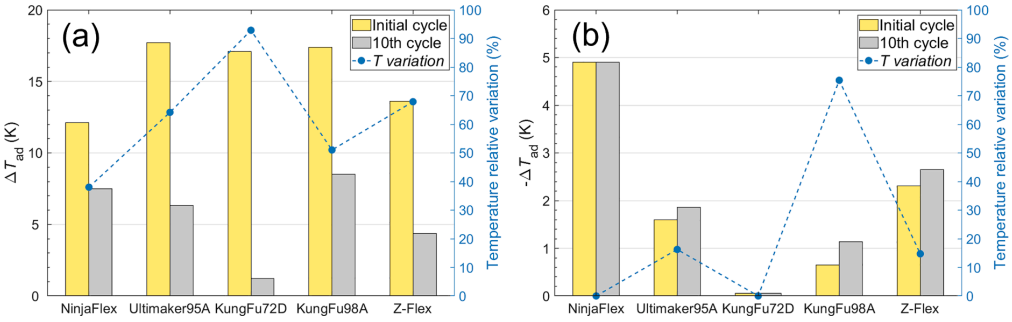

Fig. 4. Adiabatic temperature change comparison for different samples undergoing the initial cycle and 10th cycle during the stretching (a) and releasing (b) processes, and the corresponding temperature variation ratio.

samples with as high a density as possible. Therefore, the effect of the spacing between beads is not considered here. Printed parts employed for eCE cooling are subjected to uniaxial stretching, which means that stacked layers inside of the sample should be able to withstand the large cyclical uniaxial stress. Three printing profiles for the dogbone-shape parts with different orientations were chosen, as illustrated in Fig. 1 (b). In the 0^o orientation the layers are stacked with the same printing pattern as the diagram shown. The dogbones with 45^o and 90^o orientations are printed with a cross-hatched structure in the stacked layers.

Elastocaloric effect measurements for each orientation were conducted with samples printed from the NinjaFlex filament as this was found to have the most promising properties. The surface temperature variation of the 0^o dogbone undergoing the four states of an elastocaloric cycle measured by IR thermography is shown in Fig. 5(a). The temperature distribution is uniform in the middle rectangular area of the dogbone, but some higher temperatures are observed at the two ends of the active area owing to the uneven stress distribution. The measured adiabatic temperature changes during loading and unloading as a function of strain are obtained from the average temperature in the middle of the active area of each dogbone. Mechanical tests return to zero strain (the original length) at the end of every cycle. Buckling occurs due to the large deformation that occurs in stage *iv* of the dogbone test. The stress-strain behavior for the different printing orientations is compared in Fig. 5(b). The tensile modulus of differently oriented dogbones is 7.9 ± 0.6 MPa for 0^o, 7.4 ± 0.8 MPa for 45^o, and 6.8 ± 0.7 MPa for 90^o. These are evaluated in an elastic strain range of 0–10%. The value of stress and tensile modulus decrease with an increase in orientation angle, during the loading process. This is in agreement with the results observed in various studies for FFF parts, where beads oriented parallel to the load direction (0^o orientation) are always stronger than beads oriented perpendicular to the load direction [59,60]. For the 0^o orientation dogbone the larger tensile modulus indicates a higher stiffness and tighter bead attachment, and thus a denser part as well as good mechanical properties are expected. Adiabatic temperature changes during loading and unloading are shown in Fig. 5(c) and 5(d), respectively. The corresponding stress-strain curves for the elastocaloric measurements subject to different strains are given in Supplementary Fig. 8. The results of ΔT_{ad} for different dogbone orientations confirm that the 0^o orientation dogbone maintains a significant elastocaloric effect in 3D printed parts. From the perspective 3D printing elastocaloric regenerators, the orientation of beads and stacked layers should be aligned parallel to the loading direction to realize the largest lifetime and eCE.

3.4. Microstructures of printed parts

The microstructures of the printed parts with different bead orientations were studied in uncycled and cycled 3D-printed parts. Fig. 6(a) and (b) show profile and cross-section views of the 0^o dogbone. Good attachment between the ellipsoid beads stacked along the z-direction is achieved by the FFF printing. Interbead voids between the extruded beads are produced during the deposition process. The printed 0^o dogbone was subjected to 100 cyclic tests to study the microstructural evolution after plastic deformation. From the cross-section view in Fig. 6 (c), it can be observed that the plastic deformation leads to a reduced mean width of the ellipsoid beads from 248 ± 13 μm to 189 ± 8 μm measured from the SEM images. Fig. 6(d and e) show the cross-section view from the 90^o dogbone before stretching and after periodic stretching and releasing. The net-like connection between the extruded beads in the 90^o dogbone differs from the bonding connection in the 0^o dogbone, which is a parallel-stacked architecture. The size of the interbead void in the 90^o uncycled dogbone is larger than that of the 0^o one and the bead width decreases to 221 ± 14 μm. After deformation, the ellipsoid bead width further diminishes to 177 ± 10 μm. From Fig. 6

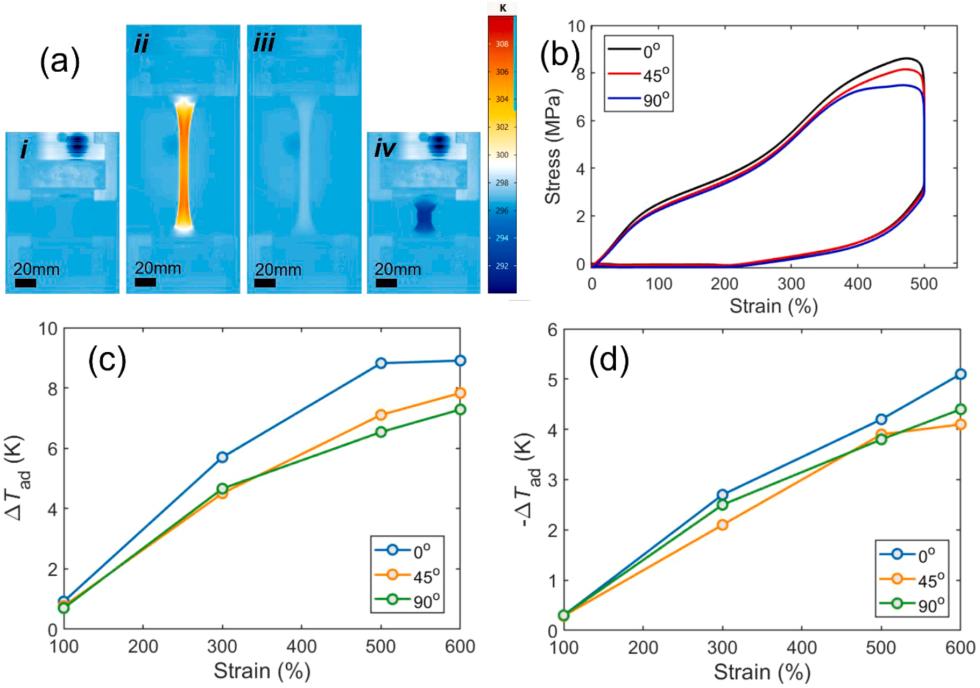

Fig. 5. Elastocaloric properties of different oriented parts: (a) IR images of printed NinjaFlex dogbone part at different states in an elastocaloric cycle; (b) Stress-strain profiles of printed NinjaFlex dogbones with different orientations; (c) Temperature change as a function of strain for different printing orientations during stretching; (d) Temperature change as a function of strain for different printing orientations during releasing.

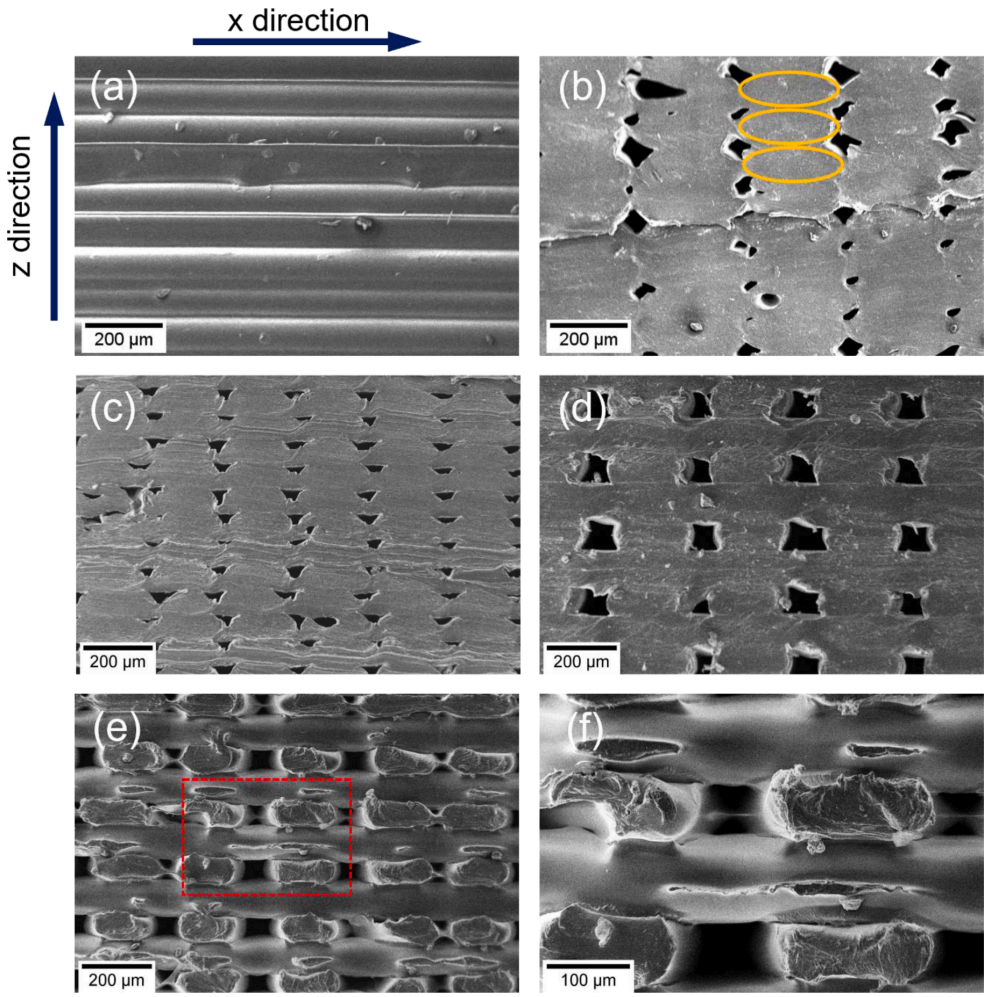

Fig. 6. Microstructures of printed parts: (a) and (b) are SEM images of the profile and cross-section views for a printed dogbone with the 0^o printing orientation, respectively; (c) is a cross-section view after cycling. (d) and (e) are SEM images of profile and cross-section views for a 90^o printed dogbone before and after training, respectively; (f) magnified SEM image from the red rectangular zone in (e).

(e), it can be observed that the beads parallel to the stretching direction are plastically deformed and constrained by the beads perpendicular to the stretching direction. Because the transverse beads are not subjected to the stretching, they experience no plastic deformation, which causes dimensional mismatches with the longitudinal beads that are deformed. This mismatch causes cracks on the transverse bead due to the alternating mechanical interaction between the longitudinal and transverse beads. One of the representative areas is magnified and shown in Fig. 6 (f) to accentuate the crack. It can be deduced that the mechanical interaction will also produce cracks on the longitudinal bead thereby reducing the mechanical properties of the part.

To evaluate the density of a printed FFF part quantitatively, the SR can be calculated by the area of the bead divided by the potential maximum area between the beads, indicated by a box around each bead [59]. The maximum area is determined by the layer height and the width of the bead, which is typically the nozzle diameter. A SR value of 0.79 is obtained for the printing at different orientations (calculating details are given in Supplementary Note 3). The actual normalized density is evaluated by calculating the area ratio between the solid and pore regimes from cross-section SEM images. The values for the uncycled and cycled parts in 0^o orientation are 0.97 and 0.95, respectively. For the 90^o orientation one, the results are 0.93 and 0.89, respectively. All these values are higher than the theoretical value because the real bead shape is not a perfect ellipsoid and it changes during the melting and depositing process. The quantitative result for the printing density also indicates that the 0^o dogbone is denser than the 90^o dogbone, both before and after undergoing the cyclic loading and unloading. This is further substantiated by the higher tensile modulus obtained in the 0^o dogbone. The voids caused by the 90^o printing will be enlarged in the longitudinal and transverse direction during the stretching. When this part is employed in an active elastocaloric regenerator, these voids inside the regenerator can absorb the liquid heat-transfer fluid during the loading and unloading processes, resulting in parasitic heat losses. However, the voids in the 0^o dogbone are disconnected, smaller, and maintain their shape under cycling. Additionally, the connection between the extruded beads in the 0^o dogbone remains tight after cyclic tests. Therefore, the 0^o orientation seems best for fabricating a full-scale elastocaloric regenerator, due to advantages both in elastocaloric

properties and density stability.

3.5. Stability of the mechanical and elastocaloric properties for printed elastomers

The stability of the mechanical properties and eCE of elastocaloric materials is an essential characteristic for evaluating the potential for caloric cooling applications, as it determines the lifetime of the device employing the given eCE materials. Fig. 7(a) shows 100 loading-unloading cycles for the parts printed with different orientations. Similar to the foregoing discussed on the printing orientation impacts on the eCE, the tensile modulus and the maximum stress also decreased with the printing orientation, increasing to 90° during the cyclic tests. As shown in Fig. 7(b), when increasing the cycle number, the stabilized stress can reach to 5.31 MPa for the 0° dogbone, and 3.45 MPa for the 90° dogbone. This can be explained by the higher alignment along the tensile direction for the 0° dogbone, as observed in the microstructural distribution for the extruded beads. The printed layers of the 0° dogbone maintain a good mechanical stability and therefore favor a higher uniaxial stress.

A 0° dogbone with a thickness of 2 mm is subjected to over 1000 cycles to examine the stability of the eCE and its mechanical properties. To avoid any buckling caused by the plastic deformation, the strain is set back to 150% instead of 0% during the releasing process. A slow strain rate of 0.33 s^{-1} is applied throughout the test. The stress-strain profiles of some cycles are selected and shown in Fig. 8(a). It was observed that the maximum loading stress decreases as the cycle number increases. The temperature evolution profile of the first 85 cycles is recorded by the IR camera as shown in Fig. 8(b). After the first several cycles, the temperature variation tends to stabilize, and the detailed temperature variation for cycles 50–56 is given in Fig. 8(c). The average cyclic temperature for the 0° dogbone reaches 3.92 K. Later, the temperature profiles for cycles 955–1015 were captured, as show in Fig. 8(d). The average cyclic temperature change from cycles 1000 to 1006 is 3.09 K,

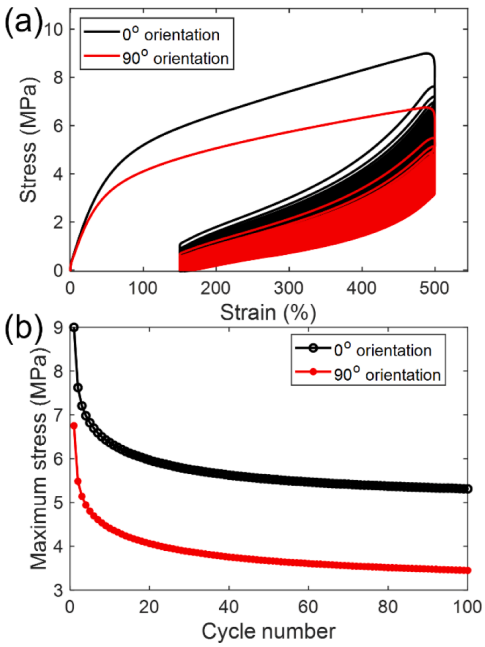

Fig. 7. (a) Stress-strain profiles of printed NinjaFlex dogbones for 100 loading-unloading cycles; (b) Evolution of the maximum stress achieved in each cycle as a function of the cycle number.

which indicates a good functional stability for the eCE of the 3D-printed NinjaFlex.

3.6. Elastocaloric cooling performance of the printed elastomers

The material coefficient of performance (COP_{mat}) is defined for evaluating and comparing potential caloric materials to be employed in caloric cooling [27]. It is calculated by the cooling energy per unit mass divided by the input work per unit mass as shown in Eq. (1). In a Brayton cycle, the cooling energy can be expressed as an integral of the specific heat capacity c_p from T_1 to T_{amb}, where the T_1 is the cold temperature obtained during the loading process and the T_{amb} is the ambient temperature. The input work is obtained from the area of the stress-strain curve. Detailed results for c_p measurements of the filament as well as the uncycled and cycled printed parts are organized and discussed in Supplementary Note 1 and Table 2.

$$COP_{mat} = \frac{Q/m}{\Delta W/m} = \frac{\int_{T1}^{T_{amb}} c_p dT}{\frac{1}{\rho_0}\oint \sigma d\varepsilon} \quad (1)$$

In practice, regenerative elastocaloric cooling will operate cyclically and the COP_{mat} calculation from the cyclic test is closer to a real elastocaloric cooling cycle. Details of COP_{mat} calculations from cyclic tests are organized in Supplementary Note 2 and Supplementary Eq. (2). Using measurements performed under near adiabatic conditions, it is found that the cyclic temperature change is dependent on the sample thickness and loading rate during cyclic tests, which is similar to the cases in active magnetic regenerators influenced by corresponding parameters such as solid thermal conductivities and operating frequencies [61,62]. Fig. 9(a and b) show the temperature change for NinjaFlex as a function of the sample thickness and loading rate. Fig. 7(a) shows that the cyclic temperature change is reduced with an increase in the thickness, due to the slow thermal diffusion from the inside to the outside. But it does not affect the temperature changes of the material under static conditions (back to room temperature after each loading and unloading process), as shown in in Fig. 9(c). The difference in the temperature change in the cyclic mode is caused by convection and radiation to the ambient, which was also observed as performance differences in a rubber-based elastocaloric heat pump employing different thicknesses of polymer membranes [34]. The loading rate dependence of the temperature change, shown in Fig. 9(b), is due to the convection with the ambient. Details for loading rate impacts on cyclic temperature change are included in Supplementary Fig. 15. If the measurements are performed in an isolated environment, the temperature change will be free from the loading rate dependence which has previously been shown in some research for the elastocaloric polymers [41].

To investigate the elastocaloric properties for different sample thicknesses, samples with three different thicknesses were tested in static mode (allowing the temperature to return to room temperature after each loading and unloading process). At the same loading rate, the time to reach room temperature is longer for a thicker sample, as shown in Fig. 9(c). This can be explained by Newton's law of cooling (see, Supplementary Note 4, Supplementary Fig. 10). The heat-transfer process of surface temperature to the ambient temperature can be characterized by the time constant ω. A smaller time constant represents a faster heat transfer with the ambient. As observed in elastocaloric measurements on filaments, the temperature increases in the stretching process are higher than the temperature decreases in the releasing process for each printed part. Comparing the fitted time constant, ω, for different dogbone thicknesses, the largest values for both temperature increase and decrease are obtained with the 1 mm printed part. The fitted values of ω are 32.80 ± 0.46 s and 56.26 ± 0.29 s for cooling and heating, respectively. The time constant for the releasing process is smaller than that of the stretching process. That is because stretching will increase the heat transfer surface area of the sample. Thus, thinner samples are expected to enhance the heat transfer and thus performance

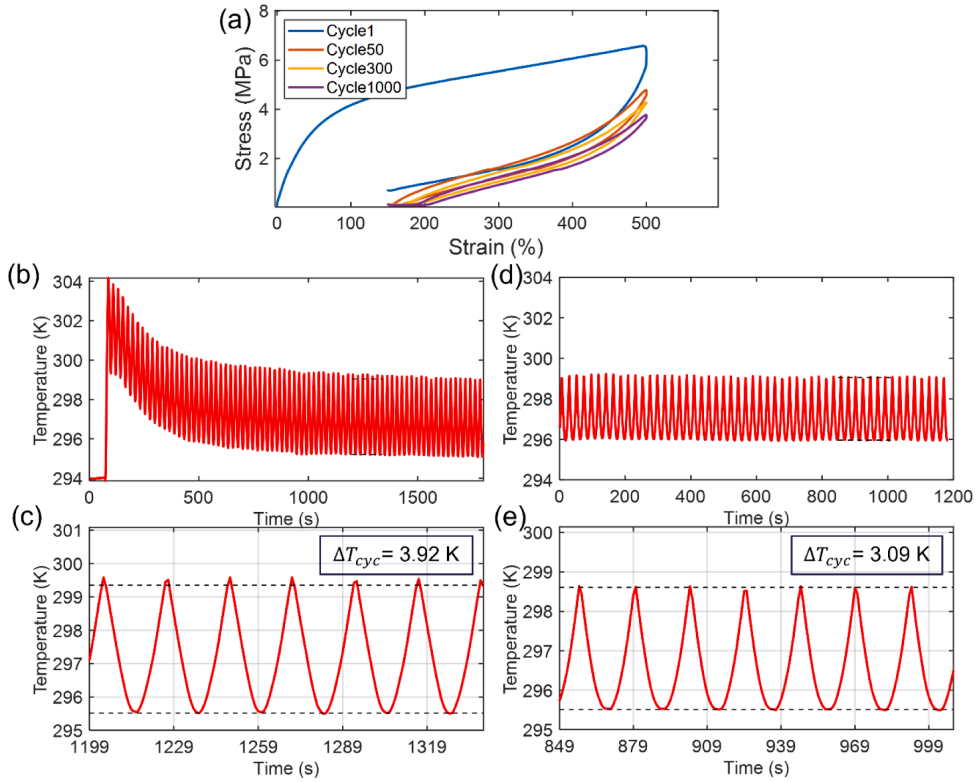

Fig. 8. Functional stability for the 2 mm printed parts over 1000 loading/unloading cycles: (a) Stress-strain behavior for the selected cycles; (b) Cyclic temperature changes for the first 85 cycles at a strain rate of 0.33 s^{-1}; (c) Stabilized temperature change evolution in cycle numbers 50–56 selected from (b); (d) Cyclic temperature changes for cycles 955–1015 at a strain rate of 0.33 s^{-1}; (e) Stabilized temperature change evolution in cycle numbers 1000–1006 selected from (d).

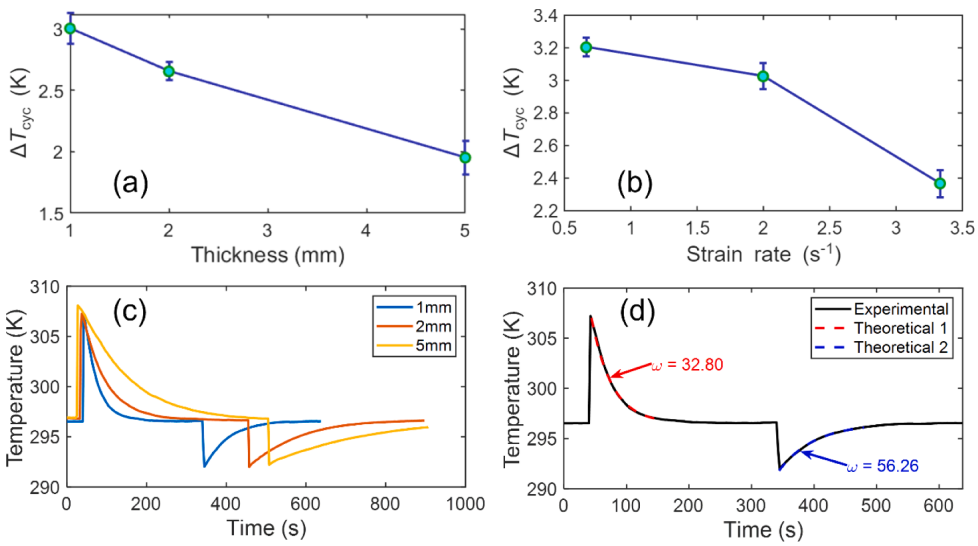

Fig. 9. Temperature variation comparison for different conditions in NinjaFlex 0° dogbones: (a) Cyclic adiabatic temperature changes for different thicknesses at a 2 s^{-1} strain rate; (b) Cyclic adiabatic temperature changes for 1 mm dogbones under different loading rates; (c) Surface temperature variation to ambient temperature by natural convection for different thickness dogbones; (d) Fits to the surface temperature versus time curves of the 1 mm dogbone.

for eCE elastomers.

Fig. 10(a) shows the cyclic temperature variation in a stable loading-unloading state. The adiabatic temperature change for the cyclic mode is defined as the distance between the top and bottom peaks during loading and unloading. When the loading-unloading process reaches cyclical steady state, the adiabatic temperature change will be stable and remains constant for the following cycles, reflecting its prominent and stabilized cycling performance. The ΔT_{cyc} for different materials during cycles 60-100 are shown in Fig. 10(b). The 0° NinjaFlex dogbone produces the largest average ΔT_{cyc} value of 3.24 K during these 40 cycles. However, we noticed that the ΔT_{cyc} for the 1 mm dogbone is less than the ΔT_{cyc} of 3.92 K obtained for the 2 mm NinjaFlex dogbone in Section 3.5. That is because the cyclic test in the stability evaluation is operated at a much lower strain rate, which would favor a higher temperature change as the results shown in Fig. 9(b). The temperature change for the Z-Flex sample is also able to reach a considerable value of 2.84 K. COP_{mat} and the input work (ΔW) as a function of the cycle number for the NinjaFlex Ultimaker95A, KungFu98A, Z-Flex materials rapidly increase during the first ten cycles and tend to stabilize in the following cycles, seeing Fig. 10(c) for NinjaFlex and Supplementary Fig. 16 for other materials. The temperature changes and the input work per unit mass in each cycle for different materials are obtained from temperature profiles given in the Supplementary Fig. 17 which exhibit a rapid decrease over the first several cycles, ending in a stable state. The average COP_{mat} and input work per unit mass during the stabilized cycles (80–100th) for different materials are compared in Fig. 10(d). The highest COP_{mat} of 3.14 with 1.74 J/g input work is observed in the NinjaFlex part at an operating frequency of ~0.1 Hz. From the stress-strain behavior of the Z-Flex printed part (Supplementary Fig. 14), it can be noticed that the input work is significantly reduced as the number of cycles is increased (among proposed materials the lowest input work of 1.63 J/g is required). Therefore, a considerable COP_{mat} of 3.04 with an input work of 1.63 J/g for Z-Flex is obtained when cycling 100 times despite its small temperature change.

The comparison of the COP_{mat} for some common elastocaloric SMAs and polymers is summarized in the Table 1. Compared to the commonly used SMAs materials, the studied 3D printed NinjaFlex and Z-Flex polymer elastomers are superior in considerably lower driving stress (~6 MPa, 500%) and provide a desirable elastocaloric performance. It can be observed that the cyclic temperature change for the NinjaFlex reaches 3.92 K which is lower than several Ni-Ti alloys but comparable to the ΔT_{cyc} of 4.6 K for the $Cu_{68.3}Al_{27.1}Ni_{4.6}$ SMA. There are some differences in the material COP calculation presented in literature. For the shape memory alloys, the COP_{mat} are obtained with a correction for the irreversibility of the phase transformation process [63]. For rubber-like materials due to less hysteresis, Eq. (1) was used for the COP_{mat} calculation [36,41]. Here the NinjaFlex, Ultimaker 95A, and KungFu 98A filaments both consist of the thermoplastic polyurethane, but there are differences in the elastocaloric effect and COP_{mat} when comparing to the reported elastocaloric TPU [36]. That results from different types of TPU being used and a maximum temperature change employed for the COP_{mat} calculations in literature.

3.7. Prospects for an operation system for large deformation eCE regenerators

Compared to the experimental system for elastocaloric cooling/heat pumping using SMAs, soft elastomeric eCE regenerators require much larger deformations (300–500%) to achieve a considerable eCE. At present, some related elastocaloric coolers based on the elastomers have been designed by inflation/deflation devices or by rolling onto a rotational wheel to trigger the eCE of polymer elastomers subjected to a large deformation [34,41]. These designs give inspiration to apply the elastomeric eCE polymers in the solid-state cooling/heat-pumping field. However, when considering the construction of an experimental active elastocaloric cooling/heat-pumping system for polymer elastomers, the large deformation raises several issues, including buckling, and fluid-channel volume change. It can be predicted that the fluid-channel

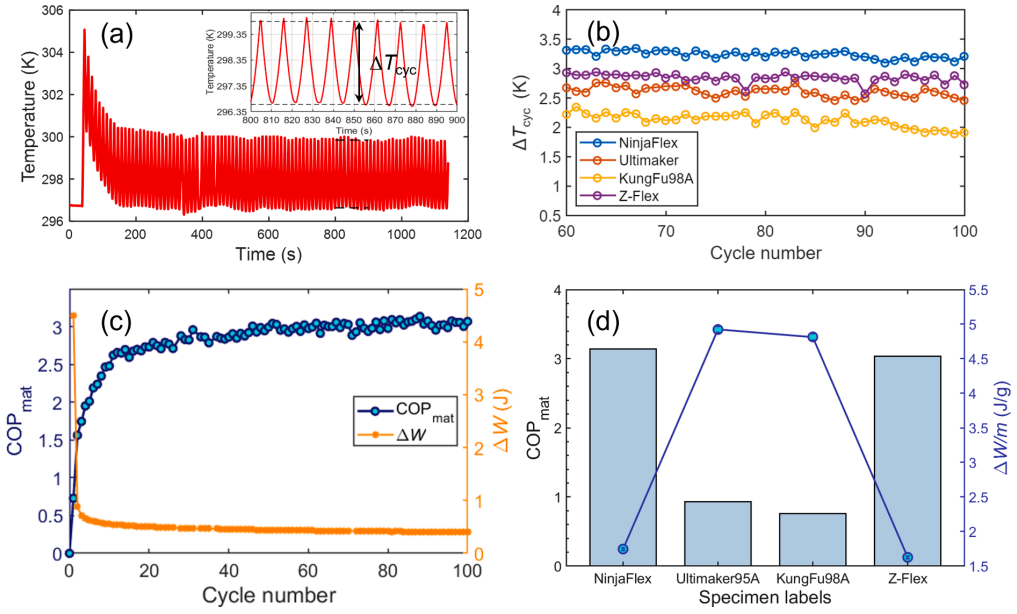

Fig. 10. Cyclic temperature characteristics and material COP_{mat} for different elastomers: (a) Time-dependent surface temperature for cyclic tests and the detailed temperature oscillation of a NinjaFlex 0° dogbone stretched at 500% strain and 0.67 s^{-1} strain rate; (b) Stabilized temperature change evolution in cycle numbers 60–100 for different materials; (c) COP_{mat} and input work evolution as a function of the number of cycles for NinjaFlex dogbone; (d) Average COP_{mat} and input work per unit mass during cycles 80–100 for different materials as printed parts in 0° orientation.

Table 1
Comparison of reported elastocaloric materials on the maximum absolute adiabatic temperature change ($|\Delta T_{ad}|$) achieved, adiabatic cyclic temperature change (ΔT_{cyc}), driving stress, strains, and COP_{mat}.

Materials	$\lvert\Delta T_{ad}\rvert$ (K)	ΔT_{cyc} (K)	$\Delta\sigma$ (MPa)	ε (%)	COP_{mat}	Refs.
NinjaFlex	12	3.24–3.92	5.7	500	3.14	
Ultimaker95A	17.8	2.84	11.7	500	0.93	This work
KungFu98A	17.2	2.62	11.3	500	0.76	
Z-Flex	13.5	2.28	6.4	500	3.04	
Ni-Ti	22	10–29	800	5	7.5	[64–66]
$(Ni_{50}Mn_{31.5}Ti_{18.5})_{99.8}B_{0.2}$	31.5	–	700	7	–	[19]
$Cu_{68.3}Al_{27.1}Ni_{4.6}$	13.6	4.6	400	7.5	9.5	[67]
$Cu_{68.2}Zn_{15.7}Al_{16.1}$	15.3	–	118	8	10.6	[68]
$Ni_{50.0}Fe_{19.0}Ga_{27.1}Co_{3.9}$	11	7.2	130	3.8	4 (system)	[69]
NR	3.5-12	2	1–4.2	600–800	2.08	[32,37,55]
Synthetic rubbers	1.7-2.1	–	5.8–10	300–600	0.23–0.3	[37]
SEBS	15.3	–	12	600	16.2	[41]
TPU	8	3.3–4.5	6.5	400	8	[36]

–: did not find.

volume inside the 3D-printed eCE regenerator changes when the regenerator undergoes a larger deformation due to the Poisson's ratio and strain-induced material volume change [70–73]. The fluid channel volume is expected to increase during the stretching process and decrease during the releasing process, which will lead to asymmetric fluid-flow volumes between the hot/cold blows. Therefore, operating a large deformation regenerator in a flow system, the empty volume from the stretching process needs to be compensated by the flow system. On the other hand, the compensated fluid from the stretching process should be expelled back to the flow system during the releasing process, otherwise, the extra fluid can increase the pressure and may cause leakage. Future work could include a tailored fluid network configuration and operation strategy capable of handling the change of fluid channel volume in an elastomeric regenerator.

4. Conclusion

We explored the elastocaloric cooling performance of five thermoplastic elastomers and demonstrated the potential for fabricating the soft elastomers directly into full-scale elastocaloric regenerators via additive manufacturing technologies. The elastocaloric effect in the five elastomeric filaments were initially investigated before manufacturing the filaments into 3D parts using FFF. Except for KungFu72D, the studied filaments show a satisfactory reversible elastocaloric effect. We found that the 3D-printed parts with the extruded beads aligned in parallel to the uniaxial strain direction can achieve an elastocaloric effect similar to the raw filament with stable mechanical behavior. NinjaFlex and Z-Flex dogbones exhibited a COP_{mat} of 3.14 and 3.04, respectively, at a low required stress of ~6 MPa, which makes them potentially attractive for elastocaloric devices. Combining AM technologies with printable elastocaloric elastomer can result in full-scale elastocaloric regenerator that can be printed directly and actuated at significantly lower forces than comparable SMA systems.

Several challenges need to be overcome for AM elastocaloric regenerator systems to achieve high performance. Since the heat-transfer fluid will flow through internal channels inside the regenerator, the AM parameters should be optimized to achieve fine regenerator geometries as well as being watertight. These would improve the fluid channel quality that could lower the flow pressure drop and enhance the heat-transfer performance. Another challenge is the large elongation required to achieve a high eCE for elastomeric regenerators, which will require special design of external equipment. There are also a number of issues that stem from the large required strains, including: softening behavior (Mullins effect), which occurs during the first cycle, and buckling during strain release caused by plastic deformation, which will bend/twist the fluid channels and influence the heat exchange. A certain number of training cycles until reaching the stabile behavior could be a solution for the softening issue of these soft elastomers. Similar to the suggested pre-elongation method implemented in natural rubbers [35], the buckling can be avoided by applying the pre-strain approach, performed by unloading to a given strain. Additionally, manipulating the pre-elongation to the eve of SIC enables higher efficient elastocaloric cooling resulting from less mechanical energy input. Overall, these achievements show a great potential to construct the soft active elastocaloric regenerator with distinct low-driven stress, opening the opportunity to develop high-performance elastocaloric cooling regenerators with optimized heat-transfer properties and structures by means of additive manufacturing.

CRediT authorship contribution statement

Kun Wang: Conceptualization, Methodology, Investigation, Validation, Data curation, Formal analysis, Visualization, Writing – original draft, Project administration. **Kurt Engelbrecht:** Supervision, Writing – review & editing, Formal analysis, Funding acquisition. **Christian R.H. Bahl:** Supervision, Writing – review & editing, Formal analysis, Funding acquisition.

Declaration of Competing Interest

The authors declare that they have no known competing financial interests or personal relationships that could have appeared to influence the work reported in this paper.

Data availability

The data that has been used is confidential.

Acknowledgments

K. Wang is grateful for financial support of the China Scholarship Council (CSC, No. 202004910369) scholarship. We wish to acknowledge Dr. Lucia Ianniciello for the help in the mechanical and IR tests.

Supplementary materials

Supplementary material associated with this article can be found, in the online version, at doi:10.1016/j.apmt.2022.101711.

References

[1] L.W. Davis, P.J. Gertler, Contribution of air conditioning adoption to future energy use under global warming, Proc. Natl. Acad. Sci 112 (2015) 5962–5967, https://doi.org/10.1073/PNAS.1423558112.
[2] J.L. Dupont, P. Domanski, P. Lebrun, The role of refrigeration in the global economy 38th note on refrigeration technologies, Int. Inst. Refrig. (2019).

[3] V.K. Pecharsky, K.A. Gschneidner, Giant magnetocaloric effect in $Gd_5(Si_2Ge_2)$, Phys. Rev. Lett. 78 (1997) 4494–4497, https://doi.org/10.1103/PhysRevLett.78.4494.
[4] V.K. Pecharsky, K.A. Gschneidner, Magnetocaloric effect and magnetic refrigeration, J. Magn. Magn. Mater. 200 (1999) 44–56, https://doi.org/10.1016/S0304-8853(99)00397-2.
[5] B. Neese, B.J. Chu, S.G. Lu, Y. Wang, E. Furman, Q.M. Zhang, Large electrocaloric effect in ferroelectric polymers near room temperature, Science 321 (2008) 821–823, https://doi.org/10.1126/science.1159655.
[6] T. Krenke, E. Duman, M. Acet, E.F. Wassermann, X. Moya, L. Manosa, A. Planes, Inverse magnetocaloric effect in ferromagnetic Ni-Mn-Sn alloys, Nat. Mater. 4 (2005) 450–454, https://doi.org/10.1038/nmat1395.
[7] J. Tušek, K. Engelbrecht, R. Millán-Solsona, L. Mañosa, E. Vives, L.P. Mikkelsen, N. Pryds, The elastocaloric effect: a way to cool efficiently, Adv. Energy Mater. 5 (2015) 1–5, https://doi.org/10.1002/aenm.201500361.
[8] B. Li, Y. Kawakita, S. Ohira-Kawamura, T. Sugahara, H. Wang, J. Wang, Y. Chen, S. I. Kawaguchi, S. Kawaguchi, K. Ohara, K. Li, D. Yu, R. Mole, T. Hattori, T. Kikuchi, S.I. Yano, Z. Zhang, Z. Zhang, W. Ren, S. Lin, O. Sakata, K. Nakajima, Z. Zhang, Colossal barocaloric effects in plastic crystals, Nature 567 (2019) 506–510, https://doi.org/10.1038/s41586-019-1042-5.
[9] US Department of Energy, Energy Savings Potential and RD&D Opportunities for Non-Vapor-Compression HVAC Technologies, US Department Energy, 2014, p. 199. http://www.osti.gov/home/%0Ahttp://www.osti.gov/servlets/purl/1220817/.
[10] X. Moya, S. Kar-Narayan, N.D. Mathur, Caloric materials near ferroic phase transitions, Nat. Mater. 13 (2014) 439–450, https://doi.org/10.1038/nmat3951.
[11] L. Mañosa, A. Planes, Materials with giant mechanocaloric effects: cooling by strength, Adv. Mater. 29 (2017), https://doi.org/10.1002/adma.201603607.
[12] R. Wang, S.L. Fang, Y.C. Xiao, E.L. Gao, N. Jiang, Y.W. Li, L.L. Mou, Y.N. Shen, W. Bin Zhao, S.T. Li, A.F. Fonseca, D.S. Galvão, M. Chen, W.Q. He, K.Q. Yu, H. B. Lu, X.M. Wang, D. Qian, A.E. Aliev, N. Li, C.S. Haines, Z.S. Liu, J. Mu, Z. Wang, S.G. Yin, M.D. Lima, B. An, X. Zhou, Z.F. Liu, R.H. Baughman, Torsional refrigeration by twisted, coiled, and supercoiled fibers, Science 366 (2019) 216–221, https://doi.org/10.1126/science.aax6182.
[13] A. Czernuszewicz, L. Griffith, J. Slaughter, V. Pecharsky, Low-force compressive and tensile actuation for elastocaloric heat pumps, Appl. Mater. Today 19 (2020), 100557, https://doi.org/10.1016/j.apmt.2020.100557.
[14] J. Cui, Y. Wu, J. Muehlbauer, Y. Hwang, R. Radermacher, S. Fackler, M. Wuttig, I. Takeuchi, Demonstration of high efficiency elastocaloric cooling with large Δt using NiTi wires, Appl. Phys. Lett. 101 (2012) 2–6, https://doi.org/10.1063/1.4746257.
[15] G.J. Pataky, E. Ertekin, H. Sehitoglu, Elastocaloric cooling potential of NiTi, Ni_2FeGa, and CoNiAl, Acta Mater. 96 (2015) 420–427, https://doi.org/10.1016/j.actamat.2015.06.011.
[16] J. Tušek, K. Engelbrecht, L.P. Mikkelsen, N. Pryds, Elastocaloric effect of Ni-Ti wire for application in a cooling device, J. Appl. Phys. 117 (2015), https://doi.org/10.1063/1.4913878.
[17] E. Bonnot, R. Romero, L. Mañosa, E. Vives, A. Planes, Elastocaloric effect associated with the martensitic transition in shape-memory alloys, Phys. Rev. Lett. 100 (2008) 1–4, https://doi.org/10.1103/PhysRevLett.100.125901.
[18] L. Ianniciello, M. Romanini, L. Mañosa, A. Planes, K. Engelbrecht, E. Vives, Tracking the dynamics of power sources and sinks during the martensitic transformation of a Cu-Al-Ni single crystal, Appl. Phys. Lett. 116 (2020), https://doi.org/10.1063/5.0006859.
[19] D. Cong, W. Xiong, A. Planes, Y. Ren, L. Mañosa, P. Cao, Z. Nie, X. Sun, Z. Yang, X. Hong, Y. Wang, Colossal elastocaloric effect in ferroelastic Ni-Mn-Ti alloys, Phys. Rev. Lett. 122 (2019), 255703, https://doi.org/10.1103/PhysRevLett.122.255703.
[20] J. Liu, T. Gottschall, K.P. Skokov, J.D. Moore, O. Gutfleisch, Giant magnetocaloric effect driven by structural transitions, Nat. Mater. 11 (2012) 620–626, https://doi.org/10.1038/nmat3334.
[21] W. Sun, J. Liu, D. Zhao, M. Zhang, Directional solidification and elastocaloric effect in a Ni45Mn44Sn11 magnetic shape memory alloy, J. Phys. D. Appl. Phys. 50 (2017), https://doi.org/10.1088/1361-6463/aa87ef.
[22] J. Tušek, K. Engelbrecht, D. Eriksen, S. Dall'Olio, J.J. Tušek, N. Pryds, A regenerative elastocaloric heat pump, Nat. Energy 1 (2016) 1–6, https://doi.org/10.1038/nenergy.2016.134.
[23] S. Qian, L. Yuan, J. Yu, G. Yan, Numerical modeling of an active elastocaloric regenerator refrigerator with phase transformation kinetics and the matching principle for materials selection, Energy 141 (2017) 744–756, https://doi.org/10.1016/j.energy.2017.09.116.
[24] V.M. Bruère, A. Lion, J. Holtmannspötter, M. Johlitz, Under-extrusion challenges for elastic filaments: the influence of moisture on additive manufacturing, Prog. Addit. Manuf. 7 (2022) 445–452, https://doi.org/10.1007/s40964-022-00300-y.
[25] L. Yuan, Y. Wang, J. Yu, A. Greco, C. Masselli, S. Qian, Numerical study of a double-effect elastocaloric cooling system powered by low-grade heat, Appl. Therm. Eng. 218 (2023), 119302, https://doi.org/10.1016/j.applthermaleng.2022.119302.
[26] C. Aprea, A. Greco, A. Maiorino, C. Masselli, The employment of caloric-effect materials for solid-state heat pumping, Int. J. Refrig. 109 (2020) 1–11, https://doi.org/10.1016/j.ijrefrig.2019.09.011.
[27] S. Qian, Y. Geng, Y. Wang, J. Ling, Y. Hwang, R. Radermacher, I. Takeuchi, J. Cui, A review of elastocaloric cooling: Materials, cycles and system integrations, Int. J. Refrig. 64 (2016) 1–19, https://doi.org/10.1016/j.ijrefrig.2015.12.001.
[28] L. Ianniciello, K. Bartholomé, A. Fitger, K. Engelbrecht, Long life elastocaloric regenerator operating under compression, Appl. Therm. Eng. 202 (2022), 117838, https://doi.org/10.1016/j.applthermaleng.2021.117838.
[29] J.P. Joule, On seme thermo-dynamic properties of solids, Philos. Trans. 149 (1859).
[30] H.J. Qi, M.C. Boyce, Stress-strain behavior of thermoplastic polyurethanes, Mech. Mater. 37 (2005) 817–839, https://doi.org/10.1016/j.mechmat.2004.08.001.
[31] T. Sui, N. Baimpas, I.P. Dolbnya, C. Prisacariu, A.M. Korsunsky, Multiple-length-scale deformation analysis in a thermoplastic polyurethane, Nat. Commun. 6 (2015) 1–9, https://doi.org/10.1038/ncomms7583.
[32] D. Guyomar, Y. Li, G. Sebald, P.J. Cottinet, B. Ducharne, J.F. Capsal, Elastocaloric modeling of natural rubber, Appl. Therm. Eng. 57 (2013) 33–38, https://doi.org/10.1016/j.applthermaleng.2013.03.032.
[33] Y. Yoshida, K. Yuse, D. Guyomar, J.F. Capsal, G. Sebald, Elastocaloric effect in poly (vinylidene fluoride-trifluoroethylene-chlorotrifluoroethylene) terpolymer, Appl. Phys. Lett. 108 (2016), 242904, https://doi.org/10.1063/1.4953770.
[34] F. Greibich, R. Schwödiauer, G. Mao, D. Wirthl, M. Drack, R. Baumgartner, A. Kogler, J. Stadlbauer, S. Bauer, N. Arnold, M. Kaltenbrunner, Elastocaloric heat pump with specific cooling power of 20.9 W g–1 exploiting snap-through instability and strain-induced crystallization, Nat. Energy 6 (2021) 260–267, https://doi.org/10.1038/s41560-020-00770-w.
[35] Z. Xie, G. Sebald, D. Guyomar, Elastocaloric effect dependence on pre-elongation in natural rubber, Appl. Phys. Lett. 107 (2015), 081905, https://doi.org/10.1063/1.4929395.
[36] G. Coativy, H. Haissoune, L. Seveyrat, G. Sebald, L. Chazeau, J.M. Chenal, L. Lebrun, Elastocaloric properties of thermoplastic polyurethane, Appl. Phys. Lett. 117 (2020), 193903, https://doi.org/10.1063/5.0023520.
[37] R. Bennacer, B. Liu, M. Yang, A. Chen, Refrigeration performance and the elastocaloric effect in natural and synthetic rubbers, Appl. Therm. Eng. 204 (2021), 117938, https://doi.org/10.1016/j.applthermaleng.2021.117938.
[38] S.L. Dart, E. Guth, Rise of temperature on fast stretching of butyl rubber, J. Chem. Phys. 13 (1945) 28–36, https://doi.org/10.1063/1.1723964.
[39] M. Tosaka, Strain-induced crystallization of crosslinked natural rubber as revealed by X-ray diffraction using synchrotron radiation, Polym. J. 39 (2007) 1207–1220, https://doi.org/10.1295/polymj.PJ2007059.
[40] Z. Xie, G. Sebald, D. Guyomar, Comparison of direct and indirect measurement of the elastocaloric effect in natural rubber, Appl. Phys. Lett. 108 (2016), 041901, https://doi.org/10.1063/1.4940378.
[41] S. Zhang, Q. Yang, C. Li, Y. Fu, H. Zhang, Z. Ye, X. Zhou, Q. Li, T. Wang, S. Wang, W. Zhang, C. Xiong, Q. Wang, Solid-state cooling by elastocaloric polymer with uniform chain-lengths, Nat. Commun. 13 (2022) 1–7, https://doi.org/10.1038/s41467-021-27746-y.
[42] H. Hou, E. Simsek, T. Ma, N.S. Johnson, S. Qian, C. Cissé, D. Stasak, N. Al Hasan, L. Zhou, Y. Hwang, R. Radermacher, V.I. Levitas, M.J. Kramer, M.A. Zaeem, A. P. Stebner, R.T. Ott, J. Cui, I. Takeuchi, Fatigue-resistant high-performance elastocaloric materials made by additive manufacturing, Science 366 (2019) 1116–1121, https://doi.org/10.1126/science.aax7616.
[43] K. Navickaitė, J. Liang, C. Bahl, S. Wieland, T. Buchenau, K. Engelbrecht, Experimental characterization of active magnetic regenerators constructed using laser beam melting technique, Appl. Therm. Eng. 174 (2020) 1–12, https://doi.org/10.1016/j.applthermaleng.2020.115297.
[44] E. Stevens, K. Kimes, D. Salazar, A. Mostafaei, R. Rodriguez, A. Acierno, P. Lázpita, V. Chernenko, M. Chmielus, Mastering a 1.2 K hysteresis for martensitic para-ferromagnetic partial transformation in Ni-Mn(Cu)-Ga magnetocaloric material via binder jet 3D printing, Addit. Manuf. 37 (2021), https://doi.org/10.1016/j.addma.2020.101560.
[45] A.D. Valentine, T.A. Busbee, J.W. Boley, J.R. Raney, A. Chortos, A. Kotikian, J. D. Berrigan, M.F. Durstock, J.A. Lewis, Hybrid 3D printing of soft electronics, Adv. Mater 29 (2017) 1–8, https://doi.org/10.1002/adma.201703817.
[46] R. Adams, S.P. Soe, R. Santiago, M. Robinson, B. Hanna, G. McShane, M. Alves, R. Burek, P. Theobald, A novel pathway for efficient characterisation of additively manufactured thermoplastic elastomers, Mater. Des. 180 (2019), 107917, https://doi.org/10.1016/j.matdes.2019.107917.
[47] N.G. Tanikella, B. Wittbrodt, J.M. Pearce, Tensile strength of commercial polymer materials for fused filament fabrication 3D printing, Addit. Manuf. 15 (2017) 40–47, https://doi.org/10.1016/j.addma.2017.03.005.
[48] C. Oztan, S. Ballikaya, U. Ozgun, R. Karkkainen, E. Celik, Additive manufacturing of thermoelectric materials via fused filament fabrication, Appl. Mater. Today 15 (2019) 77–82, https://doi.org/10.1016/j.apmt.2019.01.001.
[49] X. Gao, S. Qi, X. Kuang, Y. Su, J. Li, D. Wang, Fused filament fabrication of polymer materials: a review of interlayer bond, Addit. Manuf. 37 (2021), 101658, https://doi.org/10.1016/j.addma.2020.101658.
[50] D. Fico, D. Rizzo, R. Casciaro, C.E. Corcione, A review of polymer-based materials for fused filament fabrication (FFF): focus on sustainability and recycled materials, Polymers 14 (2022) 465, https://doi.org/10.3390/polym14030465.
[51] D. Herzog, V. Seyda, E. Wycisk, C. Emmelmann, Additive manufacturing of metals, Acta Mater. 117 (2016) 371–392, https://doi.org/10.1016/j.actamat.2016.07.019.
[52] Z. Liu, D. Zhao, P. Wang, M. Yan, C. Yang, Z. Chen, J. Lu, Z. Lu, Additive manufacturing of metals: Microstructure evolution and multistage control, J. Mater. Sci. Technol. 100 (2022) 224–236, https://doi.org/10.1016/j.jmst.2021.06.011.
[53] S. Jasmee, G. Omar, N.A.B. Masripan, A.A. Kamarolzaman, A.S. Ashikin, F.C. Ani, Hydrophobicity performance of polyethylene terephthalate (PET) and thermoplastic polyurethane (TPU) with thermal effect, Mater. Res. Express 5 (2018), 096304, https://doi.org/10.1088/2053-1591/aad81e.

[54] K.K. Nielsen, H.N. Bez, L. Von Moos, R. Bjørk, D. Eriksen, C.R.H. Bahl, Direct measurements of the magnetic entropy change, Rev. Sci. Instrum. 86 (2015), 103903, https://doi.org/10.1063/1.4932308.
[55] N. Candau, E. Vives, A.I. Fernández, M.L. Maspoch, Elastocaloric effect in vulcanized natural rubber and natural/wastes rubber blends, Polymer 236 (2021), 124309, https://doi.org/10.1016/j.polymer.2021.124309.
[56] N. Candau, L. Chazeau, J.M. Chenal, C. Gauthier, J. Ferreira, E. Munch, C. Rochas, Characteristic time of strain induced crystallization of crosslinked natural rubber, Polymer 53 (2012) 2540–2543, https://doi.org/10.1016/j.polymer.2012.04.027.
[57] G.A. Holzapfel, J.C. Simo, Entropy elasticity of isotropic rubber-like solids at finite strains, Comput. Methods Appl. Mech. Eng. 132 (1996) 17–44, https://doi.org/10.1016/0045-7825(96)01001-8.
[58] V.N. Khiêm, M. Itskov, Journal of the mechanics and physics of solids analytical network-averaging of the tube model : strain-induced crystallization in natural rubber, J. Mech. Phys. Solids 116 (2018) 350–369, https://doi.org/10.1016/j.jmps.2018.04.003.
[59] C. Koch, L. Van Hulle, N. Rudolph, Investigation of mechanical anisotropy of the fused filament fabrication process via customized tool path generation, Addit. Manuf. 16 (2017) 138–145, https://doi.org/10.1016/j.addma.2017.06.003.
[60] A. Nasirov, I. Fidan, Prediction of mechanical properties of fused filament fabricated structures via asymptotic homogenization, Mech. Mater. 145 (2020), 103372, https://doi.org/10.1016/j.mechmat.2020.103372.
[61] K.K. Nielsen, K. Engelbrecht, The influence of the solid thermal conductivity on active magnetic regenerators, J. Phys. D. Appl. Phys. 45 (2012), 145001, https://doi.org/10.1088/0022-3727/45/14/145001.
[62] K.K. Nielsen, C.R.H. Bahl, A. Smith, K. Engelbrecht, U.L. Olsen, N. Pryds, The influence of non-magnetocaloric properties on the performance in parallel-plate AMRs, Int. J. Refrig. 37 (2014) 127–134, https://doi.org/10.1016/j.ijrefrig.2013.09.022.
[63] S. Qian, J. Ling, Y. Hwang, R. Radermacher, I. Takeuchi, Thermodynamics cycle analysis and numerical modeling of thermoelastic cooling systems, Int. J. Refrig. 56 (2015) 65–80, https://doi.org/10.1016/j.ijrefrig.2015.04.001.
[64] Y.J. He, Q.P. Sun, Frequency-dependent temperature evolution in NiTi shape memory alloy under cyclic loading, Smart Mater. Struct. 19 (2010), https://doi.org/10.1088/0964-1726/19/11/115014.
[65] H. Hou, S. Qian, I. Takeuchi, Materials, physics, and systems for multicaloric cooling, Nat. Rev. Mater. 7 (2021) 633–652, https://doi.org/10.1038/s41578-022-00428-x.
[66] J. Tušek, K. Engelbrecht, L.P. Mikkelsen, N. Pryds, Elastocaloric effect of Ni-Ti wire for application in a cooling device, J. Appl. Phys. 117 (2015), 124901, https://doi.org/10.1063/1.4913878.
[67] C. Bechtold, C. Chluba, R.L. De Miranda, E. Quandt, High cyclic stability of the elastocaloric effect in sputtered TiNiCu shape memory films, Appl. Phys. Lett. 101 (2012), 091903, https://doi.org/10.1063/1.4748307.
[68] L. Mañosa, A. Planes, E. Vives, E. Bonnot, R. Romero, The use of shape-memory alloys for mechanical refrigeration, Funct. Mater. Lett. 2 (2009) 73–78, https://doi.org/10.1142/S1793604709000594.
[69] Y. Li, D. Zhao, J. Liu, S. Qian, Z. Li, W. Gan, X. Chen, Energy-efficient elastocaloric cooling by flexibly and reversibly transferring interface in magnetic shape-memory alloys, ACS Appl. Mater. Interfaces 10 (2018) 25438–25445, https://doi.org/10.1021/acsami.8b07703.
[70] T.L. Smith, Volume changes and dewetting in glass bead-polyvinyl chloride elastomeric composites under large deformations, Trans. Soc. Rheol. 3 (1959) 113–136, https://doi.org/10.1122/1.548847.
[71] G.N. Greaves, A.L. Greer, R.S. Lakes, T. Rouxel, Poisson's ratio and modern materials, Nat. Mater. 10 (2011) 823–837, https://doi.org/10.1038/nmat3134.
[72] A. Clausen, F. Wang, J.S. Jensen, O. Sigmund, J.A. Lewis, Topology optimized architectures with programmable Poisson's ratio over large deformations, Adv. Mater. 27 (2015) 5523–5527, https://doi.org/10.1002/adma.201502485.
[73] Y.X. Xu, J.Y. Juang, Measurement of nonlinear poisson's ratio of thermoplastic polyurethanes under cyclic softening using 2d digital image correlation, Polymers 13 (2021), https://doi.org/10.3390/polym13091498.

Supplementary Information for

Additive manufactured thermoplastic elastomers for low-stress driven elastocaloric cooling

This Supplementary Information file includes:

Supplementary Notes 1 to 5
Supplementary Figures 1 to 17
Supplementary Tables 1 to 3
Supplementary References 1 to 9

Supplementary Note 1. DSC measurements for specific heat capacity

The specific heat capacity (c_p) for the materials, including the virgin filaments, uncycled printed samples and cycled printed samples, were investigated and used for materials COP calculations. Due to the weak elastocaloric performance for Kungfu98A, it was not printed for the following studies so its c_p measurement was only measured in the filament form. The specific heat capacity of materials is measured experimentally at temperatures within the temperature range of 275-315 K, fully covering the temperature range of operation. The cycled printed samples are cycled 100 times before the DSC measurements. Eliminating the uncertain values near the test temperature edges, the results for c_p listed in the Supplementary Table 2 are obtained from the average value around the temperature change range 290-310 K. Here, the values are nearly constant with the temperature increase and no latent heat is observed in the temperature range. It is noted that the heat capacity of the uncycled printed material has a slight decrease compared to the original filament. Maybe the reason is that the melting and solidification during the fused filament fabrication process changes its thermal properties due to the hard segment contents variation [1,2]. After cyclic tests, the heat capacity of the materials increases, which also happens in natural rubbers when subjected to a larger uniaxial deformation [3]. The c_p values from the cycled material are closer to the real situation in which materials are employed for the elastocaloric cooling. Thus these are used for the materials COP calculations.

Supplementary Note 2. Cyclic tests for elastocaloric elastomers

As observed in filaments as well as the printed dogbone, the elastocaloric effect in elastomers is usually accompanied by a large deformation which leads to buckling during the

releasing process. Assuming the materials are employed in an active elastocaloric regenerator, this buckling will push fluid in the channels and even worse some channels get twisted and it becomes hard for the heat transfer fluid to move through, increasing the pressure drop and the input work for the flow system. To avoid the buckling in the rubber-like elastomers, some technical tricks can be imposed such as performing pre-elongation of the sample and controlling by going back to zero force instead of zero strain [4,5]. The cyclic tests performed in the mechanical stability test are controlled by releasing until a strain in the range of when the stress in the material reaches zero in the NinjaFlex filament cyclic test (see, Supplementary figure 1, which is about 50%-150%). The pre-strain (strain returns to 150%) approach also applies to the cycled printed samples which are implemented for the SEM analysis, cyclic elastocaloric characterization, and the COP calculations.

Supplementary Note 3. Solidify ratio evaluation for printed samples

For the fused filament fabrication (FFF) printed part, the sample density is associated with the solidity ratio (SR) which can be calculated theoretically via the area of the ellipsoid bead divided by the potential maximum area between the beads (the rectangle area with the nozzle diameter and layer height) [6], written as the following equation:

$$SR = \frac{S_{ellipsoid}}{S_{Rectangle}} = \frac{ab\pi}{hD} \tag{1}$$

where the a, b, h and D are the semi-major, semi-minor axes of the ellipsoid bead and the layer height and the nozzle diameter. The SR is a normalized density for the printed part. The layer height is 0.0943 mm, obtained from the printed part height divided by the layer number generated in the printing G-code, and D is 0.3 mm for the printing. The parameters a and b are obtained from the measurement on the SEM images.

Supplementary Note 4. Characterization of surface temperature variation vs time

When conducting the cyclic elastocaloric measurements, the cyclic temperature change is dependent on the sample thickness and the loading rate. That is because the heat exchange of the sample to the surroundings is time-dependent and the thermal diffusion for the solid material is related to the sample dimension [7–9]. We apply Newton's law of cooling:

$$T = T_{\mathrm{amb}} + (T_{\mathrm{i}} - T_{\mathrm{amb}})e^{-\frac{t}{\omega}} \tag{2}$$

Here T_{amb} is the ambient temperature, T_{i} is the initial temperature for cooling start, and t is time. The surface temperature change of the sample in the ambient temperature can be characterized by the time constant ω. The printed dogbones in different thicknesses are tested during an elastocaloric cooling cycle, and the fitting is shown in Supplementary figure 10 for the NinjaFlex material.

Supplementary Note 5. Calculations of $\mathrm{COP_{mat}}$

The measurements of c_p for the elastomeric materials show a weak temperature dependence and can be considered to be constant. The average c_p values near room temperature are listed in Supplementary Table 2. Thus the $\mathrm{COP_{mat}}$ calculation is simplified to the measured values of $\Delta T_{\mathrm{ad}} c_p$ divided by the input work per unit mass:

$$\mathrm{COP}_{\mathrm{mat}} = \frac{Q/m}{\Delta W/m} = \frac{\int_{T_1}^{T_2} c_p dT}{\frac{1}{\rho l_0}\oint \sigma d\varepsilon} = \frac{\Delta T_{\mathrm{ad}} c_p}{\frac{1}{m}\oint F dl} \quad (3)$$

The input work per unit mass can be obtained from the integral area of the closed force-displacement loop divided by the effective mass in the gauge length in the dogbone sample. The integration and the temperature change for proposed printed dogbones are extracted from the stress-displacement curves and temperature-time curves from Supplementary figures 11-14, which are measured in the cyclic test returning to a preset displacement at 22.5 mm to avoid buckling.

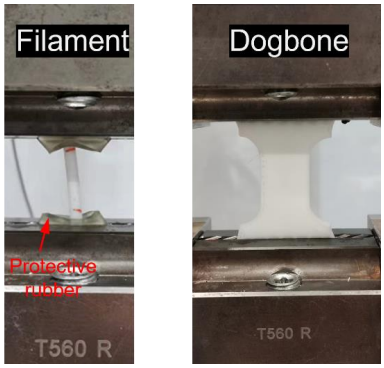

Supplementary Figure 1. Physical images for the elastomeric filament and dogbone mechanical tests.

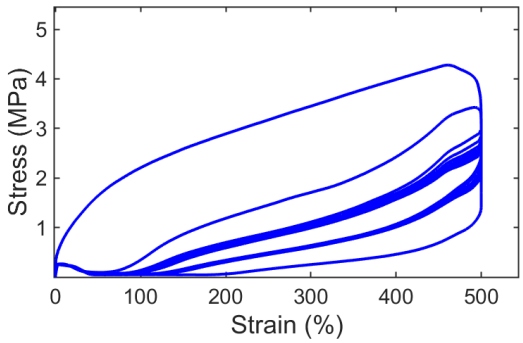

Supplementary Figure 2. Stress-strain curves of the NinjaFlex filament undergoing ten cyclic tests.

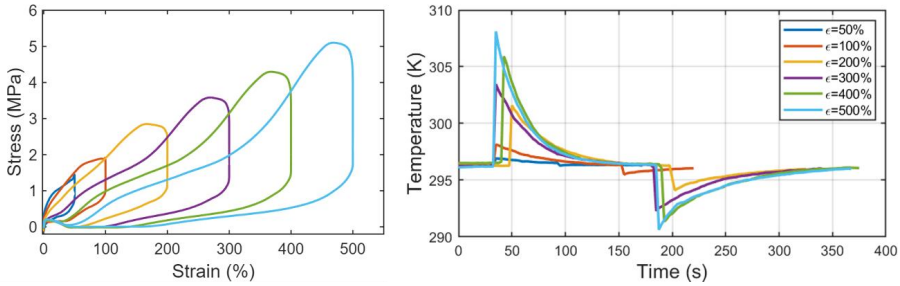

Supplementary Figure 3. Stress-strain behavior and the surface temperature variation as a function of time under different strains for the NinjaFlex filament.

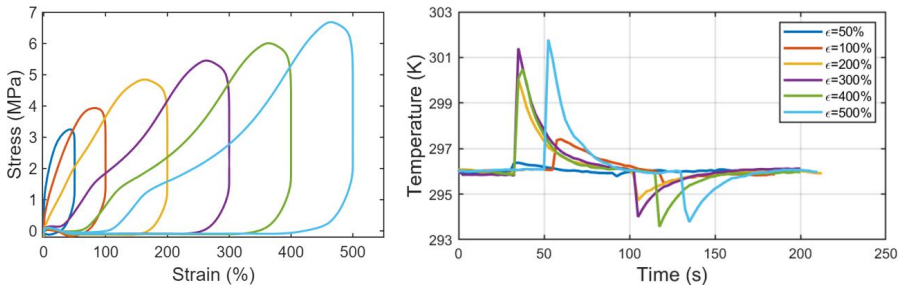

Supplementary Figure 4. Stress-strain behavior and the surface temperature variation as a function of time under different strains for the Ultimaker filament.

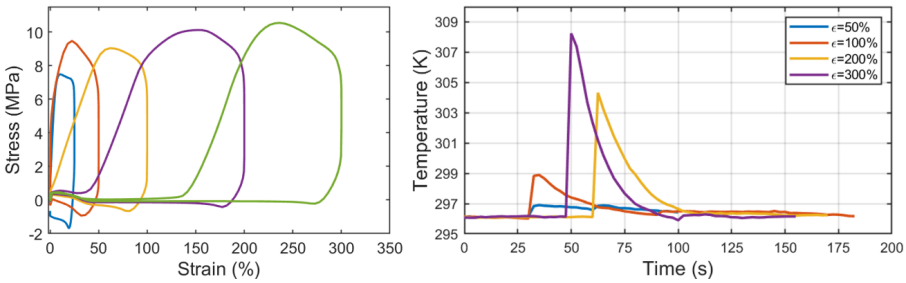

Supplementary Figure 5. Stress-strain behavior and the surface temperature variation as a function of time under different strains for the KungFu72D filament.

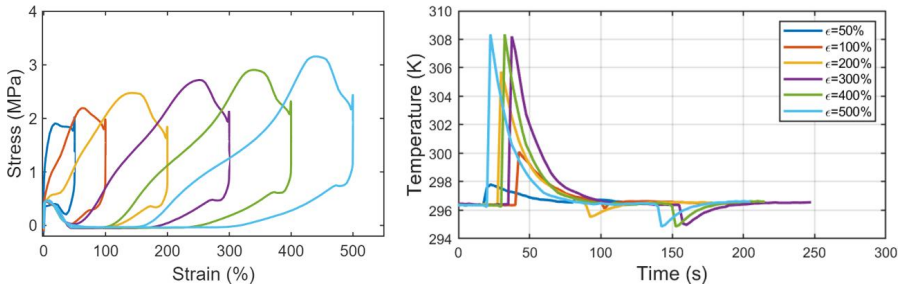

Supplementary Figure 6. Stress-strain behavior and the surface temperature variation as a function of time under different strains for the KungFu98A filament.

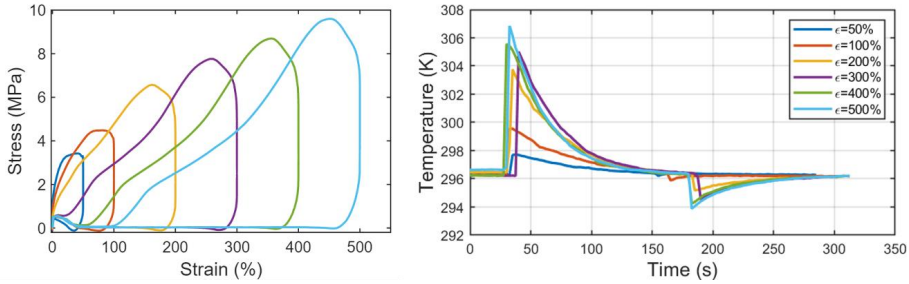

Supplementary Figure 7. Stress-strain behavior and the surface temperature variation as a function of time under different strains for the Z-Flex filament.

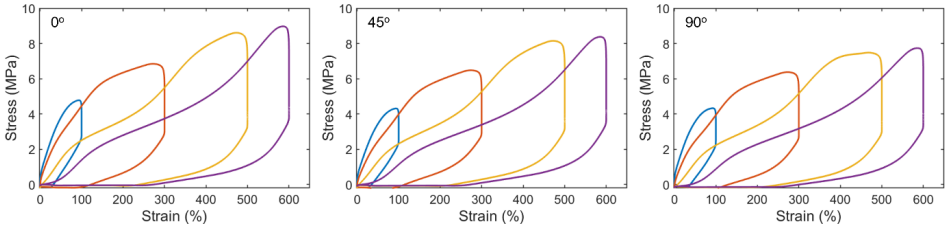

Supplementary Figure 8. Stress-strain behavior for different orientations of the printed samples, at different applied strains.

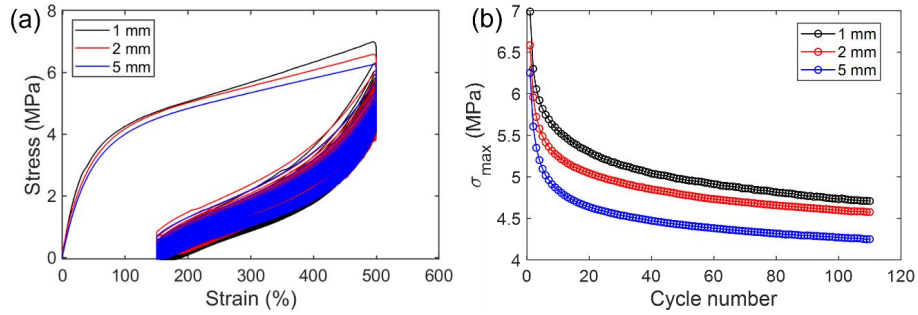

Supplementary Figure 9. (a) Stress-strain behavior of 110 cycles for different thicknesses of the printed parts; (b)The maximum stress evolution in each cycle as a function of the cycle number for different thickness printed parts.

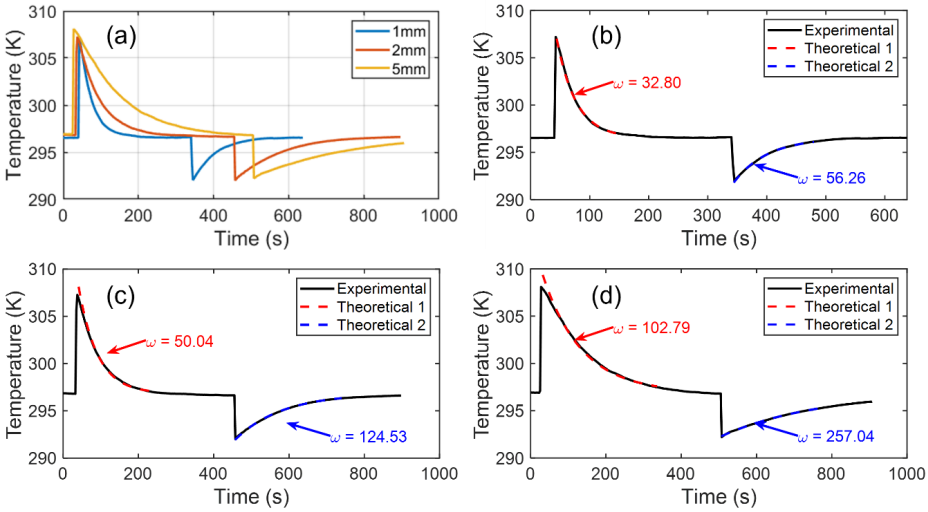

Supplementary Figure 10. (a) the surface temperature variation as a function of time under the same loading rate and strain for NinjaFlex dogbones with different thicknesses; (b)-(d) the fitting results of the parameter ω based on Newton's law of cooling for 1, 2, and 5 mm NinjaFlex dogbones, respectively.

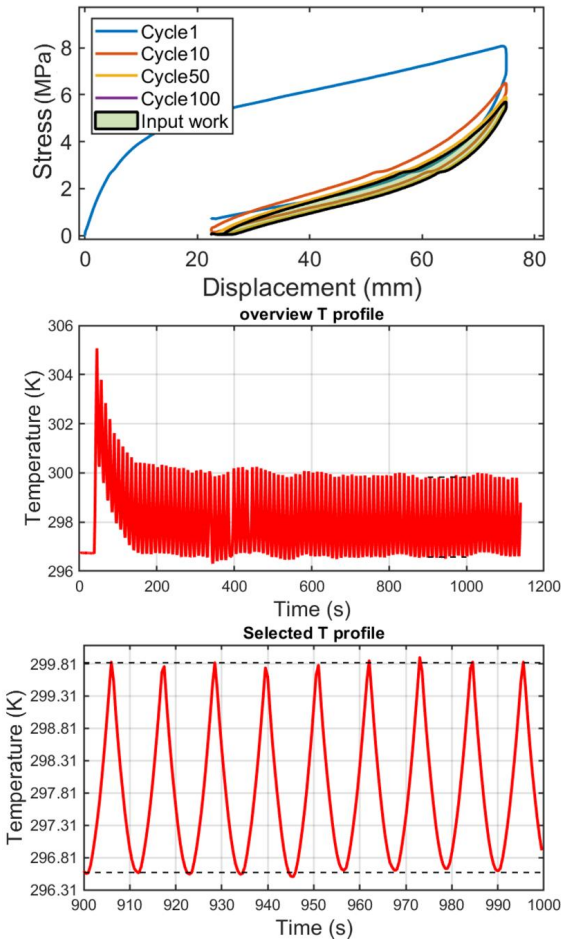

Supplementary Figure 11. The cyclic Stress-strain behavior, the cyclic temperature variation, and the zoomed temperature-time curves for NinjaFlex dogbone sample in 0^{o} orientation.

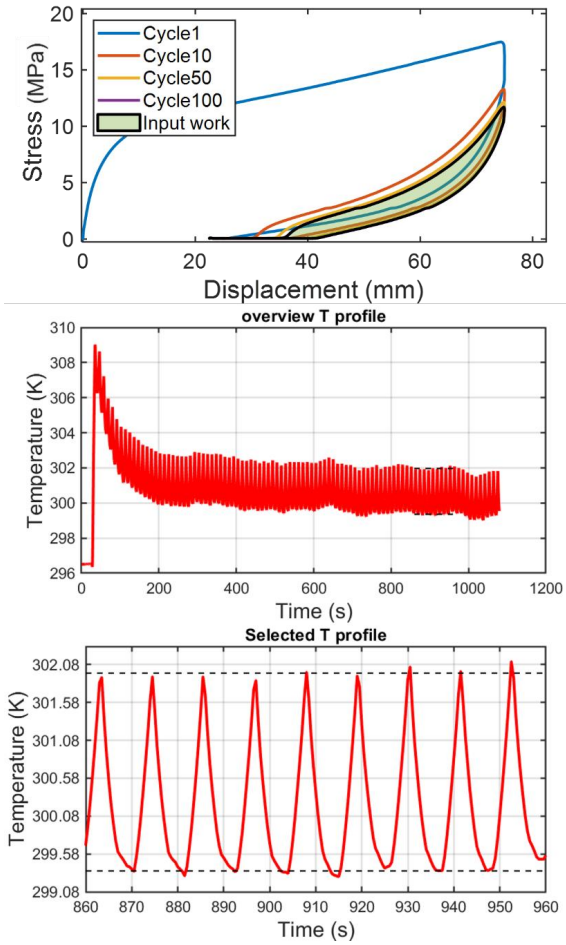

Supplementary Figure 12. The cyclic Stress-strain behavior, the cyclic temperature variation, and the zoomed temperature-time curves for the Ultimaker dogbone sample in 0^{o} orientation.

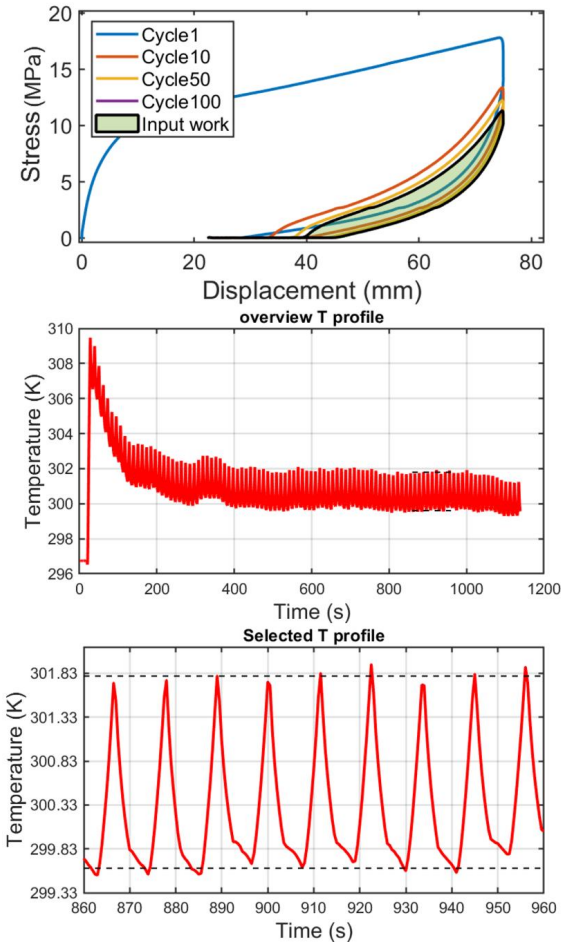

Supplementary Figure 13. The cyclic Stress-strain behavior, the cyclic temperature variation, and the zoomed temperature-time curves for the Kungfu98A dogbone sample in 0^{o} orientation.

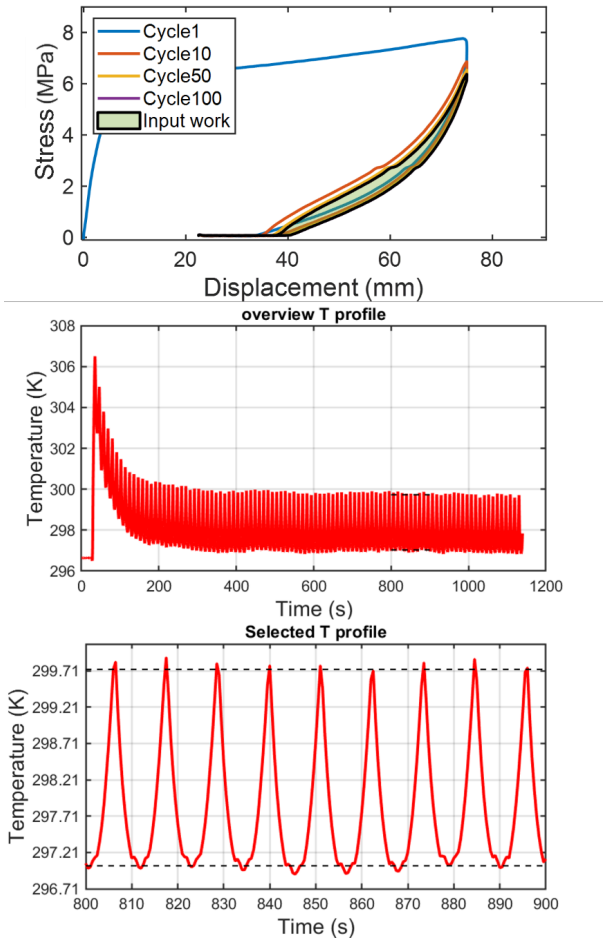

Supplementary Figure 14. The cyclic Stress-strain behavior, the cyclic temperature variation, and the zoomed temperature-time curves for the Z-Flex dogbone sample in 0º orientation.

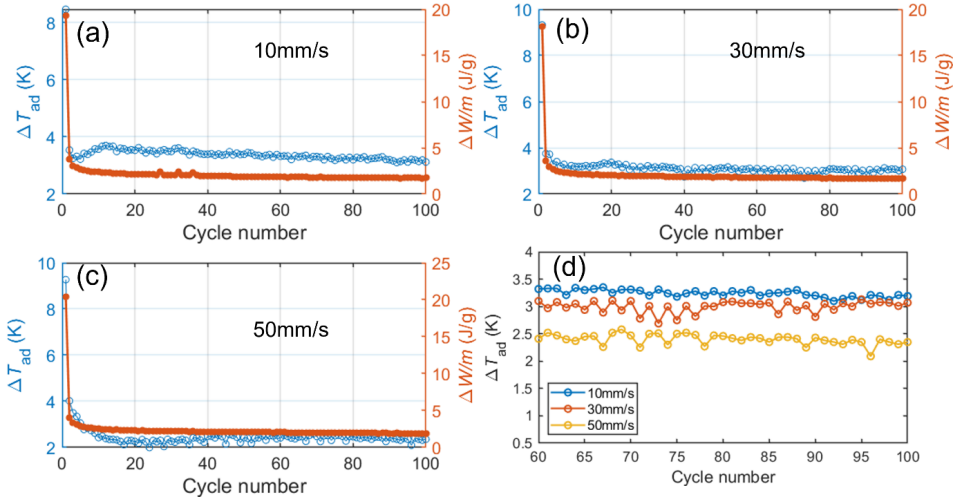

Supplementary Figure 15. Adiabatic temperature changes and input work per unit mass as a function of the number of cycles at different loading rates and the equilibrium temperature changes in the last 40 cycles, for a 1 mm NinjaFlex dogbone sample.

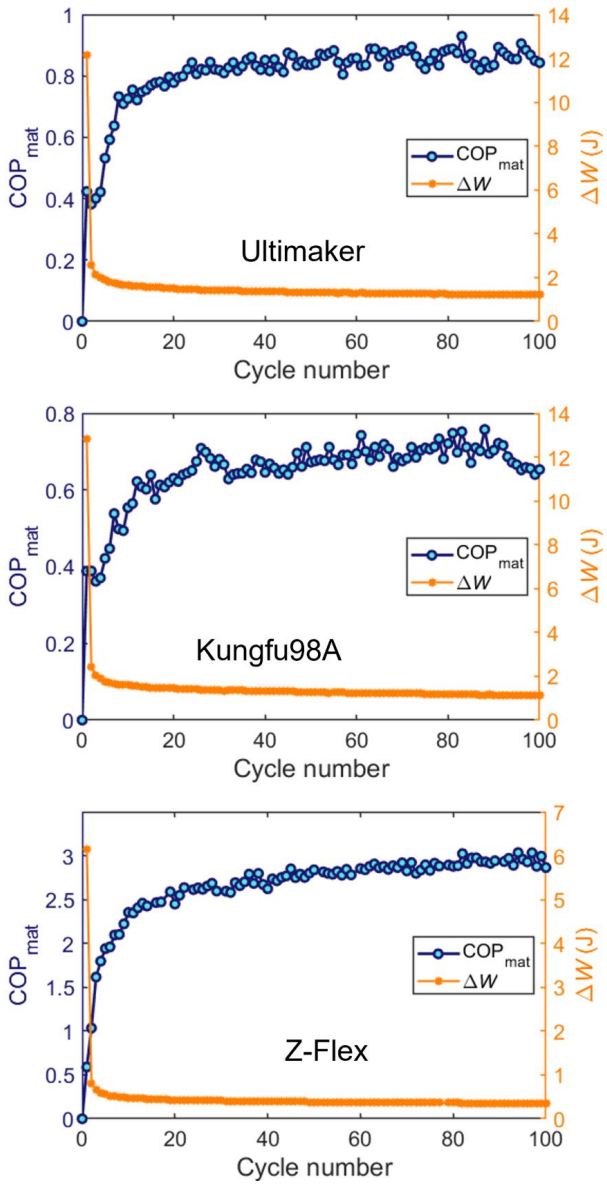

Supplementary Figure 16. COP_{mat} and input work evolution as a function of the number of cycles for Ultimaker, KungFu98A, and Z-Flex dogbones.

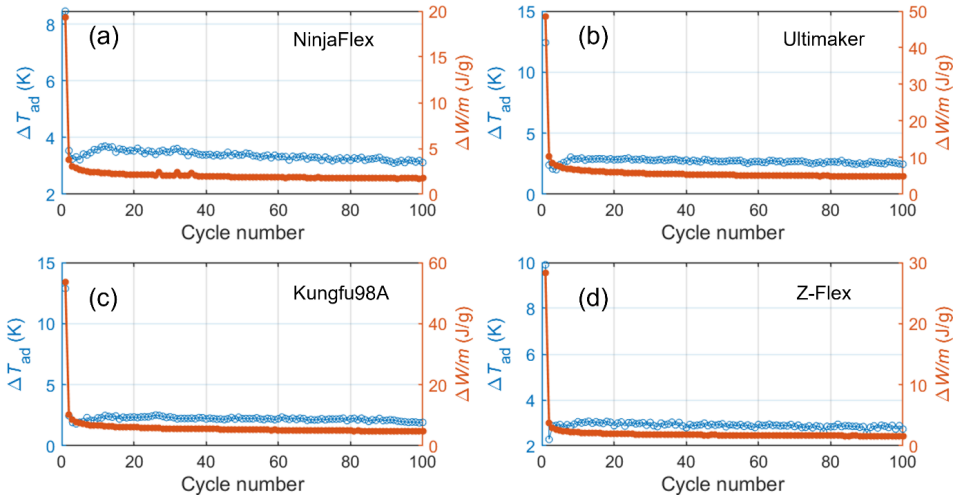

Supplementary Figure 17. Adiabatic temperature changes and input work per unit mass as a function of the number of cycles for different materials.

Supplementary Table 1. Information of experimental filaments and the corresponding 3D printing parameters

Filaments	Material (g/cm2)	Diameter (mm)	Shore hardness	Nozzle temperature (°C)	Bed temperature (°C)	Print speed (mm/s)
1. NinjaFlex	TPU	2.85	85A	228	40	15
2. Ultimaker95A	TPU	2.85	95A	230	70	20
3. KungFu72D	TPU	1.75	72D	225	45	15
4. KungFu98A	TPU	1.75	98A	225	45	15
5. Z-Flex	TPPE	1.75	83A	220	50	15

Supplementary Table 2. The specific heat capacity values for studied materials in different forms are measured by DSC.

Materials	c_p of filament (J/g*K)	c_p of uncycled printed specimen (J/g*K)	c_p of cycled specimen (J/g*K)
1. NinjaFlex	1.707	1.619	1.659
2. Ultimaker95A	1.625	1.560	1.657
3. KungFu72D	1.455	--	--
4. KungFu98A	1.595	1.587	1.618
5. Z-Flex	1.670	1.706	1.686

--: did not measure due to for the sample not being printed.

Supplementary Table 3. Transducers and sensor information employed in the experimental equipment in the paper.

Experimental devices	Related transducers	Type	Accuracies/ Uncertainties
IR camera	IR detector	InSb	Temperature accuracy

(InfraTec 9400)			0.02 K
Mechanical tester (Zwick/Roell EZ030)	Force sensor	Xforce K load cell 30 kN	Uncertainties 1%
DSC	Peltier-cells	Optotec OT08	Temperature range 27.0-68.0 °C
	Temperature control bath	Julabo CF40	Temperature stability ±0.03 °C
Filament dryer	Wanhao	Box2	Maximum temperature 80 °C

Supplementary References:

[1] R.J. Zdrahala, R.M. Gerkin, S.L. Hager, Polyether-Based Thermoplastic Polyurethanes. I. Effect of the Hard-Segment Content, J. Appl. Polym. Sci. 24(9) (2000) 2041–2050.

[2] A. Stribeck, B. Eling, E. Pöselt, M. Malfois, E. Schander, Melting, Solidification, and Crystallization of a Thermoplastic Polyurethane as a Function of Hard Segment Content, Macromol. Chem. Phys. 220 (2019) 1–10. https://doi.org/10.1002/macp.201900074.

[3] D. Nieto Simavilla, J.D. Schieber, D.C. Venerus, Evidence of Deformation-Dependent Heat Capacity and Energetic Elasticity in a Cross-Linked Elastomer Subjected to Uniaxial Elongation, Macromolecules. 51 (2018) 589–597. https://doi.org/10.1021/acs.macromol.7b02139.

[4] Z. Xie, G. Sebald, D. Guyomar, Elastocaloric effect dependence on pre-elongation in natural rubber, Appl. Phys. Lett. 107 (2015). https://doi.org/10.1063/1.4929395.

[5] G. Coativy, H. Haissoune, L. Seveyrat, G. Sebald, L. Chazeau, J.M. Chenal, L. Lebrun, Elastocaloric properties of thermoplastic polyurethane, Appl. Phys. Lett. 117 (2020). https://doi.org/10.1063/5.0023520.

[6] C. Koch, L. Van Hulle, N. Rudolph, Investigation of mechanical anisotropy of the fused filament fabrication process via customized tool path generation, Addit. Manuf. 16 (2017) 138–145. https://doi.org/10.1016/j.addma.2017.06.003.

[7] H. Oßmer, Elastocaloric Microcooling, Karlsruher Instituts Für Technol. (2017) 230.

[8] N. Candau, E. Vives, A.I. Fernández, M.L. Maspoch, Elastocaloric effect in vulcanized natural rubber and natural/wastes rubber blends, Polymer (Guildf). 236 (2021) 124309. https://doi.org/10.1016/j.polymer.2021.124309.

[9] S. Zhang, Q. Yang, C. Li, Y. Fu, H. Zhang, Z. Ye, X. Zhou, Q. Li, T. Wang, S. Wang, W. Zhang, C. Xiong, Q. Wang, Solid-state cooling by elastocaloric polymer with uniform chain-lengths, Nat. Commun. 13 (2022) 1–7. https://doi.org/10.1038/s41467-021-27746-y.

II

ARTICLE

D.2 Articles II

K. Wang *et al.*
Volume compensation of large-deformation 3D-printed soft elastomeric elastocaloric regenerators
Appl. Phys. Lett. (2023), https://doi.org/10.1063/5.0177761

RESEARCH ARTICLE | NOVEMBER 28 2023

Volume compensation of large-deformation 3D-printed soft elastomeric elastocaloric regenerators

Kun Wang ; Johannes T. B. Overvelde ; Kurt Engelbrecht ; Rasmus Bjørk ; Christian R. H. Bahl

Appl. Phys. Lett. 123, 223904 (2023)
https://doi.org/10.1063/5.0177761

Applied Physics Letters ARTICLE pubs.aip.org/aip/apl

Volume compensation of large-deformation 3D-printed soft elastomeric elastocaloric regenerators

Cite as: Appl. Phys. Lett. **123**, 223904 (2023); doi: 10.1063/5.0177761
Submitted: 24 September 2023 · Accepted: 10 November 2023 ·
Published Online: 28 November 2023

Kun Wang,[1,a)] Johannes T. B. Overvelde,[2] Kurt Engelbrecht,[1] Rasmus Bjørk,[1] and Christian R. H. Bahl[1]

AFFILIATIONS

[1]Department of Energy Conversion and Storage, Technical University of Denmark, Anker Engelunds Vej 301, 2800 Kgs. Lyngby, Denmark
[2]Autonomous Matter Department, AMOLF, 1098XG Amsterdam, The Netherlands

[a)]**Author to whom correspondence should be addressed:** kunwa@dtu.dk

ABSTRACT

Elastomeric elastocaloric regenerators have great potential for use in low-stress elastocaloric cooling devices. However, these regenerators display an asymmetric fluid exchange when operating in an active elastocaloric cooling cycle, due to the large required strains and associated volume change. During strain, the fluid volume increases, which passively forces fluid flow into the regenerator; when the strain is released, the fluid volume decreases, which results in a fluid flow out of the regenerator. During a traditional elastocaloric cooling cycle, there are also active fluid flow periods provided by fluid displacers or pumps. Here, we study the passive fluid flow in high-strain regenerators using a numerical model and experiments in two types of regenerators. Hyperelastic models are used to fit the experimentally measured mechanical behavior of thermoplastic polyurethane elastocaloric elastomers, and the model is subsequently used to conduct finite-element simulations predicting regenerator volume changes for an applied strain of 200%–600%. We validated the results using a specifically designed setup for measuring volume changes using pressure differences on a parallel-plate regenerator. For a strain range of 200%–600%, the predicted volume change ratio is 69.5%, closely matching the experimental value of 66.7%. We observed that the middle region of the regenerator experiences a higher volume change, which can be accurately accounted by the numerical model.

Elastocaloric materials (eCMs) that exhibit temperature increase and decrease in response to a uniaxial strain loading/unloading have seen a growing interest in recent years, especially as a promising alternative to conventional vapor-compression refrigerants. As elastocaloric cooling cycles are based on a solid-state refrigerant in contact with a water-based heat transfer fluid, the technology will have a lower global warming potential than refrigerants used in vapor compression.[1–3] Elastocaloric cooling is considered one of the promising solid-state refrigeration technologies (i.e., magnetocaloric,[4–6] electrocaloric,[7,8] elastocaloric,[9–12] and barocaloric[13,14]) and can potentially have a higher coefficient of performance (COP) and a net-zero greenhouse gas emission.[15,16] Elastocaloric cooling specifically was selected as the most promising non-vapor compression refrigeration technology by the US Department of Energy in 2014.[17] The investigation of high-performance elastocaloric materials and regenerators is crucial for driving the progress and widespread adoption of elastocaloric cooling technologies.

Soft elastomers, such as natural rubbers, thermoplastic polyurethane (TPU), and synthetic polymers, have recently emerged as potential materials for elastocaloric applications in cooling and heating.[18–22] These materials exhibit much lower applied stress requirements to trigger the elastocaloric effect (eCE), typically several MPa or even less. In contrast, elastocaloric alloys require several hundred MPa of applied stress, highlighting the need for mechanically robust systems.[10,16,23] Overcoming the challenge of high applied stress remains an ongoing engineering endeavor in elastocaloric refrigeration, hindering the miniaturization of cooling systems and limiting their potential applications. Recently, elastocaloric cooling prototypes using soft elastomers have been demonstrated with a comparably high COP = 6 and temperature span >8 K,[20,21,24] which provides an avenue for developing lower-stress and miniaturized eCE devices.

Active caloric regenerators act as a combination of refrigerant and heat exchangers and can extend the operating temperature span for the thermodynamic cycle.[25,26] The heat generation and absorption

as well as exchange between the source and sink take place in the regenerator structure. Over the past few decades, significant research efforts have been dedicated to exploring and constructing improved heat-transfer mechanisms and robust mechanical structures for magnetic and elastocaloric regenerators.[27–30] In recent years, additive manufactured (AM) technologies have become mature and especially adept at fabricating complex 3D structures, capable of increasing freedom of the structural design. There are an increasing number of studies with the goal of implementing AM methods to the fabrication of caloric regenerators or caloric materials preparation, some of which shows satisfactory or even enhanced performance compared to traditional regenerators.[22,29,31] Our previous studies show the great potential to implement AM to fabricate full-scale active eCE regenerators, potentially improving the temperature span.[22]

Operating as an active eCE regenerator, elastomer-based regenerators are subjected to four steps: loading, the cold-to-hot blow (cold blow), unloading, and hot-to-cold blow (hot blow). Figure 1(a) illustrates the fluid-channel volume change evolution over an elastocaloric thermodynamic cycle. The temperature variation associated with corresponding loading-unloading steps of elastocaloric elastomers is shown in Fig. 1(b) as obtained from our previous work.[22] During the first process 1–2, the regenerator is stretched resulting in a temperature increase. At the same time, the fluid-channel volume increases as the regenerator undergoes large strains, as shown in Fig. 1(a). The volume change is expressed as $V_f - V_i$ indicating the difference of the final and initial fluid-channel volume.

Importantly, it has been observed in a rubber-tube eCE cooler and in elastomers[24,32] that large strains cause the volume of fluid channels to change in an unclear manner, which results in asymmetric hot and cold blows as well as potentially unwanted heat transfer between the fluid and eCM during the loading and unloading processes. However, this effect has never been specifically investigated.

In this work, we study the volume change produced by the large deformation in elastomeric regenerators both experimentally and numerically to understand how to realize a regenerative elastocaloric cooling system with continuous fluid compensations. We study different fluid channels to investigate the geometrical impacts on volume changes, as illustrated in Fig. 1. Hyperelastic models are implemented in finite element (FE) simulations to predict volume changes of eCE regenerators. The corresponding regenerators are 3D-printed for validation of volume changes under large deformations.

The extra increased volume should be compensated to ensure the best-possible fluid flow profile throughout the cycle. In continuous flow systems, compensating for volume increases of the channel is typically inevitable due to the resulting negative pressure. Accordingly, a tailored fluidic compensation strategy can be devised to accommodate this volume change. The strategy involves managing compensations from the hot or cold reservoirs during the loading process and returning them to the reservoirs during the unloading process, depending on the specific cooling or heating implementations. Quantifying the amount of compensation volume is necessary for the development of high-performance regenerative elastomeric eCE regenerators.

We consider two typical regenerator fluid channels, namely parallel-plates (PP) and square channels, as shown in Fig. 1(c). For both regenerator geometries, the external regenerator shape is a dog-bone to avoid stress concentrations. The PP regenerator comprises 18 identical channels with a height of 4 mm while the square channel regenerator consists of 18 × 5 channels uniformly distributed in the

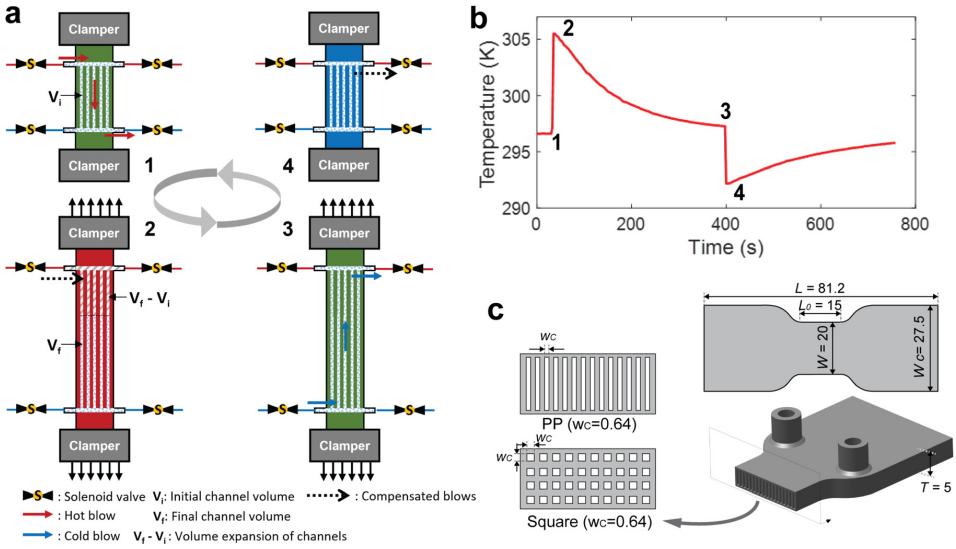

FIG. 1. Schematic illustration of the volume change induced by large deformation and the corresponding steps in an elastocaloric cycle, (a) and (b); schematic regenerator and two selected fluid channels labeled with the related geometric dimension (unit in mm), (c). Note that the schematic channels differ from the real numbers of channels, which are 18 for PP channels and 18 × 5 for square channels.

regenerator. Both the PP channel and the square channel have a channel length of 36 mm in the same regenerator shape.

TPU possesses various complex mechanical properties, such as hysteresis, softening, Mullins effect, and time dependence.[33,34] In this study, we have simplified the constitutive model based on the actual operating conditions of eCE regenerators. These regenerators undergo alternating loading and unloading at a constant strain rate, ultimately reaching a steady thermal exchange status and mechanical equilibrium. To accurately capture the fluid-channel volume change during cyclic loading, we start with FE simulations by employing hyperelastic constitutive models to fit the equilibrium stress–strain response for large-deformation eCE regenerators. Explicit FE methods are implemented in the simulation for the volume change predication. Hyperelasticity is also commonly employed to simplify phenomenological models for rubber-like materials.[35–37]

We use hyperelastic constitutive models to fit the uniaxial stress–strain response of the elastocaloric TPUs. The hyperelastic model is based on different strain potential density functions, W. We assume that our printed elastomers are isotropic. The constitutive relationship based on the theory of continuum mechanics can then be expressed by the three invariants of the right Cauchy-Green deformation tensor C.[38] For rubber-like elastomers during uniaxial tensile tests, the mechanical response is close to incompressibility ($J = 1$) under small stretches. However, when applying large strains, Poisson's ratio and mechanical responses will be highly strain-dependent.[39,40] For our cases, the applied strain reaches large strains 500%–600% where volume changes play an important role and the incompressibility constraint is no longer satisfactory. Here, we choose the Mooney–Rivlin model and Ogden model to fit the stress–strain response of TPU elastomers. The Mooney–Rivlin strain energy function can be expressed as[41]

$$W = \sum_{i,j=0}^{N} C_{ij}(\bar{I}_1 - 3)^i(\bar{I}_2 - 3)^j + \sum_{i=1}^{N} \frac{1}{d_i}(J-1)^{2i}, \quad (1)$$

and the Ogden strain energy function can be expressed as[42]

$$W = \sum_{i=1}^{N} \frac{\mu_i}{\alpha_i^2}\left(\bar{\lambda}_1^{\alpha_i} + \bar{\lambda}_2^{\alpha_i} + \bar{\lambda}_3^{\alpha_i} - 3\right) + \sum_{i=1}^{N} \frac{1}{d_i}(J-1)^{2i}. \quad (2)$$

In these strain energy function expressions, the invariants are modified in principal stretches (marked with the overline) form based on the deviatoric-volumetric multiplicative split for compressible material models.[39,43] See details in methods of the supplementary material.

To approach stabilized mechanical behavior, the standard sample was loaded for 20 cycles at a strain rate of $1\,s^{-1}$ which reaches equilibrium, as shown in Fig. 2(a) (see experimental details in the supplementary material). The performed strain range 0%–500% is based on our desired operating range for a prototype. The equilibrium stress–strain response of loading process of the 20th cycle is employed for the hyperelastic model fitting by removing the creep regime. Basically, this bucking is always observed due to creep caused extension, even upon full contraction of the loading conditions. The fitting results are shown in Fig. 2(b). The fitting error can be evaluated as

$$\text{error}\,(\%) = \frac{\int_{\varepsilon_0}^{\varepsilon} |\sigma_{\text{sim}} - \sigma_{\text{exp}}|\, d\varepsilon}{\int_{\varepsilon_0}^{\varepsilon} \sigma_{\text{exp}}\, d\varepsilon} \times 100\%. \quad (3)$$

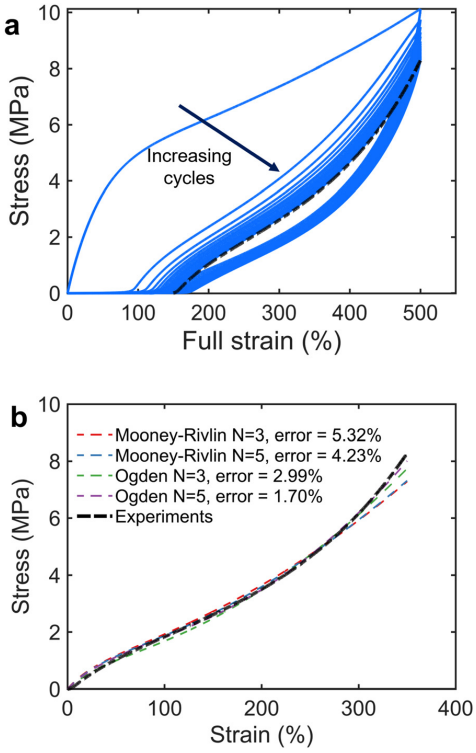

FIG. 2. Hyperelastic model fitting for the stress–strain response of TPU elastomers: (a) 20 tensile cycles (blue) with the equilibrium curve for fitting (black) and (b) comparison of hyperelastic fittings.

The fitting parameters for these four models are summarized in Table I. Comparing the fitting results, the N = 5 Ogden model achieves the best fitting and is, therefore, implemented in the FE simulation for the 3D-printed regenerator fluid-channel volume change prediction.

Next, a FE modeling of the regenerator to find the volume change was conducted. Half of the regenerator was modeled due to the symmetry and the inlet structures were also neglected in the simulation. We applied a strain in a sequence from 0 to 600% and the volume change ratio ($\delta V = \frac{V_f - V_i}{V_i} \times 100\%$) calculated is shown in Figs. 3(a) and 3(c). It can be seen that the volume change ratio in the PP-channel regenerator is higher than that of the square channel. Furthermore, the PP channel has a higher stress in the middle active region of the regenerator due to its smaller cross-sectional area. In principle, the stress should be similar. However, this section is softer due to less material; thus, more deformation goes there, so it should experience a higher stress. To visualize the fluid channels geometry variation under large deformation, the fluid channels of the initial and final states at a strain of 600% are shown in Figs. 3(b) and 3(d) for PP channels and square channels, respectively. Comparing the deformed channels in Figs. 3(a) and 3(b), we observe that the PP channels are

TABLE I. The fitting results list of the different hyperelastic models with different parameter numbers.

Hyperelastic models	Number	List of parameters										
Mooney model	N = 3	C10	C01	C11	d_1							
		0.205	0.458	0.051	5.385×10^{-5}							
	N = 5	C10	C01	C20	C11	C02	d_1					
		0.414	0.228	0.041	0.048	5.994×10^{-4}	0.159					
Ogden model	N = 3	μ_1	α_1	μ_2	α_2	μ_3	α_3	d_1				
		50.515	0.048	0.048	4.796	−0.052	−0.382	0.167				
	N = 5	μ_1	α_1	μ_2	α_2	μ_3	α_3	μ_4	α_4	μ_5	α_5	d_1
		1.556	0.397	0.397	2.835	0.005	7.489	2.835	0.326	2.285	0.035	1.003

subject to a buckling along the Z-axis (thickness direction), which is significant at the boundary channels while this is not observed for the square channels. This buckling might be the reason for the observed reduction in stability in the Z-axis of thin plate walls between the channels when undergoing a large uniaxial strain.[44] As a consequence, the PP channel buckling contributes to an increased volume change ratio in the PP channels. In addition, higher strains (~53 mm, 600%) are obtained by PP channels.

To validate the simulation results, experimental measurements were conducted to determine the actual volume change in the fluid channels during the stabilized mechanical process. The experimental setup was designed based on pressure difference measurements (see details in the supplementary material). The idea is to apply the same pressure to the regenerator and the air tank 2 (reference pressure) when the pressure gets stabilized to seal the regenerator as a closed volume. During the loading process, the volume change can be determined by monitoring pressure changes between the regenerator and air tank 2. The experimental fluidic system shown in Figs. 4(a) and 4(b) is the physical setup, where the regenerator pressure is denoted as *P1* and the reference pressure from air tank 2 is denoted as *P2*. The volume change ratio can be calculated based on the ideal gas law equation ($PV = nRT$),

$$\delta V = \frac{V_f - V_i}{V_i} = \frac{P_i}{P_f} - 1 = \frac{P_2}{P_1} - 1. \tag{4}$$

Taking into account impacts from the temperature changes of the regenerator and the connected tubes volume between the regenerator

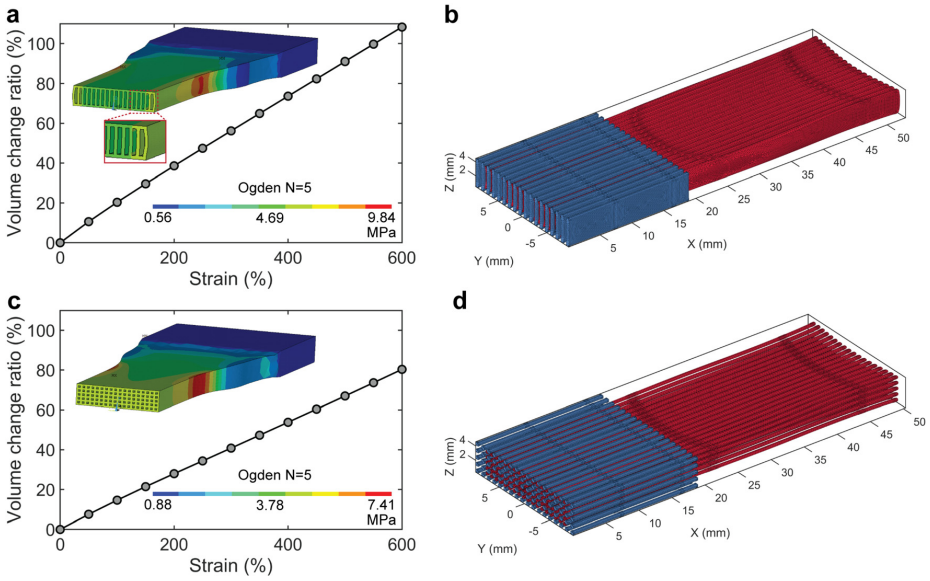

FIG. 3. Simulation results for PP channels (a) and square channels (c) volume change prediction as a function of strain (Von Mises stress at 600% for the insets), and corresponding 3D-fluid channels (b) and (d) under 600% strain where X = 0 mm is symmetric plane (Y–Z) and the clamped area is at X = 25.5 mm and X = 85.5 mm for initial (blue) and deformed (red) channels. (There is a 7.5 mm distance between the channel end and clamped area before loading.)

Applied Physics Letters ARTICLE pubs.aip.org/aip/apl

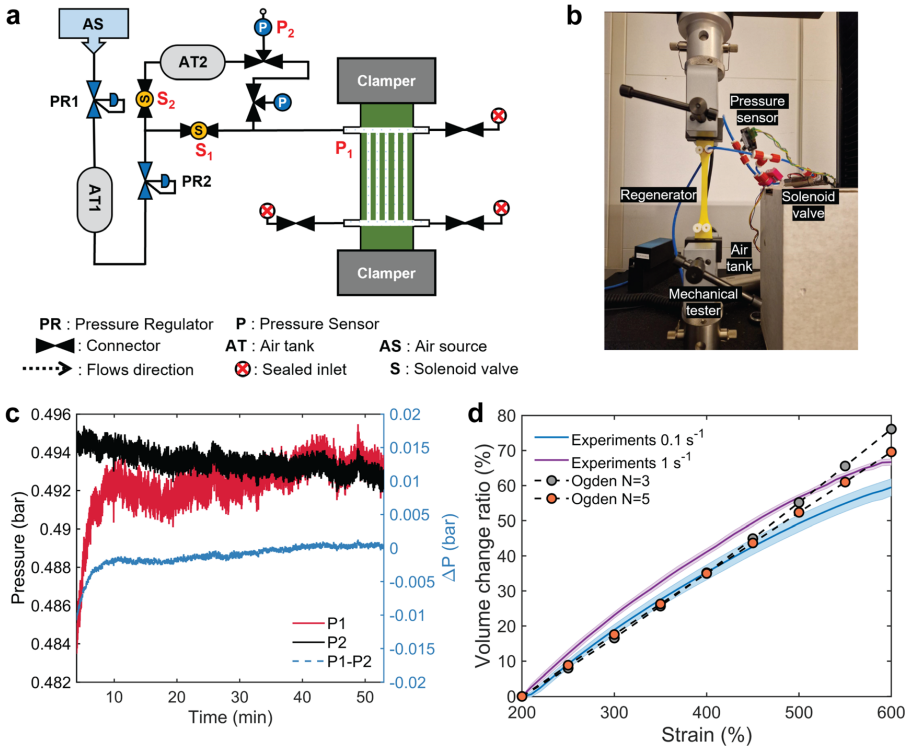

FIG. 4. Pneumatic experimental setup and simulation validation. (a) Fluidic circuit for pressure difference measurements (P1: regenerator pressure, P2: air tank 2 pressure). (b) Physical picture for the setup. (c) Airtight examination by monitoring pressure holding. (d) Comparison of volume change ratio as a function of strains at different loading rates (simulations performed at 1 s^{-1} loading rate).

and the pressure sensor, the actual volume change ratio of the regenerator can be calibrated to be (see details in the supplementary material about pressure change calibrations)

$$\delta V_R = \left(1+\frac{1}{\alpha}\right)\left(C\frac{P_i}{P_f}-1\right), \tag{5}$$

in which α and C are the temperature and volume calibration ratio, respectively. The temperature ratio (C) is defined as

$$C = \frac{P_f V_f}{P_i V_i} = \frac{T_f}{T_i}. \tag{6}$$

The volume ratio between regenerator channels and connection tubes is defined as α,

$$\alpha = \frac{V_R}{V_{\text{tube}}}. \tag{7}$$

The α value is 0.985 for PP channels, and the C value is 1.01 at 600%.

The PP regenerator is employed for the volume-change validation experimentally. Before measurements, the airtightness of the device and the regenerator need to be ensured. We applied a 0.5 bar pressure to tank 2 and the regenerator and closed the two solenoid valves [at 20 min in Fig. 4(c)] and waited for 30 min to confirm the pressure maintenance. The results of pressure differences ($P1–P2$) are stabilized approaching to zero indicating no air leakage in the regenerator and, thus, a good airtightness of the sample. The volume change measurements are performed under cyclic operation along X-axis at different strain rates for a strain range of 200%–600% to avoid creep. The volume change ratio as a function of strain at rates of 0.1 and 1 s^{-1} is shown in Fig. 4(d) along with the simulation results normalized to 200% strain to remove the creep regime. From the experimental results at different loading rates, the higher loading rate shows a larger volume change ratio. From the experimental results, we noticed that the regenerator subjected to a higher loading rate exhibited a larger volume change ratio. This is because the lower loading rate allows more creep deformation to occur.[33,45] The simulation results at 1 s^{-1} were slightly lower than the experimental results overall. This difference could be because the simulations did not include certain connecting structures between the regenerator fluid channels and the fluid inlet and outlet, which were present in the experiments and could also be that in

experiments the cross section is different due to the printing accuracy. Here, the Ogden model was applied to the simulation for comparison. It is noteworthy that the Ogden 3 and 5 models provide satisfactory predictions for the regenerator volume change in our desired operating range. When strains exceed 500%, there is an over estimation for Ogden 3 due to the constrained strain range (500%) employed for the hyperelastic fittings in Fig. 2. It can be anticipated that by employing a larger strain range during the hyperelastic model fitting, more accurate predictions can be obtained.

Operating in an eCE cycle, the ratio (V^*) of displaced fluid volume (V_{disp}) and regenerator volume (V_R) or utilization is one of evaluating factors for the eCE regenerator performance to measure how much heat extracted from the regenerator by heat-transfer fluids.[12,46,47] The V^* shows to be 1 for the best COP in a NiTi-based prototype at 1.7%,[46] which means the same V_{disp} and V_R. In this volume increased case, the V^* can be rewritten as

$$V^* = \frac{V_{disp}}{0.5 \times (V_{R,i} + V_{R,f})} = \frac{V_{disp}}{V_{R,i} + 0.5 V_{R,i} \delta V_R}. \quad (8)$$

For the PP regenerator, with a δV_R of 66.7%, the equivalent V^* will be 0.74, indicating decrease in V^* when the fluidic channel volume increases by large deformation. In previous regenerative coolers,[12,24] it has been demonstrated that the optimized V^*/utilization ratio provides enhanced cooling power and temperature span. However, this strain-induced volume change leads to the deviatoric V^* and asymmetric hot-cold blows and further will reduce the temperature span. It suggests a tailored flow system allowing compensating this volume change to maintain a satisfactory temperature span during practical operation.

In an actual 3D printed elastocaloric regenerator, the volume change also may be position-dependent. Simulation results can quantify the volume change distribution along the tensile direction. We consider the fluid channels segmented into 15 segments to examine the volume change distribution along the tensile axis. Figures 5(a) and 5(c) show the results for the PP channels and square channels under 600% strain, and the volume change ratio of each segment is plotted in Figs. 5(b) and 5(d). We observed after 20 mm of regenerator length the volume change ratio gradually decreases in a certain coordinate range for both PP channels (up to 48 mm) and square channels (up to 40 mm) and then slightly increases. This decrease in volume change along the regenerator length direction is due to the compression exerted by the rounded section of the dogbone-shaped regenerator, by observing deformed structures in Figs. 3(a) and 3(c). The volume change ratio increases at the channel end could be attributed to the boundary effect near the clamped side.

In conclusion, Ogden hyperelastic models achieve a good fit for the stress–strain response of eCE TPU elastomers and corresponding FE simulations for the prediction of regenerator volume compensations exhibit excellent agreement with experimental results. The PP regenerator shows higher volume change compared to the square-channel regenerator under significant deformation, due to thin-plate buckling instability. Subjecting the PP regenerator to a 200%–600% strain results in a 66.7% volume change ratio. A nonuniform volume change behavior is observed along the stretching direction, particularly in the rounded region of the dogbone-shaped regenerators. These results hold promise for accurately predicting volume compensation in

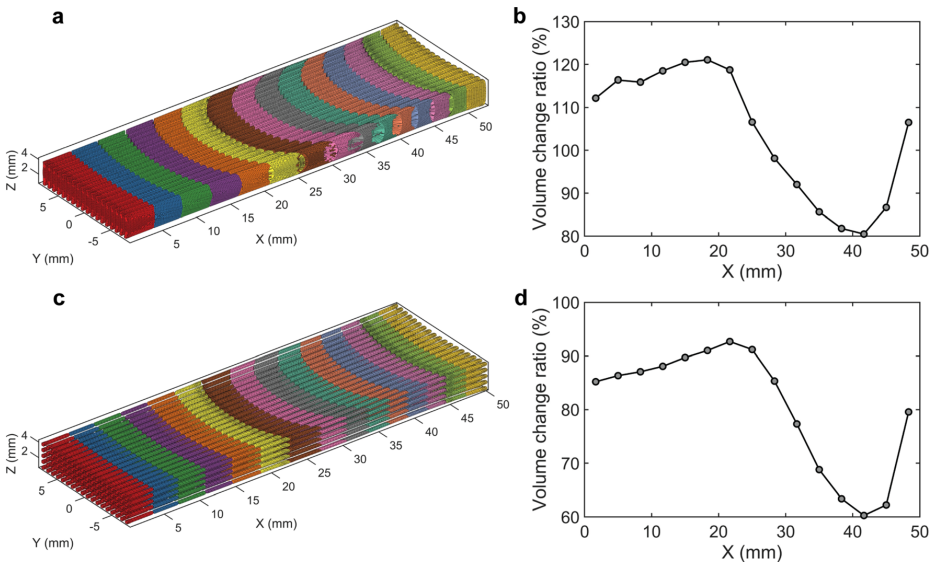

FIG. 5. Volume change distribution (volume change as a function of the X coordinate at 600%) along the tensile direction for the different volume channels: (a) and (b) for the parallel-plate channel; (c) and (d) for the square channel; in the figure of 3D-fluid channels, Y–Z is symmetric plane and X = 85.5 mm is clamped area. (Actually, there is a 7.5 mm distance between the channel end and clamped area.)

soft, large-deformation eCE regenerators and inspiring the design and modeling of active large-deformation regenerators.

See the supplementary material for experimental details and methods for the hyperelastic model fitting. The modeling conditions and calibrations of pressure change measurements are also included.

K. Wang is grateful for financial support from the Otto Mønsted Foundation and China Scholarship Council scholarship. This work is part of Dutch Research Council (NWO) and was partly performed at the research institute AMOLF. We wish to acknowledge Dr. Shibo Zou for the valuable discussion on fluidic setups and Paul Ducarme and Alberto Comoretto for the help in FE simulations.

AUTHOR DECLARATIONS

Conflict of Interest

The authors have no conflicts to disclose.

Author Contributions

Kun Wang: Conceptualization (equal); Data curation (equal); Formal analysis (equal); Investigation (equal); Methodology (equal); Project administration (equal); Software (equal); Validation (equal); Writing – original draft (equal); Writing – review & editing (equal). **Johannes T.B. Overvelde:** Funding acquisition (equal); Software (equal); Supervision (equal); Writing – review & editing (equal). **Kurt Engelbrecht:** Supervision (equal); Writing – review & editing (equal). **Rasmus Bjørk:** Funding acquisition (equal); Supervision (equal); Writing – review & editing (equal). **Christian R. H. Bahl:** Funding acquisition (equal); Supervision (equal); Writing – review & editing (equal).

DATA AVAILABILITY

The data that support the findings of this study are openly available in data.dtu.dk at https://doi.org/10.11583/DTU.23695065, Ref. 48.

REFERENCES

[1]M. O. McLinden, J. S. Brown, R. Brignoli, A. F. Kazakov, and P. A. Domanski, Nat. Commun. **8**, 14476 (2017).
[2]N. Abas, A. R. Kalair, N. Khan, A. Haider, Z. Saleem, and M. S. Saleem, Renewable Sustainable Energy Rev. **90**, 557–569 (2018).
[3]United Nations, *Handbook for the Montreal Protocol on Substances That Deplete the Ozone Layer*, 14th ed. (Ozone Secretariat, 2020).
[4]V. K. Pecharsky and K. A. Gschneidner, Jr., Phys. Rev. Lett. **78**, 4494–4497 (1997).
[5]O. Tegus, E. Brück, K. Buschow, and F. De Boer, Nature **415**, 150–152 (2002).
[6]J. Liu, T. Gottschall, K. P. Skokov, J. D. Moore, and O. Gutfleisch, Nat. Mater. **11**, 620–626 (2012).
[7]B. Neese, B. Chu, S.-G. Lu, Y. Wang, E. Furman, and Q. Zhang, Science **321**, 821–823 (2008).
[8]P. Bai, Q. Zhang, H. Cui, Y. Bo, D. Zhang, W. He, Y. Chen, and R. Ma, Adv. Mater. **35**, 2209181 (2023).
[9]E. Bonnot, R. Romero, L. Mañosa, E. Vives, and A. Planes, Phys. Rev. Lett. **100**, 125901 (2008).
[10]D. Cong, W. Xiong, A. Planes, Y. Ren, L. Mañosa, P. Cao, Z. Nie, X. Sun, Z. Yang, X. Hong *et al.*, Phys. Rev. Lett. **122**, 255703 (2019).
[11]J. Tušek,, A. Žerovnik, M. Čebron, M. Brojan, B. Žužek, K. Engelbrecht, and A. Cadelli, Acta Mater. **150**, 295–307 (2018).
[12]S. Qian, D. Catalini, J. Muehlbauer, B. Liu, H. Mevada, H. Hou, Y. Hwang, R. Radermacher, and I. Takeuchi, Science **380**, 722–727 (2023).
[13]B. Li, Y. Kawakita, S. Ohira-Kawamura, T. Sugahara, H. Wang, J. Wang, Y. Chen, S. I. Kawaguchi, S. Kawaguchi, K. Ohara *et al.*, Nature **567**, 506–510 (2019).
[14]D. Matsunami, A. Fujita, K. Takenaka, and M. Kano, Nat. Mater. **14**, 73–78 (2015).
[15]X. Moya, S. Kar-Narayan, and N. D. Mathur, Nat. Mater. **13**, 439–450 (2014).
[16]H. Hou, S. Qian, and I. Takeuchi, Nat. Rev. Mater. **7**, 633–652 (2022).
[17]U.S. Department of Energy. "Energy savings potential and RD&D opportunities for non-vapor-compression HVAC technologies," Technical Report (2014).
[18]D. Guyomar, Y. Li, G. Sebald, P.-J. Cottinet, B. Ducharne, and J.-F. Capsal, Appl. Therm. Eng. **57**, 33–38 (2013).
[19]Z. Xie, G. Sebald, and D. Guyomar, Appl. Phys. Lett. **107**, 081905 (2015).
[20]F. Greibich, R. Schwödiauer, G. Mao, D. Wirthl, M. Drack, R. Baumgartner, A. Kogler, J. Stadlbauer, S. Bauer, N. Arnold *et al.*, Nat. Energy **6**, 260–267 (2021).
[21]S. Zhang, Q. Yang, C. Li, Y. Fu, H. Zhang, Z. Ye, X. Zhou, Q. Li, T. Wang, S. Wang *et al.*, Nat. Commun. **13**, 9 (2022).
[22]K. Wang, K. Engelbrecht, and C. R. Bahl, Appl. Mater. Today **30**, 101711 (2023).
[23]L. Porenta, P. Kabirifar, A. Žerovnik, M. Čebron, B. Žužek, M. Dolenec, M. Brojan, and J. Tušek, Appl. Mater. Today **20**, 100712 (2020).
[24]G. Sebald, G. Lombardi, G. Coativy, J. Jay, L. Lebrun, and A. Komiya, Appl. Therm. Eng. **223**, 120016 (2023).
[25]K. K. Nielsen, J. Tusek, K. Engelbrecht, S. Schopfer, A. Kitanovski, C. R. H. Bahl, A. Smith, N. Pryds, and A. Poredos, Int. J. Refrig. **34**, 603–616 (2011).
[26]S. Qian, J. Yu, and G. Yan, Renewable Sustainable Energy Rev. **69**, 535–550 (2017).
[27]A. Kitanovski, U. Plaznik, U. Tomc, and A. Poredoš, Int. J. Refrig. **57**, 288–298 (2015).
[28]J. Liang, K. Engelbrecht, K. K. Nielsen, K. Loewe, H. Vieyra, A. Barcza, and C. R. Bahl, Appl. Therm. Eng. **186**, 116519 (2021).
[29]K. Navickaitė, J. Liang, C. Bahl, S. Wieland, T. Buchenau, and K. Engelbrecht, Appl. Therm. Eng. **174**, 115297 (2020).
[30]Y. Zhu, J. Hur, S. Cheng, Q. Sun, W. Li, and S. Yao, Int. J. Heat Mass Transfer **176**, 121372 (2021).
[31]H. Hou, E. Simsek, T. Ma, N. S. Johnson, S. Qian, C. Cissé, D. Stasak, N. Al Hasan, L. Zhou, Y. Hwang *et al.*, Science **366**, 1116–1121 (2019).
[32]N. Candau, C. Pradille, J.-L. Bouvard, and N. Billon, Polym. Test. **56**, 314–320 (2016).
[33]H. J. Qi and M. C. Boyce, Mech. Mater. **37**, 817–839 (2005).
[34]C. Prisacariu, *Polyurethane Elastomers: From Morphology to Mechanical Aspects* (Springer Science & Business Media, 2011).
[35]R. S. Rivlin and D. Saunders, Philos. Trans. R. Soc., A **243**, 251–288 (1951).
[36]D. Haines and W. Wilson, J. Mech. Phys. Solids **27**, 345–360 (1979).
[37]Y. Wang, W. Luo, J. Huang, C. Peng, H. Wang, C. Yuan, G. Chen, B. Zeng, and L. Dai, Macromol. Theory Simul. **29**, 2000009 (2020).
[38]K. Upadhyay, G. Subhash, and D. Spearot, J. Mech. Phys. Solids **124**, 115–142 (2019).
[39]M. Pelliciari, S. Sirotti, and A. M. Tarantino, J. Mech. Phys. Solids **176**, 105308 (2023).
[40]M. F. Beatty and D. O. Stalnaker, J. Appl. Mech. **53**, 807–813 (1986).
[41]R. S. Rivlin, Philos. Trans. R. Soc., A **241**, 379–397 (1948).
[42]R. W. Ogden, *Non-Linear Elastic Deformations* (Courier Corporation, 1997).
[43]J. C. Simo and T. J. Hughes, *Computational Inelasticity* (Springer Science & Business Media, 2006), Vol. 7.
[44]R. Brighenti, Eng. Struct. **27**, 265–276 (2005).
[45]J. S. Bergström and M. Boyce, J. Mech. Phys. Solids **46**, 931–954 (1998).
[46]J. Tušek, K. Engelbrecht, D. Eriksen, S. Dall'Olio, J. Tušek, and N. Pryds, Nat. Energy **1**, 16134 (2016).
[47]J. Tušek, K. Engelbrecht, R. Millán-Solsona, L. Manosa, E. Vives, L. P. Mikkelsen, and N. Pryds, Adv. Energy Mater. **5**, 1500361 (2015).
[48]K. Wang, J. T. B. Overvelde, K. Engelbrecht, R. Bjørk, and C. R. H. Bahl (2023), "Data set for 'Volume compensation of large-deformation 3D-printed soft elastomeric elastocaloric regenerators,'" data.dtu.dk. https://doi.org/10.11583/DTU.23695065

V

ARTICLE

D.3 Articles V

B.G.F. Eggert *et al.*
Study of the magnetostructural transition in critical-element free Mn1−xNi1−xFe2xSi0.95Al0.05
AIP Advances (2023), https://doi.org/10.1063/9.0000511

RESEARCH ARTICLE | FEBRUARY 03 2023

Study of the magnetostructural transition in critical-element free $Mn_{1-x}Ni_{1-x}Fe_{2x}Si_{0.95}Al_{0.05}$

Special Collection: 67th Annual Conference on Magnetism and Magnetic Materials

Bruno G. F. Eggert ; Kun Wang ; Sina Jafarzadeh ; Christian R. Bahl ; Bjørn C. Hauback ; Christoph Frommen

AIP Advances 13, 025215 (2023)
https://doi.org/10.1063/9.0000511

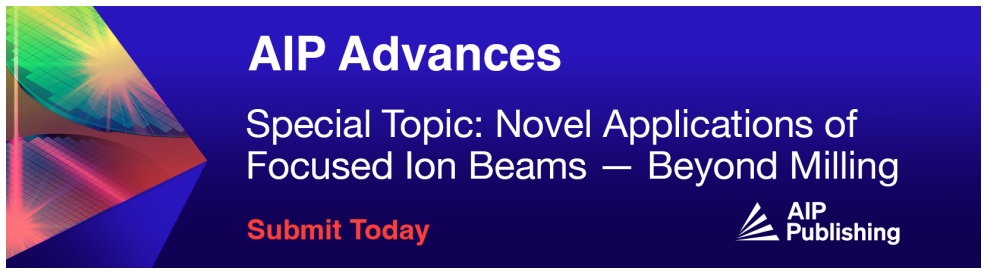

AIP Advances ARTICLE scitation.org/journal/adv

Study of the magnetostructural transition in critical-element free $Mn_{1-x}Ni_{1-x}Fe_{2x}Si_{0.95}Al_{0.05}$

Cite as: AIP Advances 13, 025215 (2023); doi: 10.1063/9.0000511
Submitted: 3 October 2022 • Accepted: 25 November 2022 •
Published Online: 3 February 2023

Bruno G. F. Eggert,[1] Kun Wang,[2] Sina Jafarzadeh,[2] Christian R. Bahl,[2] Bjørn C. Hauback,[1] and Christoph Frommen[1,a)]

AFFILIATIONS

[1] Department for Hydrogen Technology, Institute for Energy Technology (IFE), P.O. Box 40, NO-2027 Kjeller, Norway
[2] Department of Energy Conversion and Storage, Technical University of Denmark (DTU), Anker Engelunds Vej B301, DK-2800 Kgs. Lyngby, Denmark

Note: This paper was presented at the 67th Annual Conference on Magnetism and Magnetic Materials.
[a)] **Author to whom correspondence should be addressed:** Christoph.frommen@ife.no

ABSTRACT

Two different heat treatments have been carried out on similar $Mn_{1-x}Ni_{1-x}Fe_{2x}Si_{0.95}Al_{0.05}$ compositions with magnetostructural transitions between hexagonal and orthorhombic crystal structures around room temperature. The samples were analyzed concerning their structural, microstructural, magnetic, and caloric properties. The results show that the introduction of a high-temperature step, before the heat treatment (1073 K/7 days) usually used in the literature for such compounds modifies the microstructure, leading to sharper transitions with shorter transition widths, and stronger latent heat peaks. Magnetic field-assisted calorimetry and vibrating sample magnetometry provide methods to assess the effect of magnetic field on the broad transitions for the sample with x = 0.32 and the sharp transitions seen in the sample with x = 0.31.

INTRODUCTION

To fully realize solid-state cooling by magnetic refrigeration, further understanding of the impact of microstructure on the magnetocaloric effect is required. Modification of the microstructure can influence transition kinetics, leading to stronger, more efficient transformations, while lowering hysteresis.[1] Besides microstructure, new compositions that modify the intrinsic aspects of transitions and allow for higher reversibility also need to be explored.

In this context, the MM'X compounds (where M and M' are transition metals and X is a p-block element) are promising candidates for use with room temperature (RT) magnetic heat conversion technologies.[2–5] This is due to their versatile martensitic (diffusionless) transitions between a ferromagnetic martensite orthorhombic (*TiNiSi* structure-type, space group: *Pnma*) crystal structure and a paramagnetic austenite with a hexagonal structure (Ni_2In structure-type, space group: $P6_3/mmc$). This can lead to a strong isothermal entropy change (ΔS_m) and reasonable adiabatic temperature change (ΔT_{ad}). Such magnetostructural transitions (MSTs) are only possible by substituting one or more elements from the parent MM'X compound, which in turn modifies the structural transition temperature (T_{str}) and Curie Temperature (T_C) of both structures, making them coincide.

Recently, modifications of the (2*a*) Mn site by Fe and (2*c*) Si site by Al (when referring to the hexagonal crystal structure) successfully induced T_{str} towards RT.[2,4,6] Similarly, (2*d*) Ni site substitution by Fe has also been discussed.[7] In previous reports, MM'X materials have been produced by arc melting succeeded by thermal treatment at temperatures around 1073 K (800 °C) for an extended period of time (4–7 days), followed by quenching to RT.[2,4,8,9] However, little attention has been given to alternative heat treatment procedures for this kind of materials.

In this article, we report on the properties of two $Mn_{1-x}Ni_{1-x}Fe_{2x}Si_{0.95}Al_{0.05}$ compounds synthesized by arc melting which are heat treated by two different methods: with a single 1073 K step for 168 hours (sample A), and a 1073 K step for 168 hours preceded by a high temperature step at 1323 K for 5 hours (sample B), being quenched in water afterwards. Further

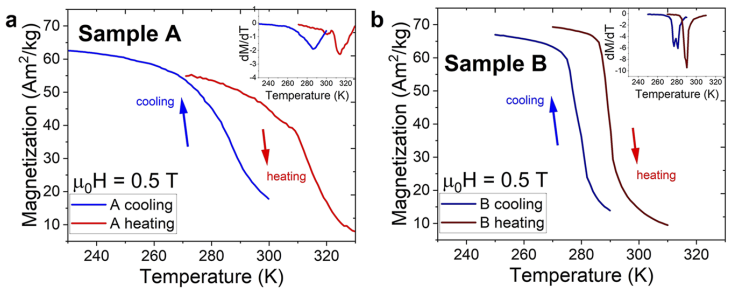

FIG. 1. Temperature-dependent magnetization for sample A and B evidencing the change in the magnetic transition due to the two different heat treatment procedures.

description of experimental and characterization methods is given in the supplementary information.

RESULTS

The magnetic transitions with an applied field of 0.5 T are presented in the temperature-dependent curves in Fig. 1. They are characterized by a decrease (or increase) of the magnetization during heating (or cooling) of the ingots. Transition values obtained from VSM are summarized in Table S1 in the supplementary material. The T_{str} value is determined from the derivative of the magnetization. The transitions in sample A (Fig. 1(a)) are broad and occur at 314 and 286 K during heating and cooling, respectively. The magnetization values during heating are changing from 55 to 8 Am^2/kg (ΔM = 47 Am^2/kg) in a temperature range of 57 K, from 272 to 329 K. The hysteresis values are also very high, reaching up to 27 K between the two transformations. In sample B, the transitions occur at 290 and 278 K during heating and cooling respectively, and are sharper, as indicated by the higher derivative of magnetization with temperature, seen in the inset of Fig. 1(b). The hysteresis values for sample B are also smaller than for sample A, reaching up to 11.3 K. An interesting feature of the cooling curve is the presence of two derivatives, indicating two different values for T_{str}. During the heating procedure, the magnetization in sample B changes from 66 to 17 Am^2/kg (ΔM = 49 Am^2/kg) in a temperature interval of 15 K, between 282 and 297 K. Therefore, the shifts in magnetization occur within smaller temperature spans in sample B, compared to sample A. To understand the difference between the transitions for the two samples, Powder X-ray Diffraction was carried out at RT, and is referred to in the supplementary material. The results indicate very similar phase contents between sample A and B. The way that such phases are distributed along the microstructure could shed light on its magnetic behavior. Therefore, optical microscopy and SEM measurements were performed.

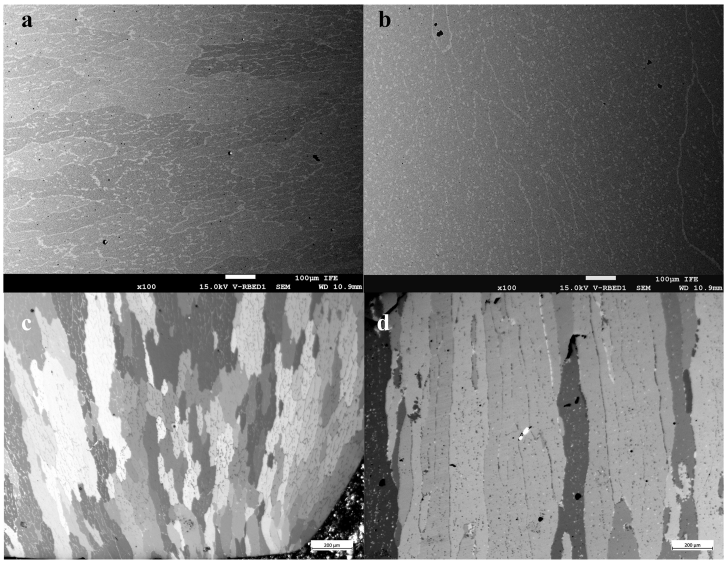

FIG. 2. Back-scattered SEM micrographs for (a) sample A and (b) sample B with 100 times magnification. Polarized optical microscopy images in (c) sample A and (d) sample B with 31.5 x magnification.

TABLE I. Chemical composition of Mn_{1-x} Ni_{1-x} Fe_{2x} $Si_{0.95}$ $Al_{0.05}$ with x = 0.32 (sample A) and 0.31 (sample B) as measured by EDS.

Sample A	Nominal composition of the alloy (formula units)	Area comp. (formula units)	Main phase composition (formula units)	Sample B	Nominal composition of the alloy (formula units)	Area comp. (formula units)	Main phase composition (formula units)
Mn(1 − x)	0.68	0.69 ± 0.01	0.67 ± 0.01	Mn (1 − x)	0.69	0.72 ± 0.01	0.69 ± 0.01
Ni(1 − x)	0.68	0.69 ± 0.01	0.66 ± 0.01	Ni (1 − x)	0.69	0.68 ± 0.01	0.64 ± 0.01
Fe(2x)	0.64 (x = 0.32)	0.64 ± 0.01	0.68 ± 0.01	Fe (2x)	0.62 (x = 0.31)	0.61 ± 0.01	0.66 ± 0.01
Si(0.95)	0.95	0.93 ± 0.01	0.94 ± 0.01	Si (0.95)	0.95	0.94 ± 0.01	0.95 ± 0.01
Al(0.05)	0.05	0.05 ± 0.01	0.05 ± 0.01	Al (0.05)	0.05	0.05 ± 0.01	0.06 ± 0.01

Back-scattered SEM micrographs for samples A and B are shown in Fig. 2. The ingots were prepared to display the solidification front of the alloys, i.e., the cross-section parallel to the arc direction during the arc melting process. For sample A (Fig. 2(a)) two phases can be seen from the contrast in the images, which correspond to the *Ni_2In*/*TiNiSi* (dark areas, the main phase) and *$MgZn_2$* hexagonal (clear areas) phases, respectively. Additionally, the secondary *$MgZn_2$* hexagonal phase can be seen inside the grains in different morphologies: as lines in sample A, and as lines and rounded precipitates in sample B (seen in Fig 2(b)).

The average composition for sample A and B as determined by area EDS measurements is similar to the nominal composition (see Table I). Regarding the area composition of the main phase (*Ni_2In* hexagonal/*TiNiSi* orthorhombic structure-type), the results display some differences from nominal compositions regarding the Ni content, which is slightly smaller than the nominal alloy composition. This can be correlated to the effect of different heat treatments, which might induce different phase fractions. The composition of the hexagonal *Ni_2In* phase is correlated to T_{str}, where higher modifications of the parent compound (Fe and Al modification) bring T_{str} to lower values. Between Fe and Al, Al has a stronger influence on the modification of T_{str}, which could explain the slightly lower T_{str} observed in sample B.

Due to the large grain sizes, the effect of the two different heat treatments can be better understood under lower magnifications in polarized light microscopy, see Figs. 2(c) and 2(d). The microstructure yielding from the regular heat treatment process is shown in Fig. 2(c), with columnar long grains yielding from the arc melting process. Different grey hues seen in the image represent different orientations in the grains, making it possible to estimate the grain sizes. The grain sizes feature great dispersion, ranging in length from tens of microns to several hundred microns.

The additional high-temperature step for sample B modifies the microstructure, as seen in Fig. 2(d). The grains have smaller variations in their crystallographic orientations, which leads to a smaller grey hue variation. Furthermore, the grains are larger compared to sample A, but with smaller size dispersion. Therefore, the higher temperature step of 5 hours at 1323 K creates substantial grain growth before the 168 hour (1 week) step. With bigger grains, a smaller amount of grain boundary areas is present in sample B compared to sample A. To further the understanding of the differences between the two samples, the transitions were analyzed with in-field DSC experiments.

Two ingots were selected, with masses of 6.41 and 4.41 mg for sample A and B, respectively. These small masses were chosen in order to minimize the risk of sample movement due to the applied field. A comparison of the transitions observed in both samples with a heating rate of 1 K/min is shown in Fig. 3, for applied fields of 0 and 1.3 T. The T_{str} and the hysteresis values for both samples are displayed in Table S1. It is possible to observe larger transition widths during cooling transformations than on heating for both samples. A broad transition spanning between 25–30 K is observed for sample A, with the cooling transformation temperature ($Tstr_{o\text{-}h}$) occurring at 287.8 K. The heating transformation temperature ($Tstr_{o\text{-}h}$) occurs at 302.0 K. Sample B features a sharper transition, with a width of 7–10 K occurring at $Tstr_{h\text{-}o}$ of 271.5 upon cooling and $Tstr_{o\text{-}h}$ of 287.8 K during heating. The absolute latent heat peak associated with the transitions in sample A is between

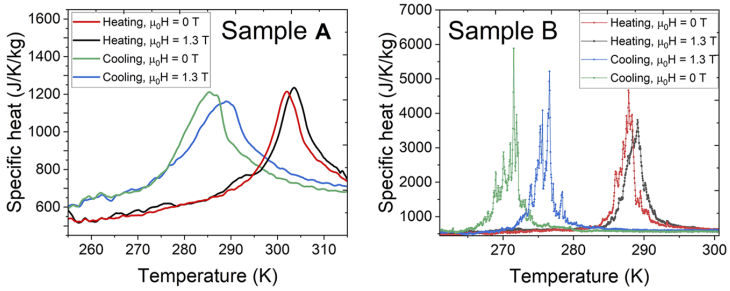

FIG. 3. Specific heat curves for sample A and B obtained from in-field DSC with applied fields of μ_0H = 0 and 1.3 T.

600–700 J/K^{-1}kg^{-1}, compared to 4000–5000 J/K.kg in sample B, which is a remarkable difference. Both samples appear to display a large thermal hysteresis of around 16 K between heating and cooling transformations.

A shift of peak positions to higher temperatures as the magnetic field is increased occurs for both transitions, with smaller shifts occurring during the heating transformation than compared to the cooling, for both samples. In both samples, the shift of $Tstr_{o\text{-}h}$ is around 1 K/T, whereas $Tstr_{h\text{-}o}$ is 2.9 and 3.9 K/T for samples A and B, respectively. This leads to smaller hysteresis values with higher applied fields.

DISCUSSION

The transformations during cooling and heating need to be analyzed separately. During heating transformation (ortho-to-hex), an anisotropic contraction occurs, with the compression along the *a* direction and an expansion in the *c* direction (based on the hexagonal unit cell).[10] This leads to an overall compression of the lattice, which induces a residual tensile stress. This residual stress impacts the material in addition to the expansion of the lattice during the hexagonal to orthorhombic (cooling) transformation, creating new surface area (cracking) to accommodate for the stresses in the brittle material. After several cycles, this will lower the cohesion between the particles, eventually pulverizing them, lowering the reversibility. However, some recent studies show promising results employing ductile metal composites that can keep cohesion of the particles and accommodate for the transformation stresses appropriately.[11]

Regarding the larger width of cooling transformations compared to heating, the release of residual tensile stress during the cooling transformation could contribute to lower the nucleation threshold of the orthorhombic phase, thus acting differently on the transitions during cooling than during heating. With a lower nucleation threshold for the martensitic phase, each grain would transition more easily, thereby spreading the transformation during cooling.

The sharp peaks in the specific heat curves for sample B (Fig. 3 and S3) can be associated to more homogeneous (lower) dispersion of the elements in the lattice (at the local level, not easily detectable by regular EDS techniques), since Mn, Ni and Fe can interchangeably occupy *2a* and *2d* sites in the *Ni$_2$In* crystal structure. This would lower the dispersion of the T_{str} values. A second reason is the increase of average grain sizes and decrease of its dispersion, which could modify the growth of new orth./hex. phases. As the mechanism of the growth of martensitic phase fronts is only deterred by interphase and grain boundaries, it would lead to a smaller volume of inhibiting agents during the transformation of sample B (with decreased volume of grain boundary areas) compared to sample A, and therefore easily transforming bigger volumes at once.

A more homogeneous structure and bigger grain sizes results in higher latent heat spikes (up to 5000 J/K^{-1}kg^{-1}), higher magnetization derivatives, and sharper transitions widths (7–10 K) for sample B. In comparison, the transitions measured by DSC for sample A span between 20–25 K, with a much smaller latent heat peak. While the transition appears broader, it is of first order, as a large thermal hysteresis is observed. A supporting evidence for the effect of grain size on the transition width is that in other MM'X system, (Mn,Fe)Ni(SiAl), melt-spun ribbons with small grain size in range of 10 microns feature much wider transition width, and subsequently, lower ΔS_m than arc-melted/bulk (Mn,Fe)Ni(Si,Al) samples undergoing long heat-treatment steps with large grain sizes.[6,9] Another method to compare both samples could be by analyzing the structural transition by temperature-dependent PXD. As the sample is typically grinded to submicrometric particles, they are not susceptible to the influence of different grain sizes, allowing each particle to transition on its own. If a sample features better homogeneity, all particles will transition within a smaller transition width.

CONCLUSION

The MST of $Mn_{1-x}Ni_{1-x}Fe_{2x}Si_{0.95}Al_{0.05}$ alloys was studied as a function of two different heat treatment procedures. The conventional heat treatment plateau at 1073 K (sample A) has been compared to a heat treatment where a high temperature step (1323 K) is introduced right before the regular heat treatment plateau, also at 1073 K (sample B). Temperature-dependent magnetization results reveal that sample A features a broad magnetization change across RT, with transitions occurring between 314 to 286 K, for heating and cooling transformations, while sample B features a sharper magnetization variation, occurring at 290 and 280 K for heating and cooling, respectively.

Despite similar phase presences, average structures and compositions as measured by PXD and SEM/EDS, much larger grains are observed for sample B than for sample A. The results indicate that the high temperature step induced better homogeneity and increased grain sizes, which would induce higher volume fractions to transform at once, leading to increased latent heat spikes. Nevertheless, a more detailed study on the isothermal entropy changes of heating and cooling transitions is required to obtain a full picture of the effect of heat treatment on the properties of $Mn_{1-x}Ni_{1-x}Fe_{2x}Si_{0.95}Al_{0.05}$ compounds.

SUPPLEMENTARY MATERIAL

See supplementary material for the description of experimental methods and further data analysis.

ACKNOWLEDGMENTS

This work was financed by The Research Council of Norway through the NANO2021 program, Project No. 287150.

AUTHOR DECLARATIONS

Conflict of Interest

The authors have no conflicts to disclose.

Author Contributions

Bruno G. F. Eggert: Conceptualization (equal); Data curation (equal); Formal analysis (equal); Investigation (equal); Methodology (equal); Visualization (equal); Writing – original draft (equal); Writing – review & editing (equal). **Kun Wang**: Investigation (equal); Resources (equal); Writing – review & editing (equal). **Sina Jafarzadeh**: Investigation (equal); Resources (equal). **Christian R. Bahl**: Investigation (equal); Resources (equal); Writing – review &

editing (equal). **Bjørn C. Hauback**: Supervision (equal); Writing – review & editing (equal). **Christoph Frommen**: Funding acquisition (equal); Project administration (equal); Supervision (equal); Writing – review & editing (equal).

DATA AVAILABILITY

The data that support the findings of this study are available from the corresponding author upon reasonable request.

REFERENCES

[1]O. Gutfleisch, T. Gottschall, M. Fries, D. Benke, I. Radulov, K. P. Skokov, H. Wende, M. Gruner, M. Acet, P. Entel, and M. Farle, Philos. Trans. R. Soc. A Math. Phys. Eng. Sci. **374**, 6607 (2016).
[2]A. Biswas, N. A. Zarkevich, Y. Mudryk, A. K. Pathak, A. V. Smirnov, V. P. Balema, D. D. Johnson, and V. K. Pecharsky, J. Appl. Phys. **129**, 193901 (2021).
[3]S. K. Pal, C. Frommen, S. Kumar, B. C. Hauback, H. Fjellvåg, and G. Helgesen, Mater. Des. **195**, 109036 (2020).
[4]C. L. Zhang, H. F. Shi, Y. G. Nie, E. J. Ye, Z. D. Han, and D. H. Wang, Appl. Phys. Lett. **105**, 242403 (2014).
[5]L. M. Moreno-Ramírez, Á. Díaz-García, J. Y. Law, A. K. Giri, and V. Franco, Intermetallics **131**, 107083 (2021).
[6]M. L. Arreguín-Hernández, C. F. Sánchez-Valdés, and J. L. Sánchez Llamazares, J. Magn. Magn. Mater. **533**, 168021 (2021).
[7]B. Nuendute, W. Hanggai, H. Yibole, B. Tana, O. Tegus, and F. Guillou, Crystals **12**, 233 (2022).
[8]C. L. Zhang, Y. G. Nie, H. F. Shi, E. J. Ye, J. Q. Zhao, Z. D. Han, H. C. Xuan, and D. H. Wang, J. Magn. Magn. Mater. **432**, 527 (2017).
[9]A. Biswas, A. K. Pathak, N. A. Zarkevich, X. Liu, Y. Mudryk, V. Balema, D. D. Johnson, and V. K. Pecharsky, Acta Mater. **180**, 341 (2019).
[10]T. Zhang, Y. Gong, B. Wang, D. Cen, and F. Xu, J. Mater. Sci. Technol. **104**, 59 (2022).
[11]H. Zhou, K. Tao, B. Chen, H. Chen, K. Qiao, Z. Yu, J. Cong, R. Huang, S. V. Taskaev, and H. Zhang, Acta Mater. **229**, 117830 (2022).

{2.7182818284}ϑφέρτυθιοπσδφγηξκλ